THESIS
4
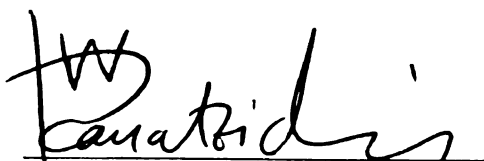O٥٥

This is tᵥ certify that the

dissertation entitled

Studies on the Reactivity of Coinage Metals and Rare Earth Metals in Alkali Metal/Polytelluride Fluxes

presented by

Rhonda Reneé Patschke

has been accepted towards fulfillment
of the requirements for

_____Ph.D._____ degree in _____Chemistry_____

Major professor

Date 12/14/99

PLACE IN RETURN BOX to remove this checkout from your record.
TO AVOID FINES return on or before date due.
MAY BE RECALLED with earlier due date if requested.

DATE DUE	DATE DUE	DATE DUE

11/00   c/CIRC/DateDue.p65-p.14

STUDIES ON THE REACTIVITY OF COINAGE METALS AND RARE

EARTH METALS IN ALKALI METAL/POLYTELLURIDE FLUXES

By

Rhonda Reneé Patschke

A DISSERTATION

Submitted to

Michigan State University

in partial fulfillment of the requirements

for the degree of

DOCTOR OF PHILOSOPHY

Department of Chemistry

1999

ABSTRACT

STUDIES ON THE REACTIVITY OF COINAGE METALS AND RARE EARTH METALS IN ALKALI METAL/POLYTELLURIDE FLUXES

By

Rhonda Reneé Patschke

Over the past decade, the polychalcogenide flux method has become an established technique for discovering new solid state compounds. The advantage to using molten fluxes is that they allow the reaction system to choose its own route (either kinetic or thermodynamic) without forcing it to a certain stoichiometry or structure type. The materials discovered by this method can be used for a wide variety of applications, including batteries, lasers, non-linear optics, photovoltaics, composites, and thermoelectrics. In order to maximize the probability that the compounds formed will possess new structure types, a quaternary system was explored in which two metals with very different coordination preferences, namely a coinage metal and a rare earth metal, were reacted in an alkali metal/polychalcogenide flux. Explorations in this system with sulfur and selenium proved to be successful, and so we decided to expand this chemistry into the polytelluride system. As a result, several new compounds were discovered and most notably, the structure types formed were very different than

those previously found in the sulfur and selenium systems. Many of the compounds contain stacking layers that can be described as a square Te net. These Te nets have a propensity to distort, which gives rise to subtle crystallographic superstructures.

In this dissertation, the synthesis, structure, and physicochemical properties of many new phases will be reported. In systems where only a rare earth metal reacted in a molten A_2Te_x flux, the family of compounds ALn_3Te_8 was discovered whose members include $CsCe_3Te_8$, $RbCe_3Te_8$, KCe_3Te_8, and KNd_3Te_8. Several quaternary phases of the type $A_wM_xLn_yTe_z$ were also discovered by reacting both a coinage metal and a rare earth metal in a molten A_2Te_x flux, including $CsCuUTe_3$, $RbCuUTe_3$, $KCuUTe_3$, $KCuCeTe_4$, $RbCuCeTe_4$, $Na_{0.8}Ag_{1.2}CeTe_4$, $K_{2.5}Ag_{4.5}Ce_2Te_9$, $K_{2.5}Ag_{4.5}La_2Te_9$, $K_2Ag_3CeTe_4$, $Rb_2Cu_3CeTe_5$, KCu_2EuTe_4, $Na_{0.2}Ag_{2.8}EuTe_4$, and $K_{0.65}Ag_2Eu_{1.35}Te_4$. In the case where a flux was not used, the ternary phase Cu_xUTe_3 (x = 0.25 and 0.33) was discovered. Finally, the cage compounds $A_2MCu_8Te_{10}$ ($K_2BaCu_8Te_{10}$, $Rb_2BaCu_8Te_{10}$, $Cs_2BaCu_8Te_{10}$, and $Rb_2EuCu_8Te_{10}$) were investigated for their promising thermoelectric properties.

ACKNOWLEDGEMENTS

First of all, I wish to thank the people who inspired me early on in my career. Without them, I might have fallen through the cracks and then certainly would not have made it here today. These people include Dr. Raghu Menon, Dr. Emel Yakali, Dr. Ken Koehler, Mrs. Ann Spector, Dr. Bruce Ault, and Dr. Barbara Stout.

As far as my time at Michigan State University is concerned, I owe a great deal to my advisor, Professor Mercouri Kanatzidis. Over the past 5 years, he has given me a tremendous amount of encouragement, support, and guidance. He has helped me to strive to be the scientist I am today and for that, I will always be grateful. I consider him to be a role model for many reasons. Mostly, however, I admire how he has managed to truly preserve his basic love for science over the years. He demonstrates this every day of his life. I only hope that I am able to do the same because I, also, want to wake up every day and be excited to go to work.

Next, I would like to thank the people with whom I have collaborated. Without them, I would not have been able to accomplish the quality of work presented throughout this dissertation. These collaborations have not only taught me how to work as a team, but also that I don't necessarily need to limit myself to questions within my research that only I can answer. These people include Prof. Carl Kannewurf, Dr. Jon Schindler, Mr. Paul Brazis, Dr. Victor Young, Prof.

Sander van Smallen, Prof. Michel Evain, Prof. Terry Tritt, Mr. Nathan Lowhorn, and Dr. George Nolas.

In addition, I would like to thank the staff at Michigan State University who helped me with the techniques I needed for my research. These people include Dr. John Heckman, Dr. Reza Loloee and Dr. Jerry, Cowen, Dr. Stan Flegler, Dr. Rui Wang, and Dr. Don Ward.

Furthermore, I would like to thank the members of the Kanatzidis group, past and present, for all of their support. These are the people who cheered me up when my experiments weren't working and celebrated with me when they were.

Last but not least, I would like to recognize my fiancée, Paul Willigan. I cannot even begin to explain how much love and support he has given me over the years. Even though he was 300 miles away, I needed him every step of the way and am looking forward to spending the rest of my life "geographically" closer to him.

TABLE OF CONTENTS

LIST OF TABLES

xvi

LIST OF FIGURES

LIST OF ABBREVIATIONS

DMF   Dimethylformamide

DTA   Differential Thermal Analysis

EDS   Energy Dispersive Spectroscopy

ICP   Inductively Coupled Plasma

IR   Infrared Spectroscopy

PDF   Pair Distribution Function

SAED   Selected Area Electron Diffraction

SEM   Scanning Electron Microscopy

SQUID   Superconducting Quantum Interference Device

TEM   Transmission Electron Microscopy

Chapter 1

The Rationale for Combining Coinage Metals and Rare Earth Metals in Molten

Alkali Metal/Polytelluride Fluxes

A. Introduction

Over the past two decades, we have watched the world undergo a technological revolution. In doing so, many electronic devices, such as computers, have become an everyday commodity and very much a necessity to our lives. Solid state chemistry has certainly played an important role in helping with this advancement. Such technologies as high density storage batteries,[1,2] photovoltaics,[3] electroluminescence,[4] nonlinear optics,[5] high T_c superconductors,[6] catalysis,[7] and thermoelectrics[8] depend on the development of new solid state materials. Therefore, much of the work within the solid state community is focused either on the improvement of known material for a specific application or the discovery of new materials for further technological advancements. These new materials are generally discovered via an "exploratory" approach by searching for new compounds in previously unexplored areas.

In the past, this "exploratory" approach involved combining high melting elements together in a vacuum and heating them at very high temperatures. This is the so-called ceramic method of synthesis. While this proved useful in discovering new compounds, there were many problems attributed to this method. First, the reactants never reached a true molten state and therefore the reaction occurred via diffusion. In order to acquire a homogeneous product, the product often had to be reground after the first heating and subsequently reheated. This "heat – grind – heat – grind" process was continued until the reaction was complete. Another problem with this method was that, due to the high

2

temperatures needed for diffusion, only the most thermodynamically stable products were obtained. The more complex compounds made up of three or four elements seemed unattainable. Finally, the products formed were often in powder form, making structure determination difficult if not impossible.

Compared to solution chemistry, where the reactants are able to undergo "infinite" diffusion, solid state chemistry was in dire need of major synthetic advancements. This is precisely what occurred, leading to such synthetic techniques as chemical vapor deposition (CVD),[9] hydrothermal and solvothermal synthesis,[10] eutetic combination of binary salts,[11] and molten fluxes.[12] The work presented in this dissertation is focused mainly on the use of molten fluxes; in particular, molten alkali metal/polychalcogenide fluxes.

B. Nature of the Polychalcogenide Flux

Only over the past 12 years has the polychalcogenide flux method become an established technique for discovering new solid state compounds. While molten salts have been used for over 100 year as a high temperature recrystallization media for a variety of binary and ternary compounds,[13] it was not until 1987 when they were used at lower temperatures to synthesize new compounds.[14] Since then, literally hundreds of new compounds have been reported.[15] One advantage to using molten fluxes is that they allow the reaction system to choose its own route (either kinetic or thermodynamic) without forcing it to a certain stoichiometry or structure type. Therefore, metastable phases that

3

could not be synthesized previously are now accessible. This is largely due to the fact that the flux is a low melting salt and thus the reaction can be carried out at relatively lower temperatures. The melting points of several alkali metal/polychalcogenide salts (A_2Q_x) are given in Table 1.2, which illustrates how the melting points more or less decrease with increasing x value. The flux, once molten, acts both as a solvent and a reactant, incorporating the chalcogenide and/or the alkali metal into the final product. In addition, the flux facilitates crystal growth. Small or poorly formed crystallites can redissolve in the flux and then reprecipitate as larger, well-formed crystals. This is called the mineralizer effect. Finally, the crystalline product, albeit powder or crystal form, can easily be isolated by dissolving the excess flux in simple polar solvents such as methanol or DMF.

Table 1.1   Melting points for some known alkali metal/polychalcogenide (A_2Q_x) species.[16,17]

Li_2S 900-975°C	Li_2S_2 369°C				
Na_2S 1180°C	Na_2S_2 490°C	Na_2S_3 228°C	Na_2S_4 275°C	Na_2S_5 252°C	
K_2S 840°C	K_2S_2 470°C	K_2S_3 252°C	K_2S_4 145°C	K_2S_5 206°C	K_2S_6 189°C
Rb_2S 530°C	Rb_2S_2 420°C	Rb_2S_3 213°C	Rb_2S_4 160°C	Rb_2S_5 225°C	Rb_2S_6 201°C
	Cs_2S_2 460°C	Cs_2S_3 217°C	Cs_2S_4 160°C	Cs_2S_5 210°C	Cs_2S_6 186°C
Na_2Se >875°C	Na_2Se_2 495°C	Na_2Se_3 313°C	Na_2Se_4 290°C		Na_2Se_6 258°C
	K_2Se_2 460°C	K_2Se_3 380°C	K_2Se_4 205°C	K_2Se_5 190°C	
Na_2Te 953°C	Na_2Te_2 348°C				Na_2Te_6 436°C
K_2Te 900°C		K_2Te_3 429°C	K_2Te_4 266°C	K_2Te_5 268°C	K_2Te_6 264°C
Rb_2Te 775°C		Rb_2Te_3 400°C		Rb_2Te_5 270°C	
Cs_2Te 820°C		Cs_2Te_3 395°C	Cs_2Te_4 221°C - 237°C	Cs_2Te_5 235°C	Cs_2Te_6 226°C

The reaction between the A_2Q_x flux and the metals occurs *in situ*. A typical reaction mixture consists of $A_2Q/M/M'/Q$ where the ratio of A_2Q/Q is varied from reaction to reaction. Although it is still unclear the actual mechanism of this reaction, conceptually it can broken down into two steps. In the first step, the A_2Q species reacts with the Q to form the A_2Q_x flux (see Scheme 1). As a result, long polychalcogenide chains are formed due to their natural ability to catenate.

Scheme 1

$$mA_2Q + nQ \xrightarrow[(1)]{\Delta} 2mA^+ + {}^-[Q-Q_x-Q]^- \xrightarrow[(2)]{M/M'} A_wM_xM'_yQ_z$$
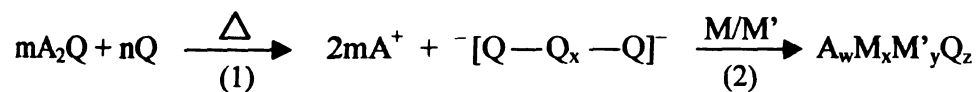
These polychalcogenide chains are made up of two types of chalcogenide atoms: i) the internal atoms that carry a zero-valent charge and ii) the terminal atoms that carry each a 1- charge. In the second step, these polychalcogenide chains react with the metals in the mixture, split, and form a metal chalcogenide framework. The internal atoms act to oxidize the metal while they themselves are reduced. The terminal atoms, due to their negative charge, act as Lewis base sites to coordinate to the metal species.

The length of these polchalcogenide chains and therefore the relative basicity of the reaction depends strongly on the A_2Q/Q ratio. If more Q (or less A_2Q) is added to the reaction mixture, longer polytelluride chains will form. Therefore, there are more internal atoms and the reaction mixture will be more oxidizing. Conversely, if more A_2Q (or less Q) is added to the reaction mixture,

6

shorter polytelluride chains will form. Therefore, there are more terminal atoms and the reaction mixture will be more reducing. By varying the A_2Q/Q ratio, it is possible to explore a chemical system under a wide range of conditions. This is important since some compounds will form only under certain conditions.

C.   Synthetic Approach

The system chosen for study in this dissertation was a quaternary one of the type $A_wM_xLn_yTe_z$, where M is a coinage metal (Cu, Ag) and Ln is a rare earth metal (lanthanide or actinide). Explorations in this system with sulfur and selenium were done previously and the results proved encouraging.[18,18] These two metals were chosen mainly for the fact that they come from very different parts of the periodic table and thus have very different coordination preferences. While the coinage metals prefer smaller coordination numbers such as 3 or 4, the rare earth metals desire larger coordination numbers ranging from 6 to 9. Also, the coinage metals are more covalent in their bonding while the rare earth metals tend to be more ionic. These differences should maximize the probability that, when the two metals come together, the compounds formed will possess new structure types. Indeed, several new structure types were formed (reviewed below) which show interesting properties such as mixed valency and enhanced conductivity. Therefore, we decided to extend this chemistry into the telluride system. As will be illustrated throughout this dissertation, most of the structure types formed are strikingly different from those found in the sulfide and selenide systems.

D. Review of Quaternary A/M/Ln/Q Phases

The first compounds reported in the A/M/Ln/Q system were $KCuCe_2S_6$ and $K_2Cu_2CeS_4$ by Kanatzidis and Sutorik in 1994.[18] Later, the three compounds $KCuLa_2S_6$, $CsCuCe_2S_6$, and $KCuCe_2Se_6$ were added to the $ACuLn_2Q_6$ family.[19] The structure of $ACuLn_2Q_6$ is two-dimensional and is composed of $[LnS_8]$ bicapped trigonal prisms that stack in one-dimension by sharing triangular faces to form chains parallel to the b-axis (see Figure 1.1). Layers are then formed when neighboring chains share monosulfides. The layers are analogous to the known phase, $ZrSe_3$.[20] Within the layers, there are tetrahedral sites where the Cu^+ ions reside. Finally, the K^+ cations reside in the interlayer gallery. The structure refinement gave a model in which one copper atom was disordered over two crystallographically distinct sites. Therefore, it was thought that the Cu^+ ions were statistically distributed over a large excess of tetrahedral sites, leading to possible ionic conductivity. However, Bensch and coworkers later discovered $KCuEu_2S_6$ and found it to possess a 2a x 2b x 2c supercell which removed the disorder from the original model.[21] In the superstructure, only one half of the copper sites are occupied which results in a periodic arrangement of the Cu^+ ions along all three axes.

The two-dimensional structure of $K_2Cu_2CeS_4$[18] is shown in Figure 1.2. The anionic layers are composed of $[CeS_6]$ octahedra and $[CuS_4]$ tetrahedra. The $[CeS_6]$ octahedra share edges in one-dimension to form chains. Layers are formed when these chains alternate with double rows of edge-sharing $[CuS_4]$ tetrahedra.

The repeat pattern across the layer is therefore [oct-tet-tet-oct-tet-tet]. The layers are separated by K^+ ions that are stabilized in a seven coordinate monocapped trigonal prismatic environment of sulfur. This structure type is not particular to the rare earth metals, as it was found to also exist for $Na_2Cu_2ZrS_4$.[22] Interestingly, the formal charges on $K_2Cu_2CeS_4$ cannot be balanced simply by invoking Cu^+, Ce^{3+}, and S^{2-}. Three possible formalisms therefore exist: $(K^+)_2(Cu^+)_2(Ce^{4+})(S^{2-})_4$, $K_2(Cu^{1+})_2(Ce^{3+})(S^{2-})_3(S^{1-})$, or $(K^+)_2(Cu^+)(Cu^{2+})(Ce^{3+})(S^{2-})_4$. Magnetic susceptibility measurements have ruled out the first possibility by verifying the existence of Ce^{3+} in the compound. Since Cu^{2+} is too oxidizing to coexist with S^{2-}, the most logical formalism was chosen to be the second one. This mixed S^{2-}/S^{1-} model places holes in the sulfur p-band, which predicts high conductivity. This was not experimentally observed, however, and it was speculated from this that the narrow valence bands in the compound are acting to limit the mobility of the S^{1-} holes and small polarons could be forming which act to frustrate the carriers.

Many other compounds found in the A/M/Ln/Q system were found to have the general formula, $AMLnQ_3$, yet they do not all possess the same structure type. There are four known structure types that exist for this stoichiometry, see Figure 1.3. Of these four, however, structure type A is the most stable. In the past five years, many members have been added to this large family, including $KCuUSe_3$,[19] $CsCuCeS_3$,[19] $CsCuUTe_3$,[23] $BaCuLnS_3$ (Ln = Sc, Y, Gd, Er),[24] $BaCuLnSe_3$ (Ln = Y, Er),[24] $BaCuDyTe_3$,[25] $BaCuLnTe_3$ (Ln = Y, La, Pr, Nd, Yb),[26] $BaAgNdS_3$,[24] $BaAgLnSe_3$ (Y, La, Er),[24] $BaAgLnTe_3$ (Ln = Y, La, Gd),[26] and $BaAuGdSe_3$.[26]

Much like $K_2Cu_2CeS_4$, this $AMLnQ_3$ structure type [A] is comprised of $[LnQ_6]$

octahedra and $[MQ_4]$ tetrahedra. However, the $[LnQ_6]$ octahedra now edge-share

with "single" rows of $[MQ_4]$ tetrahedra instead of the "double" rows found in

$K_2Cu_2CeS_4$. Therefore, the repeat pattern across the layer is [oct-tet-oct-tet]. A

slightly distorted version of this structure type also exists in which some of the

bonds are lengthened, due to the larger rare-earth elements used. This causes the

symmetry to drop for the above phases from Cmcm to Pnma. The compounds that

crystallize in this space group are $BaCuLnS_3$ (Ln = Ce, Nd),[24,27] β-$BaCuLaSe_3$,[24,27]

$BaCuCeSe_3$,[24] and $BaCuLaTe_3$.[26]

The second structure type [B] having the general formula $AMLnQ_3$ is

shown in Figure 1.3B. The structure is related to the previous two structure types

in that the layers are comprised of $[LnQ_6]$ octahedra and $[MQ_4]$ tetrahedra. In this

case, however, the layers are made up of alternating *pairs* of octahedra and *pairs*

of tetrahedra. Therefore, the repeat pattern across the layer is [oct-oct-tet-tet-oct-

oct]. Interestingly, the compounds that adopt this structure type are more

specifically of the type $AMMQ_3$, since both metals are transition metals (e.g.,

$NaCuTiS_3$, $NaCuZrSe_3$, $NaCuZrTe_3$).[22] However, it is not unreasonable to assume

that a rare earth metal could take the place of the octahedral transition metal.

The third structure type [C] having the formula $AMLnQ_3$ is shown in

Figure 1.3C. It is three-dimensional and, interestingly, is not related to either of

the above structure types [A or B]. To date, only one compound is known to adopt

this structure type, $BaAgErS_3$.[15c,28] It crystallizes in the monoclinic space group,

C2/m and is made up of [ErS$_6$] octahedra and [AgS$_5$] trigonal bipyramids. The [ErS$_6$] octahedra share edges in a zigzag manner to form double-chains that run down the b-axis. These chains then share corners along the a-axis to form two-dimensional layers. The layers are further connected into a three-dimensional framework through pairs of corner sharing [AgS$_5$] trigonal bipyramids (Ag$_2$S$_9$ units). The Ba^{2+} ions occupy the sites inside the channels and are stabilized in a 7-coordinate monocapped trigonal prsmatic environment.

The fourth structure type [D] having the formula AMLnQ$_3$ is shown in Figure 1.3D. The two compounds that adopt this structure type (BaCuLaS$_3$ and α-BaCuLaSe$_3$)[24,27] crystallize in the orthorhombic space group, Pnma. However, since this structure type is different from that of the second structure type [B], which also crystallizes as Pnma, this structure will be denoted as Pnma (II) while structure type [B] will be denoted as Pnma (I). The structure is made up of [LaS$_7$] monocapped trigonal prisms that make edge sharing connections with [CuS$_4$] tetrahedra to form a three-dimensional framework. Interestingly, α–BaLaCuSe$_3$ can be transformed to the β–phase of BaLaCuSe$_3$ (structure type A) by annealing at elevated temperatures. Conversely, the α–phase can be generated from the β–phase by mechanical grinding. The reason that these two structures can be converted back and forth is that they are structurally very similar. In the α–phase the La atoms are 6-coordinate octahedral while in the β–phase, they are 7-coordinate monocapped trigonal prismatic. The transition from the α–phase to the

β-phase involves a distortion of the octahedral La atoms so that they may bond to another sulfur atom from adjacent layers.

Another structure type that was found in the A/M/Ln/Q system was $KCuGd_2S_4$.[29] The structure of this compound is shown in Figure 1.4 and is again made up of $[GdS_6]$ octahedra and $[CuS_4]$ tetrahedra. Structurally, it is very similar to $BaAgErS_3$ (structure type [C] of $AMLnQ_3$). In $BaAgErS_3$, double chains of $[ErS_6]$ octahedra are connected into a three-dimensional framework through pairs of corner sharing $[AgS_5]$ trigonal bipyramids (Ag_2S_9 units). These same $[LnQ_6]$ double chains exist in $KCuGd_2S_4$, only now they are connected into a three-dimensional framework by single $[CuS_4]$ tetrahedra units. As a result, there is less Cu (per Gd) in the chemical formula and the channels that run through this structure are smaller. Although the channels are smaller in $KCuGd_2S_4$, the coordination environment inside the channel is larger. While the Ba^{2+} ions in $BaAgErS_3$ are monocapped trigonal prismatic, the K^+ ions in $KCuGd_2S_4$ are bicapped trigonal prismatic. This could be attributed to the fact that the ionic radii of K^+ (1.52 Å) is slightly larger than that of Ba^{2+} (1.49 Å). However, a more logical explanation may be the different coordination environments around the coinage metals. In $BaAgErS_3$, the silver atoms are trigonal bipyramidal while the copper atoms in $KCuGd_2S_4$ are tetrahedral. Therefore, the different sized tunnels that host the alkali/alkali earth metals could simply be a manifestation of the different coordination environments around the coinage metals.

Finally, the compound $K_6Cu_{12}U_2S_{15}$ was synthesized in our lab by A.C. Sutorik and further characterized by myself.[30] This three-dimensional compound is shown in Figure 1.5. Although the structure is too complex to discuss in much detail here, the basic building block is one of a [US_6] octahedra which edge shares with six [CuS_3] trigonal planar units. Much like $K_2Cu_2CeS_4$, the charges cannot be balanced on this compound without invoking some S^{2-}/S^{1-} mixed valency. This mixed valency again places holes in the valence band and predicts high conductivity. Unlike $K_2Cu_2CeS_4$, however, where the narrow valence bands limit the carrier's mobility, $K_6Cu_{12}U_2S_{15}$ shows metallic behavior. This can be attributed to its highly covalent, three-dimensional framework.
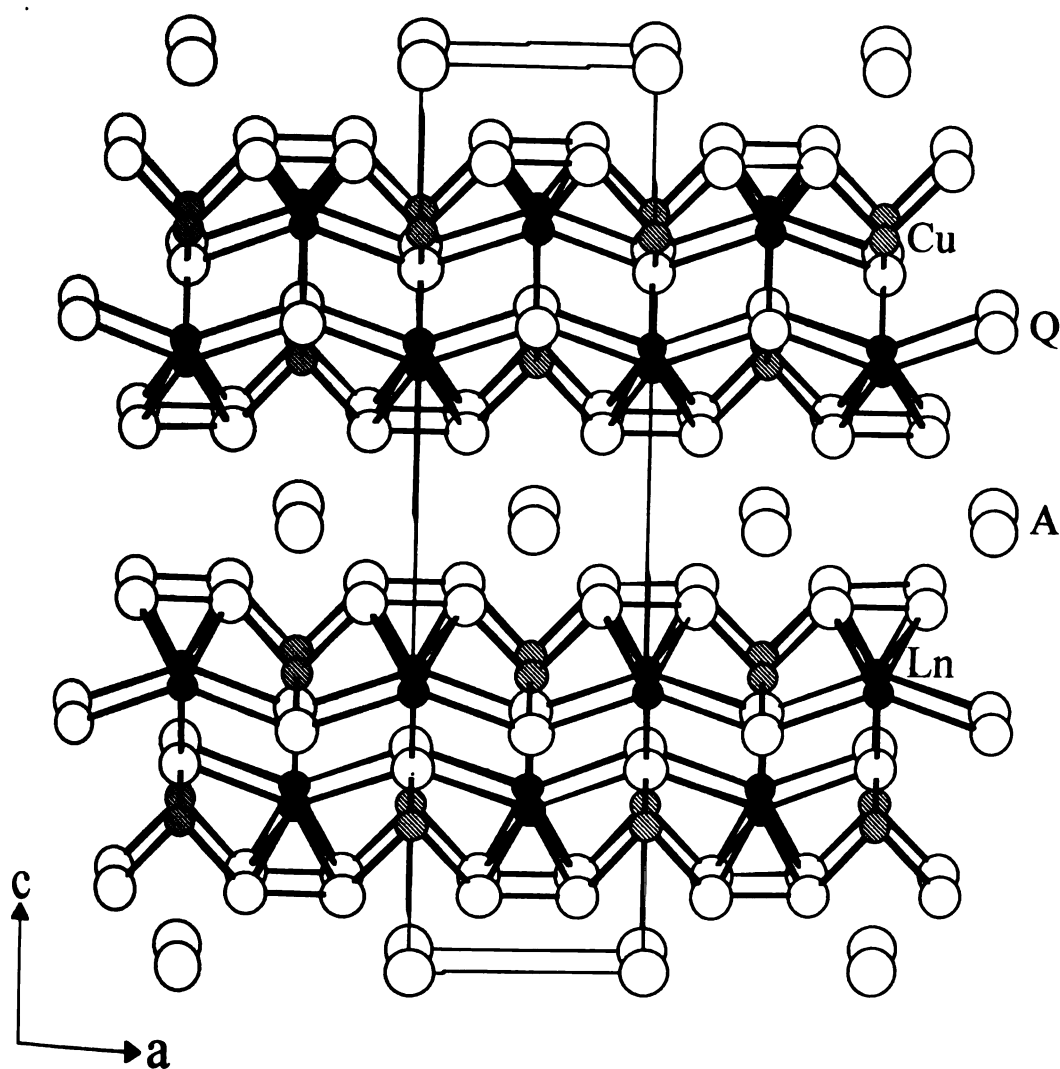
Figure 1.1 Extended structure of $ACuLn_2Q_6$ as seen down the b-axis. Black circles represent Ln atoms, striped circles represent Cu atoms, and large open circles represent A and Q atoms.
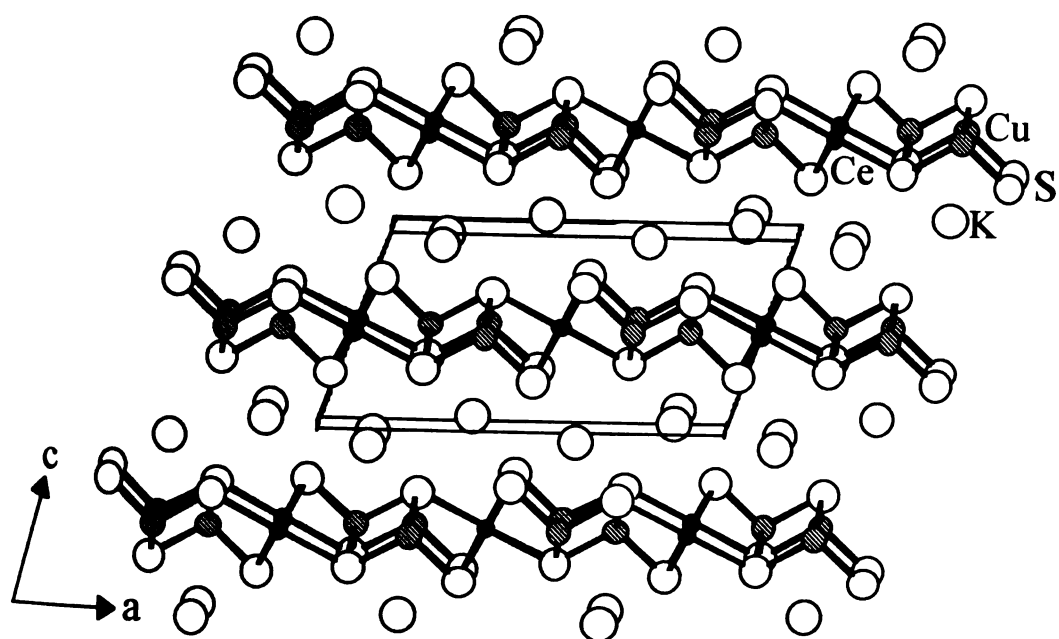
Figure 1.2 Extended structure of $K_2Cu_2CeS_4$ as seen down the b-axis. Black circles represent Ce atoms, striped circles represent Cu atoms, and large open circles represent K and S atoms.
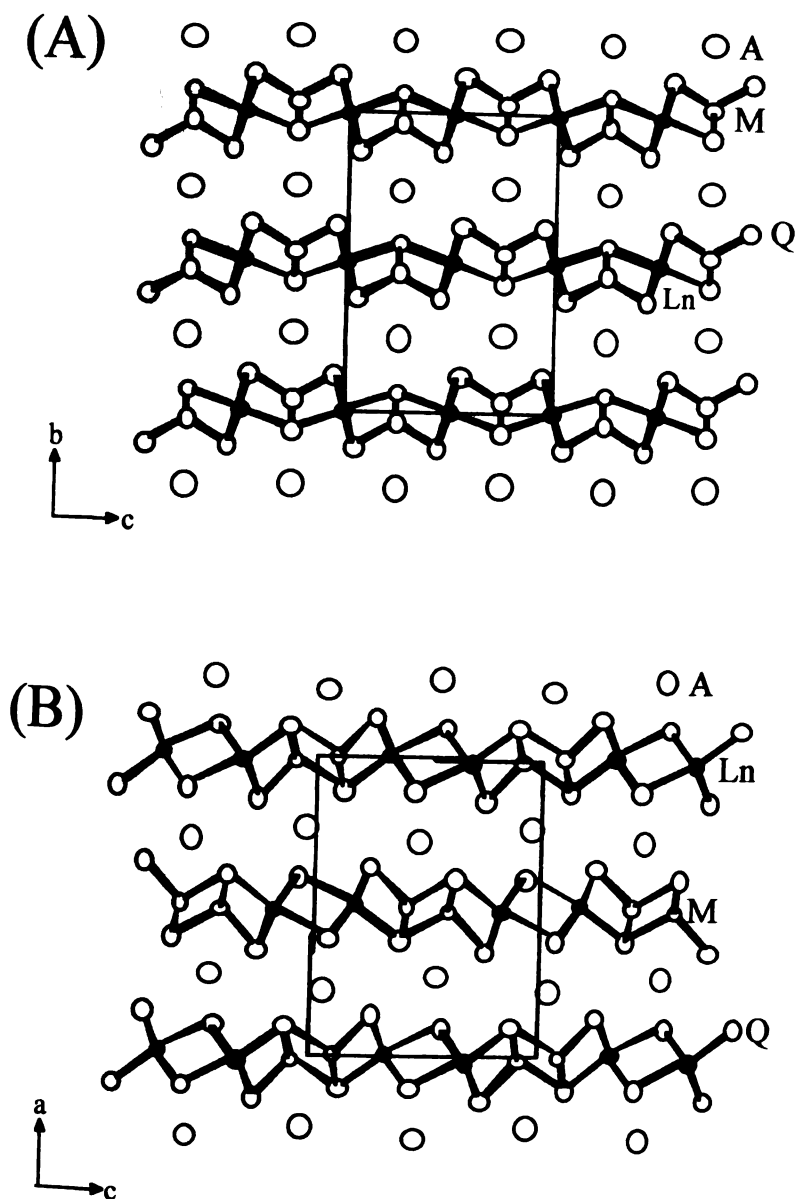
Figure 1.3 (A) Cmcm structure type of $AMLnQ_3$ (e.g.; $KCuUSe_3$) and (B) Pnma (I) structure type of $AMLnQ_3$ (e.g.; $NaCuTiS_3$). The small open circles represent M atoms, the black circles represent Ln atoms, and the large open circles represent A and Q atoms.

16
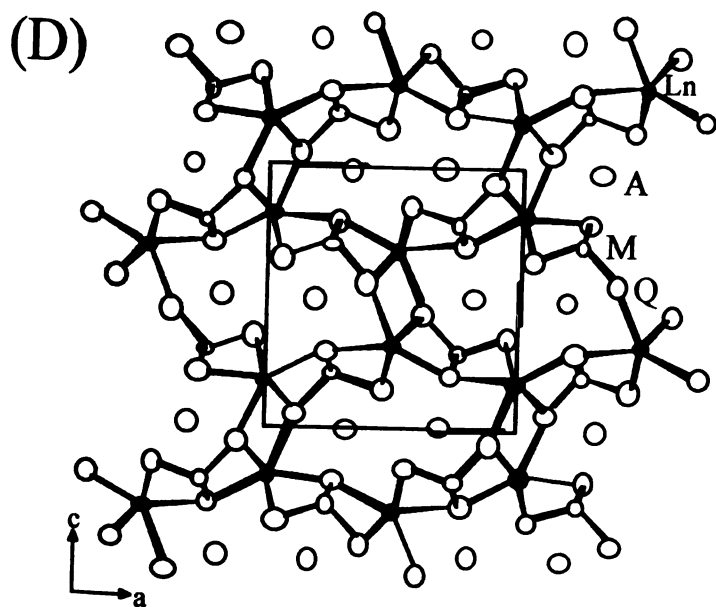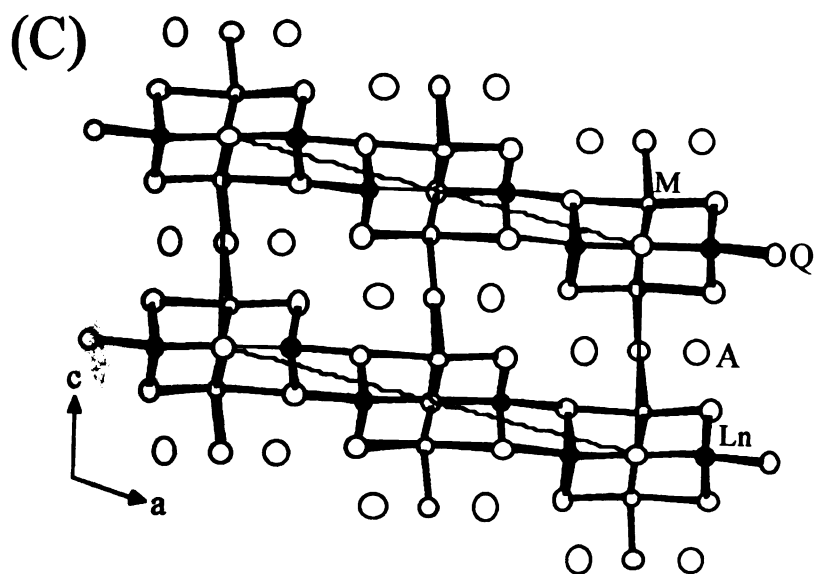
Figure 1.3 continued (C) C2/m structure type of AMLnQ$_3$ (e.g.; BaAgErS$_3$) and (D) Pnma (II) structure type of AMLnQ$_3$ (e.g.; BaCuLaS$_3$). The small open circles represent M atoms, the black circles represent Ln atoms, and the large open circles represent A and Q atoms.
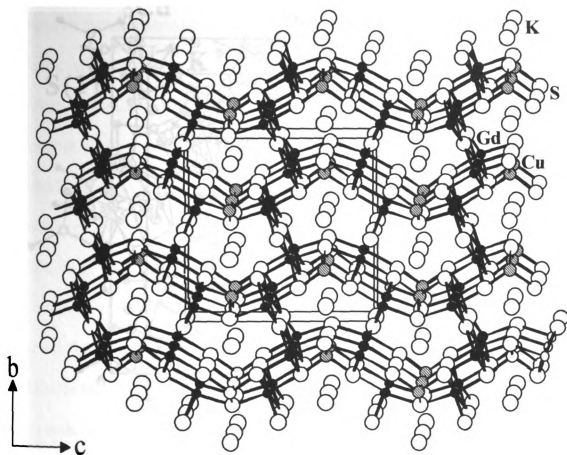
Figure 1.4 Extended structure of $KCuGd_2S_4$ as seen down the a-axis. Black circles represent Gd atoms, striped circles represent Cu atoms, and large open circles represent K and S atoms.

18
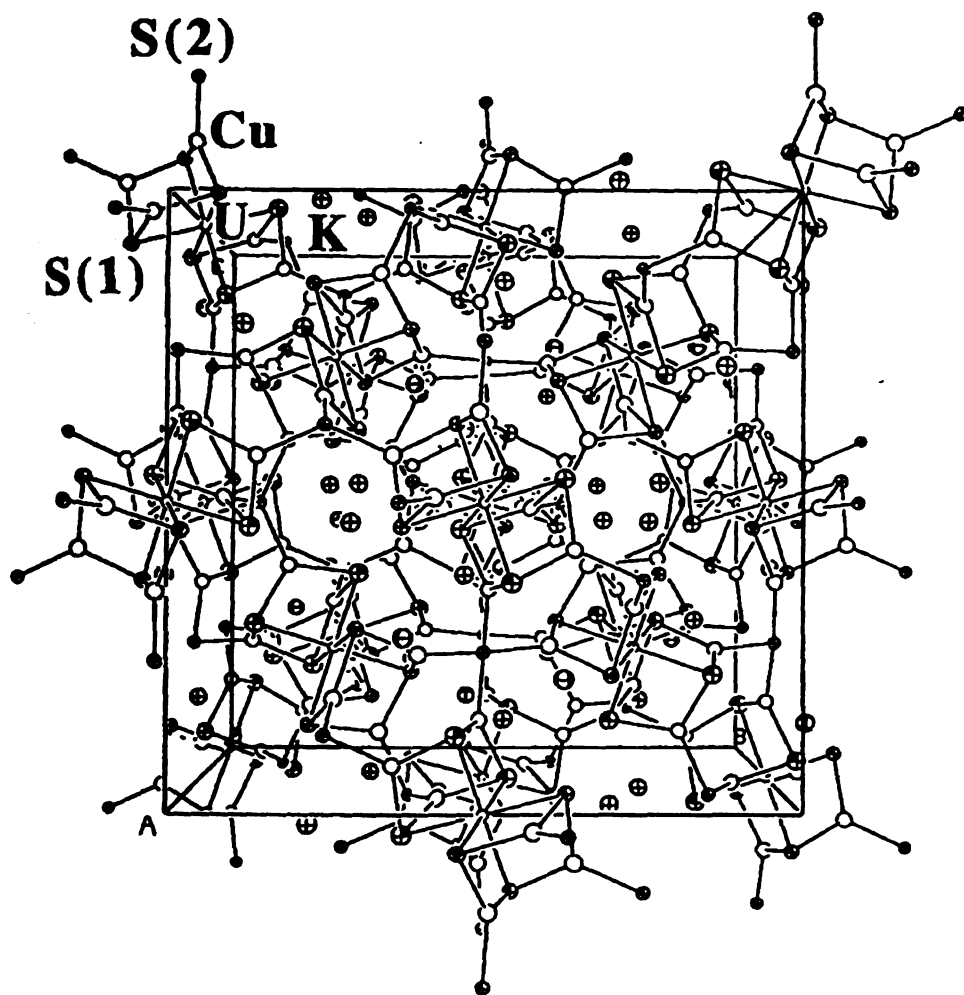
Figure 1.5   ORTEP representation of the extended structure of $K_6Cu_{12}U_2S_{15}$. Crossed ellipses represent K atoms, large open ellipses represent Cu atoms, small open ellipses represent U atoms, and octant shaded ellipses represent U atoms.

E. Te net distortions

In moving from Q = S, Se to Q = Te, it is important to understand the differences between these chalcogens. One important difference is the greater tendency for the latter to associate through Te – Te bonding interactions because of the more diffuse nature of its orbitals. Tellurium is less electronegative and can therefore stabilize longer than normal bond distances. Roald Hoffmann recently described tellurium's behavior as a "constant flirtation with other tellurium partners, in the range between a bond and no bond".[31] This has been illustrated in the alkali metal rich tellurides[32] where such Te – Te "flirting" has resulted in the formation of one-dimensional chains (infinite[33] and spirocyclic[34]), cyclohexane-like Te_6 rings,[35] and puckered crown shaped Te_8 rings[36]. When a transition metal or a rare earth metal is added to the synthesis, two-dimensional Te nets have been observed, for example in $NdTe_3$[37] and $K_{0.33}Ba_{0.67}AgTe_2$[38]. This is not to say that the units found in the alkali metal rich tellurides are not found here. In fact, such compounds as $\alpha-UTe_3$[39] and ATh_2Te_6 (A = Cs, Cu)[40] possess one-dimensional infinite chains in their structure. However, these Te nets are of particular interest because they have been found to undergo structural distortions that not only result in interesting superstructures but also have a drastic affect on the physical properties of the material. This is illustrated in the binary rare earth telluride compounds, $LnTe_3$. The extended structure of $LnTe_3$ as viewed down the c-axis is shown below.[41]
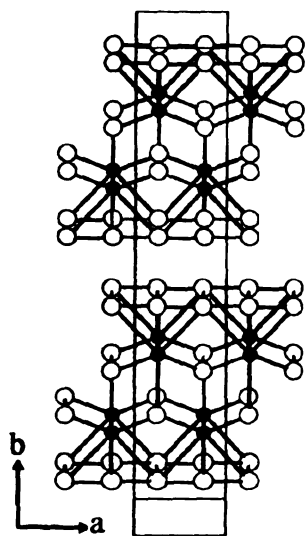
The two-dimensional structure is made up of corrugated, cubic rare earth telluride slabs that alternate with planar Te nets. The Ln atoms (black circles) are each coordinated to nine Te atoms (white circles) in a monocapped square antiprismatic geometry. The Te net appears as perfectly square with all Te-Te bond distances equal around 3.1Å. This Te net, shown below, is what will be referred to as an "ideal" configuration.
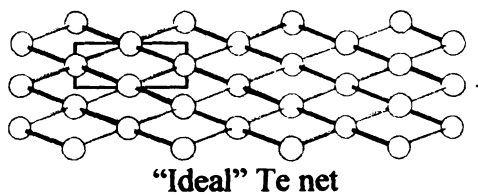
"Ideal" Te net

In terms of physical properties, if the Te net is truly "ideal", the material should be metallic. This is because the electronic bands that give rise to a material's conductive nature are entirely derived from this square Te net. In other words, the energy levels at the Fermi Level are primarily made up of Te p-orbitals and the

21

bands associated with the rare-earth telluride slab do not contribute at all to the Fermi surface. Due to the more diffuse nature of the Te p-orbitals, there is good overlap and the electron density is considered to be "delocalized" across the net. This gives rise to the high conductivity. However, since the average charge per Te atom in these nets is usually less than 2^- (0.5^- in the case of $LnTe_3$), the nets are considered to be "electron deficent" and are therefore susceptible to distort. Below is a cartoon illustration of the electronic band structure of a material with a Te net in an "ideal" configuration and one that has a "distorted" Te net.

Scheme 1

"Ideal" Te net

"Distorted" Te net

Metal

Semiconductor
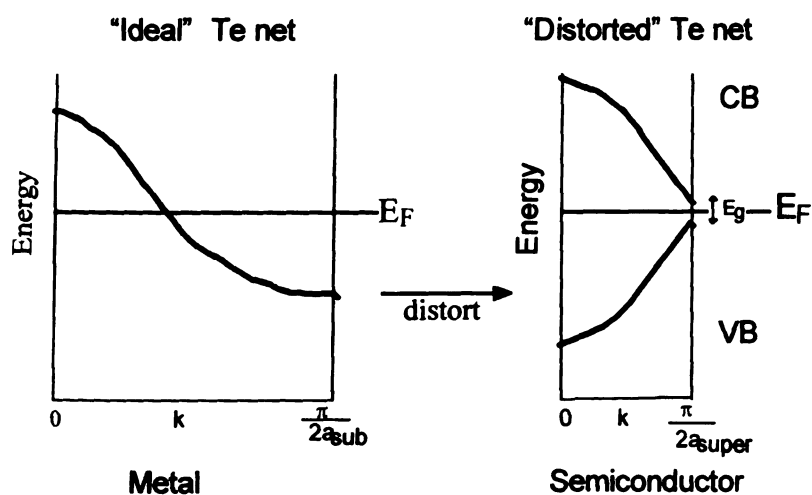
This distortion in the Te net lowers the total energy of the system by decreasing the energy of the filled Te p-orbitals which localizes the electron density into fully occupied bonding orbitals. Consequently, a gap is opened up at the Fermi Level and the physical properties of the material changes from metallic to semiconducting.

For LnTe₃ (Ln = Nd, Sm), the standard crystallographic determination presented an "ideal" Te net.[37] Consistent with this model, tight binding calculations predicted metallic properties. However, the conductivity measurements reported for pressed pellets of $LaTe_3$ and $ErTe_3$ suggest semiconducting behavior.[42] This led Lee and DiMasi to re-examine these $LnTe_3$ materials to try and better correlate the structure with the properties.[43] By using electron diffraction, they identified superlattice reflections indicating the presence of incommensurate distortions, consistent with modulations in the square Te nets in $LnTe_3$ (Ln = La, Sm, Gd, Tb, Dy, Ho, Er, Tm).[44]

Certainly, these distortions are not specific to square nets. However, they are most commonly found to exist in low-dimensional compounds. The low dimensionality simply makes the compounds more susceptible to distort. Examples include the chainlike transition metal trichalcogenides,[45] the layered transition metal dichalcogenides,[46] and the red[47] and purple[48] bronzes. More recent examples include $K_3Cu_8S_6$,[49] V_3Te_4,[50] and $SmTe_{1.84}$,[51] $LaSe_{1.9}$,[52,53] $DySe_{1.84}$,[53,54,55] and $RbDy_3Se_8$[52,53,54]. Distorted chalcogen nets have been observed for both stoichiometric[56] [LnQ_2] and chalcogen deficient[57] [LnQ_{2-x}] compounds. The chalcogen deficiency leads to vacancies[58] in the net, which drives the system to distort.

As far as the chalcogen nets are concerned, there are two main ways for them to distort, via a Charge Density Wave (CDW) or a Site Occupancy Wave (SOW). A CDW type distortion is defined as a sinusodial atomic displacement,

23

combined with an electron-phonon coupling, which together produce either a gap or a deep valley at the Fermi level by lowering the energy of the occupied states while at the same time raising the energy of the unoccupied states.[59] The wave vector of the distortion, or modulation, can occur in any direction in the plane of the Te net. Another way to think about a CDW type distortion is as a Jahn-Teller type distortion in which large displacments of atoms cause the atomic coordination to be reduced.[60] This is evident if we think about a simple system like elemental tellurium. Te has two unoccupied states in degenerate p-orbitals and requires two nearest neighbors in order to fill its valence shell through covalent bonding. Therefore, the desired coordination number for Te is two. There are two phases of elemental tellurium:[61] a high pressure phase and an ambient pressure phase. Under high pressure, the coordination number of Te is six (octahedral). However, at ambient pressure, the coordination number drops to two in the form of rings or chains. This is an indication that there in fact is a significant driving force for these atoms to reduce their coordination.

An example of a CDW type distortion is shown below, see Scheme 2.

Scheme 2
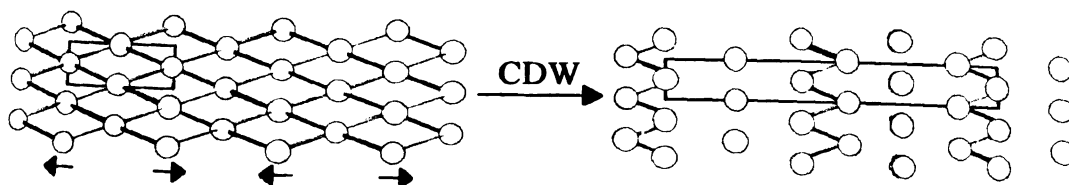
Depicted on the left is a Te net in an "ideal" configuration with a unit cell that correctly describes its periodicity. If the atoms above the arrows distort in the direction described, a new Te net results which is shown on the right. It is made up of alternating infinite Te chains and monotellurides and the coordination within the net drops from four to two and zero. Consequently, a new, larger unit cell (may be commensurate or incommensurate) is needed to redescribe the periodicity of the Te net, which is referred to as the supercell. The original unit cell is called the subcell.

Another way that these Te nets can respond to various electronic situations is via a Site Occupancy Wave (SOW). In this case, some of the Te atoms are actually removed from the solid state lattice, creating ordered vacancies. An example of this is shown below in Scheme 3.

Scheme 3
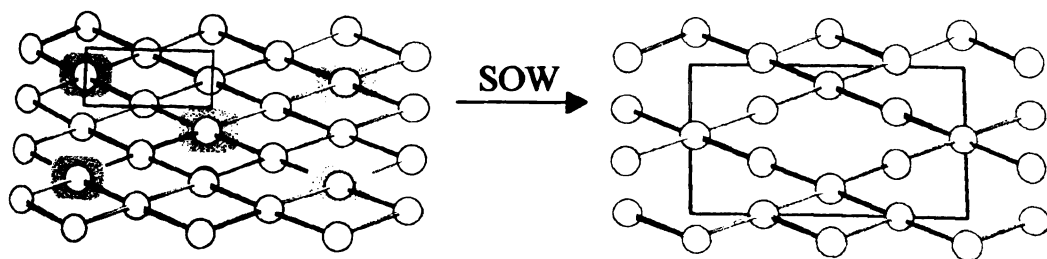
Again, on the left is a Te net in an "ideal" configuration. If the Te atoms that are highlighed are removed from the net, the resulting net is shown on the right. This time, only some of the Te atoms experience a lowering of their coordination

number. As in the case of a CDW type distortion, a larger unit cell is needed to redescribe the periodicity of the Te net, which is the supercell.

In either case (CDW or SOW), a superstructure exists that better describes the true picture of the compound. Since the nature of the Te net dictates the electrical properties of the material, it is very important to achieve a structural model that is as close to the truth as possible. Otherwise, wrong correlations could be made between the structure and the properties and even worse, wrong conclusions could be made about the chemistry. As will be shown throughout this dissertation, many of the compounds found in the A/M/Ln/Te system possess Te nets that undergo CDW or SOW type distortions. In fact, what we have learned in doing this research is that perfectly square Te nets are quite unstable. Unfortunately, however, the crystallographic reflections that give rise to the supercells that describe these distorted Te nets are oftentimes so weak that they cannot be detected by standard X-ray diffraction techniques. In these cases, electron diffraction methods have been employed to try and elucidate the existence and identity of the supercells. In addition, conductivity measurements have been invaluable in helping to shed light on the situation. One must be careful, though, when interpreting the conductivity measurements alone. If, for example, a material is determined to be metallic, one might conclude that there is no distortion in the Te net. Yet, the more subtle distortions only partially open a gap at the Fermi level, causing the material to remain metallic. Therefore, it is best to

couple the conductivity measurements with electron diffraction before making any

conclusions.

References

1. (a) *The Sodium-Sulfur Battery*, Sudworth, J.L.; Tilley, A.R. Eds., Chapman and Hall, New York, 1985. (b) Fischer, W. *Mater. Res. Soc. Symp. Proc.* **1989**, *135*, 541. (c) Powers, R.W.; Karas, B.R. *J. Electrochem. Soc.* **1989**, 136, 2787.

2. (a) Whittingham, M.S. in *Solid State Ionic Devices*, July 18-23, 1988, Singapore; Chowdari, B.V.R., Radhakrishna, S., Eds.; World Scientific: Singapore, 1988; pp 55-74. (b) Bowden, W.L.; Barnette, L.H.; Demuth, D.L. *J. Electrochem. Soc.* **1989**, *136*, 1614. (c) Murphy, D.W.; Trumbore, F.A. *J. Electrochem. Soc.* **1976**, *123*, 960.

3. (a) Etman, M.; Katty, A.; Levy-Clement, C.; Lemasson, P. *Mater. Res. Bull* **1982**, 17, 579. (b) Katty, A.; Soled, S.; Wold, A. *Mater. Res. Bull.* **1977**, 12, 663.

4. Ballman, A.A.; Byer, R.L.; Eimerel, D.; Feigelson, R.S.; Feldman, B.J.; Goldberg, L.S.; Menyuk, N.; Tang, C.L. *Applied Optics* **1987**, 26, 224.

5. (a) West, A.R. *Solid State Chemistry and Its Applications*; John Wiley & Sons: New York, 1984, p 540-552. (b) Xia, Y.; Chen, C.; Tang, D.; Wu, B. *Adv. Mater.* **1995**, 7, 79.

6. (a) Malik, S.K.; Vijayaraghavan, R. *Rev. Solid State Sci.* **1988**, 2, 75. (b) Chevrel, R.; Sergent, M.; Prigent, J. *J. Solid State Chem.* **1971**, 3, 515. (c) Hebard, A.F.; Rosseinsky, M.J.; Haddon, R.C.; Murphy, D.W.; Glarum, S.H.; Palstra, T.T.M.; Ramirez, A.P.; Kortan, A.R. *Nature* **1991**, 350, 600.

7. (a) Chianelli, R.R.; Pecoraro, T.A.; Halbert,T.R.; Pan, W.-H.; Stiefel, E.I. *J. Catal.*, **1984**, 86, 226. (b) Pecoraro, T.A.; Chianelli, R.R. *J. Catal.* **1981**, 67, 430. (c) Harris, S.; Chianelli, R.R. *J. Catal.* **1984**, 86, 400.

8. Rowe, D.M.; Bhandari, C.M. *Modern Thermoelectrics*, Holt, Rinehart, and Winston, London, 1983, p. 103. (b) Borkowski, K; Pyzluski, J. *J. Mater. Res. Bull.* **1987**, 22, 381.

9. Steigerwald in *Inorganometallic Chemistry*, T.P. Fehlner, Ed. Plenum Press, New York, 1992, 333.

10. Rabenau, A. *Angew. Chem. Int. Ed. Engl.*, **1985**, 24, 1026.

[11] (a) Chen, L.R. *Commun. Theor. Phys.* **1992**, 17 (3), 285. (b) Chen, L.R. *Commun. Theor. Phys.* **1992**, 13 (2), 147.

[12] (a) Elwell, D.; Scheel, H.J. *Crystal Growth from High-Temperature Solutions;* Academic Press: London, 1975. (b) *Molten Salts Handbook;* Janz, G.J., Eds.; Academic Press: New York, 1967. (c) Mamantov, G. *Molten Salts;* Marcel Dekker: New York, 1969.

[13] (a) Scheel, H.J. *J. Cryst. Growth* **1974**, 24/25, 669. (b) Sanjines, R.; Berger, H.; Levy, F. *J. Mater. Res. Bull.* **1988**, 23, 549. (c) Garner, R.W.; White, W.B. *J. Cryst. Growth.* **1970**, 7, 343.

[14] Sunshine, S.A.; Kang, D.; Ibers, J.A. *J. Am. Chem. Soc.*, **1987**, 109, 6202.

[15] (a) Kanatzidis, M.G. *Chem. Mater.* **1990**, 2, 353. (b) Sutorik, A.C.; Kanatzidis, M.G. *Prog. Inorg. Chem.* **1995**, 43, 151. (c) Wu, P.; Ibers, J.A. *J. Alloys Comp.* **1995**, 229, 206. (d) Pell, M.A.; Ibers, J.A. *Chem. Ber./Recueil* **1997**, 130, 1. (e) Narducci, A.A.; Ibers, J.A. *Chem. Mater.* **1998**, 10, 2811.

[16] (a) Pearson, T.G.; Robinson, P.L. *J. Chem. Soc.*, **1931**, 1304. (b) Mathewson, G.H. *J. Am. Chem. Soc.*, **1907**, *29*, 867. (c) Klemm, W.; Sodomann, H.; Langmesser, P. *Z. Anorg. Allg. Chem.*, **1939**, *241*, 281. (d) *Gmelin's Handbuch der Anorganischen Chemie*, Verlag Chemie, Weiheim/Brgstr, FRG **1966**, Sodium, Suppl. Part 3, p. 1202-1205 and references therein.

[17] *Binary Alloy Phase Diagrams* (Ed.: T.B. Massalski), William W. Scott, Jr., Materials Park, Ohio **1990**, pp 1395, 2392, 2737, and 3193.

[18] Sutorik, A.C.; Albritton-Thomas, J.; Kannewurf, C.R.; Kanatzidis, M.G. *J. Am. Chem. Soc.* **1994**, *116*, 7706.

[19] Sutorik, A.C.; Albritton-Thomas; Hogan, T.; Kannewurf, C.R.; Kanatzidis, M.G. *Chem. Mater.* **1996**, *8*, 751.

[20] (a) Krönert, W.; Plieth, K. *Z. Allg. Anorg. Chem.* **1965**, *3*, 207. (b) Furuseth, S.; Brattas, L.; Kjekshus, A. *Acta. Chem. Scand.* **1975**, A29, 623.

[21] Bensch, W.; Dürichen, P. *Chem. Ber.* **1996**, 129, 1489.

[22] Mansuetto, M.F.; Ibers, J.A. *J. Solid State Chem.* **1995**, *130*, 1.

[23]   Cody, J.A.; Ibers, J.A. *Inorg. Chem.* **1995**, 34, 3165.

[24]   Wu, P.; Christuk, A.E.; Ibers, J.A. *J. Solid State Chem.* **1994**, 110, 337.

[25]   Huang, F.-Q.; Choe, W.; Lee, S.; Chu, J.S. *Chem. Mater.* **1998**, 10, 1320.

[26]   Yang, Y.; Ibers, J.A. *J. Solid State Chem.* **1999**, 147, 366.

[27]   Christuk, A.E.; Wu, P.; Ibers, J.A. *J. Solid State Chem.* **1994**, 110, 330.

[28]   Wu, P.; Ibers, J.A. *J. Solid State Chem.* **1994**, 110, 156.

[29]   Stoll, P.; Dürichen, P; Näther, C.; Bensch, W. *Z. Anorg. Allg. Chem.* **1998**, 624, 1807.

[30]   Sutorik, A.C.; Patschke, R.; Schindler, J.; Kannewurf, C.R.; Kanatzidis, M.G *Chem. Eur. J.*, In press (2000).

[31]   Hoffman, R. *American Scientist* **1996**, 84, 327.

[32]   (a) Sheldrick, W.S.; Wachhold, M.; Jobic, S.; Brec, R.; Canadell, E. *Advanced Materials* **1997**, 9, No 8, 669. (b) Kanatzidis, M.G. *Angew. Chem. Int. Ed. Engl.* **1995**, 34, No. 19, 2109

[33] Li_2Te_6: Böttcher, P.; Keller, R. *J. Less Common Met.* **1985**, 109, 311 and references therein.

[34] Rb_2Te_5: Böttcher, P.; Kretschmann, U. *J. Less Common Met.* **1983**, 95, 81.

[35] $RbTe_6$: Sheldrick, W.S.; Schaaf, B. *Z. Naturforsch. B* **1994**, 49, 993.

[36] Cs_3Te_{22}: Sheldrick, W.S.; Wachhold, M. *Angew. Chem.* **1995**, 107, 490; *Angew. Chem. Int. Ed. Engl.* **1995**, 34, 450.

[37]   (a) Norling, B.K.; Steinfink, H. *Inorg. Chem.* **1966**, 5, 1488. (b) Noel, H.; Levet, J.C. *J. Solid State Chem.* **1989**, 79, 28.

[38]   (a) Zhang, Z.; Li, J.; Foran, B.; Lee, S.; Guo, H.-Y.; Hogan,T.; Kannewurf, C.R.; Kanatzidis, M.G. *J. Am. Chem. Soc.* **1995**, 117, 10513. (b) Hanko, J.A.; Kanatzidis, M.G.; Evain, M.; Gourdon, O.; Boucher, F.; Petricek, V. *Inorg Chem.*, In press.

[39] Breeze, E.W.; Brett, N.H.; White, J. *J. Nucl. Mat.* **1971**, 39, 157.

[40] (a) Cody, J.A.; Ibers, J.A. *Inorg. Chem.* **1996**, 35, 3836. (b) Narducci, A.A.; Ibers, J.A. *Inorg. Chem.* **1998**, 37, 3798.

[41] Stowe, K.Z. *Anorg. Allg. Chem.* **1996**, 622, 1419.

[42] (a) Ramsey, T.H.; Steinfink, H.; Weiss, E.J. *J. Appl. Phys.* **1965**, 36, 548. (b) Haase, D.J.; Steinfink, H. *J. Appl. Phys.* **1966**, 37, 2246.

[43] DiMasi, E.; Foran, B.; Aronson, M.C.; Lee, S. *Chem. Mater.* **1994**, 6, 1867.

[44] (a) DiMasi, E.; Aronson, M.C.; Mansfield, J.F.; Foran, B.; Lee, S. *Phys. Rev. B.* **1995**, 55(20), 14516. (b) Gweon, G.H.; Denlinger, J.D.; Clack, J.A.; Allen, J.W.; Olson, C.G.; DiMasi, E.; Aronson, M.C.; Foran, B.; Lee, S. *Phys. Rev. Lett.* **1998**, 81, No. 4., 886

[45] (a) NbSe$_3$: Comés, R.; Lambert, M.; Launois, H.; Zeller, H.R. *Phys. Rev. B.* **1973**, 8, 571. (b) ZrTe$_3$: Eaglesham, D.J.; Steeds, J.W.; Wilson, J.A. *J. Phys. C.: Solid State Phys.* **1984**, 17, L697.

[46] (a) Peierls, R.E.; *Quantum Theory of Solids*, Oxford University Press, Oxford, England, **1955**. (b) Fröhlich, H. *Proc. R. Soc. A.* **1954**, 223, 296. (c) *Electronic Properties of Inorganic Quasi-One-Dimensional Compounds*, Eds. P. Monceau **1985**. (d) Whangbo, M.-H.; Canadell, E. *J. Am. Chem. Soc.* **1992**, 114, 9587. (e) Rovira, C.; Whangbo, M.-H. *Inorg. Chem.* **1993**, 32, 4094. (f) Whangbo, M.-H.; Ren, J.; Canadell, E.; Louder, D.; Parkinson, B.A.; Bengel, H.; Maganov, S.N. *J. Am. Chem. Soc.* **1993**, 115, 3760. (g) Liang, X.; Lieber, C.M. *Science* **1989**, Vol 243, 1703 (h) Burk, B.; Thompson, R.E.; Clarke, J.; Zettl, A. *Science* **1992**, Vol 257, 362.

[47] (a) A$_{0.33}$MoO$_3$: Hillenius, S.J.; Coleman, R.V.; Fleming, R.M.; Cava, R.J. *Phys. Rev. B.* **1981**, 23, 1567. (b) Ba$_{0.15}$WO$_3$: Canadell, E.; Whangbo, M.-H. *Inorg. Chem.* **1994**, 33(9), 1864.

[48] (a) KMo$_6$O$_{17}$, Na$_{0.9}$Mo$_6$O$_{17}$, Li$_{0.9}$Mo$_6$O$_{17}$: Dumas, J.; Schlenker, C. *Int. J. Mat. Phys.* **1993**, 7, 4045. (b) Whangbo, M.-H.; Canadell, E.; Foury, P.; Pouget, J.-P. *Science* **1991**, Vol 252, 96.

[49] Sato, H.; Kojima, N.; Suzuki, K.; Enoki, T. *J. Phys. Soc. Japan* **1993**, 62, 647.

[50]   Ohta, S.; Kaneko, T.; Yoshida, H. *J. Phys. Soc. Japan* **1990**, 59, 3827.

[51]   Park, S.-M.; Park, S.-J.; Kim, S.-J. *J. Solid State Chem.* **1998**, 146, 300.

[52]   Lee, S.; Foran, B. *J. Am. Chem. Soc.* **1994**, 116, 154

[53]   Lee, S.; Foran, B. *J. Am. Chem. Soc.* **1996**, 118, 9139.

[54]   Foran, B.; Lee, S.; Aronson, M.C. *Chem. Mater.* **1993**, 5, 974.

[55]   van der Lee, A.; Hoistad, L.M.; Evain, M.; Foran, B.J.; Lee, S. *Chem. Mater.* **1997**, 9, 218.

[56]   (a) Marcon, J.-P.; Pascard, R. *C.R. Acad. Sc. Paris* **1968**, 266, 270. (b) Bénazeth, S.; Carré, D.; Laruelle, P. *Acta. Cryst.* **1982**, B38, 33. (c) Chen, J.H.; Dorhout, P.K. *J. Solid State Chem.* **1995**, 117, 318.

[57]   (a) Lin, W.; Steinfink, H.; Weiss, E.J. *Inorg. Chem* **1965**, 4, 877. (b) Ramsey, T.H.; Steinfink, H.; Weiss, E.J. *Inorg. Chem.* **1965**, 4, 1154. (c) Wang, R.; Steinfink, H.; Bradley, W.F. *Inorg. Chem.* **1966**, 5, 142. (d) Webb, A.W.; Hall, H.T. *Inorg. Chem.* **1970**, 9, 1084. (e) Cannon, J.F.; Hall, H.T. *Inorg. Chem.* **1970**, 9, 1639. (f) DiMasi, E.; Foran, B.; Aronson, M.C.; Lee, S. *Phys. Rev. B.* **1996**, 54(19), 13587.

[58]   (a) Plambeck-Fischer, P.; Abriel, W.; Urland, W. *J. Solid State Chem.* **1989**, 78, 164. (b) Urland, W.; Plambeck-Fischer, P.; Grupe,M. *Z. Naturforsch* **1989**, 44b, 261. (c) Grupe, M.; Urland, W. *J. Less-Common Met.* **1991**, 170, 271. (d) Kim, S.-J.; Oh, H.-J. *Bull. Korean Chem. Soc.* **1995**, 16, 515.

[59]   Wilson, J.A.; DiSalvo, F.J.; Mahajan, S. *Adv. Phys.* **1975**, 24, 117.

[60]   (a) Albright, T.A.; Burdett, J.K.; Whangbo, M.-H. *Orbital Interactions in Chemistry*, Wiley, New York **1985**. (b) Whangbo, M.-H.; Canadell, E. *J. Am. Chem. Soc.* **1992**, 114, 9587.

[61]   Martin, R.M.; Lucovsky, G.; Helliwell, K. *Phys. Rev. B.* **1976**, 13, 1383.

Chapter 2

Reactions of Rare Earth Metals in Molten Alkali Metal/Polytelluride Fluxes:

Discovery of the ALn$_3$Te$_8$ Family (A = Cs, Rb, K; Ln = Ce, Nd)

A. Introduction

Many high symmetry, low-dimensional compounds contain stacking layers which can be described as square lattice networks composed of one element. Examples include compounds of the Cu_2Sb structure type,[1] the related ZrSiSe structures,[2] the PbO and anti-PbO structures,[3] the $BaAl_4$,[4] $ThCr_2Si_2$[5] and $CaBe_2Ge_2$[6] structure types, the $SrZnSb_2$ structure,[7] and other less popular structure types.[8] The chemical, physical, and electronic properties of these compounds are largely decided by these square nets, and by their interaction with the remaining part of the structure. However, only a few were known for tellurium at the start of this research, e.g., $LnTe_2$, Ln_2Te_5, and $LnTe_3$,[9] $CsTh_2Te_6$,[10] $K_{0.33}Ba_{0.67}AgTe_2$,[11] and Cs_3Te_{22}[12]. These square nets can have different electronic structures, which can lead to instabilities and structural distortions within the nets.[13] These distortions are associated with several interesting physical phenomena such as charge density waves and can lead to anomalies in the charge transport properties. When the formal oxidation state of all Te atoms in the net is -2, a stable square net is observed (e.g. NaCuTe).[14] In this case, the term "square net" is used to describe the arrangement of the Te^{2-} ions in which there is no bonding at all between the Te^{2-} ions. However, when the formal oxidation state is less than -2, or when there are atomic vacancies in the square net, structural distortions are possible leading to Te···Te bonding interactions and the formation of Te_x^{n-} species. These distortions are manifested through the formation of a superstructure with respect to the ideal

square net.[11] A family of compounds having the formula ALn_3Te_8 (A = Cs, Rb, K; Ln = Ce; Nd) has been discovered which displays a defect square Te net and an unprecedented intense charge density wave, leading to the formation of infinite zig-zag $(Te_2^{2-})_n$ chains and Te_3^{2-} anions. Interestingly, this charge density wave has recently been predicted on theoretical grounds,[15,16] and this report constitutes the first experimental confirmation.

B. Experimental Section

1. **Reagents** – The following reagents were used as obtained: Potassium metal, analytical reagent, Spectrum Chemical Mfg. Corp., Gardena, CA; Rubidium metal, 99.5%, Alfa Aesar, Ward Hill, MA.; Cesium metal, 99.98%, Alfa Aesar, Ward Hill, MA; Copper metal, electrolytic dust, Fisher Scientific, Fairlawn, NJ; Cerium metal, < 250 mesh, Alfa Aesar, Ward Hill, MA; Neodynium metal, < 250 mesh, Alfa Aesar, Ward Hill, MA; Tellurium powder, 100 mesh, 99.95% purity, Aldrich Chemical Co., Milwaukee, WI; N, N, - Dimethylformamide (DMF) was used as obtained in analytical reagent grade from Aldrich Chemical Co., 99.8% purity, Milwaukee, WI.

Potassium Telluride, K_2Te – The following procedure was modified from that given in the literature.[17] 11.50g (0.29 mol) K was sliced in an N_2 filled glovebox and combined with 18.50g (0.14 mol) Te in a 1000 mL single neck round bottom flask. This mixture represents a slight excess of K and slight

deficiency of Te. The flask was connected to a glass adapter with a stopcock joint and removed from the glovebox. The flask and adapter was then connected to a condenser apparatus and chilled to -78°C using a dry ice/acetone bath. Approximately 800mL of NH_3 were condensed, under an N_2 atmosphere, onto the reagents, giving a purple solution. The solution was stirred via a Teflon coated magnetic stir bar and the reaction mixture was maintained at -78° for up to 24 hours. The dry ice was then removed and the NH_3 was allowed to evaporate off as the flask warmed up to room temperature under a constant flow of N_2 (approximately 10 hours). A second portion of NH_3 was added and the process was repeated to ensure complete reaction of the reagents. The resulting pale yellowish-grey powder was evacuated on a Schlenck line for approximately 5 hours and taken into an N_2 filled glovebox where it was ground to a fine powder. Due to its propensity to decompose even under an inert glovebox atmosphere, the material was stored in a glass ampoule clamped shut with a ground glass lid.

Rubidium Telluride, Rb₂Te – In an N_2 filled glovebox, a 500g ampoule of Rb metal was heated to 80°C in an oil bath. Once the Rb metal was molten, 13.08g (0.15 mol) was transferred to a 1000 mL three neck round bottom flask. The two side necks were closed off with ground glass stoppers, and the center neck was connected to a glass adapter with a stopcock joint. The flask and adapter was removed from the glovebox, connected to a condenser apparatus, and chilled to -78°C using a dry ice/acetone bath. Approximately 400mL of NH_3 were condensed onto the Rb metal, under an N_2 flow, giving a dark blue solution. One

36

of the side arm stoppers was gently removed and a Teflon coated magnetic stir bar was added to the solution, followed by 17.52g (0.21 mol) of Te. The glass stopper was replaced and an additional 400mL of NH_3 was condensed into the flask. From this point on, the reaction proceeds as described above for K_2Te. A bright yellow powder resulted which was evacuated on a Schlenck line for 5 hours, taken into a N_2 filled glovebox, ground to a fine powder, and stored in the same manner as for K_2Te.

Cesium Telluride, Cs_2Te – The procedure was the same as desribed above for Rb_2Te. Amounts of 20.07g (0.15 mmol) Cs and 9.63g (0.07 mmol) were used, which represent a slight excess of Cs and a slight deficiency of Te. A bright yellow powder resulted which was taken into the glovebox and stored in the same manner as for K_2Te.

2. Synthesis - All manipulations were carried out under a dry nitrogen atmosphere in a Vacuum Atmospheres Dri-Lab glovebox.

$CsCe_3Te_8$ (I) – Initial investigations into the $Cs_2Te/Cu/Ce/Te$ system produced the ternary compound, $CsCe_3Te_8$, as a result of phase separation in which the Cu did not incorporate into any of the Ce-containing products. Amounts of 0.393g Cs_2Te (1.0 mmol), 0.032g Cu (0.5 mmole), 0.070g Ce (0.5 mmol), 0.383g Te (3.0 mmol) were weighed into a vial in an N_2 filled glovebox. The reactants were thoroughly mixed and loaded into a 9 mm silica ampoule. The ampoule was removed from the glovebox, evacuated on a Schlenck line to less

than 2.0×10^{-4} mbar, and flame sealed. The reactants were heated to 550°C for 4 days, cooled to 100°C at 4°C/hr, and quenched to 50°C in 4 hours. The ampoule was opened with a glass cutter and placed into a 100 mL tube containing a side arm attachment to allow for the purging of N_2 and filled with degassed DMF. As the excess Cs_2Te_x flux dissolved in the DMF, the solution turned a dark purple color. Successive portions of degassed DMF were added until the solution remained clear. The product was washed with ether and dried under a constant flow of N_2. The remaining material consisted of a red-brown powder as the major phase and black hexagonal-shaped plate crystals as a minor phase. The identity of the red-brown powder was confirmed by EDS to be $CeTe_3$ while the hexagonal crystals analyzed as ternary having an average composition of $Cs_{1.0}Ce_{2.7}Te_{5.9}$.

The reaction conditions were then optimized to produce $CsCe_3Te_8$ as a major phase by removing the Cu from synthesis, raising the reaction temperature, and using stoichiometric amounts of the reactants. The optimized reaction mixture consisted of 0.079g Cs_2Te (0.2 mmol), 0.168g Ce (1.2 mmol), and 0.383g Te (3.0 mmol) which was heated to 850° C for 5 days, cooled to 400°C at 4°C/hr and 100°C at 10°C/hr, and quenched to room temperature in 1 hour. Although these conditions showed significant improvements in forming the desired product, they still did not yield a pure product. However, the small amount of $CeTe_3$ powder which resulted could be removed from the crystals by simply sonicating the mixture. The identity of the hexagonal crystals was confirmed by comparing the

powder X-ray diffraction pattern of the product against one calculated using single crystal X-ray data (see Table 2.1).

RbCe₃Te₈ (II) – The synthetic route to the formation of RbCe₃Te₈ was very similar to that of CsCe₃Te₈. The compound was initially discovered from reactions in the $Rb_2Te/Cu/Ce/Te$ system and further optimization was needed to produce the pure compound. The optimized reaction consisted of amounts of 0.358g Rb_2Te (1.2 mmol), 0.126g Ce (0.9) mmol), and 0.612g Te (4.8 mmol) that were weighed into vial in an N_2 filled glovebox, thoroughly mixed, and loaded into a 9 mm silica ampoule. The ampoule was removed from the glovebox, evacuated on a Schlenck line to less than 2.0 x 10^{-4} mbar, and flame sealed. The reactants were heated to 400°C in 12 hours, isothermed at this temperature for 12 hours, raised to 850°C in 22 hours, and isothermed at this temperature for 6 days. The reaction was then cooled to 400°C at 4.5°C/hr followed by quenching to 50°C in 4 hours. The product was isolated in the manner described above for CsCe₃Te₈. The remaining material consisted of a small amount of red-brown powder while the major phase was copper-colored hexagonal shaped plates. Typical yields were 26%, based on Ce. The identity of the red-brown powder was confirmed by EDS to be $CeTe_3$ while the hexagonal crystals analyzed as ternary having an average composition of $Rb_{1.0}Ce_{4.8}Te_{11.2}$. The identity of the hexagonal plates was confirmed by comparing the powder X-ray diffraction pattern of the product against one calculated using single crystal X-ray data (see Table 2.2).

KCe₃Te₈ (III) – A mixture of 0.309g K_2Te (1.5 mmol), 0.126g Ce (0.9 mmol), and 0.612g Te (4.8 mmol) was thoroughly mixed in a scintillation vial in an N_2 filled glovebox and loaded into a 9 mm silica ampoule. The ampoule was removed from the glovebox and evacuated on a Schlenck line to $< 2.0 \times 10^{-4}$ mbar and flame sealed. The reactants were heated to 400°C in 12 hours, isothermed at this temperature for 12 hours, raised to 850°C in 22 hours, and isothermed at this temperature for 6 days. The reaction was then cooled to 400°C at 4.5°C/hr followed by quenching to 50°C in 4 hours. The product was isolated in the manner described above for $CsCe_3Te_8$. The remaining material consisted of a small amount of red-brown powder while the major phase consisted of copper colored hexagonal-shaped plate crystals. Typical yields were 41%, based on Ce. The identity of the red-brown powder was confirmed by EDS to be $CeTe_3$ while the hexagonal crystals analyzed as ternary having an average composition of $K_{1.0}Ce_{3.5}Te_{8.2}$. The identity of the hexagonal crystals was confirmed by comparing the powder X-ray diffraction pattern of the product against one calculated using single crystal X-ray data (see Table 2.3).

KNd₃Te₈ (IV) – The synthetic route to the formation of KNd_3Te_8 was very similar to that of ACe_3Te_8 (A = Cs, Rb). The compound was initially discovered from reactions in the $K_2Te/Cu/Nd/Te$ system and further optimization was needed to produce the compound pure. The optimized reaction consisted of amounts of 0.309g K_2Te (1.5 mmol), 0.130g Nd (0.9 mmol), and 0.612g Te (4.8 mmol) which were weighed into a vial in an N_2 filled glovebox, thoroughly mixed, and loaded

40

into a 9 mm silica ampoule. The ampoule was removed from the glovebox and evacuated on a Schlenck line to $< 2.0 \times 10^{-4}$ mbar and flame sealed. The reactants were heated to 400°C in 12 hours, isothermed at this temperature for 12 hours, raised to 850°C in 22 hours, and isothermed at this temperature for 6 days. The reaction was then cooled to 400°C at 4.5°C/hr followed by quenching to 50°C in 4 hours. The product was isolated in the manner described above for $CsCe_3Te_8$. The remaining material consisted of a small amount of greenish-grey powder while the major phase consisted of silvery, black hexagonal-shaped plate crystals. The identity of the greenish-grey powder was confirmed by EDS to be $NdTe_3$ while the hexagonal crystals analyzed as ternary having an average composition of $K_{1.0}Nd_{3.9}Te_{6.4}$. The identity of the hexagonal crystals was confirmed by comparing the powder X-ray diffraction pattern of the product against one calculated using single crystal X-ray data (see Table 2.4).

Table 2.1 Calculated and Observed X-ray Powder Diffraction Pattern for $CsCe_3Te_8$ (I)

h k l	d_{calc} (Å)	d_{obs} (Å)	I/I_{max} (obs) (%)
0 0 1	14.6676	14.9437	1.19
0 0 2	7.3338	7.4007	3.14
0 0 3	4.8892	4.9182	2.49
0 0 4	3.6669	3.6817	25.16
1 3 2	3.3522	3.3512	1.20
0 4 0	3.2490	3.2672	1.80
1 4 0	3.0541	3.0576	4.40
0 0 5	2.9335	2.9425	100.00
0 0 6	2.4446	2.4505	10.82
1 2 -6	2.2965	2.2922	0.55
0 0 7	2.0954	2.0989	1.95
0 0 8	1.8334	1.8361	5.85
1 1 -9	1.6350	1.6315	0.66
3 5 -6	1.6096	1.6130	0.45

Table 2.2 Calculated and Observed X-ray Powder Diffraction Pattern for RbCe$_3$Te$_8$ (II)

h k l	d_{calc} (Å)	d_{obs} (Å)	I/I$_{max}$ (obs) (%)
0 0 1	14.1852	15.48415	7.6
1 1 0	7.3653	7.26646	33.8
0 0 3	4.7284	4.75831	13.1
2 0 -2	4.0800	4.07829	6.8
0 0 4	3.5463	3.54577	100.0
2 2 2	3.1086	3.10736	2.4
2 3 -2	2.9704	2.96543	56.3
0 0 5	2.8370	2.83265	94.1
2 3 2	2.7413	2.74177	35.2
2 0 -5	2.5852	2.58091	7.3
2 3 -4	2.4761	2.47396	23.4
0 0 6	2.3642	2.36725	68.8
0 6 0	2.1665	2.15922	6.3
2 3 -7	1.7894	1.78768	3.0
4 0 4	1.7698	1.76979	6.3
4 3 -5	1.7450	1.74353	13.5
0 6 5	1.7219	1.72274	4.3
5 2 1	1.6810	1.68111	2.6
2 6 -5	1.6605	1.65617	7.0
4 3 -6	1.6369	1.63680	9.1
5 3 1	1.6149	1.61386	13.9
5 3 2	1.5604	1.56038	12.5

Table 2.3   Calculated and Observed X-ray Powder Diffraction Pattern for KCe_3Te_8 (III)

h k l	d_{calc} (Å)	d_{obs} (Å)	I/I_{max} (obs) (%)
0 1 1	9.4636	8.3925	18.8
0 0 2	6.8921	6.9301	5.0
0 0 3	4.5947	4.5455	6.6
0 0 4	3.4461	3.3915	73.9
0 4 0	3.2540	3.2054	20.3
0 3 3	3.1545	3.1430	6.9
2 1 3	2.8987	2.8947	5.3
2 3 2	2.7249	2.7123	94.6
2 4 0	2.6311	2.6321	3.9
2 3 3	2.4527	2.4660	3.1
3 2 2	2.4048	2.3995	4.5
4 0 -1	2.2657	2.2650	12.6
4 0 0	2.2359	2.2360	3.6
0 6 1	2.1430	2.1420	11.1
0 1 7	1.9470	1.9449	100.0
3 5 3	1.8770	1.8760	42.4
4 2 3	1.8182	1.8168	3.2
2 3 6	1.7566	1.7555	1.9
1 2 8	1.5933	1.5898	9.3

Table 2.4   Calculated and Observed X-ray Powder Diffraction Pattern for KNd_3Te_8 (IV)

h k l	d_{calc} (Å)	d_{obs}(Å)	I/I_{max} (obs) (%)
0 0 1	13.6692	12.95992	19.2
0 2 1	5.8095	5.80944	4.4
2 1 1	3.8325	3.82916	30.6
0 4 0	3.2090	3.21164	100.0
3 1 -1	2.9039	2.90268	77.7
1 3 3	2.8429	2.85832	29.3
1 4 -2	2.8182	2.82570	30.8
3 2 1	2.5561	2.55832	10.7
1 2 5	2.3285	2.33094	18.1
0 6 0	2.1665	2.20959	14.5
0 6 1	2.1136	2.11526	5.0
1 6 -1	2.0675	2.06435	11.0
4 1 -4	1.9869	1.99423	20.9
4 0 3	1.8710	1.86784	16.9
1 6 -3	1.8208	1.82325	59.0
2 7 0	1.6936	1.69531	23.5
1 4 -7	1.6826	1.67759	3.9
0 2 8	1.6511	1.64719	24.9
4 3 -6	1.6070	1.60734	7.7

3. Physical Measurements

Semiquantitative Energy Dispersive Spectroscopy (EDS) - The analyses were performed using a JEOL JSM-6400V scanning electron microscope (SEM) equipped with either a Noran TN-5500 or a Noran Vantage energy dispersive spectroscopy (EDS) detector, depending on when the data were collected. Data were acquired on several crystals using an accelerating voltage of 25 kV and 40 sec accumulation time.

Powder X-ray Diffraction - Analyses were performed using a calibrated Rigaku Rotoflex rotating anode powder diffractometer controlled by an IBM computer and operating at 45 kV/ 100 mA with a 1°/min scan rate, employing Ni-filtered Cu radiation. Samples were ground to a fine powder and mounted by spreading the sample onto a piece of double sided scotch tape affixed to a glass slide. Powder patterns were calculated using the Cerius2 software.[18]

X-ray Crystallography - *$CsCe_3Te_8$ and $RbCe_3Te_8$*: A single crystal of each was mounted on the tip of a glass fiber. Intensity data were collected on a Rigaku AFC6S four-circle automated diffractometer equipped with a graphite-crystal monochromator. The unit cell parameters were determined from a least-squares refinement using the setting angles of 20 carefully centered reflections in the $8° \leq 2\theta \leq 30°$ range. The data were collected with an ω-2θ scan technique over one-quarter of the sphere of reciprocal space, up to 60° in 2θ. Crystal stability was monitored with three standard reflections whose intensities were checked every

150 reflections. No significant decay was detected during the data collection period. An empirical absorption correction based on Ψ-scans was applied to all data during initial stages of refinement. A DIFABS[19] correction was applied after full isotropic refinement, after which full anisotropic refinement was performed. The structures were solved by direct methods using the SHELXS-86[20] package of crystallographic programs and full matrix least squares refinement was performed using the TEXSAN software package[21]. Crystallographic data for these compounds are given in Table 2.5.

KCe₃Te₈: A single crystal was mounted on the tip of a glass fiber. Intensity data were collected at 173.1K on a Siemens SMART Platform CCD diffractometer using graphite monochromatized Mo Kα radiation. The data were collected over a full sphere of reciprocal space, up to 50° in 2θ. The individual frames were measured with an ω rotation of 0.3° and an acquisition time of 40 sec. The SMART[22] software was used for the data acquisition and SAINT[23] for the data extraction and reduction. The absorption correction was performed using SADABS.[24] The structure was solved by direct methods using the SHELXTL[25] package of crystallographic programs. The complete data collection parameters and details of the structure solution and refinement is given in Table 2.5.

KNd₃Te₈: A single crystal was mounted on the tip of a glass fiber. Intensity data were collected on a Nicolet P3 four-circle automated diffractometer equipped with a graphite-crystal monochromator. The unit cell was determined by

taking a rotational photo of the crystal and selecting 15-20 reflections from the resulting film. These reflections were manually centered and indexed, a least square refinement was performed, followed by a unit cell transformation to give the highest symmetry cell. The data was collected over one-quarter of the sphere of reciprocal space, up to 60° in 2θ. The structure was solved in the same manner as described for $CsCe_3Te_8$ and $RbCe_3Te_8$ and the complete data collection parameters and details of the structure solution and refinement is given in Table 2.5.

Transmission Electron Microscopy - Electron diffraction studies were carried out on a JEOL 100CX transmission electron microscope (TEM) using an electron beam generated by a CeB_6 filament and an acceleration voltage of 120 kV. After the samples were ground to a fine powder in acetone, the specimens were prepared by dipping a carbon-coated grid in the suspension. The samples showed no decomposition under the electron beam.

Magnetic Susceptibility Measurements - The magnetic response of the compound was measured over the range of 2-300K using an MPMS Quantum Design SQUID magnetometer. Samples were ground to a fine powder to minimize anisotropic effects, and corrections for the diamagnetism of the compound and PVC sample containers were applied. Magnetic susceptibility as a function of field strength (at a constant temperature of 300K) was first investigated to determine if the samples experienced saturation of their magnetic signal. For all samples, the magnetization increased linearly with increasing field over the range

48

investigated (0-10,000G). Subsequent temperature-dependent studies were then performed at a constant field. From the temperature dependent data, the molar magnetic susceptibility, χ_M, was calculated and a plot of $1/\chi_M$ vs T was used to derive the effective magnetic moment, μ_{eff}, from the following formula:

$$\mu_{eff} = 2.818 \times (\chi_M)^{1/2}$$

where χ_M is the inverse of the slope taken from the linear region of the plot.

Charge Transport Measurements - DC electrical conductivity and thermopower studies were performed at room temperature. Conductivity measurements were performed in the usual four-probe geometry with 60- and 25-mm diameter gold wires used for the current and voltage electrodes, respectively. Measurements of the sample cross-sectional area and voltage probe separation were made with a calibrated binocular microscope. Conductivity data were obtained with the computer-automated system described elsewhere.[26] Thermoelectric power measurements were made by using a slow AC technique[27] which requires the production of a slowly varying periodic temperature gradient across the samples and measuring the resulting sample voltage. Samples were suspended between quartz block heaters by 60-mm gold wires thermally grounded to the block with GE 7031 varnish. The gold wires were used to support and conduct heat to the sample, as well as to measure the voltage across the sample resulting from the applied temperature gradient. The magnitude of the applied temperature gradient was generally 1.0K. Smaller temperature gradients gave

essentially the same results but with lower sensitivity. In both measurements, the gold electrodes were held in place on the sample with conductive gold paste. Mounted samples were placed under vacuum (10^{-3} Torr) and heated to 320 K for 2-4 h to cure the gold contacts. For a variable-temperature run, data (conductivity or thermopower) were acquired during sample warming. The average temperature drift rate during an experiment was kept below 0.3 K/min. Multiple variable-temperature runs were carried out for each sample to ensure reproducibility and stability. At a given temperature, reproducibility was within $\pm$ 5%.

Table 2.5   Crystallographic Data for ALn_3Te_8 (A = Cs, Rb, K; Ln = Ce, Nd)

Formula	$CsCe_3Te_8$	$RbCe_3Te_8$
a, (Å)	9.057(2)	9.051(2)
b, (Å)	12.996(3)	12.996(3)
c, (Å)	14.840(3)	14.376(3)
β, (deg)	98.74(2)	98.87(2)
V, (Å^3)	1726.4(7)	1670.8(7)
Space Group	$P2_1/a$ (#14)	$P2_1/a$ (#14)
Z value	4	4
F.W (g/mol)	1574.06	1526.63
$d_{cal.}$, (g/cm^3)	6.056	6.069
μ, (cm^{-1})	232.41	246.98
crystal (mm^3)	0.18x0.27x0.09	0.23x0.45x0.02
Radiation	Mo Kα	Mo Kα
$2\theta_{max.}$, (deg)	50.0	50.0
Temp., (°C)	293	293
No. data collected	3412	3301
No. unique data	3193	3096
No. $F_o^2 > 3\sigma (F_o^2)$	1591	1565
No. variables	110	110
R/R$_w$, % [a]	4.9/6.3	6.8/7.9
GOF	2.29	3.12

[a] $R = \Sigma(|F_o| - |F_c|)/\Sigma |F_o|$ $R_w = \{ \Sigma(w (|F_o| - |F_c|)^2/\Sigma w| F_o|^2 \}^{1/2}$

Tab...

\3:

I

R

Table 2.5 continued Crystallographic Data for ALn_3Te_8 (A =Cs, Rb, K; Ln = Ce, Nd)

Formula	KCe_3Te_8	KNd_3Te_8
a, (Å)	9.0630(3)	8.956(1)
b, (Å)	13.0164(4)	12.836(2)
c, (Å)	13.9677(3)	13.856(3)
β, (deg)	99.305(1)	99.42(1)
V, (Å^3)	1626.05(8)	1571.4(8)
Space Group	$P2_1/a$ (#14)	$P2_1/a$ (#14)
Z value	4	4
F.W (g/mol)	1480.26	1492.62
$d_{cal.}$, (g/cm^3)	6.047	6.308
μ, (cm^{-1})	225.40	246.46
crystal (mm^3)	0.18x0.18x0.02	0.18x0.21x0.03
Radiation	Mo Kα	Mo Kα
$2\theta_{max.}$, (deg)	50.0	50.0
Temp., (K)	173	188
No. data collected	3769	2373
No. unique data	3768	2200
No. $F_o^2 > 3\sigma (F_o^2)$	3270	654
No. variables	110	110
R/R$_w$, % [a]	9.4/11.4	5.4/6.2
GOF	2.20	2.56

[a] $R = \Sigma(|F_o| - |F_c|)/\Sigma |F_o|$ $R_w = \{ \Sigma(w (|F_o| - |F_c|)^2/\Sigma w| F_o|^2 \}^{1/2}$

C. Results and Discussion

Structure Description - The four isostructural compounds, ALn_3Te_8 (A = Cs, Rb, K; Ln = Ce, Nd), resulted from initial investigations into the A/Cu/Ln/Te (Ln = Ce, Nd) systems. Their two-dimensional structure is shown in Figure 2.1. The Ln and Te atoms make up the anionic layers and the alkali cations reside in the interlayer gallery. The Ln atoms possess three crystallographic positions with two distinct coordination environments, shown in Figure 2.2. Two of the Ln atoms are eight coordinate with a bicapped trigonal prismatic environment of Te. The third Ln atom is nine coordinate with a tricapped trigonal prismatic environment of Te. The atomic coordinates and isotropic displacement parameters are given in Table 2.6 and the anisotropic displacement parameters in Table 2.7 for ALn_3Te_8 (A = Cs, Rb, K; Ln = Ce, Nd).

The anionic layer of these compounds is a derivative of the $NdTe_3$ structure type, differing only in the occupancy of the square Te net. From a fully occupied $NdTe_3$ lattice, one tellurium atom is removed, causing the remaining Te atoms to "condense" into Te_3^{2-} oligomers and zig-zag $(Te_2^{2-})_n$ polymers arranged in an unusual pattern, shown in Figure 2.3. The bonding in the zig-zag chains consists of almost equal Te-Te distances of 2.989(3)Å and 3.010(3)Å for $CsCe_3Te_8$. The Te-Te distances in the trimerized Te_3^{2-} unit are 2.836(3)Å and 2.847(3)Å, longer than the normal Te-Te bond length of 2.76Å found in $(Ph_4P)_2Te_4$.[28] The formal oxidation states are therefore $A^+(Ln_3Te_3)^{3+}(Te_3^{2-})(Te_2^{2-})_n$. Selected distances and

53

bond angles for ALn_3Te_8 (A = Cs, Rb, K; Ln = Ce, Nd) are shown in Table 2.8. The structure observed for the defect square net in ALn_3Te_8 can be thought of as a 2a x 3b superstructure of the $NdTe_3$ structure, which is thought to have an ideal square sublattice.

The pattern of the Te net in ALn_3Te_8 was previously predicted on theoretical grounds by Lee and Foran[15] in reporting the structure of $RbDy_3Se_8$.[16] This compound was solved in a disordered model in the orthorhombic space group Cmcm with a=4.0579(6)Å, b=26.47(1)Å, and c=3.890(9)Å, but Weissenberg and precession photographs indicated a very weak superstructure with $a_{super} = 4a_{sub}$, $b_{super} = 3b_{sub}$, and $c_{super} = c_{sub}$. This superstructure could not be resolved crystallographically. HOMO-LUMO energy calculations were made using Hückel theory to predict the superstructure pattern of $RbDy_3Se_8$. Although the 2a x 3b superstructure of ALn_3Te_8 is different from the 4a x 3b superstructure found in $RbDy_3Se_8$, one of the two lowest energy patterns predicted for the Se net in its superstructure is depicted in the Te net of ALn_3Te_8.
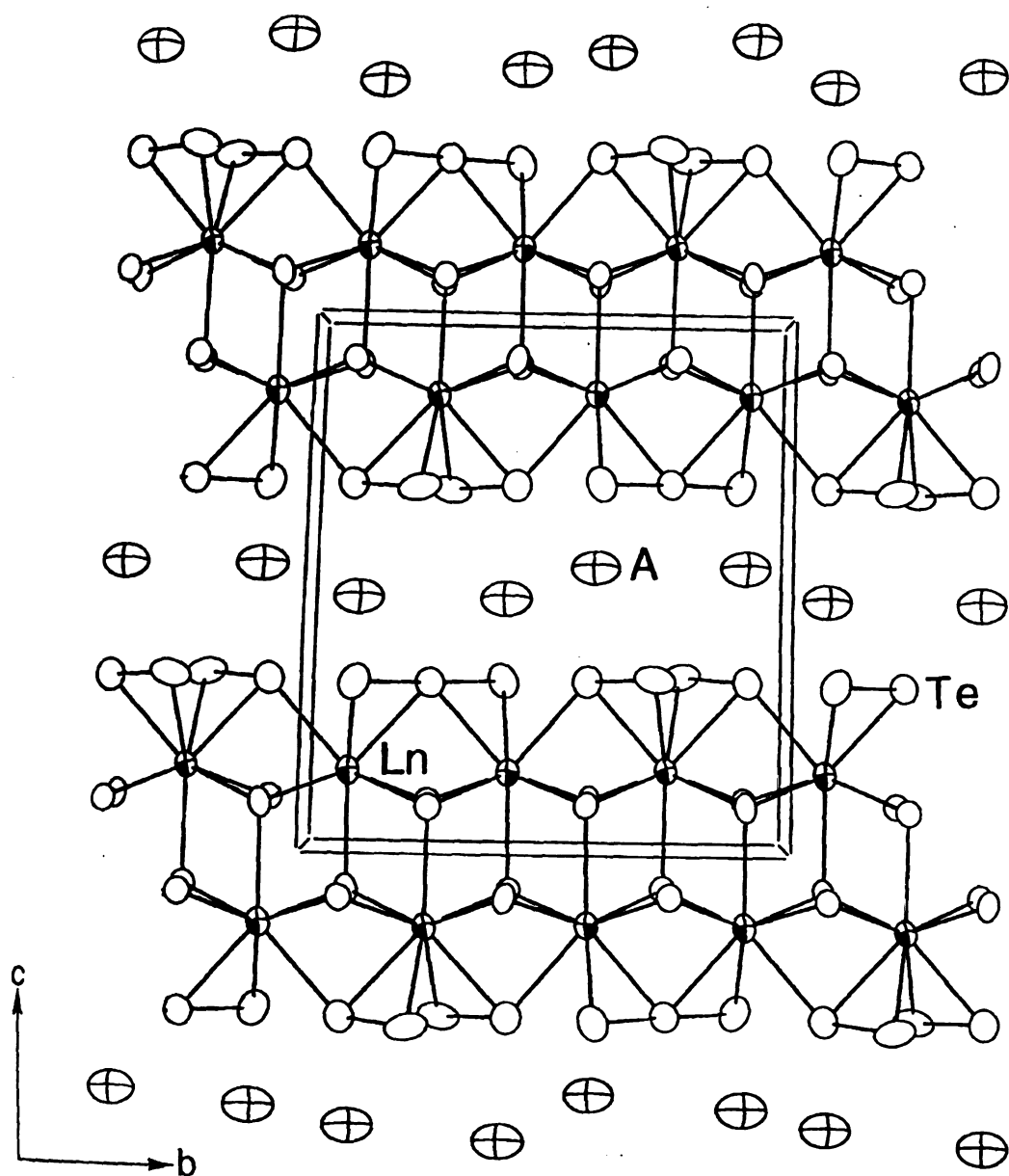
Figure 2.1 ORTEP representation of the structure of ALn_3Te_8 as seen parallel to anionic layer. (circles with nonshaded octants: A = Cs, Rb, K; large open circles: Te; circles with shaded octants: Ln = Ce, Nd).
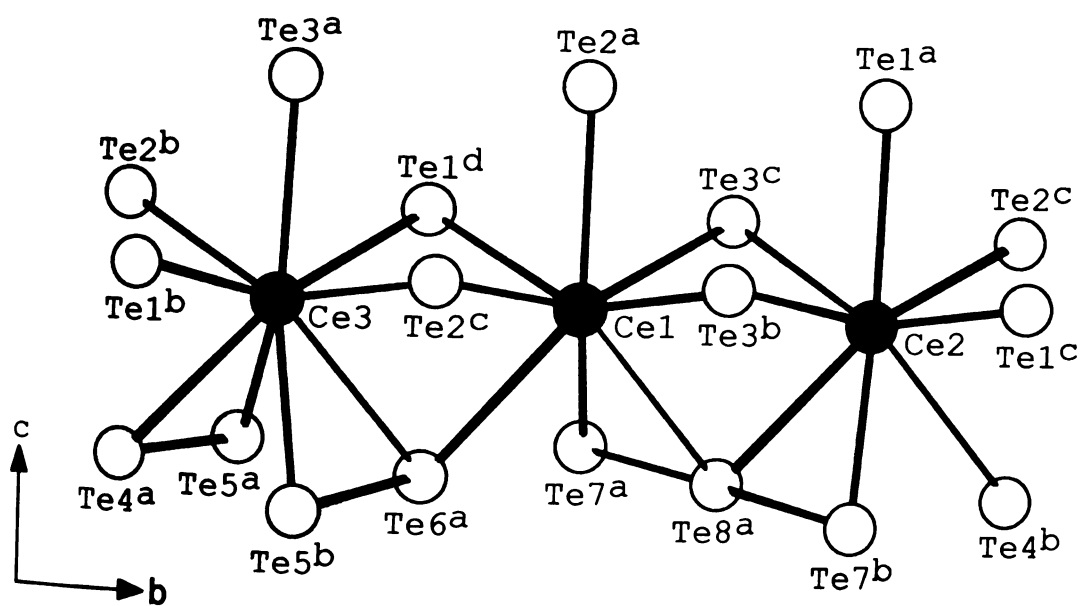
Figure 2.2 A fragment of $CsCe_3Te_8$ showing the coordination environment of the Ce atoms.
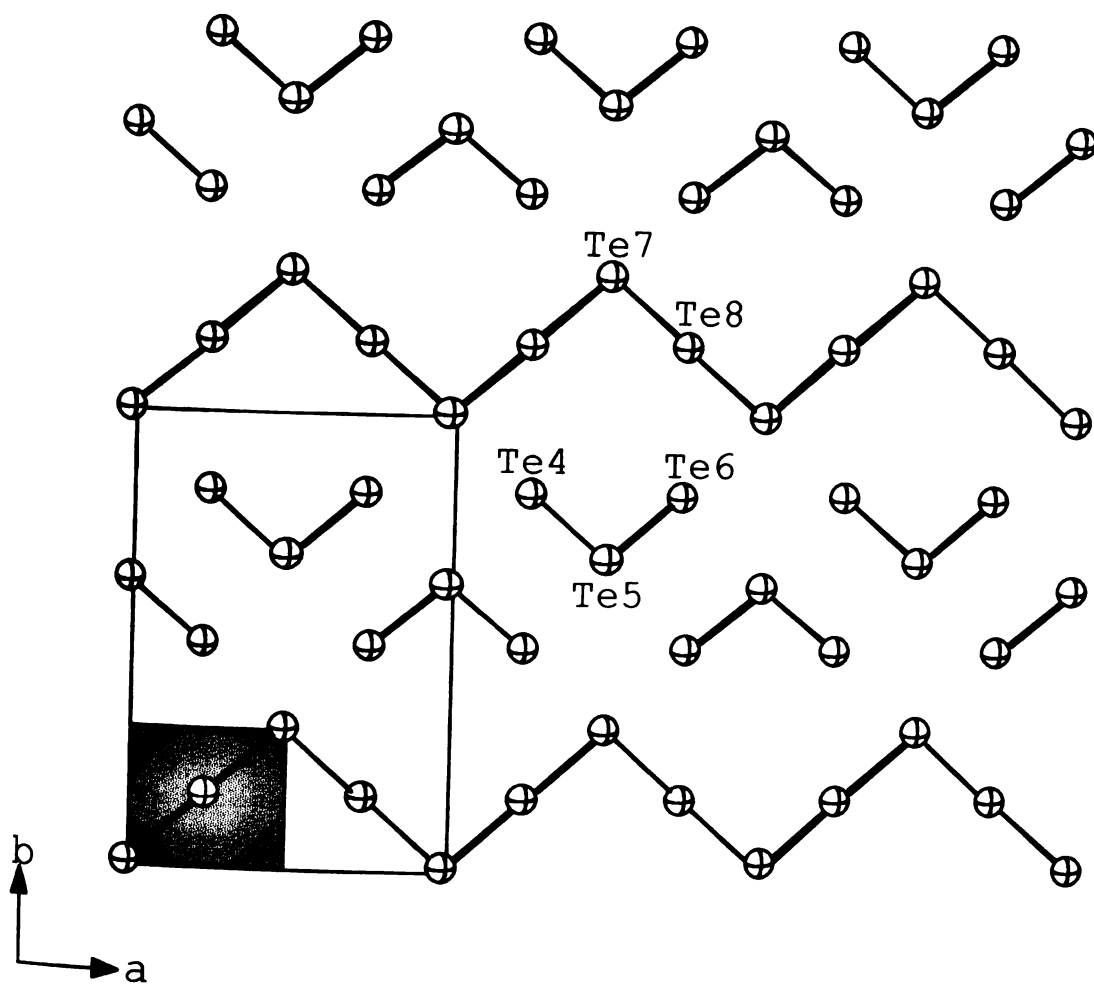
Figure 2.3 View of the Te "net" of $CsCe_3Te_8$ showing the Te_3^{2-} units and the infinite zigzag $(Te_2^{2-})_n$ chains. The shaded area indicates the unit cell of the hypothetical parent structure of $NdTe_3$. The Te square net in the $NdTe_3$ structure is, of course, fully occupied.

Table

Param

Stand

GaCe

RsCe

Table 2.6 Fractional Atomic Coordinates and Equivalent Isotropic Displacement Parameters (B_{eq}) for ALn_3Te_8 (A = Cs, Rb, K; Ln = Ce, Nd) with Estimated Standard Deviations in Parentheses.

$CsCe_3Te_8$

atom	x	y	z	B_{eq}^{a}, Å^2
Ce(1)	0.5958(2)	0.4160(2)	0.8597(1)	0.68(6)
Ce(2)	0.9158(2)	0.5850(2)	0.1413(1)	0.70(6)
Ce(3)	0.9113(2)	0.2494(1)	0.1458(1)	0.67(7)
Te(1)	0.8562(2)	0.5856(2)	0.9167(1)	0.71(7)
Te(2)	0.6478(2)	0.4199(2)	0.0844(1)	0.67(7)
Te(3)	0.8555(2)	0.2459(2)	0.9209(1)	0.71(8)
Te(4)	0.9434(2)	0.4195(2)	0.3148(1)	1.06(8)
Te(5)	0.7052(3)	0.2795(2)	0.3222(2)	1.22(8)
Te(6)	0.4631(2)	0.4206(2)	0.3144(1)	1.05(8)
Te(7)	0.2033(2)	0.5987(2)	0.3121(1)	1.12(8)
Te(8)	0.0482(3)	0.2496(2)	0.6901(1)	1.0(1)
Cs(1)	0.2573(2)	0.4065(2)	0.5301(1)	2.16(9)

$RbCe_3Te_8$

atom	x	y	z	B_{eq}^{a}, Å^2
Ce(1)	0.5942(4)	0.4159(2)	0.8551(2)	0.3(2)
Ce(2)	0.9167(4)	0.5849(2)	0.1466(2)	0.3(2)
Ce(3)	0.9124(4)	0.2496(2)	0.1514(2)	0.3(2)
Te(1)	0.8553(4)	0.5856(2)	0.9139(3)	0.4(2)
Te(2)	0.6486(4)	0.4200(2)	0.0871(3)	0.3(2)
Te(3)	0.8548(5)	0.2460(2)	0.9184(3)	0.4(2)
Te(4)	0.9466(5)	0.4195(3)	0.3258(3)	0.7(2)
Te(5)	0.7078(5)	0.2795(3)	0.3332(3)	1.1(2)
Te(6)	0.4662(5)	0.4204(3)	0.3256(3)	0.7(2)
Te(7)	0.2058(5)	0.5991(2)	0.3225(3)	1.3(2)
Te(8)	0.0450(6)	0.2494(3)	0.6788(3)	0.7(2
Rb(1)	0.2581(8)	0.4066(4)	0.5320(4)	2.1(3)

[a] B values for anisotropically refined atoms are given in the form of the isotropic equivalent displacement parameter defined as $B_{eq} = (4/3)[a^2B(1,1) + b^2B(2,2) + c^2B(3,3) + ab(\cos\gamma)B(1,2) + ac(\cos\beta)B(1,2) + ac(\cos\beta)B(1,3) + bc(\cos\alpha)B(2,3)]$

Tabl...

Dispi...

Esti...

KCa...

I...

N...

Table 2.6 continued   Fractional Atomic Coordinates and Equivalent Isotropic Displacement Parameters (U_{eq}) for ALn_3Te_8 (A = Cs, Rb, K; Ln = Ce, Nd) with Estimated Standard Deviations in Parentheses.

KCe_3Te_8

atom	x	y	z	U_{eq}^a, Å^2
Ce(1)	0.5931(2)	0.4153(2)	0.8507(2)	0.44(1)
Ce(2)	0.9180(2)	0.5840(2)	0.1510(2)	0.44(1)
Ce(3)	0.9140(2)	0.2489(2)	0.1558(2)	0.44(1)
Te(1)	0.8546(2)	0.5871(2)	0.9115(2)	0.44(1)
Te(2)	0.6489(2)	0.4220(2)	0.0895(2)	0.44(1)
Te(3)	0.8538(3)	0.2482(2)	0.9155(2)	0.44(1)
Te(4)	0.9495(3)	0.4177(3)	0.3357(2)	0.49(1)
Te(5)	0.7104(4)	0.2761(3)	0.3428(3)	0.55(1)
Te(6)	0.4679(3)	0.4206(3)	0.3357(2)	0.49(1)
Te(7)	0.2079(3)	0.6015(2)	0.3322(3)	0.54(1)
Te(8)	0.0426(3)	0.2503(2)	0.6683(2)	0.47(1)
K(1)	0.2590(1)	0.4051(8)	0.5358(9)	0.63(1)

U_{eq} is defined as one-third of the trace of the orthogonalized U_{ij} tensor.

KNd_3Te_8

atom	x	y	z	B_{eq}^a, Å^2
Nd(1)	0.6042(3)	0.4106(3)	0.8492(2)	0.8(1)
Nd(2)	0.9299(3)	0.5795(3)	0.1476(2)	0.8(1)
Nd(3)	0.9141(2)	0.254(1)	0.1548(2)	1.5(1)
Te(1)	0.8607(4)	0.5804(3)	0.9176(3)	1.4(1)
Te(2)	0.6544(4)	0.4143(4)	0.0933(3)	1.2(1)
Te(3)	0.8533(3)	0.245(1)	0.9167(2)	1.5(1)
Te(4)	0.9473(4)	0.4179(3)	0.3268(3)	1.6(1)
Te(5)	0.7102(4)	0.2777(2)	0.3411(3)	1.4(1)
Te(6)	0.4690(4)	0.4227(3)	0.3409(3)	1.5(1)
Te(7)	0.2076(4)	0.5967(3)	0.3303(3)	1.7(1)
Te(8)	0.0423(3)	0.247(1)	0.6704(2)	1.7(1)
K(1)	0.259(1)	0.409(1)	0.5357(9)	2.4(4)

[a] B values for anisotropically refined atoms are given in the form of the isotropic equivalent displacement parameter defined as $B_{eq} = (4/3)[a^2B(1,1) + b^2B(2,2) + c^2B(3,3) + ab(\cos\gamma)B(1,2) + ac(\cos\beta)B(1,3) + bc(\cos\alpha)B(2,3)]$

Table 2.7 Anisotropic Displacement Parameters (Å) for ALn_3Te_8 (A = Cs, Rb, K; Ln = Ce, Nd) with Standard Deviations in Parentheses

$CsCe_3Te_8$

atom	U11	U22	U33	U12	U13	U23
Ce(1)	0.0079(9)	0.0073(7)	0.010(1)	0.0001(9)	0.0010(7)	0.0001(8)
Ce(2)	0.0075(9)	0.0067(7)	0.012(1)	0.0001(9)	0.0006(7)	0.0006(8)
Ce(3)	0.008(1)	0.007(1)	0.010(1)	0.0002(8)	0.0011(8)	0.0008(8)
Te(1)	0.008(1)	0.0063(8)	0.013(1)	-0.000(1)	0.0017(8)	0.001(1)
Te(2)	0.015(1)	0.011(1)	0.014(1)	-0.001(1)	0.0017(9)	0.001(1)
Te(3)	0.007(1)	0.009(1)	0.010(1)	0.0003(9)	0.0011(9)	0.0002(9)
Te(4)	0.008(1)	0.008(1)	0.010(1)	0.000(1)	0.012(8)	0.0006(9)
Te(5)	0.013(1)	0.012(1)	0.015(1)	0.000(1)	0.022(9)	0.000(1)
Te(6)	0.012(1)	0.013(1)	0.018(1)	-0.001(1)	0.0043(9)	0.003(1)
Te(7)	0.012(1)	0.024(1)	0.010(1)	-0.000(1)	0.029(9)	0.003(1)
Te(8)	0.013(1)	0.011(1)	0.013(1)	-0.0007(9)	0.001(1)	0.001(1)
Cs(1)	0.030(1)	0.035(1)	0.017(1)	-0.001(1)	0.005(1)	0.000(1)

$RbCe_3Te_8$

atom	U11	U22	U33	U12	U13	U23
Ce(1)	0.004(3)	0.001(2)	0.007(2)	-0.002(2)	0.003(2)	-0.001(2)
Ce(2)	0.004(3)	0.001(2)	0.005(2)	0.003(2)	0.002(3)	0.001(2)
Ce(3)	0.003(3)	0.002(2)	0.007(2)	0.001(2)	0.004(2)	0.001(2)
Te(1)	0.005(3)	0.004(2)	0.006(3)	-0.000(2)	0.002(3)	-0.001(2)
Te(2)	0.002(3)	0.004(2)	0.005(3)	-0.000(2)	0.002(3)	0.002(2)
Te(3)	0.004(3)	0.006(2)	0.005(3)	-0.002(2)	0.001(3)	-0.001(2)
Te(4)	0.009(3)	0.010(2)	0.008(3)	-0.001(2)	0.002(3)	-0.004(2)
Te(5)	0.004(3)	0.032(2)	0.007(3)	0.002(2)	-0.002(3)	0.005(2)
Te(6)	0.010(3)	0.010(2)	0.009(3)	0.001(2)	0.004(3)	0.000(2)
Te(7)	0.017(3)	0.010(2)	0.021(3)	-0.000(3)	-0.000(3)	0.002(2)
Te(8)	0.008(3)	0.006(2)	0.011(3)	-0.001(2)	0.003(3)	-0.001(2)
Rb(1)	0.033(5)	0.035(3)	0.008(4)	-0.002(4)	-0.005(4)	-0.002(3)

Table

A = C

KCa

Table 2.7 continued   Anisotropic Displacement Parameters (Å) for ALn_3Te_8
$(A = Cs, Rb, K; Ln = Ce, Nd)$ with Standard Deviations in Parentheses

KCe_3Te_8

atom	U11	U22	U33	U12	U13	U23
Ce(1)	0.028(1)	0.045(1)	0.056(1)	0.006(1)	0.004(1)	0.003(1)
Ce(2)	0.030(1)	0.047(1)	0.053(1)	-0.008(1)	0.002(1)	-0.007(1)
Ce(3)	0.027(1)	0.051(1)	0.054(1)	-0.009(1)	0.000(1)	-0.005(1)
Te(1)	0.030(1)	0.044(1)	0.054(1)	0.004(1)	0.003(1)	-0.008(2)
Te(2)	0.027(1)	0.044(1)	0.058(1)	-0.003(1)	0.002(1)	0.004(1)
Te(3)	0.028(1)	0.056(1)	0.050(1)	0.004(1)	0.001(1)	-0.006(2)
Te(4)	0.034(1)	0.058(1)	0.054(1)	0.007(1)	0.000(1)	0.001(2)
Te(5)	0.032(1)	0.101(2)	0.052(1)	0.002(1)	0.001(1)	0.010(2)
Te(6)	0.036(1)	0.055(1)	0.056(1)	-0.007(1)	0.003(1)	0.001(2)
Te(7)	0.038(1)	0.034(1)	0.072(1)	0.000(1)	0.002(1)	0.003(1)
Te(8)	0.036(1)	0.044(1)	0.054(1)	0.006(1)	0.002(1)	-0.001(2)
K(1)	0.045(5)	0.062(5)	0.070(4)	-0.004(5)	-0.003(5)	0.001(6)

KNd_3Te_8

atom	U11	U22	U33	U12	U13	U23
Nd(1)	0.005(1)	0.017(1)	0.010(2)	0.011(1)	0.008(1)	0.001(2)
Nd(2)	0.004(1)	0.019(1)	0.009(2)	0.009(1)	0.003(1)	0.003(1)
Nd(3)	0.027(1)	0.019(1)	0.010(1)	0.000(4)	0.003(1)	0.005(5)
Te(1)	0.024(2)	0.013(2)	0.013(3)	-0.001(2)	-0.002(2)	0.006(2)
Te(2)	0.020(2)	0.034(2)	-0.011(2)	0.004(2)	-0.004(1)	0.001(2)
Te(3)	0.028(1)	0.024(2)	0.007(2)	0.004(5)	0.004(1)	0.010(5)
Te(4)	0.031(2)	0.032(2)	-0.004(2)	-0.003(3)	-0.005(1)	0.002(2)
Te(5)	0.028(1)	0.015(2)	0.009(2)	0.000(1)	0.002(1)	0.003(1)
Te(6)	0.026(2)	0.016(2)	0.010(2)	-0.001(2)	-0.008(1)	0.005(2)
Te(7)	0.028(1)	0.027(1)	0.009(2)	0.001(2)	0.005(1)	0.006(2)
Te(8)	0.029(1)	0.025(1)	0.011(2)	-0.002(6)	0.002(1)	0.017(5)
K(1)	0.038(5)	0.035(5)	0.015(7)	0.000(7)	-0.006(5)	0.016(7)

Table

Stand

Cell
Cell
Cell
Cell
Test
Test
Cos

Table 2.8 Selected Distances (Å) and Bond Angles (deg) for CsCe$_3$Te$_8$ with Standard Deviations in Parentheses.

Ce1 – Te1^d	3.244(3)	Ce1 – Te2^a	3.296(3)	Ce1 – Te7^a	3.356(3)
Ce2 – Te3^b	3.249(3)	Ce2 – Te3^c	3.251(3)	Ce2 – Te4^b	3.336(3)
Ce2 – Te8^a	3.278(3)	Ce3 – Te3^a	3.300(3)	Ce3 – Te4^a	3.322(3)
Ce3 – Te6^a	3.316(3)	Te4 – Te5	2.836(3)	Te4 – Te7	3.317(3)
Te4 – Te8	4.277(2)	Te5 – Te6	3.510(3)	Te6 – Te5	2.847(3)
Te6 – Te7	3.297(3)	Te6 – Te8	4.284(2)	Te7 – Te8	2.988(3)
Cs1 – Te4	3.944(3)	Cs1 – Te7	4.057(3)	Cs1 – Te8	3.841(3)

Te1^d-Ce3-Te2^c	88.35(7)	Te1^a-Ce2-Te2^c	74.81(6)
Te1^b-Ce3-Te3^a	74.08(6)	Te1^a-Ce2-Te4^b	139.82(9)
Te3^a-Ce3-Te4^a	139.05(8)	Te4^b-Ce2-Te7^b	59.46(6)
Te4^a-Ce3-Te5^a	49.39(6)	Te4^b-Ce2-Te8^a	81.17(6)
Te1^d-Ce1-Te2^a	74.90(6)	Te7^a-Te8^a-Te7^b	178.8(1)
Te1^d-Ce1-Te2^c	89.03(7)	Ce3-Te2^c-Ce1	82.70(6)
Te2^a-Ce1-Te6^a	139.27(9)	Ce1-Te3^b-Ce2	82.80(7)
Te6^a-Ce1-Te7^a	59.16(6)		

Table 2

Standar

Ce1

Ce2

Ce2

Ce3

Te4

Te6

Rb3

Table 2.9 Selected Distances (Å) and Bond Angles (deg) for $RbCe_3Te_8$ with Standard Deviations in Parentheses.

Ce1 – Te1[d]	3.247(6)	Ce1 – Te2[a]	3.291(5)	Ce1 – Te7[a]	3.357(7)
Ce2 – Te3[b]	3.253(6)	Ce2 – Te3[c]	3.252(6)	Ce2 – Te4[b]	3.332(5)
Ce2 – Te8[a]	3.282(5)	Ce3 – Te3[a]	3.317(5)	Ce3 – Te4[a]	3.317(5)
Ce3 – Te6[a]	3.316(5)	Te4 – Te5	2.840(6)	Te5 – Te6	2.842(6)
Te4 – Te8	4.305(5)	Te5 – Te6	3.509(5)	Te6 – Te5	2.841(4)
Te6 – Te7	3.304(4)	Te6 – Te8	4.278(5)	Te7 – Te8	2.986(4)
Rb1 – Te4	3.760(9)	Rb1 – Te7	3.886(7)	Rb1 – Te8	3.686(8)

Te1[d]-Ce3-Te2[c]	88.1(2)	Te1[a]-Ce2-Te2[c]	74.7(1)
Te1[b]-Ce3-Te3[a]	73.9(1)	Te1[a]-Ce2-Te4[b]	139.8(1)
Te3[a]-Ce3-Te4[a]	139.0(1)	Te4[b]-Ce2-Te7[b]	59.5(1)
Te4[a]-Ce3-Te5[a]	49.6(1)	Te4[b]-Ce2-Te8[a]	81.2(1)
Te1[d]-Ce1-Te2[a]	74.8(1)	Te7[a]-Te8[a]-Te7[b]	179.3(2)
Te1[d]-Ce1-Te2[c]	88.9(2)	Ce3-Te2[c]-Ce1	82.8(1)
Te2[a]-Ce1-Te6[a]	139.3(1)	Ce1-Te3[b]-Ce2	82.9(2)
Te6[a]-Ce1-Te7[a]	59.2(1)		

Standa

Ca1

Ca2

Ca2

Ce3

Ta4

Ta6

K1-

Table 2.10 Selected Distances (Å) and Bond Angles (deg) for KCe_3Te_8 with Standard Deviations in Parentheses.

Ce1 – Te1^d	3.248(2)	Ce1 – Te2^a	3.294(2)	Ce1 – Te7^a	3.359(2)
Ce2 – Te3^b	3.256(2)	Ce2 – Te3^c	3.256(2)	Ce2 – Te4^b	3.334(2)
Ce2 – Te8^a	3.298(2)	Ce3 – Te3^a	3.307(2)	Ce3 – Te4^a	3.328(2)
Ce3 – Te6^a	3.322(2)	Te4 – Te5	2.848(2)	Te5 – Te6	2.850(2)
Te4 – Te8	4.322(2)	Te5 – Te6	3.476(2)	Te6 – Te5	2.882(2)
Te6 – Te7	3.325(2)	Te6 – Te8	4.293(2)	Te7 – Te8	2.973(2)
K1 – Te4	3.641(7)	K1 – Te7	3.755(7)	K1 – Te8	3.549(7)

Te1^d-Ce3-Te2^c	88.13(5)	Te1^a-Ce2-Te2^c	74.54(5)
Te1^b-Ce3-Te3^a	74.04(5)	Te1^a-Ce2-Te4^b	139.82(6)
Te3^a-Ce3-Te4^a	138.98(6)	Te4^b-Ce2-Te7^b	59.38(5)
Te4^a-Ce3-Te5^a	49.58(5)	Te4^b-Ce2-Te8^a	80.98(5)
Te1^d-Ce1-Te2^a	74.80(5)	Te7^a-Te8^a-Te7^b	179.7(1)
Te1^d-Ce1-Te2^c	88.87(5)	Ce3-Te2^c-Ce1	82.78(4)
Te2^a-Ce1-Te6^a	139.25(6)	Ce1-Te3^b-Ce2	82.84(5)
Te6^a-Ce1-Te7^a	59.06(5)		

Table

Standa...

N...
N...
N...
N...
T34...
Te6...
X1 -

Table 2.11 Selected Distances (Å) and Bond Angles (deg) for KNd$_3$Te$_8$ with Standard Deviations in Parentheses.

Nd1 – Te1[d]	3.196(5)	Nd1 – Te2[a]	3.338(5)	Nd1 – Te7[a]	3.227(5)
Nd2 – Te3[b]	3.191(9)	Nd2 – Te3[c]	3.321(8)	Nd2 – Te4[b]	3.220(5)
Nd2 – Te8[a]	3.34(1)	Nd3 – Te3[a]	3.257(4)	Nd3 – Te4[a]	3.159(9)
Nd3 – Te6[a]	3.41(1)	Te4 – Te5	2.815(5)	Te5 – Te6	2.851(5)
Te4 – Te8	4.302(4)	Te5 – Te6	3.462(5)	Te6 – Te5	2.851(4)
Te6 – Te7	3.221(5)	Te6 – Te8	4.166(3)	Te7 – Te8	2.957(4)
K1 – Te4	3.68(1)	K1 – Te7	3.70(1)	K1 – Te8	3.57(2)

Te1[d]-Nd3-Te2[c]	88.1(2)	Te1[a]-Nd2-Te2[c]	75.6(1)
Te1[b]-Nd3-Te3[a]	73.4(2)	Te1[a]-Nd2-Te4[b]	139.5(2)
Te3[a]-Nd3-Te4[a]	140.0(4)	Te4[b]-Nd2-Te7[b]	60.6(1)
Te4[a]-Nd3-Te5[a]	50.6(1)	Te4[b]-Nd2-Te8[a]	81.8(2)
Te1[d]-Nd1-Te2[a]	73.7(1)	Te7[a]-Te8[a]-Te7[b]	178.9(4)
Te1[d]-Nd1-Te2[c]	87.9(2)	Nd3-Te2[c]-Nd1	82.7(2)
Te2[a]-Nd1-Te6[a]	139.3(2)	Nd1-Te3[b]-Nd2	82.96(8)
Te6[a]-Nd1-Te7[a]	58.4(1)		

65

Transmission Electron Microscopy - Electron diffraction studies on KNd_3Te_8 revealed an additional, possibly *incommensurate*, superstructure along the a-axis. The reflections associated with this new superstructure are very weak and occur along the a^* direction with $a^*_{super} = 0.429a^*_{sub}$, where a_{sub} is the length of the the KNd_3Te_8 cell (i.e., 8.956 Å). An optical densitometric scan obtained from electron diffraction photographs of the (hk0) reciprocal plane along the (h60) row of reflections is shown in Figure 2.4. The weak reflections between the (160), (260), and (360) reflections are due to the additional $0.429a^*_{sub}$ superlattice, which corresponds to a 2.33 a_{sub} (i.e.~ 21Å) lattice dimension. These results suggest an additional oligomerization and/or fragmentation along the chains of the Te trimers and/or the infinite zig-zag chains.

Figure 2.4   (A) Selected are electron diffraction pattern of KNd_3Te_8 with the beam perpendicular to the layers ([001] direction)   (B) Densitometric intensity scan along the b^*-axis of the electron diffraction pattern

Electron Diffraction of KNd$_3$Te$_8$

2.33a x 1b supercell

(060) (160) 0.429a* (260) 0.429a* (360) (460)

Intensity/Arbitrary Units

Reciprocal Angstroms

RbCe

Sn+C

the ma

linear

for sev

ation in

ge of

ben c
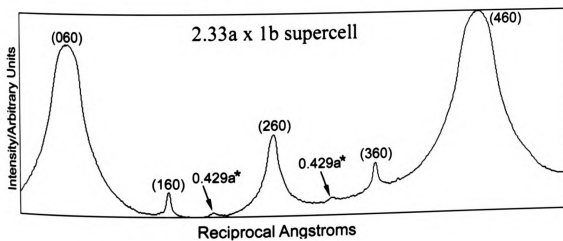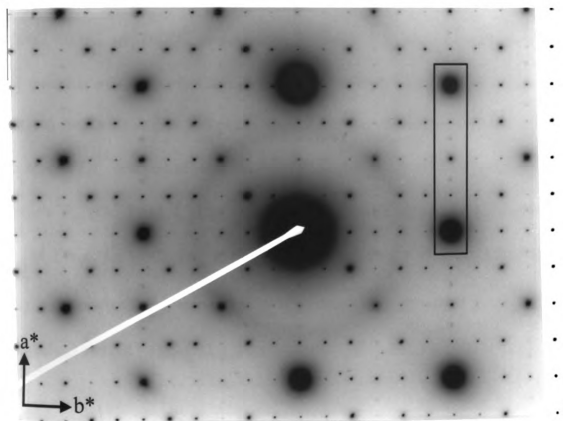
C:\ 2

Magnetic Susceptibility Measurements - The magnetic susceptibilities of $RbCe_3Te_8$, KCe_3Te_8, and KNd_3Te_8 were measured over the range 5-300K at 5000G, 6000G, and 6000G, respectively. A plot of $1/\chi_M$ vs T for each shows that the materials exhibit nearly Curie-Weiss behavior with only slight deviation from linearity beginning below 50K, see Figure 2.5. Such deviation has been reported for several Ln^{3+} compounds and has been attributed to crystal field splitting of the cation's $^2F_{5/2}$ (Ce^{3+}) and $^4I_{9/2}$ (Nd^{3+}) ground state.[29] At temperatures above 150K, a μ_{eff} of $2.76\mu_B$ for $RbCe_3Te_8$, $3.07\mu_B$ for KCe_3Te_8 and $3.33\mu_B$ for KNd_3Te_8 has been calculated. These values are in accordance with the usual range for Ce^{3+} (2.3-2.5μ_B) and Nd^{3+} (3.5-3.62 μ_B) compounds.
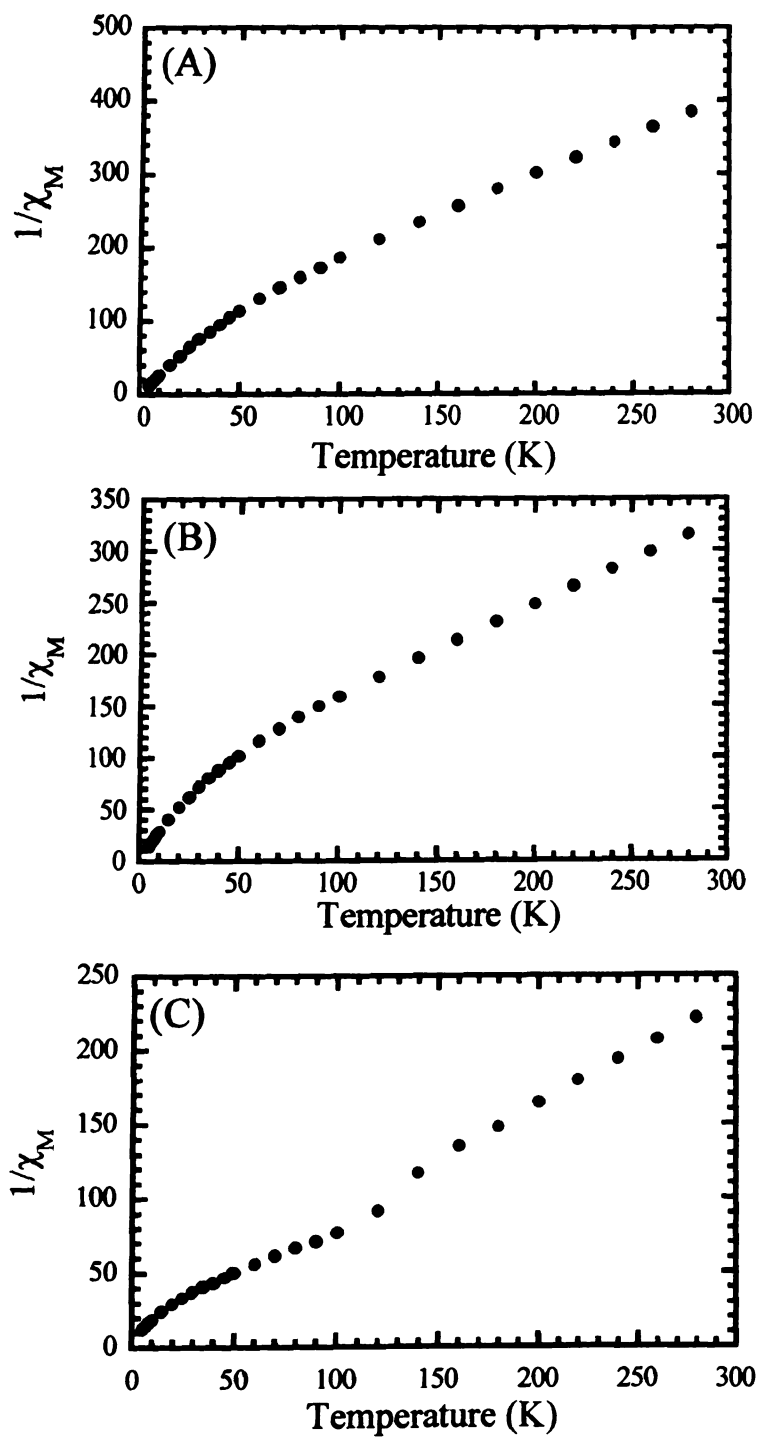
Figure 2.5 Inverse molar magnetic susceptibility $(1/\chi_M)$ plotted against temperature (2-300K) for (A) $RbCe_3Te_8$, (B) KCe_3Te_8, and (C) KNd_3Te_8.

Charge Transport Properties - Electrical conductivity data as a function of temperature for a single crystal of KNd_3Te_8 and room temperature pressed pellets of $CsCe_3Te_8$ and $RbCe_3Te_8$ show that these materials are semiconductors with room temperature values ranging from 0.01 to 0.1 S/cm, see Figure 2.6A. The conductivities for $CsCe_3Te_8$ and $RbCe_3Te_8$ decrease with decreasing temperature. For KNd_3Te_8, however, the data do not follow the typical thermally activated behavior of semiconductors, suggesting a complicated electronic band structure at the Fermi level. Considering that grain boundaries in the pressed pellets of $CsCe_3Te_8$ and $RbCe_3Te_8$ can inhibit their conductivities, it is difficult to deduce which material is the most conductive. It can be said, however, that the pressed pellets of $CsCe_3Te_8$ and $RbCe_3Te_8$ are only slightly less conductive than the single crystal of KNd_3Te_8. Also, the faster decline of the conductivity in the pellets at lower temperatures can be attributed to thermal deactivation at the grain boundaries.

Thermoelectric power data obtained on KNd_3Te_8 and $CsCe_3Te_8$ show a very large Seebeck coefficient at room temperature of 500 and 400 $\mu V/K$, respectively. The thermopower of $RbCe_3Te_8$ has a much lower value of 200 $\mu V/K$ at room temperature. The decreasing Seebeck coefficients with decreasing temperatures, their positive signs, and their large magnitude (see Figure 2.6B) confirm that these compounds are p-type, narrow gap semiconductors.

Considering that the structures of ALn_3Te_8 (A = Cs, Rb, K; Ln = Ce, Nd) are related to that of the $NdTe_3$ structure type, similar charge transport measurements were made on a room temperature pressed of the binary phase $CeTe_3$, for comparison. As shown in Figure 2.7A, the conductivity has switched from that of a semiconductor for ALn_3Te_8 (A = Cs, Rb, K; Ln = Ce, Nd) to that of a metal for $CeTe_3$ and the room temperature conductivity has increased by several orders of magnitude from 0.01-0.1 S/cm to 700 S/cm. In addition, the thermopower data has decreased from 200-500 $\mu V/K$ for ALn_3Te_8 (A = Cs, Rb, K; Ln = Ce, Nd) to 6-9 $\mu V/K$ for $CeTe_3$ at room temperature. The thermopower data of $CeTe_3$ neither follows the normal behavior for that of a semiconductor nor a metal and appears to reach a local minimum around 125K. It can be concluded from this data that the structural differences imposed upon $CeTe_3$ to form ALn_3Te_8 (A = Cs, Rb, K; Ln = Ce, Nd) have dramatically affected the physical properties.

σ (S/cm)

s (μV/K)
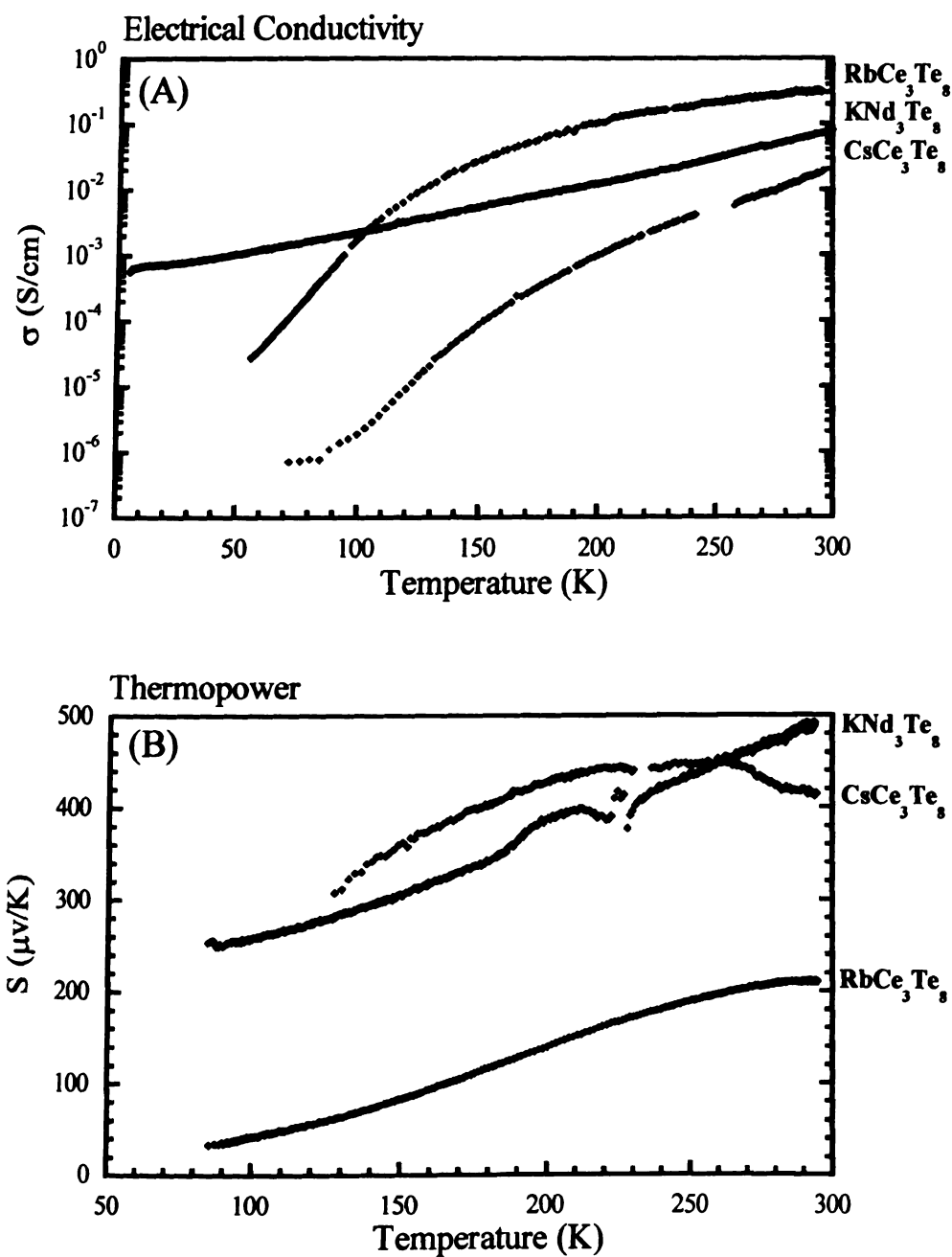
Figure 2.6 (A) Four probe, electrical conductivity [logσ (S/cm)] and (B) Thermopower (S/cm) data plotted against temperature (K) for room temperature pressed pellets of $CsCe_3Te_8$ and $RbCe_3Te_8$ and a single crystal of KNd_3Te_8.

Electrical Conductivity
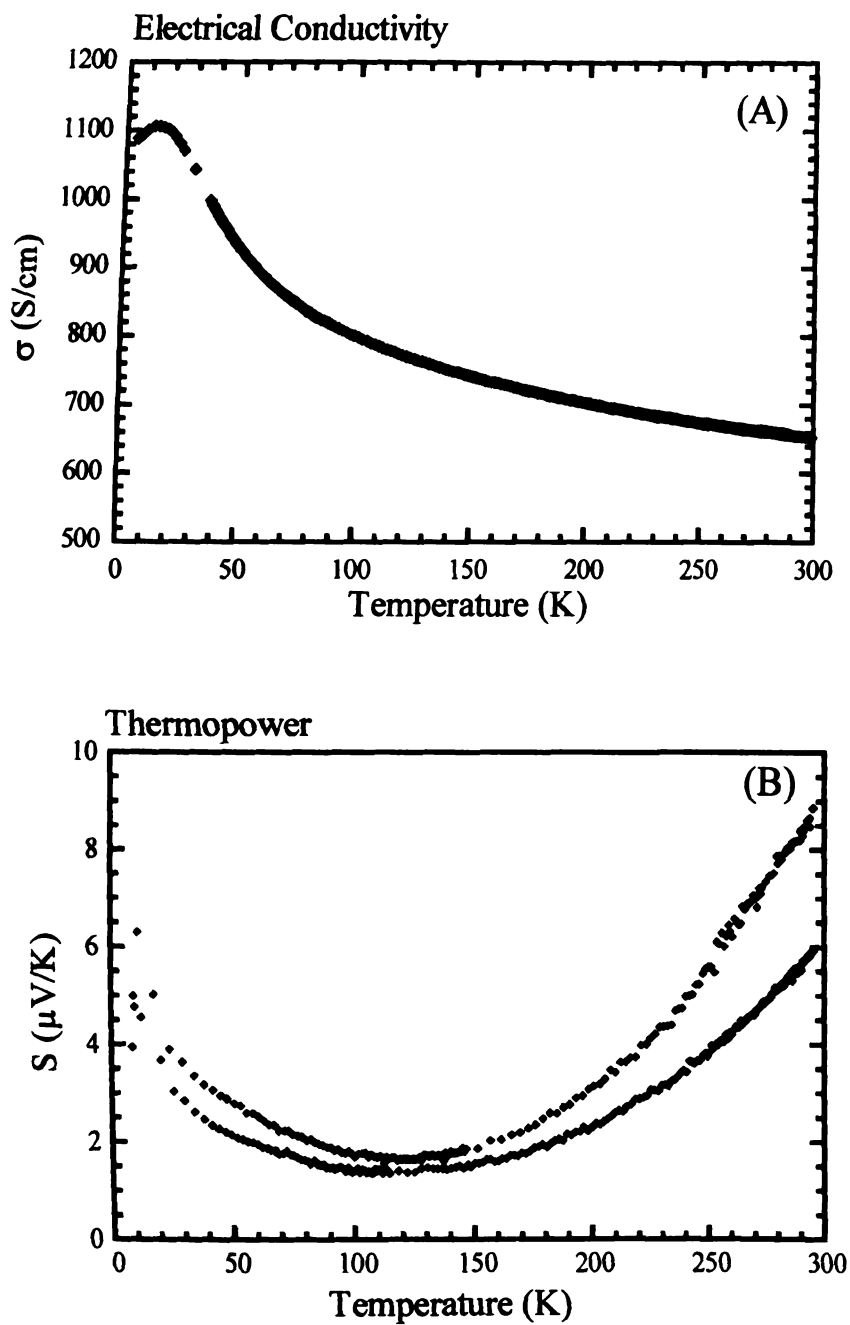
Thermopower

Figure 2.7 (A) Four probe, electrical conductivity (S/cm) and (B) Thermopower (μV/K) data plotted against temperature (K) for a room temperature pressed pellets of $CeTe_3$

D. Conclusions

To conclude, a series of compounds having the formula ALn_3Te_8 (A = Cs, Rb, K; Ln = Ce, Nd) has been discovered which possesses a two-dimensional structure very similar to that of the binary phase, $LnTe_3$. The major difference is that now an alkali metal has been inserted between the layers. In addition, a site occupancy wave type distortion exists in the Te net of this compound, giving rise to Te_3^{2-} trimers and infinite zig-zag $(Te_2^{2-})_n$ chains. From the charge transport measurements, it is evident that these structural modifications have drastically affected the physical properties of the material. A gap has opened up at the Fermi Level and the properties have switched from metallic for $CeTe_3$ to semiconducting for ALn_3Te_8 (A = Cs, Rb, K; Ln = Ce, Nd).

From a chemical point of view, it would be interesting to see if there is any relationship between the type of metal inserted between the layers and the distortion in the Te net. To try and answer this question, many attempts were made to synthesize a ternary compound in the $Ba_xLn_yTe_z$ system with hopes that a similar compound would form with Ba^{2+} ions inserted between the layers of $LnTe_3$. Unfortunately, a compound of this type could not be synthesized. In fact, this system proved to be especially challenging as the barium (as Ba or BaTe) did not incorporate into the product at all. In all cases, phase separation was observed to BaTe and $CeTe_3$. It would be

worth pursuing this system further since, to date, no $Ba_xLn_yTe_z$ phases are

known.

References

[1] Erlander, M.; Hägg, G; Westgren, A. *Ark. Kemi. Mineral. Geol.* **1935**, 12B(1), No. 1, 1-6.

[2] Haneveld, A.J.K.; Jellinek, F. *Recl. Trav. Chim. Pays-Bas.* **1964**, 83, 776.

[3] Boher, P.; Garnier, P.; Gavarri, J.R.; Hewat, A.W. *J. Solid State Chem.* **1985**, 57, 343.

[4] (a) Andress, K.R.; Alberti, E. *Z. Metallkd* **1935**, 27(6), 126. (b) Das, D.K.; Pitman, D.T. *Trans. Am. Inst. Min., Metall., Pet Eng.* **1957**, 209, 1175.

[5] Ban, Z.; Sikirica, M. *Acta. Crystallogr.* **1965**, 18, 594.

[6] Zheng, C.; Hoffman, R. *J. Am. Chem. Soc.* **1986**, 108, 3078.

[7] (a) Brechtel, E.; Cordier, G.; Schäfer, H.Z. *Z. Naturforsch., B: Anorg. Chem., Org. Chem.* **1979**, 34, 251; *Z. Naturforsch., B: Anorg. Chem., Org. Chem.* **1980**, 35, 1; *J. Less-Common Met.* **1981**, 79, 131. (b) Cordier, G.; Eisenmann, B.; Schäfer, H.Z. *Z. Anorg. Allg. Chem.* **1976**, 426, 205. (c) Cordier, G.; Schäfer, H.Z. *Z. Naturforsch., B: Anorg. Chem., Org. Chem.* **1976**, 32, 383. (d) May, N.; Schäfer, H.Z. *Z. Naturforsch., B: Anorg. Chem., Org. Chem.* **1974**, 29, 20. (e) Dorrscheidt, W.; Savelsberg, G.; Stöhr, J.; Schäfer, H.Z. *J. Less Common Met.* **1982**, 83, 269.

[8] (a) $LnNi_2Si_3$ (Ln=Sc,U): Ya Kotur, B.; Bodak, O.I; Gladyshevski, E.I. *Sov. Phys. Crystallogr.* **1978**, 23, 101. (b) $ScNiSi_3$: Ya Kotur, B.; Bodak, O.I.; Mys'kiv, M.G.; Gladyshevskii, E.I. *Sov. Phys. Crystallogr.* **1977**, 22, 151. (c) $SmNiGe_3$: Bodak, O.I.; Pecharskii, V.K.; Ya Mruz, O.; Yu Zarodnik, V.; Vivits'ka, G.M.; Salamakha, P.S. *Dopov. Akad. Nauk. Ukr. RSR , Ser. B.* **1985**, 2, 36.

[9] (a) Lin, W.; Steinfink, H.; Weiss, F. *Inorg. Chem.* **1965**, 4, 877; Wang, R.; Steinfink, H.; Bradley, W.F. *Inorg. Chem.* **1966**, 5, 142. (b) Pardo, M.-P.; Flahaut, J.; Domange, L.C.R. *Bull. Soc. Chim. Fr.* **1964**, 3267. (c) Ramsey, T.H.; Steinfink, H.; Weiss, E. *Inorg. Chem.* **1965**, 4, 1154. (d) Norling, B.K.; Steinfink, H. *Inorg. Chem.* **1966**, 5, 1488.

[10] Cody, J.A; Ibers, J.A. *Inorg. Chem.* **1996**, 35, 3836.

[11] Zhang, X.; Li, J.; Foran, B.; Guo, H.-Y.; Hogan, T.; Kannewurf, C.R.; Kanatzidis, M.G. *J. Am. Chem. Soc.* **1995**, 117, 10513.

[12] Sheldrick, W.J.; Wachhold, M. *Angew. Chem.* **1995**, 107, 490.; *Angew. Chem. Int. Ed. Engl.* **1995**, 34, 40.

[13] Kanatzidis, M.G. *Angew. Chem.* **1995**, 107, 2281; *Angew. Chem. Int. Ed. Engl.* **1995**, 34, 2109.

[14] Savelsberg, G.; Schäfer, H. *Z. Naturforsch, B.* **1978**, 33, 370.

[15] Lee, S.; Foran, B. *J. Am. Chem. Soc.* **1994**, 116, 154.

[16] Foran, B.; Lee, S.; Aronson, M. *Chem. Mat.* **1993**, 5, 974.

[17] Feher, F. *Handbuch der Praparativen Anorganischen Chemie:* Brauer, G., Ed.; Ferdinand Enke: Stuttgart, Germany, **1954**, 280.

[18] CERIUS^2, Version 2.0, Molecular Simulations Inc., Cambridge, England, 1995.

[19] Walker, N.; Stuart, D. *Acta Cryst.* **1983**, 17, 42.

[20] Sheldrick, G.M., in *Crystallographic Computing 3*; Sheldrick, G.M.; Kruger, C.; Doddard, R., Eds.; Oxford University Press: Oxford, England, **1985**, 175.

[21] Gilmore, G.J., *Appl. Cryst.* **1984**, 17, 42.

[22] SMART: Siemens Analytical Xray Systems, Inc., Madison, WI, 1994.

[23] SAINT: Version 4.0, Siemens Analytical Xray Systems, Inc., Madison WI, 1994-1996.

[24] SADABS: Sheldrick, G.M. University of Göttengen, Germany, to be published.

[25] Sheldrick, G.M. SHELXTL, Version 5; Siemens Analytical Xray Systems, Inc.; Madison, WI, 1994.

[26] Lyding, J.W.; Marcy, H.O.; Marks, T.J.; Kannewurf, C.R. *IEEE Trans. Instrum. Meas.* **1988**, 37, 76.

27   Marcy, H.O.; Marks, T.J.; Kannewurf, C.R. *IEEE Trans. Instrum. Meas.* **1990,** 39, 756.

28   Huffman, J.C.; Haushalter, R.C. *Z. Anorg. Allg. Chem.* **1984,** 518, 203.

29   Greenwood, N. N.; Earnshaw, A. *Chemistry of the Elements;* Pergamon Press: New York, 1984; p 1443.

Chapter 3

Structure and Properties of ACuUTe$_3$ (A = Cs, Rb, K):

A Comparison with KCuUSe$_3$

A. Int

discove

forml

arth n

ynthe

scustu

nd it

rysta

hop:

discos

DP u

G:Cu

E: T

R:Ag

Whls

Z:p

Sip

G:

Sp

Z:

A. Introduction

Recently, there have been several reports in the literature marking the discovery of new members of a large family of compounds with the general formula, $AMLnQ_3$ (A = alkali metal; M = coinage metal; Ln = Group IV or rare earth metal; Q = chalcogenide). Approximately 30 new compounds have been synthesized with this stoichiometry. However, they do not all adopt the same structure type. There are four known structure types that exist for this stoichiometry, see Figure 3.1. Nevertheless, the majority of these compounds do crystallize in one structure type [type a] and therefore this will be the focus of this chapter. The details of the remaining three structures (types b-d) can be found elsewhere[1-8] (also described in Chapter 1).

Members of the $AMLnQ_3$ family that crystallize in this [type a] structure type include $NaCuZrS_3$,[1,2] $KCuUSe_3$,[2,3] $KCuZrQ_3$ (Q = S, Se, Te),[2,4] $KCuHfS_3$,[4] $CsCuCeS_3$,[2,3] $CsCuUTe_3$,[2,5] $BaCuLnS_3$ (Ln = Sc, Y, Gd, Er),[6] $BaCuLnSe_3$ (Ln = Y, Er),[6] $BaCuDyTe_3$,[7] $BaCuLnTe_3$ (Ln = Y, La, Pr, Nd, Yb),[8] $BaAgNdS_3$[6] and $BaAgLnSe_3$ (Ln = Y, La, Er)[6], $BaAgLnTe_3$ (Ln = Y, La, Gd),[8] and $BaAuGdSe_3$[8]. While several of these compounds were solved from single crystal x-ray data, many others were simply confirmed as isomorphous from their powder x-ray diffraction patterns. In these cases, unit cells were determined either from a least square refinement on reflections indexed from these powder diffraction patterns or from Weissenberg or precession photographs taken on single crystals. A remarkable aspect of this structure is that it can be stablized for such a wide

variety

are si

types

makes

in term

their p

KCuZ

semico

the

synthe

diver

self-as

self-as

as

the a

the

the

variety of elements. It can form sulfide, selenide, *and* telluride analogs. This is rare since most multinary tellurides tend to adopt completely different structure types than the sulfides. The fact that there are no Q-Q bonds in this structure makes this even more interesting.

Although most of these compounds have not been physically characterized in terms of their charge transport properties, the data that is available suggest that their properties are as varied as their elemental compositions. For example, in the $KCuZrQ_3$ (Q = Se, Se, Te) series,[2,4] $KCuZrS_3$ is an insulator, $KCuZrSe_3$ is a semiconductor and $KCuZrTe_3$ is a metal. This suggests that the properties can be tuned simply by varying the chalcogenide. The compound $KCuUSe_3$ was synthesized in our lab and was determined to be a semiconductor.[2,3] While the thermopower at room temperature was very high, the electrical conductivity seemed quite low. In order to optimize these properties for themoelectric application, the electrical conductivity must be enhanced. We therefore decided to make some isostructural tellurides and study their properties. The larger size of the tellurium atoms are expected to narrow the bandgap and as a result, the materials should possess a higher electrical conductivity. Here, we report the synthesis, structure, and physicochemical properties of $ACuUTe_3$ (A = Cs, Rb, K)
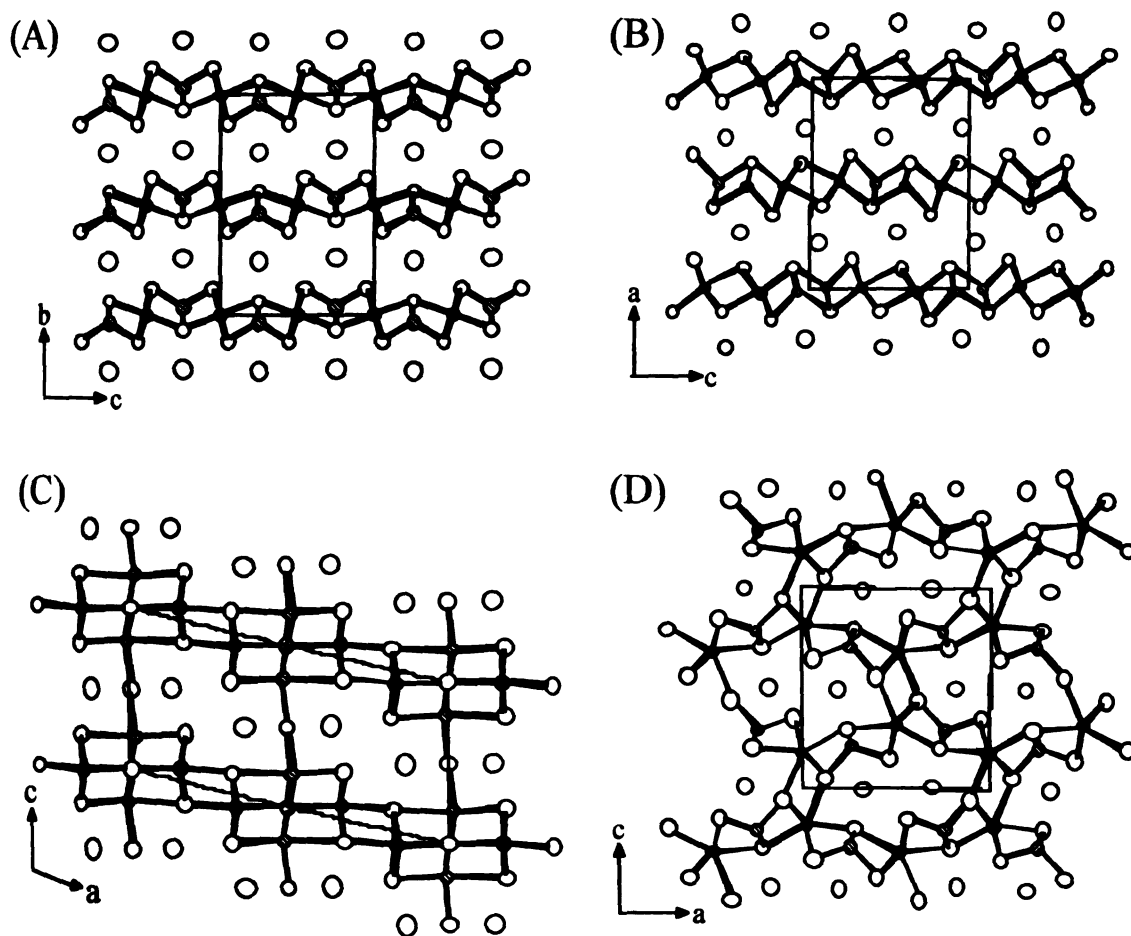
Figure 3.1 The four structure types of $AMLnQ_3$ (A = alkali or alkaline earth metal, M = coinage metal, M' =Group IV or rare earth metal, Q = chalcogenide). (A) Cmcm structure (e.g.; $KCuZrS_3$), (B) Pnma (I) structure (e.g.; $NaCuTiS_3$), (C) C2/m structure (e.g.; $BaAgErS_3$), and (D) Pnma (II) structure (e.g.; $BaCuLaS_3$). The small open circles represent M, the black circles represent Ln, and the large open circles represent A and Q.

B. Exp

metal.

R. Hi S

ti3. A

For law

102 m

isor

6. Las

is des

Eas

The

6-3

ra

ra

Va

B. Experimental Section

1. Reagents – The following reagents were used as obtained: Potassium metal, analytical reagent, Spectrum Chemical Mfg. Corp., Gardena, CA; Rubidium metal, 99.5%, Alfa Aesar, Ward Hill, MA.; Cesium metal, 99.98%, Alfa Aesar, Ward Hill, MA; Copper metal, electrolytic dust, Fisher Scientific, Fairlawn, NJ; uranium metal, 60 mesh, Cerac, Milwaukee, WI; Tellurium powder, 100 mesh, 99.95% purity, Aldrich Chemical Co., Milwaikee, WI.

Cesium Telluride, Cs_2Te – Syntheses of these materials was performed as described in Chapter 2, Section B.1

Rubidium Telluride, Rb_2Te – Syntheses of these materials was performed as described in Chapter 2, Section B.1.

Potassium Telluride, K_2Te – Syntheses of these materials was performed as described in Chapter 2, Section B.1.

2. Synthesis –All manipulations were carried out under a dry nitrogen atmosphere in a Vacuum Atmospheres Dri-Lab glovebox.

$ACuUTe_3$ (A = Cs, Rb, K) (I-III) - Amounts of A_2Te (0.5 mmol), Cu (1.0 mmol), U (1.0 mmol), and Te (2.5 mmol) were weighed into a vial in an N_2 filled glovebox. The reagents were thoroughly mixed and loaded into a 9mm carbon coated silica ampoule. The ampoule was removed from the glovebox, evacuated on a Schlenck line to less than 2.0×10^{-4} mbar, and flame-sealed. The reactants were heated to 850°C in 12 hours, isothermed at that temperature for 6 days, and

cooled

compo

obtaine

GaCuU

the pro

This id

provide

enable

diffe

cooled to room temperature at a rate of -4°C/hr. No isolation was needed since the compounds were prepared from direct combination of the elements. The products obtained consisted of black microcrystalline powders in ≈100%. The identity of $CsCuUTe_3$ was confirmed by comparing the powder X-ray diffraction pattern of the product against one calculated using single crystal X-ray data (see Table 3.1). The identities of $RbCuUTe_3$ and $KCuUTe_3$ were confirmed by comparing the powder X-ray diffraction patterns of the products against ones calculated using the atomic coordinates from the single crystal X-ray data for $CsCuUTe_3$ with the new unit cell parameters (see Tables 3.2-3.3).

CsCu

Table 3.1 Calculated and Observed X-ray Powder Diffraction Pattern for $CsCuUTe_3$ (I)

h k l	d_{calc} (Å)	d_{obs} (Å)	I/I_{max} (obs) (%)
0 2 0	8.3305	8.3814	100.0
0 2 2	4.6864	4.7054	14.96
1 1 0	4.1881	4.1921	17.55
0 2 3	3.4415	3.4331	24.34
1 1 2	3.3684	3.3778	9.82
1 3 1	3.2684	3.2870	28.62
1 3 2	2.9241	2.9393	16.33
0 0 4	2.8342	2.8451	15.63
1 1 3	2.8057	2.8184	8.44
0 6 1	2.6971	2.6946	7.93
1 5 0	2.6401	2.6567	12.13
0 6 2	2.4937	2.5096	18.10
1 5 2	2.3932	2.4070	21.48
1 1 4	2.3473	2.3553	12.49
0 6 3	2.2377	2.2507	3.89
1 5 3	2.1642	2.1759	10.25
2 2 0	2.0940	2.0981	19.47
2 2 1	2.0592	2.0640	5.77
2 2 2	1.9643	1.9693	16.96
2 4 1	1.8930	1.8978	9.54
2 2 3	1.8316	1.8375	11.94

Table 3.1 continued Calculated and Observed X-ray Powder Diffraction Pattern for $CsCuUTe_3$ (I)

h k l	d_{calc} (Å)	d_{obs} (Å)	I/I_{max} (obs) (%)
0 6 5	1.7563	1.7661	4.16
0 4 6	1.7223	1.7291	7.26
2 6 1	1.6876	1.6900	4.44
2 6 2	1.6342	1.6441	6.12
0 6 6	1.5622	1.5647	3.81

Table 3.2   Calculated and Observed X-ray Powder Diffraction Pattern for RbCuUTe$_3$ (II)

h k l	d$_{calc}$ (Å)	d$_{obs}$(Å)	I/I$_{max}$ (obs) (%)
0 2 0	8.3035	8.1762	100.0
0 0 2	5.6685	5.7700	14.05
0 2 2	4.6929	4.6944	14.79
1 1 1	3.9347	4.0455	13.02
0 2 3	3.4496	3.4538	28.25
1 3 0	3.4125	3.3973	46.75
1 3 2	2.9263	2.9183	36.39
0 0 4	2.8442	2.8656	22.04
1 1 3	2.8127	2.8301	15.68
0 2 4	2.6908	2.6903	15.09
1 5 1	2.5682	2.5925	15.09
1 5 2	2.3919	2.4272	25.89
1 1 4	2.3539	2.3608	34.76
0 4 4	2.3464	2.3313	13.91
1 3 4	2.1848	2.1839	19.38
2 0 2	2.0250	2.0101	40.24
0 0 6	1.8962	1.8913	25.44
1 1 6	1.7277	1.7329	11.83
2 4 4	1.5919	1.5898	12.28
1 9 3	1.5496	1.5461	12.87

KC:U

Table 3.3   Calculated and Observed X-ray Powder Diffraction Pattern for KCuUTe₃ (III)

h k l	d_{calc} (Å)	d_{obs} (Å)	I/I$_{max}$ (obs) (%)
0 2 0	7.6880	7.7533	100.0
0 0 2	5.6785	5.6998	19.06
0 2 2	4.6815	4.5880	12.51
1 1 1	3.9203	3.9266	11.17
1 3 0	3.3922	3.4073	31.24
0 4 2	3.3431	3.3186	53.18
1 3 2	2.9166	2.8671	52.64
0 0 4	2.8393	2.8430	35.32
1 1 3	2.8050	2.8054	12.24
0 6 0	2.7572	2.7421	11.57
0 2 4	2.6854	2.6703	16.72
1 5 1	2.5585	2.5759	11.17
1 3 3	2.5292	2.5173	16.05
1 1 4	2.3481	2.3473	40.13
0 0 5	2.3407	2.3021	37.79
1 5 3	2.1577	2.1680	18.19
1 7 0	2.0885	2.0908	16.52
1 5 4	1.9279	1.9324	18.26
2 4 1	1.8869	1.8767	13.04
1 7 3	1.8182	1.8283	29.10
1 1 6	1.7241	1.7240	11.24
0 2 7	1.5921	1.5918	10.57

for the

B.3: P

Charge

ohect

difficu

This da

Effectiv

for RE

O-Cu J

Table

Table

H-bo

Struc

This r

Re-Sp

Res,

Hj.

3. Physical Measurements – The instrumentation and experimental setup for the following measurements are the same as described in Chapter 2, Section B.3: Powder X-ray Diffraction, Magnetic Susceptibility Measurements, and Charge Transport Measurements.

Unit Cell Determinations – X-ray powder diffraction data was collected on a Rigaku Denki/RW400F2 (Rotaflex) rotating anode X-ray diffractometer controlled by an IBM computer and operating at 45 kV/100 mA. The data was collected with a 1°/min scan rate from 2 to 60° 2θ, employing Nil-filtered Cu radiation. A U-fit program[9] was used to calculate new cell parameters for $RbCuUTe_3$ (II) and $KCuUTe_3$ (III) from the known cell parameters for $CsCuUTe_3$ (I). The unit cell parameters for all three compounds are given in Table 3.4.

Infrared Spectroscopy - Optical diffuse reflectance measurements were made on a finely ground sample at room temperature. The spectrum was recorded in the Mid-IR region (6000 – 400 cm^{-1}) with the use of a Nicolet MAGNA-IR 750 Spectrometer equipped with a collector diffuse reflectance of Spectra-Tech Inc. The measurement of diffuse reflectivity can be used to obtain values for the bandgap which agree rather well with the values obtained by absorption measurements from single crystals of the same material. Absorption (α/S) data were calculated from the reflectance data using the Kubelka-Munk function[10]

where

and S

provi

smalle

determ

offse

the o

$$\alpha/S = (1 - R)^2/2R$$

where R is the reflectance at a given wavenumber, α is the absorption coefficient, and S is the scattering coefficient. The scattering coefficient has been shown to be practically wavenumber independent for particles larger than 5μm, which is smaller than the particle size of the samples used here. The bandgap was determined as the intersection point between the energy axis at the absorption offset and the line extrapolated from the linear portion of the absorption edge in the α/S vs E(eV) plot.

F

Table 3.4 Unit Cell Parameters for $ACuUTe_3$ (A = Cs, Rb, K)

Formula	CsCuUTe3	RbCuUTe3	KCuUTe3
a, (Å)	4.3387(2)	4.3339(4)	4.3168(9)
b, (Å)	16.664(2)	16.607(3)	16.543(3)
c, (Å)	11.388(2)	11.377(1)	11.357(1)
V, (Å^3)	823.3(4)	818.9(4)	811.0(4)
Space Group	Cmcm (#63)	Cmcm (#63)	Cmcm (#63)

C.

Si

Cs. R

the [U

octahe

share

These

occup

fields

3.4. I

subtra

spin

of the

in the

C. Results and Discussion

Structure Description – The three isostructural compounds, $ACuUTe_3$ (A =

Cs, Rb, K), are built from two basic building blocks; the $[CuTe_4]$ tetrahedra and

the $[UTe_6]$ octahedra.   One-dimensional chains are formed when the $[UTe_6]$

octahedra share edges down the a-axis, see Figure 3.2. These chains then corner

share at axial positions to form two-dimensional corrugated layers, see Figure 3.3.

These layers alone possess the anti-Pd_3Te_2 structure type in which Te atoms

occupy both the octahedral sites and the interlayer gallery positions.[11] Within the

folds of these layers, however, the Cu atoms reside in tetrahedral sites, see Figure

3.4. It is interesting to note that the insertion of Cu at these sites does not add or

subtract from the dimensionality of the framework and the structure remains intact

upon removal of these copper atoms. The overall effect is a simple repeat pattern

of the two basic building blocks alternating across the layer. A view perpendicular

to the layers is shown in Figure 3.5.
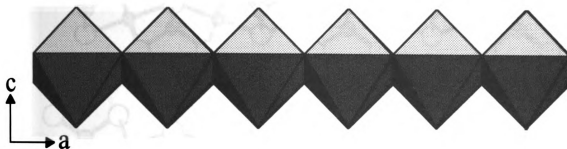
Figur

Figure 3.2 Polyhedral representation of the one-dimensional chains built from edge sharing connections of [UTe$_6$] octahedrons in ACuUTe$_3$ (A = Cs, Rb, K)
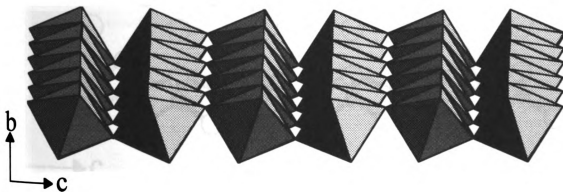
Figure 3.3 Polyhedral representation of the two-dimensional corrugated layers built from corner sharing connections of the one-dimensional chains in ACuUTe$_3$ (A = Cs, Rb, K)
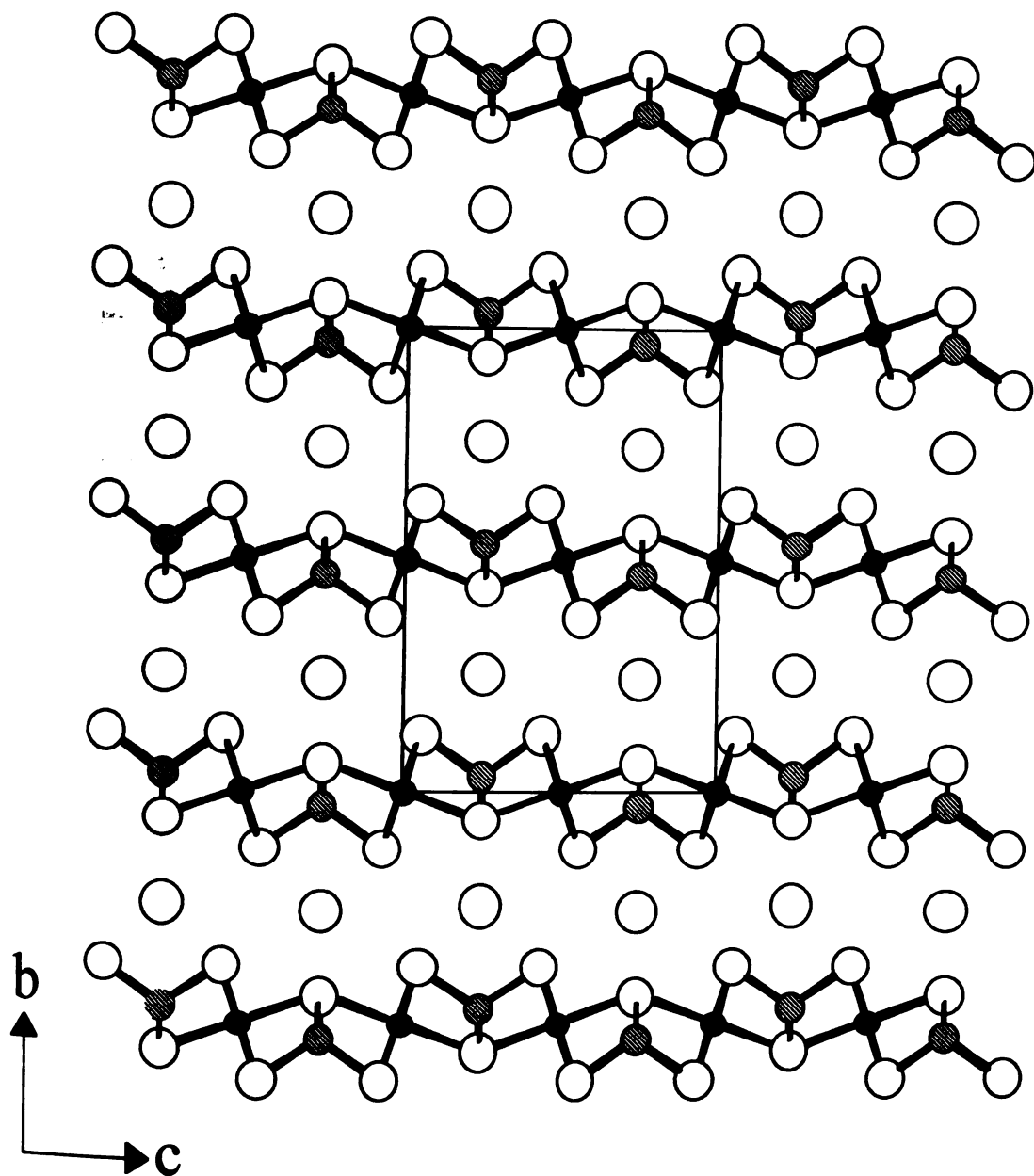
Figure 3.4 Extended structure of ACuUTe$_3$ (A = Cs, Rb, K) highlighting how the copper atoms sit in the folds of the layers. The black circles represent U, the striped circles represent Cu, and the open circles represent A and Te.
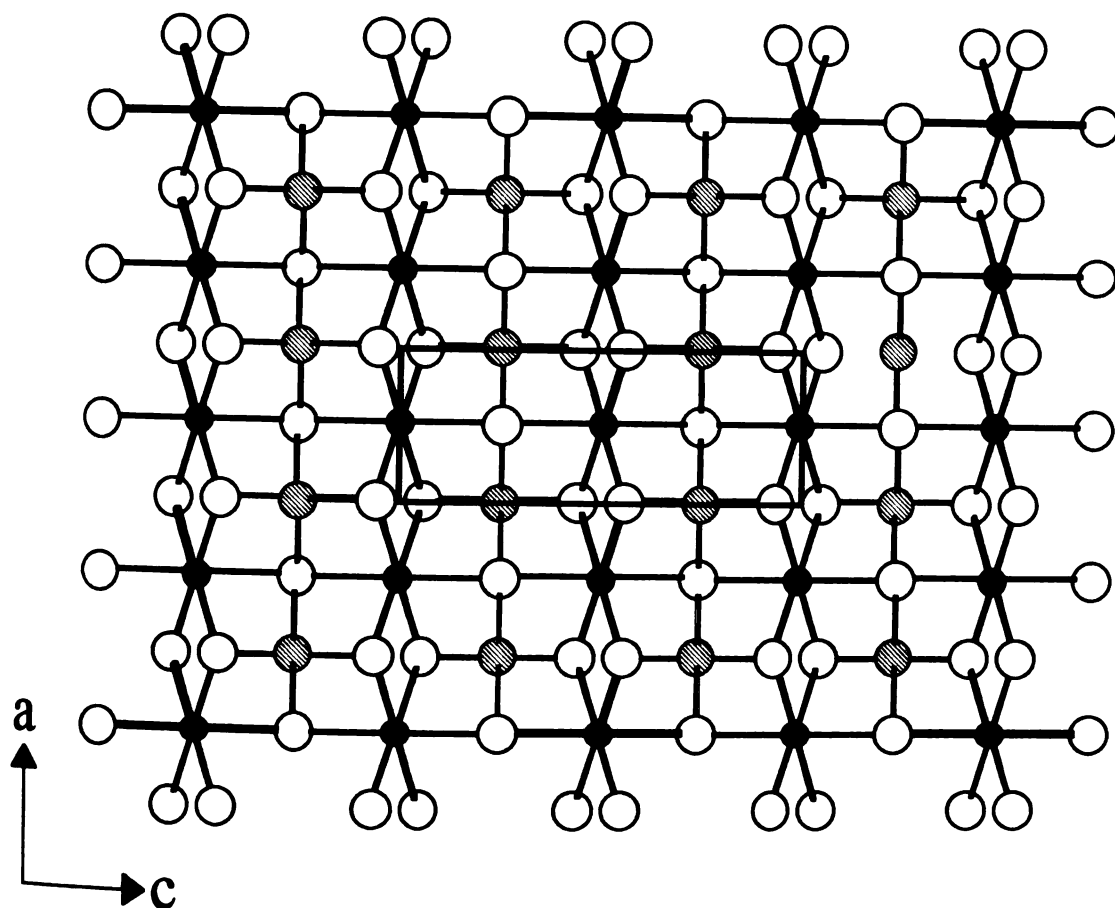
Figure 3.5 View perpendicular to a single anionic layer of ACuUTe$_3$ (A = Cs, Rb, K). The black circles represent U, the striped circles represent Cu, and the open circles represent Te.

Magnetic Susceptibility Measurements - The magnetic susceptibilities of

$CsCuUTe_3$, $RbCuUTe_3$, and $KCuUTe_3$ were measured over the range 5-300K at

3000G. A plot of $1/\chi_M$ vs T for each shows that the materials exhibit nearly Curie-

Weiss behavior above 140K, see Figure 3.6. Below this temperature, there is a

negative deviation from the straight line extrapolated from higher temperatures.

This phenomenon has been reported for several Ln^{4+} compounds and can be

attributed to crystal field splitting of the U^{4+} cation's ground state. At temperatures

above 140K, a μ_{eff} of $3.49\mu_B$ for $CsCuUTe_3$, $3.69\mu_B$ for $RbCuUTe_3$ for and $4.14\mu_B$

for $KCuUTe_3$ has been calculated. These values are in accordance with what has

been theoretically calculated for a $5f^2$ U^{4+} ion (3.58 μ_B)[12] and experimentally

observed for several solid state transition metal/U^{4+}/chalcogenides (3.0-3.6 μ_B)[13].

From the data, it is evident that the compounds are valence precise and the

formula can be written as $(A^+)(Cu^+)(U^{+4})(Te^{2-})_3$. We should therefore expect the

materials to exhibit semiconducting behavior.
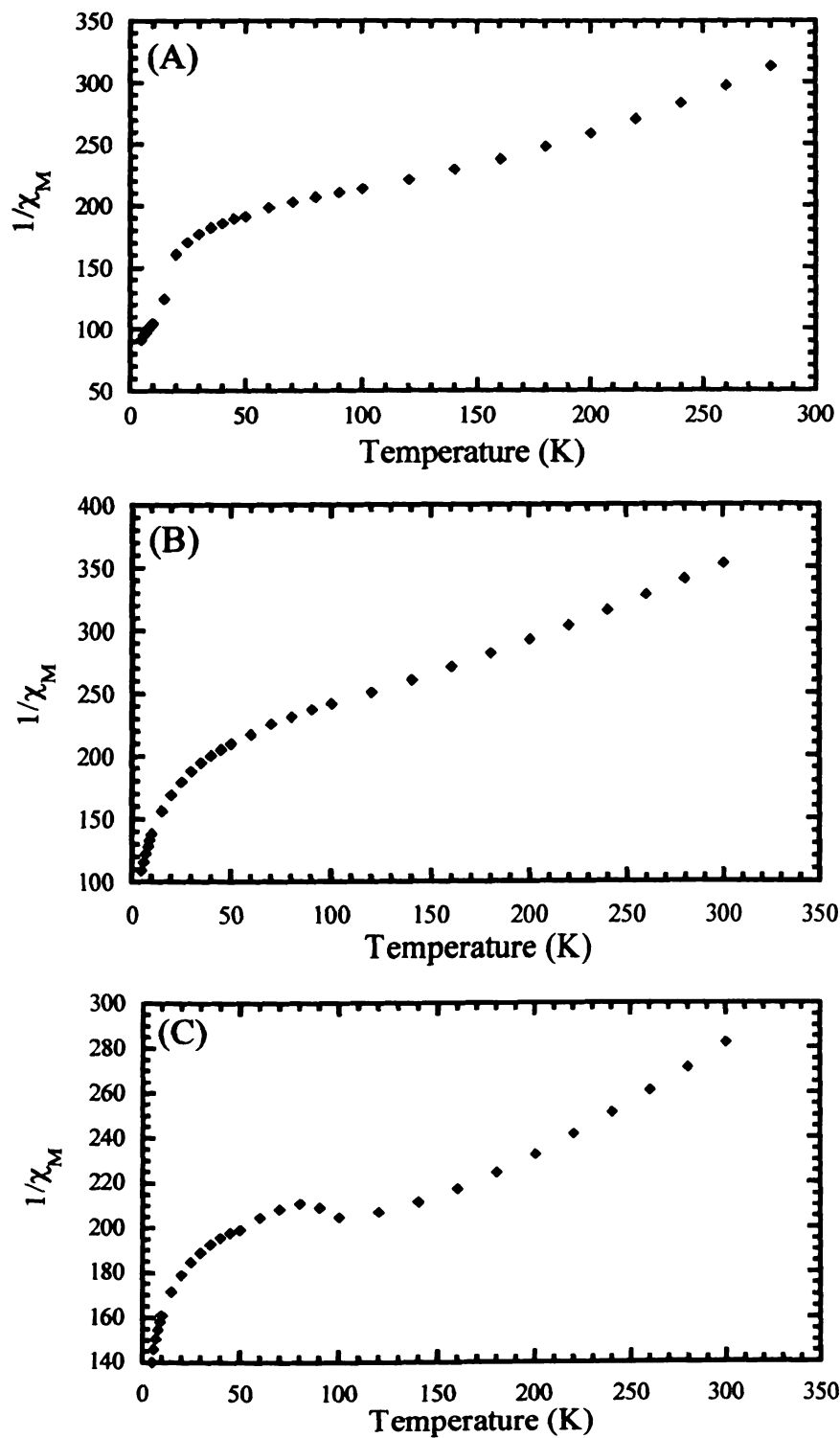
Figure 3.6 Inverse molar magnetic susceptibility ($1/\chi_M$) plotted against temperature (2-300K) for (A) $CsCuUTe_3$, (B) $RbCuUTe_3$ and (C) $KCuUTe_3$.

the th

the co

with

behav

diffic

howe

effec

GCu

ad

meas

effe

the

s -

Cu

Th

te

p

e

y

s

Charge Tranport Properties -   Both the electrical conductivity and the thermopower was measured for hot pressed pellets (270°C) of $ACuUTe_3$ and the composite plots are shown in Figure 3.7. The electrical conductivity decreases with decreasing temperature for all three compounds, indicating semiconducting behavior with room temperature values ranging from 0.01 - 0.1 S/cm.   It is difficult to determine which of the three compounds is the most conductive, however, since the measurement is very sample dependent and grain boundary effects in the pellet act to artificially inhibit the conductivity. This is evident in $CsCuUTe_3$, where two measurements were made on two different pressed pellets and the results are quite different.   In comparison to $KCuUSe_3$, whose measurements were made on single crystals, the conductivity does not seem to differ significantly. The room temperature value for this compounds was reported to be 0.02 S/cm. However, if we assume that the conductivity of a pressed pellet is ~100 times less conductive than a single crystal, the true conductivity of $ACuUTe_3$ will be much higher than that for $KCuUSe_3$.   The thermopower measurements, which are not affected by grain boundaries in the sample pellet because it is a zero current technique[14], give positive Seebeck coefficients at room temperature of 100 $\mu V/K$ for $KCuUTe_3$ and 200 $\mu V/K$ for $CsCuUTe_3$. These values are 3-6 times less than $KCuUSe_3$ (600 $\mu V/K$ at room temperature). This is also an indication that the electrical conductivities of $ACuUTe_3$ are significantly higher than that of $KCuUSe_3$ since a decrease in thermopower is usually accompanied by an increase in conductivity.

Electrical Conductivity

(A)

a - KCuUTe3
b - CsCuUTe3
c - CsCuUTe3
d - RbCuUTe3

Thermopower

(B)
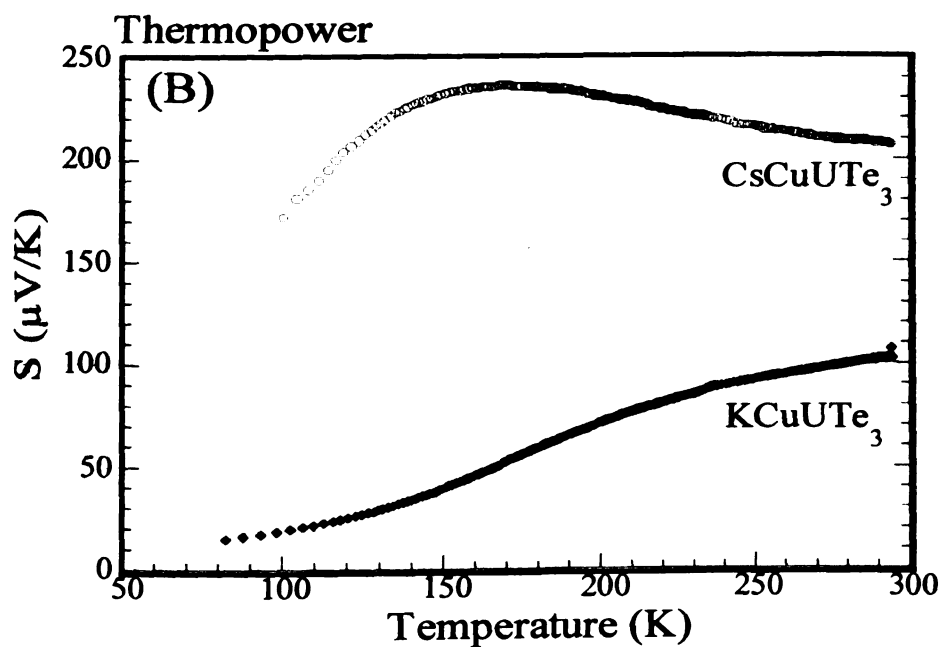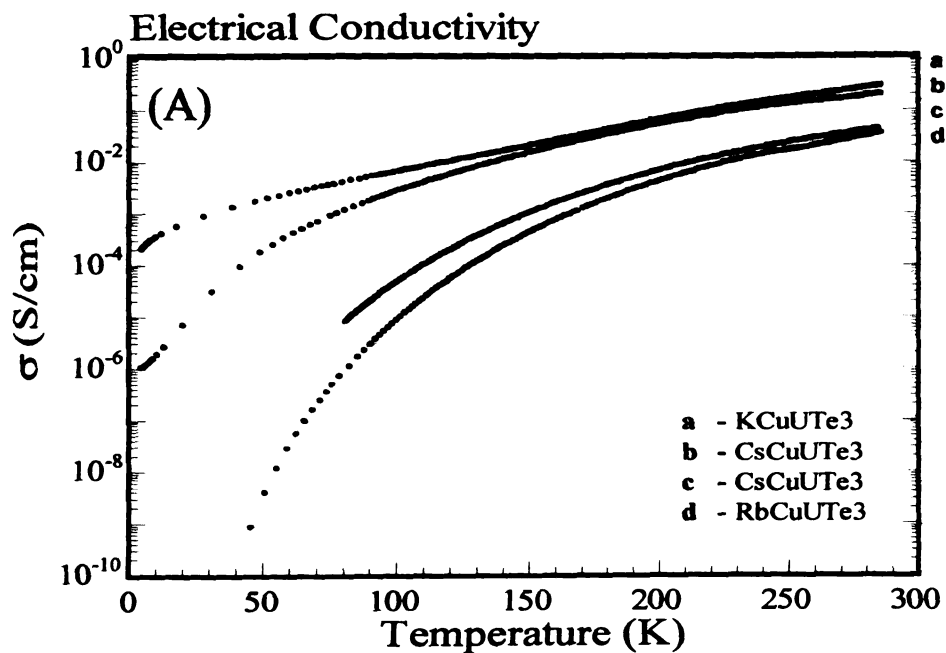
CsCuUTe$_3$

KCuUTe$_3$

Figure 3.7 (A) Variable temperature, four probe electrical conductivity data for hot pressed pellets of ACuUTe$_3$ (A = Cs, Rb, K). (B) Variable temperature thermopower data for hot pressed pellets of ACuUTe$_3$ (A = Cs, K).

meas

3.8.

show

these

1613

at the

and

obse

ma

851

Infrared Spectroscopy - The diffuse reflectance optical spectra were measured in the Mid-IR region for all three compounds and are shown in Figure 3.8. From the charge transport properties, it is expected that these materials will show an optical bandgap in this region. However, any optical bandgap present in these region is masked by the presence of four peaks at $3511cm^{-1}$ (0.43 eV), $1613cm^{-1}$ (0.20 eV), $1349cm^{-1}$ (0.17 eV), and $898cm^{-1}$ (0.11 eV). These peaks are at the same exact position for all three compounds and may be attributed to d-f and/or f-f transitions on the uranium center. This is not unusual and has been observed for several other compounds with U^{4+} ions.[15,16] Another explanation may be that that water is being absorbed onto the crystals and some of these peaks (3511 and 1613 cm^{-1}) are coming from the O-H bending modes of water.
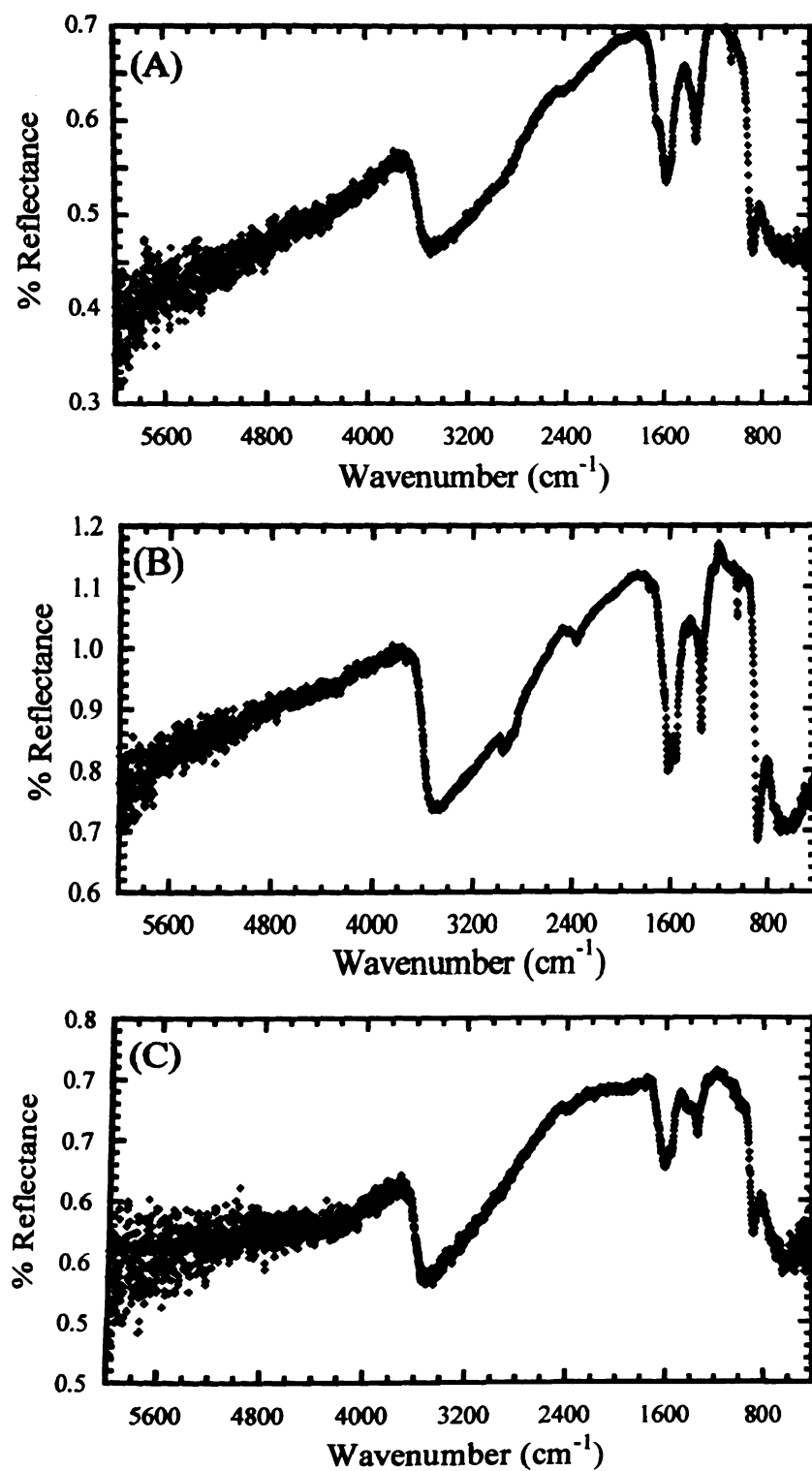
Figure 3.8 Diffuse reflectance optical spectra for (A) CsCuUTe₃, (B) RbCuUTe₃ and (C) KCuUTe₃ (in the Mid-IR region)

102

Cation Effect on ACuUTe₃ - For the purpose of this study, attempts were also made to synthesize the isostructural $NaCuUTe_3$ and $LiCuUTe_3$ members. The x-ray powder x-ray diffraction patterns of these products, however, indicated that the [type a] structure was not formed. For the sodium synthesis, the compound formed was indeed $NaCuUTe_3$ but it now adopts another structure type of the $AMM'Q_3$ family [type b] (see Figure 3.1). This is not surprising since many members of this [type b] structure type contain sodium as its cation (e.g.: $NaCuTiS_3$, $NaCuZrSe_3$, and $NaCuZrTe_3$). This change in structure is due solely to the fact that a different alkali metal was used. In both structure types [type a and b], the basic building blocks are $[MQ_4]$ tetrahedrons (TET) and $[M'Q_6]$ octahedrons (OCT). The difference lies in the way that they order across the layer. In the first [type a] structure type, the repeat pattern across the layer is ~TET – OCT - TET – OCT~. In the second [type b] structure type, the repeat pattern changes to ~TET - TET - OCT – OCT~. Each building block is now paired and these pairs alternate across the layer, consequently causing the coordination environment around the alkali metal to be reduced from bicapped trigonal prismatic [type a] to monocapped trigonal prismatic [type b]. Because this reduced coordination environment is more stable for a sodium cation than any larger cation, this [type b] structure type forms.

For the lithium synthesis, the x-ray powder diffraction pattern was less conclusive. While it bears some resemblance to that of the pattern for the second structure type [type b], there are many more peaks that could not be indexed. One

could postulate that since lithium is even smaller, the structure could have undergone another modification where the layers have now come so close to one another that they have joined together to form a three-dimensional framework. This is called the "counterion effect".[17] The third and fourth structure types [types c and d] that make up the AMM'Q family are three-dimensional and it is therefore feasible that the lithium compound could adopt one of these structures. But upon careful comparison of the x-ray diffraction patterns, it was determined that this is not the case. Another possibility is that the lithium did not incorporate into the product and a ternary $Cu_xU_yTe_z$ phase has formed. If this were true, the excess Li_2Te_x would have washed away during isolation in DMF as a flux. However, no color change was observed in the DMF solution during this step. To really determine which compound has formed, crystals of suitable size are needed for single crystal x-ray diffraction studies and this has not been done.

D. C

basi

fron

of el

struc

Cs.

men

This

elec

and

elec

stab

by e

*Re

349

D. Conclusions

The structure [type a] of AMM'Q$_3$ is very simple. Made up of two very basic building blocks, [the [MQ$_4$] tetrahedra and the [M'Q$_6$] octahedra], the framework has proven to be very stable and is capable of adopting a wide variety of elemental combinations. The series ACuUTe$_3$ (A = Cs, Rb, K) adopts this structure type. Compared to KCuUSe$_3$, the electrical properties of ACuUTe$_3$ (A = Cs, Rb, K) appear to be significantly enhanced. However, amongst the three members of ACuUTe$_3$, there is not much difference in the conductivity values. This is most likely due to the fact that the structure is very anisotropic and the electrical conductivity is mostly due to the carriers that are traveling parallel to and not perpendicular to the layers. Therefore, it can be concluded that the electrical properties of these materials are more strongly affected by the chalcogenide chosen for the framework than the alkali metal residing between the layers. Finally, upon investigation into this structure type [type a] with sodium, it was determined that for NaCuUTe$_3$ the structure changes to another member of the AMM'Q$_3$ structure types [type b].

References

---

1   Mansuetto, M.F.; Kean, P.M.; Ibers, J.A. *J. Solid State Chem.* **1993**, 105, 580.

2   Pell, M.A.; Ibers, J.A. *Chem. Ber./Recueil* **1997**, 130, 1.

3   Sutorik, A.C.; Albritton-Thomas, J.; Hogan, T.; Kannewurf, C.R.; Kanatzidis, M.G. *Chem. Mater.* **1996**, 8, 751.

4   Mansuetto, M.F.; Keane, P.M.; Ibers, J.A. *J. Solid State Chem.* **1992**, 101, 257.

5   Cody, J.A. Ibers, J.A. *Inorg. Chem.* **1995**, 34, 3165.

6   Wu, P.; Christuk, A.E.; Ibers, J.A. *J. Solid State Chem.* **1994**, 110, 337.

7   Huang, F.Q.; Choe, W.; Lee, S.; Chu, J.S. *Chem. Mater.* **1998**, 10, 1320.

8   Yang, Y.; Ibers, J.A. *J. Solid State Chem.* **1999**, 147, 366.

9   M. Evain, U-fit: "A cell parameter refinement program", Institut des Matériaux, Nante, France.

10 (a) Wendlandt, W.W.; Hecht, H.G. *Reflectance Spectroscopy*; Interscience Publishers: New York, 1966. (b) Kotüm, G. *Reflectae Spectroscopy*; Springer-Verlag: New York, 1969. (c) Tandon, S.P.; Gupta, J.P. *Phys. Status Solidi* **1970**, 38, 363.

11 Matkovic, P.; Schubert, K. *J. Less-Common Met.* **1977**, 52, 217.

12 Greenwood, N. N.; Earnshaw, A. *Chemistry of the Elements;* Pergamon Press: New York, 1984; p 1443.

13 Noel, H.; Troc, R. *J. Solid State Chem.* **1979**, 27, 123.

14 Cheetham, A.K.; Day, P. "Solid State Chemistry; Techniques", Oxford: Clarendon, 1986.

15 Choi, K.-S.; Kanatzidis, M.G. *Chem. Mater.* **1999**, 11, 2613.

16   (a) Grønvold, F.; Drowart, J.; Westrum, E.F., Jr. *The Chemical Thermodynamics of Actinide Elements and Compounds*; International Atomic Energy Agency: Vienna, 1984; pp 161-200 and references therein. (b) Clifton, J.R.; Gruen, D.M.; Ron, A. *J. Chem. Phys.* **1969**, 51, 224. (c) Schoenes, J. *Phys Rev.* **1980**, 63, 301.

17   Kanatzidis, M.G. *Phosphorous, Sulfur, and Silicon* **1994**, 93, 159.

Chapter 4

Novel Polytelluride Compounds Containing Distorted Nets of Tellurium

A. Introduction

Explorations into the chemistry of complex lanthanide chalcogenides, particularly quaternary systems of the type A/M/Ln/Q (A = alkali metal, M = transition metal, Ln = lanthanide metal, and Q = chalcogen), suggest that phase stabilization is most facile when the transition metal used is a coinage metal, namely Cu. This may be rationalized by the mobile nature of Cu^+ ions, even at low temperatures, which helps diffuse the ion over long distances and facilitates its quick arrival at phase thermodynamic minima. The introduction of Cu into the synthetic chemistry of lanthanide chalcogenides has already produced several quaternary compounds, including $K_2Cu_2CeS_4$,[1] $KCuCe_2S_6$,[1,2] $KCuLa_2S_6$,[2] $CsCuCe_2S_6$,[2] $KCuCe_2Se_6$,[2] $CsCuCeS_3$,[2] and $KCuUSe_3$.[2] These findings were quickly followed by a rapid expansion in this area by independent investigators, producing the compounds $BaErAgS_3$,[3] $CsCuUTe_3$,[4,6] $CsTiUTe_5$,[4,6] $Cs_8Hf_5UTe_{30.6}$,[4,5,6] $BaMLnQ_3$ (Ln = La, Ce, Nd, Dy; M = Cu, Ag; Q = S, Se),[7,8] $K_{1.5}Dy_2Cu_{2.5}Te_5$,[8] and $K_{0.5}Ba_{0.5}DyCu_{1.5}Te_3$.[8] We have since expanded this chemistry to include both Cu and Ag in the telluride system. One important difference between Te_x^{2-} and Q_x^{2-} (Q = S, Se) ions is the greater tendency for the former to associate through Te-Te bonding interactions because of the more diffuse nature of its orbitals.[9,10,11] For example, in $SmTe_3$,[12] Te-Te interactions lead to interesting superstructures. This characteristic can easily lead to mixed valency, which in turn can produce interesting physical phenomena.

By using molten alkali metal/polytelluride fluxes, several new quaternary phases have been discovered with the general formula $A_wM_xLn_yTe_z$ (A = alkali metal, Ln = lanthanide metal, M = coinage metal). Reactions with cerium produced the compounds $KCuCeTe_4$,[13] $RbCuCeTe_4$, $Na_{0.8}Ag_{1.2}CeTe_4$, and $K_{2.5}Ag_{4.5}Ce_2Te_9$, while lanthanum presented the isostructural $K_{2.5}Ag_{4.5}La_2Te_9$. Although these compounds possess new structure types, they still retain components of the known binary rare earth tellurides ($NdTe_3$[14] and $ZrSe_3$[15]-type). Since both of these binary structure types require a metal with an oxidation state > +3, we decided to circumvent their formation completely by investigating reactions with a divalent lanthanide metal. Only a few lanthanides are stable as +2 ions, however, including Sm ($4f^6$), Eu ($4f^7$), Tm ($4f^{13}$) and Yb ($4f^{14}$). Of these, europium was selected first because it is one of the most stable.[16] Prior to our work, the only reported quaternary europium chalcogenide of this type was $KCuEu_2S_6$.[17] Our explorations with europium produced $Cu_{0.66}EuTe_2$,[18] KCu_2EuTe_4,[18] $Na_{0.2}Ag_{2.8}EuTe_4$,[18] and $K_{0.65}Ag_2Eu_{1.35}Te_4$, all of which are best described as Eu^{2+} compounds. The compounds reported here (with the exception of $K_{0.65}Ag_2Eu_{1.35}Te_4$) possess what appears to be perfectly square Te nets. With the aid of electron diffraction, however, we find most of them to be modulated.

B.   Experimental Section

1. Reagents – The following reagents were used as obtained: Sodium metal, analytical reagent, Spectrum Chemical Mfg. Corp., Gardena, CA; Potassium metal, analytical reagent, Spectrum Chemical Mfg. Corp., Gardena, CA; Rubidium metal, 99.5%, Alfa Aesar, Ward Hill, MA.; Copper metal, electrolytic dust, Fisher Scientific, Fairlawn, NJ; Cerium metal, < 250 mesh, Alfa Aesar, Ward Hill, MA; Lanthanum metal, 40 mesh, Cerac, Milwaukee, WI; Europium metal powder, 99.9%, ; < 250 mesh, Alfa Aesar, Ward Hill, MA; Europium metal chunk, 99.9%, Chinese Rare Earth Information Center, Inner Mongolia, China; Tellurium powder, 100 mesh, 99.95% purity, Aldrich Chemical Co., Milwaukee, WI; Tellurium shots, 99.9% pure, Noranda Advanced Materials, Saint-Laurent, Quebec, Canada. Lithium Chloride, 99.8% pure, 20 mesh, Cerac Specialty Inorganics, Milwaukee, WI; Potassium Chloride, crystals, JT Baker, Phillipsburg, NJ; N, N, - Dimethylformamide (DMF) was used as obtained in analytical reagent grade from Aldrich Chemical Co., 99.8% purity, Milwaukee, WI. The europium metal chunk was cut into fine shavings with a hacksaw and flamed under vacuum in a sealed silica ampoule to remove the oxide coating before being used. The tellurium shots were ground to a fine powder before being used.

Silver Powder – A silver coin (99.9% purity) weighing 31.54g was dissolved in 250 mL of dilute (7.5N) nitric acid. The solution was heated to 60°C in an acid-resistant fume hood until the silver coin was completely dissolved. The solution was neutralized with ammonium hydroxide and the silver was reduced

with formic acid until a pH of 7-8 was reached. The resulting pale grey solid was filtered, washed with copious amounts of distilled water and acetone, and dried in vacuum overnight. The final yield was 31.095g.

Sodium Telluride, Na₂Te – The following procedure was modified from that given in the literature.[19] 8.05g (0.35 mol) Na was sliced in an N_2 filled glovebox and combined with 21.95g (0.17 mol) Te in a 1000 mL single neck round bottom flask. This mixture represents a slight excess of Na and slight deficiency of Te. The flask was connected to a glass adapter with a stopcock joint and removed from the glovebox. The flask and adapter was then connected to a condenser apparatus and chilled to -78°C using a dry ice/acetone bath. Approximately 800mL of NH_3 were condensed, under an N_2 atmosphere, onto the reagents, giving a dark blue solution. The solution was stirred via a Teflon coated magnetic stir bar and the reaction mixture was maintained at -78° for up to 24 hours. The dry ice was then removed and the NH_3 was allowed to evaporate off as the flask warmed up to room temperature under a constant flow of N_2 (approximately 10 hours). A second portion of NH_3 was added and the process was repeated to ensure complete reaction of the reagents. The resulting peach colored powder was evacuated on a Schlenck line for approximately 5 hours and taken into an N_2 filled glovebox where it was ground to a fine powder. Due to its propensity to decompose even under an inert glovebox atmosphere, the material was stored in a glass ampoule clamped shut with a ground glass lid.

Potassium Telluride, K₂Te – Synthesis of this material was performed as described in Chapter 2, Section B.1.

Rubidium Telluride, Rb₂Te – Synthesis of this material was performed as described in Chapter 2, Section B.1.

2. Synthesis – All manipulations were carried out under a dry nitrogen atmosphere in a Vacuum Atmospheres Dri-Lab glovebox.

KCuCeTe₄ (I) – Amounts of 0.206g K_2Te (1.0 mmol), 0.032g Cu (1.0 mmol), 0.070g Ce (0.5 mmol), 0.303g Te (3 mmol) were weighed into a vial and mixed with 0.5g of a LiCl/KCl (45:55) eutectic flux in a N_2 filled glovebox. The reagents were then loaded into a 13 mm silica ampoule. The ampoule was removed from the glovebox, evacuated on a Schlenck line to less than 2.0×10^{-4} mbar, and flame sealed. The reactants were heated to 400°C in 12 hours, isothermed at that temperature for 10 hours, raised to 700°C in 22 hours, and isothermed at that temperature for 5 days. The tube was then cooled to 400°C at – 3°C/hr and quenched to room temperature in 4 hours. The excess K_2Te_x flux was removed with successive portions of DMF, under N_2 atmosphere, until the solution remained clear. The LiCl/KCl eutectic flux was then removed by washing with water to reveal very thin, square copper-colored plates. A small portion of red-brown $CeTe_3$ powder was also present, but could be removed from the plates by simply sonicating the sample. Typical yields were 46%, based on Ce. Phase homogeneity was confirmed by comparing the powder X-ray

113

diffraction pattern of the product against one calculated using the crystallographically determined atomic coordinates, see Table 4.1. Semiquantitative microprobe analysis on single crystals gave an average composition of $K_{1.0}Cu_{1.04}Ce_{1.18}Te_{3.88}$.

RbCuCeTe₄ (II) – Amounts of 0.358g Rb_2Te (1.2 mmol), 0.019g Cu (0.3 mmol), 0.042g Ce (0.3 mmol), 0.612g Te (4.8 mmol) were weighed into a vial in a N_2 filled glovebox. The reagents were then loaded into a 13 mm silica ampoule. The ampoule was removed from the glovebox, evacuated on a Schlenck line to less than 2.0×10^{-4} mbar, and flame sealed. The reactants were heated to 400°C in 12 hours, isothermed at that temperature for 6 hours, raised to 800°C in 18 hours, and isothermed at that temperature for 4 days. The tube was then cooled to 400°C at –4°C/hr and quenched to room temperature in 4 hours. The excess Rb_2Te_x flux was removed with successive portions of DMF, under N_2 atmosphere, until the solution remained clear. The final product consisted of very thin, square copper-colored plates. A small portion of red-brown $CeTe_3$ powder was also present, but could be removed from the plates by simply sonicating the sample. Semiquantitative microprobe analysis on single crystals gave an average composition of $Rb_{0.96}Cu_{1.15}Ce_{1.0}Te_{3.67}$.

Na₀.₈Ag₁.₂CeTe₄ (III) – Amounts of 0.208g Na_2Te (1.20 mmol), 0.065g Ag (0.60 mmol), 0.042g Ce (0.30 mmol), 0.612g Te (4.80 mmol) were weighed into a vial and loaded into a 13 mm silica ampoule. The ampoule was removed from the glovebox, evacuated on a Schlenck line to less than 2.0×10^{-4} mbar, and

114

flame sealed. The reactants were heated to 400°C in 12 hours, isothermed at that temperature for 12 hours, raised to 850°C in 22 hours, and isothermed at that temperature for 6 days. The tube was then cooled to 400°C at −4.5°C/hr and quenched to room temperature in 4 hours. The excess Na_2Te_x flux was removed, under N_2 atmosphere, with DMF to reveal very thin, square copper-colored plates. A small portion of red-brown $CeTe_3$ powder was also present, but could be removed from the plates by simply sonicating the sample. Typical yields were 34%, based on Ce. Phase homogeneity was confirmed by comparing the powder X-ray diffraction pattern of the product against one calculated using the crystallographically determined atomic coordinates, see Table 4.2. Semiquantitative microprobe analysis on single crystals gave an average composition of $Na_{0.4}Ag_{0.6}Ce_{1.0}Te_{2.9}$.

$K_{2.5}Ag_{4.5}Ce_2Te_9$ *(IV)* – Amounts of 0.247g K_2Te (1.20 mmol), 0.146g Ag (1.35 mmol), 0.084g Ce (0.60 mmol), 0.612g Te (4.80 mmol) were weighed into a vial and loaded into a 13 mm silica ampoule. The ampoule was removed from the glovebox, evacuated on a Schlenck line to less than 2.0×10^{-4} mbar, and flame sealed. The reactants were heated to 400°C in 12 hours, isothermed at that temperature for 12 hours, raised to 850°C in 22 hours, and isothermed at that temperature for 6 days. The tube was then cooled to 400°C at −4.5°C/hr and quenched to room temperature in 4 hours. The excess K_2Te_x flux was removed, under N_2 atmosphere, with DMF to reveal very thin, square copper-colored plates. A small portion of red-brown $CeTe_3$ powder was also present, but could be

removed from the plates by simply sonicating the sample. Typical yields were 74%, based on Ag. Phase homogeneity was confirmed by comparing the powder X-ray diffraction pattern of the product against one calculated using the crystallographically determined atomic coordinates, see Table 4.3. Semiquantitative microprobe analysis on single crystals gave an average composition of $K_{2.5}Ag_{5.3}Ce_{2.0}Te_{9.9}$.

$K_{2.5}Ag_{4.5}La_2Te_9$ (V) – Amounts of 0.247g K_2Te (1.20 mmol), 0.146g Ag (1.35 mmol), 0.083g La (0.60 mmol), 0.612g Te (4.80 mmol) were weighed into a vial and mixed with 0.5g of a LiCl/KCl (45:55) eutectic flux in a N_2 filled glovebox. The reagents were then loaded into a 13 mm silica ampoule. The ampoule was removed from the glovebox, evacuated on a Schlenck line to less than 2.0×10^{-4} mbar, and flame sealed. The reactants were heated to 400°C in 8 hours, isothermed at that temperature for 10 hours, raised to 800°C in 8 hours, and isothermed at that temperature for 5 days. The tube was then cooled to 400°C at – 4°C/hr and quenched to room temperature in 4 hours. The excess K_2Te_x flux was removed with successive portions of DMF, under N_2 atmosphere, until the solution remained clear. The LiCl/KCl eutectic flux was then removed by washing with water to reveal very thin, square copper-colored plates. A small portion of red-brown $LaTe_3$ powder was also present, but could be removed from the plates by simply sonicating the sample. Typical yields were 80%, based on Ag. Phase homogeneity was confirmed by comparing the powder X-ray diffraction pattern of the product against one calculated using the

crystallographically determined atomic coordinates, see Table 4.4. Semiquantitative microprobe analysis on single crystals gave an average composition of $K_{2.5}Ag_{5.4}La_{1.6}Te_{10.5}$.

$Cu_{0.66}EuTe_2$ (VI) – Initial investigations into the quaternary $Rb_2Te/Cu/Eu/Te$ system led to the serendipitous discovery of $Cu_{0.66}EuTe_2$. The compound was found as a minor product from a reaction mixture of 0.298g Rb_2Te (1.0 mmol), 0.032g Cu (0.5 mmol), 0.038g Eu (0.25 mmol), and 0.510g Te (4.0 mmol). The mixture was weighed into a vial and loaded into a 13 mm silica ampoule. The ampoule was then removed from the glovebox, evacuated on a Schlenck line to less than 2.0 x 10^{-4} mbar, and flame sealed. The reactants were heated to 400°C in 12 hours, isothermed at that temperature for 12 hours, raised to 850°C in 22 hours, and isothermed at that temperature for 6 days. The tube was then cooled to 400°C at –4°C/hr and quenched to room temperature in 4 hours. The excess Rb_2Te_x flux was removed, under N_2 atmosphere, with DMF to reveal very thin, square copper-colored plates. Phase homogeneity was confirmed by comparing the powder X-ray diffraction pattern of the copper-color plates in the product against one calculated using the crystallographically determined atomic coordinates, see Table 4.5. Semiquantitative microprobe analysis on the single crystal used for X-ray data collection gave an average composition of $Cu_{0.66}Eu_{1.0}Te_{2.0}$.

After the initial discovery of $Cu_{0.66}EuTe_2$, further reactions were carried out to synthesize this compound in a logical fashion. Although this compound has not

been synthesized pure, it has been reproduced in powder form from a direction combination reaction of the elements. This reaction consisted of a mixture of 0.042g Cu (0.66 mmol), 0.280g EuTe (1.0 mmol), and 0.128g Te (1.0 mmol) that was heated to 800°C in 30 hours, isothermed at that temperature for 6 days, and slow cooled to 100°C in 150 hours. The tube was then quenched to room temperature in 4 hours. Since there was no flux used and the reaction was that of a direct combination, no isolation step was necessary. The powder X-ray diffraction pattern of the product clearly showed the presence of this compound, but was not 100% pure. Since the product was that of a heterogenous powder, it was not possible to carry out further characterization of this material.

KCu₂EuTe₄ (VII) – Amounts of 0.165g K_2Te (0.8 mmol), 0.025g Cu (0.4 mmol), 0.061g Eu (0.4 mmol), 0.306g Te (2.8 mmol) were weighed into a vial and loaded into a 13 mm silica ampoule. The ampoule was removed from the glovebox, evacuated on a Schlenck line to less than 2.0×10^{-4} mbar, and flame sealed. The reactants were heated to 400°C in 12 hours, isothermed at that temperature for 12 hours, raised to 850°C in 22 hours, and isothermed at that temperature for 6 days. The tube was then cooled to 400°C at –4°C/hr and quenched to room temperature in 4 hours. The excess K_2Te_x flux was removed, under N_2 atmosphere, with DMF to reveal very thin, square copper-colored plates. Phase homogeneity was confirmed by comparing the powder X-ray diffraction pattern of the product against one calculated using the crystallographically

determined atomic coordinates, see Table 4.6. Semiquantitative microprobe analysis on single crystals gave an average composition of $K_{0.8}Cu_{1.9}Eu_{1.0}Te_{3.4}$.

$Na_{0.2}Ag_{2.8}EuTe_4$ (VIII) – Amounts of 0.208g Na_2Te (1.2 mmol), 0.097g Cu (0.9 mmol), 0.046g Eu (0.3 mmol), 0.612g Te (4.8 mmol) were weighed into a vial and loaded into a 13 mm silica ampoule. The ampoule was removed from the glovebox, evacuated on a Schlenck line to less than 2.0 x 10^{-4} mbar, and flame sealed. The reactants were heated to 400°C in 12 hours, isothermed at that temperature for 12 hours, raised to 850°C in 22 hours, and isothermed at that temperature for 6 days. The tube was then cooled to 400°C at –4°C/hr and quenched to room temperature in 4 hours. The excess Na_2Te_x flux was removed, under N_2 atmosphere, with DMF to reveal very thin, square copper-colored plates. Typical yields were 67%, based on Ag. Phase homogeneity was confirmed by comparing the powder X-ray diffraction pattern of the product against one calculated using the crystallographically determined atomic coordinates, see Table 4.7. Semiquantitative microprobe analysis on single crystals gave an average composition of $Na_{0.5}Ag_{1.1}Eu_{1.0}Te_{3.2}$.

$K_{0.65}Ag_2Eu_{1.35}Te_4$ (IX) – Amounts of 0.206g K_2Te (1.0 mmol), 0.140g EuTe (0.5 mmol), 0.054g Ag (0.5 mmol), 0.510g Te (4.0 mmol) were weighed into a vial and loaded into a 9 mm silica ampoule. The ampoule was removed from the glovebox, evacuated on a Schlenck line to less than 2.0 x 10^{-4} mbar, and flame sealed. The reactants were heated to 450°C in 12 hours, isothermed at that temperature for 3 days, cooled to 150°C at –4°C/hr, and quenched to room

temperature in 4 hours. The excess K_2Te_x flux was removed, under N_2 atmosphere, with DMF to reveal square silver-black plates. Typical yields were 95%, based on Ag. Phase homogeneity was confirmed by comparing the powder X-ray diffraction pattern of the product against one calculated using the crystallographically determined atomic coordinates, see Table 4.8. Semiquantitative microprobe analysis on single crystals gave an average composition of $K_{0.79}Ag_{2.0}Eu_{1.2}Te_{4.4}$.

Table 4.1 Calculated and Observed X-ray Powder Diffraction Pattern for KCuCeTe$_4$ (I)

h k l	d$_{calc}$ (Å)	d$_{obs}$(Å)	I/I$_{max}$ (obs) (%)
0 0 1	21.3040	21.0782	9.23
0 0 2	10.6520	10.6081	4.62
0 0 3	7.1013	7.0762	47.43
0 0 4	5.3260	5.3109	12.97
0 0 5	4.2608	4.2508	9.28
0 0 6	3.5507	3.5430	76.09
0 0 7	3.0434	3.0370	100.00
0 0 8	2.6630	2.6579	10.36
0 0 9	2.3671	2.3626	26.67
1 1 7	2.1859	2.1717	3.05
0 0 10	2.1304	2.1266	6.18
0 0 11	1.9367	1.9331	12.31
2 1 4	1.8601	1.8616	4.26
0 0 12	1.7753	1.7722	1.78
0 0 13	1.6388	1.6363	1.96

Table 4.

Na, Ag,

h
0
0
0
0
1
1
0
0
0
1
0
0
0

Table 4.2 Calculated and Observed X-ray Powder Diffraction Pattern for $Na_{0.8}Ag_{1.2}CeTe_4$ (III)

h k l	d_{calc} (Å)	d_{obs} (Å)	I/I_{max} (obs) (%)
0 0 2	10.1255	10.1255	2.30
0 0 3	6.7503	6.7528	21.70
0 0 4	5.0627	5.0706	8.61
0 0 6	3.3752	3.3803	73.31
1 0 4	3.3424	3.3256	11.96
1 1 1	3.1103	3.0899	16.93
0 0 7	2.8930	2.8981	100.00
0 0 8	2.5314	2.5392	17.54
0 0 9	2.2501	2.2547	8.79
1 1 7	2.1300	2.1518	9.52
0 0 10	2.0251	2.0298	8.69
0 0 11	1.8410	1.8454	39.54
0 0 12	1.6876	1.6916	4.49

Table 4.3 Calculated and Observed X-ray Powder Diffraction Pattern for $K_{2.5}Ag_{4.5}Ce_2Te_9$ (IV) (based on superstructure)

h k l	d_{calc} (Å)	d_{obs}(Å)	I/I_{max} (obs) (%)
0 4 0	12.6103	13.5574	59.66
0 6 0	8.4069	8.5382	100.00
0 8 0	6.3052	6.4468	14.92
0 10 0	5.0441	5.1244	14.12
0 14 0	3.6030	3.6338	6.01
0 16 0	3.1526	3.1804	23.37
2 12 -1	2.9792	2.9852	9.92
0 18 0	2.8023	2.8254	8.55
3 15 0	2.6872	2.6996	15.45
0 20 0	2.5221	2.5346	0.97
3 17 0	2.4721	2.4880	2.69
4 14 -1	2.3731	2.3899	8.90
0 22 0	2.2966	2.2485	9.41
0 24 0	2.1017	2.1217	7.28
0 26 0	1.9401	1.9563	4.13
3 25 0	1.8390	1.8384	4.97
2 26 -1	1.7629	1.7628	2.38
2 10 2	1.7397	1.7328	2.41
3 7 2	1.6656	1.6656	1.59
2 30 0	1.6309	1.6318	3.28
8 10 0	1.5907	1.5890	2.62
0 32 0	1.5763	1.5756	2.42

123

Tabl

K₃A

Table 4.4   Calculated and Observed X-ray Powder Diffraction Pattern for $K_{2.5}Ag_{4.5}La_2Te_9$ (V) (based on superstructure)

h k l	d_{calc} (Å)	d_{obs} (Å)	I/I_{max} (obs) (%)
0 4 0	12.6820	13.3791	59.7
0 6 0	8.4546	8.6594	32.7
0 8 0	6.3410	6.4301	16.1
0 10 0	5.0728	5.1072	5.2
3 7 0	3.8444	3.8414	6.3
0 14 0	3.6234	3.6416	35.7
3 9 0	3.5334	3.5320	9.9
0 16 0	3.1705	3.1747	100.0
0 12 1	3.0100	3.0885	9.6
2 6 1	2.9923	2.9914	49.9
3 11 −1	2.9168	2.9204	27.2
4 10 0	2.8251	2.8245	45.7
2 10 1	2.7061	2.7050	70.2
0 20 0	2.5364	2.5395	8.9
3 17 0	2.4928	2.4927	8.6
2 14 1	2.3983	2.3968	47.3
6 2 −1	2.3223	2.3278	9.1
4 16 −1	2.2531	2.2550	47.9
5 15 0	2.1200	2.1231	67.3
0 26 0	1.9511	1.9576	44.2
4 14 −2	1.8457	1.8476	4.2
0 28 0	1.8117	1.8189	2.7

Table 4.4 continued   Calculated and Observed X-ray Powder Diffraction Pattern for $K_{2.5}Ag_{4.5}La_2Te_9$ (V) (based on superstructure)

h k l	d_{calc} (Å)	d_{obs} (Å)	I/I_{max} (obs) (%)
6 10 -2	1.7652	1.7658	4.8
5 15 1	1.7379	1.7375	19.8
8 2 0	1.6969	1.6967	21.7
6 14 -2	1.6707	1.6713	12.6
0 20 2	1.6372	1.6351	13.3
4 2 2	1.5965	1.5969	41.8
3 15 2	1.5454	1.5456	21.7

Table 4.5 Calculated and Observed X-ray Powder Diffraction Pattern for $Cu_{0.66}EuTe_2$ (VI)

h k l	d_{calc} (Å)	d_{obs} (Å)	I/I_{max} (obs) (%)
0 0 3	3.4201	3.4879	16.40
1 0 2	3.3749	3.3639	17.41
1 1 1	3.0275	3.0004	10.62
1 1 2	2.6958	2.6645	100.00
1 1 3	2.3243	2.3222	28.74
2 0 0	2.2405	2.2951	11.66
0 1 4	2.2261	2.2151	24.29
1 2 1	1.9668	1.9641	11.40
0 1 5	1.8657	1.8506	8.76
0 0 6	1.7100	1.7137	10.19
0 2 4	1.6874	1.6656	16.19
0 1 6	1.5977	1.6039	2.69
2 2 0	1.5792	1.5737	19.64

Tab

KCu

Table 4.6   Calculated and Observed X-ray Powder Diffraction Pattern for KCu_2EuTe_4 (VII)

h k l	d_{calc} (Å)	d_{obs} (Å)	I/I_{max} (obs) (%)
0 0 1	11.3650	11.3156	15.41
0 0 2	5.6825	5.6657	30.34
0 0 3	3.7883	3.7750	100.00
1 1 0	3.1371	3.1213	6.02
0 0 4	2.8413	2.8326	54.94
0 0 5	2.2730	2.2669	14.12
0 0 6	1.8942	1.8897	7.53
0 0 7	1.6215	1.6169	7.07

Table 4.7   Calculated and Observed X-ray Powder Diffraction Pattern for $Na_{0.2}Ag_{2.8}EuTe_4$ (VIII)

h k l	d_{calc} (Å)	d_{obs} (Å)	I/I_{max} (obs) (%)
0 0 1	11.1120	11.2785	28.75
0 0 2	5.5560	5.5304	44.89
0 0 3	3.7040	3.6898	27.27
1 0 2	3.4767	3.4559	18.75
1 0 3	2.8488	2.8506	11.59
0 0 4	2.7780	2.7889	76.59
1 1 2	2.7414	2.7477	100.00
1 1 3	2.4004	2.4058	11.25
1 0 4	2.3576	2.3592	17.27
2 0 0	2.2287	2.2357	21.14
1 1 4	2.0840	2.0922	27.73
2 1 0	1.9934	1.9934	17.73
2 0 3	1.9096	1.9050	11.14
0 0 6	1.8520	1.8585	24.89
2 0 4	1.7384	1.7450	1.011
1 0 6	1.7102	1.6820	8.41
2 1 4	1.6196	1.6384	8.75
1 1 6	1.5967	1.5987	8.64
2 2 0	1.5759	1.5753	9.55

Tab

K.

Table 4.8   Calculated and Observed X-ray Powder Diffraction Pattern for $K_{0.65}Ag_2Eu_{1.35}Te_4$ (IX)

h k l	d_{calc} (Å)	d_{obs}(Å)	I/I_{max} (obs) (%)
0 0 2	11.3997	11.3421	8.22
0 0 4	5.6999	5.6901	43.79
0 0 6	3.7999	3.7866	42.06
1 0 4	3.5314	3.5358	2.39
0 14 0	3.2342	3.2333	12.36
0 0 8	2.8499	2.8426	110.00
1 10 4	2.7846	2.7831	7.97
1 4 8	2.3549	2.3514	3.69
1 17 1	2.2804	2.2892	1.94
0 20 0	2.2640	2.2622	2.84
2 0 0	2.2495	2.2508	2.18
0 20 2	2.2206	2.2294	2.40
1 10 8	2.1257	2.1223	0.96
0 22 0	2.0891	2.0873	1.20
1 16 6	2.0264	2.0274	1.04
2 5 5	1.9691	1.9771	0.69
2 10 4	1.8994	1.8957	26.29
2 13 3	1.8338	1.8345	1.64
0 20 8	1.7727	1.7713	1.33
2 13 7	1.6345	1.6341	2.75
1 3 13	1.6245	1.6253	4.64
2 20 0	1.5957	1.5952	0.73

3. Physical Measurements – The instrumentation and experimental setup for the following measurements are the same as described in Chapter 2, Section B.3: Semiquantitative Energy Dispersive Spectroscopy (EDS), Powder X-ray Diffraction (PXRD), Transmission Electron Microscopy (TEM), Infrared Spectroscopy (IR), Magnetic Susceptibility Measurements, and Charge Transport Measurements.

Single Crystal X-ray Diffraction – Intensity data for $KCuCeTe_4$ (I), $Na_{0.8}Ag_{1.2}CeTe_4$ (III), and KCu_2EuTe_4 (VII) were collected on a Rigaku AFC6S four-circle automated diffractometer equipped with a graphite crystal monochromator. A single crystal of each was mounted on the tip of a glass fiber. The unit cell parameters were determined from a least-squares refinement using the setting angles of 20 carefully centered reflections in the $8° \leq 2\theta \leq 30°$ range. The data were collected with an ω-2θ scan technique over one-half (I), one-quarter (III), and the full (VIII) sphere of reciprocal space, up to $60°$ in 2θ. Crystal stability was monitored with three standard reflections whose intensities were checked every 150 reflections. No significant decay was detected during the data collection periods. The data was corrected for Lorentz-polarization effects and an empirical absorption correction based on Ψ-scans was applied to all data during initial stages of refinement. The structures were solved by direct methods using the SHELXS-86[20] package of crystallographic programs and full matrix least squares refinement was performed using the TEXSAN software package[21].

130

Complete data collection parameters and details of all structure solutions and refinements are given in Tables 4.19 and 4.11.

Intensity data for $RbCuCeTe_4$ (II), $K_{2.5}Ag_{4.5}Ce_2Te_9$ (IV), $K_{2.5}Ag_{4.5}La_2Te_9$ (V), $Cu_{0.66}EuTe_2$ (VI), $Na_{0.2}Ag_{2.8}EuTe_4$ (VIII), and $K_{0.65}Ag_2Eu_{1.35}Te_4$ (IX) were collected on a Siemens SMART Platform CCD diffractometer using graphite monochromatized Mo Kα radiation. A single crystal of each was mounted on the tip of a glass fiber. The data were collected over one-half (II, VI) and a full (IV, V, VIII, IX) sphere of reciprocal space, up to 50° in 2θ. The individual frames were measured with an ω rotation of 0.3° and acquisition times ranging from 40 to 80 sec/frame. The SMART[22] software was used for the data acquisition and SAINT[23] for the data extraction and reduction. The absorption correction was performed using SADABS.[24] The structure was solved by direct methods using the SHELXTL[25] package of crystallographic programs. Complete data collection parameters and details of all structure solutions and refinements are given in Tables 4.9-4.11.

Table 4.9 Crystallographic Data for $KCuCeTe_4$ (I), $RbCuCeTe_4$ (II), and $Na_{0.8}Ag_{1.2}CeTe_4$ (III)

	$KCuCeTe_4$	$RbCuCeTe_4$	$Na_{0.8}Ag_{1.2}CeTe_4$
crystal habit, color	plate, copper	plate, copper	plate, copper
Diffractometer	Rigaku AFC6S	Siemens SMART Platform CCD	Rigaku AFC6S
Radiation	Mo-Kα (0.71069Å)	Mo-Kα (0.71073Å)	Mo-Kα (0.71069Å)
Crystal Size, mm^3	0.29 x 0.29 x 0.03	0.18 x 0.31 x 0.02	0.23 x 0.23 x 0.02
Temperature, K	293	173	293
Crystal System	orthorhombic	orthorhombic	orthorhombic
Space Group	Pmmn (#59)	Pmmn (#59)	Pmmn (#59)
a, Å	4.436(1)	4.4330(9)	4.450(3)
b, Å	4.4499(9)	4.4697(9)	4.448(4)
c, Å	21.304(2)	21.951(4)	20.25(1)
V, Å^3	420.5(4)	434.95(15)	401.3(5)
Z	2	2	2
μ, mm^{-1}	22.020	26.219	22.690
index ranges	$0 \leq h \leq 5$	$-5 \leq h \leq 0$	$0 \leq h \leq 5$
	$-5 \leq k \leq 5$	$-5 \leq k \leq 5$	$0 \leq k \leq 5$
	$-25 \leq l \leq 25$	$-28 \leq l \leq 28$	$-24 \leq l \leq 24$
$2\theta_{max}$, deg	50	50	50
sec/frame	N/A	40	N/A
total data	1701	2645	1837
unique data	498	641	815
R(int)	0.065	0.156	0.032
no. parameters	30	30	28
final R/Rw[a], %	6.36/5.76	N/A	7.20/9.20
final R1/wR2[b], %	N/A	10.34/27.37	N/A
GOF	2.609	N/A	4.92
Goof	N/A	1.048	N/A

[a]$R = \Sigma (|F_o| - |F_c|) / \Sigma |F_o|$ $Rw = \{ \Sigma [w(F_o - F_c)^2] / \Sigma [w (F_o)^2] \}^{1/2}$

[b]$R1 = \Sigma (|F_o| - |F_c|) / \Sigma |F_o|$ $wR2 = \{ \Sigma [w(F_o^2 - F_c^2)^2] / \Sigma [w (F_o^2)^2] \}^{1/2}$

Table 4.10 Crystallographic Data for $K_{2.5}Ag_{4.5}Ce_2Te_9$ (IV), $K_{2.5}Ag_{4.5}La_2Te_9$ (V), and $Cu_{0.66}EuTe_2$ (VI)

	$K_{2.5}Ag_{4.5}Ce_2Te_9$	$K_{2.5}Ag_{4.5}La_2Te_9$	$Cu_{0.66}EuTe_2$
crystal habit, color	plate, copper	plate, copper	plate, copper
Diffractometer	Siemens SMART Platform CCD	Siemens SMART Platform CCD	Rigaku AFC6S
Radiation	Mo-Kα (0.71069Å)	Mo-Kα (0.71073Å)	Mo-Kα (0.71069Å)
Crystal Size, mm^3	0.31 x 0.22 x 0.04	0.44 x 0.13 x 0.02	0.44 x 0.13 x 0.02
Temperature, K	293	293	293
Crystal System	Orthorhombic	Orthorhombic	Tetragonal
Space Group	Immm (#71)	Immm (#71)	P4/mmm (#129)
a, Å	4.4844(9)	4.5224(6)	4.4810(16)
b, Å	4.5116(9)	4.5110(9)	4.4810(16)
c, Å	50.859(10)	50.618(10)	10.260(3)
V, Å^3	1029.0(4)	1032.6(4)	206.02(12)
Z	2	2	2
μ, mm^{-1}	21.514	21.166	32.196
index ranges	$-5 \leq h \leq 5$	$-5 \leq h \leq 5$	$0 \leq h \leq 5$
	$-5 \leq k \leq 4$	$-6 \leq k \leq 6$	$-5 \leq k \leq 5$
	$-65 \leq l \leq 64$	$-65 \leq l \leq 63$	$-11 \leq l \leq 12$
$2\theta_{max}$, deg	50	50	50
sec/frame	60	80	N/A
total data	3348	3271	1169
unique data	754	777	141
R(int)	0.0761	0.1186	0.1083
no. parameters	41	41	61
final R1/wR2[a], %	8.21/22.40	7.05/17.03	7.94/25.07
GooF	1.129	1.008	1.477

[a]$R1 = \Sigma (|F_o| - |F_c|)/\Sigma|F_o|$ $wR2 = \{\Sigma [w(F_o^2 - F_c^2)^2] / \Sigma [w (F_o^2)^2]\}^{1/2}$

Table 4.11 Crystallographic Data for KCu_2EuTe_4 (VII), $Na_{0.2}Ag_{2.8}EuTe_4$ (VIII), and $K_{0.65}Ag_2Eu_{1.35}Te_4$ (IX)

	KCu_2EuTe_4	$Na_{0.2}Ag_{2.8}EuTe_4$	$K_{0.65}Ag_2Eu_{1.35}Te_4$
crystal habit, color	plate, copper	plate, copper	plate, copper
Diffractometer	Rigaku AFC6S	Siemens SMART Platform CCD	Siemens SMART Platform CCD
Radiation	Mo-Kα (0.71073Å)	Mo-Kα (0.71073Å)	Mo-Kα (0.71073Å)
Crystal Size, mm³	0.40 x 0.40 x 0.04	0.13x 0.39 x 0.01	0.21 x 0.21 x 0.02
Temperature, K	293	293	293
Crystal System	Tetragonal	Tetragonal	Orthorhombic
Space Group	P4mm (#99)	P4mm (#99)	Abm2 (#39)
a, Å	4.4365(6)	4.4544(6)	4.4989(9)
b, Å	4.4365(6)	4.4544(6)	45.279(9)
c, Å	11.365(2)	11.106(2)	22.799(5)
V, Å³	223.69(6)	220.37(6)	4644.4(16)
Z	1	1	20
μ, mm⁻¹	24.789	26.044	25.682
index ranges	$-5 \le h \le 5$	$-5 \le h \le 5$	$-5 \le h \le 5$
	$-5 \le k \le 5$	$-5 \le k \le 5$	$-57 \le h \le 57$
	$-13 \le l \le 13$	$-13 \le l \le 14$	$-29 \le h \le 29$
$2\theta_{max}$, deg	50	50	50
sec/frame	N/A	40	80
total data	1597	1941	22152
unique data	295	361	5116
R(int)	0.1473	0.1114	0.0824
no. parameters	23	23	180
final R1/wR2ᵃ, %	7.35/17.88	7.30/20.35	6.46/27.80
Goof	1.198	1.078	2.148

[a]$R1 = \Sigma(|F_o| - |F_c|)/\Sigma|F_o|$ $wR2 = \{\Sigma[w(F_o^2 - F_c^2)^2]/\Sigma[w(F_o^2)^2]\}^{1/2}$

C. Results and Discussion

1. $A_xM_{(2-x)}CeTe_4$ (I -III)

Structure Description of $A_xM_{(2-x)}CeTe_4$ (A = Na, K, Rb; M = Cu,Ag) (I -III)

$KCuCeTe_4$ forms a two-dimensional structure composed of two "distinct" layers, $[CuTe]^-$ and $[CeTe_3]$, see Figure 4.1. Because each layer is known to exist independently, $KCuCeTe_4$ can be regarded an intergrowth compound and a more descriptive formula would be $K^+[CuTe]^-[CeTe_3]$. The $[CuTe]^-$ layer can be described as an ideal anti-PbO structure type, made up of ribbon tetrahedral $[CuTe_4]$ units that share edges in two dimensions, see Figure 4.2A. The $[CeTe_3]$ layer adopts the $NdTe_3$ structure type, and has 9-coordinate Ce in a monocapped square anti-prismatic environment of Te, see Figure 4.2B. The $[CuTe]^-$ and $[CeTe_3]$ layers are separated by potassium ions and stack in an A-B-A-B order parallel to the c-axis. The potassium cations are stabilized between the layers in a square antiprismatic coordination environment of Te, see Figure 4.2C. $RbCuCeTe_4$ and $Na_{0.8}Ag_{1.2}CeTe_4$ are isostructural to $KCuCeTe_4$. The non-stoichiometry in the formula of $Na_{0.8}Ag_{1.2}CeTe_4$ is due to a 20% disorder on the sodium site with silver. The fractional atomic coordinates, isotropic and anisotropic temperature factors, bond distances, and bond angles for all three compounds is given in Tables 4.12-4.16.

The $[CeTe_3]$ layer contains a square Te lattice net, see Figure 4.2D. Within this net, all the Te-Te distances are equal at 3.14 Å, which is longer than the the

normal Te-Te bond of 2.8 Å but shorter than the van der Waals contact of 3.8-4.0 Å. Tellurium square nets are rare and only few are known, e.g., $LnTe_2$, Ln_2Te_5, and $LnTe3$,[26] $CsTh_2Te_6$,[27] $K_{0.33}Ba_{0.67}AgTe_2$,[11] Cs_3Te_{22},[28] and ALn_3Te_8 (A = Cs, Rb , K; Ln = Ce , Nd)[9]. Depending on the electron-count, these nets can have different electronic structures, which can lead to instabilities and structural distortions within them.[29] These distortions can lead to interesting physical phenomena such as charge density waves and anomalies in the charge transport properties. When the formal oxidation state of all Te atoms in the net is -2, a stable square net is observed (e.g. NaCuTe).[30] However, when the formal oxidation state is < -2, or when there are atomic vacancies in the square net, structural distortions are possible leading to Te⋯Te bonding interactions and the formation of Te_x^{n-} species within the net. These distortions are manifested through the formation of a superstructure with respect to the ideal square net.[11]

An intriguing fact about this structure is that the $[CuTe]^-$ layer in $KCuCeTe_4$ is different from that found in KCuTe.[31] In KCuTe, a layered boron nitride type structure is seen while the $[CuTe]^-$ layer with the same alkali ion in the quaternary phase adopts the structure of NaCuTe (i.e. anti-PbO), see Figure 4.3. So, in a way, the $KCuCeTe_4$ has enforced a higher energy, presumably metastable, structure on KCuTe by sandwiching it

between $CeTe_3$ layers. The driving force for the stability of $KCuCeTe_4$ is therefore unknown unless some electron transfer exists between the two different metal chalcogenide layers.
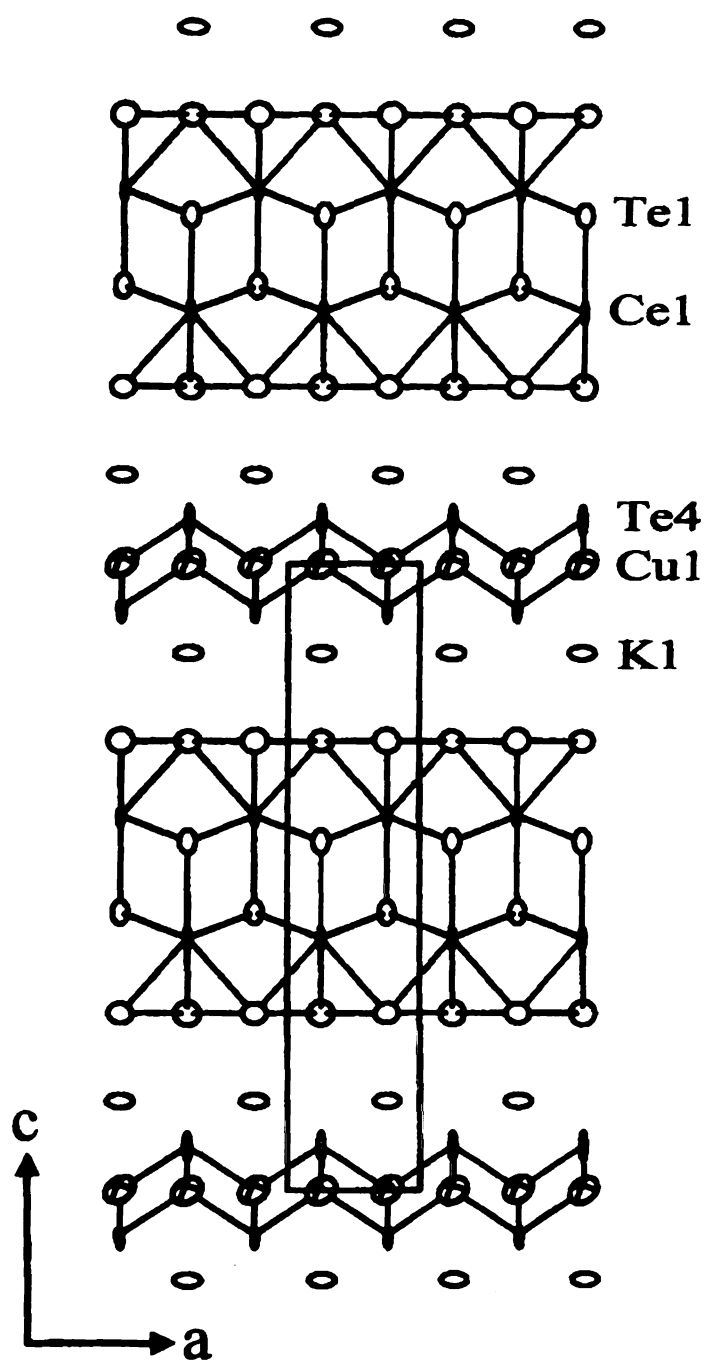
Figure 4.1   ORTEP representation of the extended structure of $KCuCeTe_4$ as seen down the b-axis (90% probability ellipsoids). The ellipses with octant shading represent Ce, the crossed ellipses represent Cu, the large open ellipses represent K and Te.

138

Figure 4.2 ORTEP representation (90% probability ellipsoid) of (A) a view perpendicular to the [CuTe⁻] layer of $KCuCeTe_4$, (B) the coordination environment around Ce in $KCuCeTe_4$, (C) the coordination environment around K in $KCuCeTe_4$, and (D) a view perpendicular to the [CeTe₃] layer in $KCuCeTe_4$. The ellipses with octant shading represent Ce, the crossed ellipses represent Cu, the large open ellipses represent K and Te.

139

Table 4.12   Fractional Atomic Coordinates and Equivalent Isotropic Displacement Parameters (U_{eq}) for $KCuCeTe_4$ (I), $RbCuCeTe_4$ (II), and $Na_{0.8}Ag_{1.2}CeTe_4$ (III) with Estimated Standard Deviations in Parentheses.

$KCuCeTe_4$

atom	x	y	z	occupancy	B_{eq}^{a}, $Å^2$
Ce	0.25	0.25	0.4022(1)	1.0	1.07(8)
Te(1)	0.25	0.25	0.5565(1)	1.0	1.1(1)
Te(2)	0.25	0.75	0.2827(1)	1.0	1.7(1)
Te(3)	0.75	0.25	0.2829(1)	1.0	1.4(1)
Te(4)	0.25	0.25	0.0703(1)	1.0	1.7(1)
Cu	0.25	0.75	0.9992(3)	1.0	2.6(2)
K	0.75	0.75	0.1427(4)	1.0	1.7(3)

$RbCuCeTe_4$

atom	x	y	z	occupancy	U_{eq}^{b}, $Å^2$
Ce	0.25	0.25	0.4050(1)	1.0	1.0(1)
Te(1)	0.25	0.25	0.5548(1)	1.0	0.9(1)
Te(2)	0.25	0.75	0.2893(2)	1.0	1.8(1)
Te(3)	0.75	0.25	0.2893(2)	1.0	1.6(1)
Te(4)	0.25	0.25	0.0677(2)	1.0	1.8(1)
Cu	0.25	0.75	0.0001(3)	1.0	2.6(2)
Rb	0.75	0.75	0.1475(2)	1.0	2.0(1)

$Na_{0.8}Ag_{1.2}CeTe_4$

atom	x	y	z	occupancy	B_{eq}^{a}, $Å^2$
Ce	0.25	0.25	0.3966(1)	1.0	0.54(3)
Te(1)	0.25	0.25	0.5594(1)	1.0	0.58(4)
Te(2)	0.25	0.75	0.2716(1)	1.0	1.03(4)
Te(3)	0.75	0.25	0.2711(1)	1.0	1.03(4)
Te(4)	0.25	0.25	0.0919(1)	1.0	0.98(4)
Ag(1)	0.25	0.75	0.9995(1)	1.0	1.30(5)
Ag(2)	0.75	0.75	0.1411(4)	0.2	0.8(1)
Na	0.75	0.75	0.1411(4)	0.8	0.8(1)

[a]B values for anisotropically refined atoms are given in the form of the isotropic equivalent displacement parameter defined as $B_{eq} = (4/3)[a^2B(1,1) + b^2B(2,2) + c^2B(3,3) + ab(\cos\gamma)B(1,2) + ac(\cos\beta)B(1,3) + bc(\cos\alpha)B(2,3)]$. [b]$U_{eq}$ is defined as one-third of the trace of the orthogonalized U_{ij} tensor.

Table 4.13 Anisotropic Displacement Parameters (Å) for KCuCeTe$_4$ (I), RbCuCeTe$_4$ (II), and Na$_{0.8}$Ag$_{1.2}$CeTe$_4$ (III) with Standard Deviations in Parentheses.

KCuCeTe$_4$

atom	U11	U22	U33	U12	U13	U23
Ce	0.0129(8)	0.0064(7)	0.022(1)	0	0	0
Te(1)	0.0116(9)	0.0051(8)	0.025(2)	0	0	0
Te(2)	0.028(1)	0.0104(8)	0.025(2)	0	0	0
Te(3)	0.025(1)	0.0114(8)	0.018(2)	0	0	0
Te(4)	0.019(1)	0.0111(9)	0.036(2)	0	0	0
Cu	0.037(2)	0.031(2)	0.032(4)	0	0	0
K	0.032(4)	0.032(4)	0.000(4)	0	0	0

RbCuCeTe$_4$

atom	U11	U22	U33	U12	U13	U23
Ce	0.003(1)	0.009(1)	0.018(2)	0	0	0
Te(1)	0.001(1)	0.007(1)	0.019(2)	0	0	0
Te(2)	0.018(2)	0.017(2)	0.018(2)	0	0	0
Te(3)	0.014(2)	0.017(2)	0.016(2)	0	0	0
Te(4)	0.006(2)	0.019(2)	0.030(2)	0	0	0
Cu	0.015(4)	0.029(4)	0.033(4)	0	0	0
Rb	0.014(2)	0.021(2)	0.025(3)	0	0	0

Na$_{0.8}$Ag$_{1.2}$CeTe$_4$

atom	U11	U22	U33	U12	U13	U23
Ce	0.0050(6)	0.0064(7)	0.022(1)	0	0	0
Te(1)	0.0050(7)	0.0051(8)	0.025(1)	0	0	0
Te(2)	0.0149(8)	0.0104(8)	0.025(1)	0	0	0
Te(3)	0.0131(8)	0.0114(8)	0.018(1)	0	0	0
Te(4)	0.0125(9)	0.0111(9)	0.036(1)	0	0	0
Ag(1)	0.016(1)	0.031(2)	0.032(1)	0	0	0

Table 4.14 Selected Distances (Å) and Bond Angles (deg) for $KCuCeTe_4$ (I) with Standard Deviations in Parentheses.

Bond Distances

Ce – Te1	3.263(1) x 4	3.287(4) x 1
Ce – Te2	3.382(3) x 2	
Ce – Te3	3.374(3) x 2	
Te2 – Te3	3.1417(6) x 4	
Cu – Te4	2.667(4) x 2	2.692(4) x 2
K – Te2	3.717(7) x 2	
K – Te3	3.725(7) x 2	
K – Te4	3.499(4) x 4	

Bond Angles

Te1 – Ce –Te1	74.35(5) x 4	85.66(4) x 2	148.7(1) x 2
Te1 – Ce – Te2	75.79(5) x 4	130.68(6) x 2	138.86(4) x 2
Te1 – Ce – Te3	75.90(5) x 3	130.56(6) x 3	138.89(4) x 2
Te2 – Ce – Te3	55.43(4) x 2	82.21(9) x 1	82.29(9) x 1
Te2 – Te3 – Te2	89.92(2) x 2	90.18(2) x 2	179.8(2) x 2
Te4 – Cu – Te4	108.22(5) x 2	111.5(2) x 1	112.5(2) x 1
Te2 – K – Te2	73.3(2) x 1		
Te2 – K – Te3	49.9(1) x 4		
Te2 – K – Te4	88.57(7) x 4	137.0(1) x 4	
Te3 – K – Te3	73.4(2) x 2		
Te3 – K – Te4	88.47(7) x 4	137.(1) x 4	
Te4 – K – Te4	79.0(1) x 2	78.7(1) x 2	127.7(3) x 2

Table 4.15 Selected Distances (Å) and Bond Angles (deg) for RbCuCeTe$_4$ (II) with Standard Deviations in Parentheses.

Bond Distances

Ce – Te1	3.269(1) x 8	3.288(4) x 1
Ce – Te2	3.384(3) x 2	
Ce – Te3	3.371(3) x 3	
Te2 – Te3	3.1476(5) x 7	
Cu – Te4	2.669(5) x 3	2.683(4) x 3
Rb – Te2	3.820(5) x 2	
Rb – Te3	3.832(5) x 3	
Rb – Te4	3.602(3) x 7	

Bond Angles

Te1 – Ce –Te1	74.33(8) x 4	85.8(4) x 2	148.66(15) x 2
Te1 – Ce – Te2	75.60(6) x 4	130.87(7) x 4	138.66(4) x 1
Te1 – Ce – Te3	75.97(5) x 4	130.49(7) x 4	138.88(5) x 2
Te2 – Ce – Te3	55.55(5) x 4		
Te2 – Te3 – Te2	89.528(17) x 4	90.472(16) x 4	179.96(18) x 4
Te4 – Cu – Te4	107.96(6) x 4	1112.3(3) x 2	
Te2 – Rb – Te2	70.93(11) x 1		
Te2 – Rb – Te3	48.58(6) x 4		
Te2 – Rb – Te4	92.24(6) x 4	138.86(9) x 4	
Te3 – Rb – Te3	71.36(11) x 1		
Te3 – Rb – Te4	91.90(6) x 4	139.19(9) x 4	
Te4 – Rb – Te4	75.95(8) x 2	76.69(8) x 2	121.80(19) x 2

Table 4.16 Selected Distances (Å) and Bond Angles (deg) for $Na_{0.8}Ag_{1.2}CeTe_4$ (III) with Standard Deviations in Parentheses.

Bond Distances

Ce – Te1	3.272(1) x 4	3.296(3) x 1
Ce – Te2	3.371(2) x 2	
Ce – Te3	3.378(3) x 2	
Te2 – Te3	3.148(1) x 4	
Ag1 – Te4	2.895(3) x 2	2.908(2) x 2
Na – Te2	3.455(6) x 2	
Na – Te3	3.449(6) x 2	
Na – Te4	3.302(3) x 4	

Bond Angles

Te1 – Ce –Te1	74.19(5) x 4	85.71(5) x 2	148.74(1) x 2
Te1 – Ce – Te2	75.82(4) x 4	130.85(5) x 4	138.66(3) x 2
Te1 – Ce – Te3	75.93(5) x 4	130.77(5) x 4	138.79(4) x 4
Te2 – Ce – Te3	55.61(4) x 4		
Te3 – Ce – Te3	82.42(3) x 1		
Te2 – Te3 – Te2	89.96(4) x 2	90.04(4) x 1	179.6(1) x 1
Te4 – Ag1 – Te4	99.9(1) x 1	100.4(1) x 1	114.30(4) x 4
Te2 – Na – Te2	80.2(2) x 1		
Te2 – Na – Te3	54.3(1) x 4		
Te2 – Na – Te4	78.27(7) x 4	131.7(1) x 4	
Te3 – Na – Te3	80.4(2) x 1		
Te3 – Na– Te4	78.16(6) x 4	131.7(1) x 4	
Te4 – Na – Te4	84.75(8) x 1	85.82(8) x 1	144.9(3) x 1

(A) NaCuTe

Na
Cu
Te
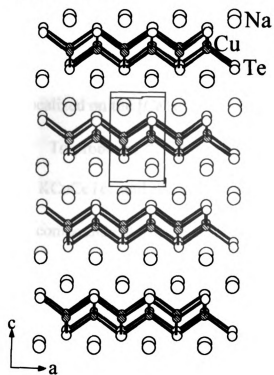
(B) KCuTe

K
Cu
Te
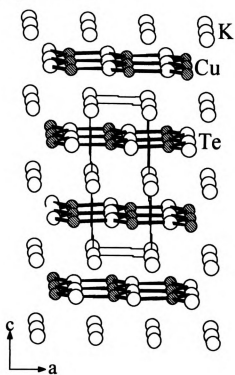
Figure 4.3   Side by side comparison of the layers in (A) NaCuTe to those in (B) KCuTe. Both structures are viewed down the b-axis.

[Ce

of th

the

form

and

be l

bot

bot

occ

dif

obs

sh

ref

(i:

d;

.:

dj

ev

th

Transmission Electron Microscopy of KCuCeTe₄ (1) – The Te net in the [CeTe₃] layer of $KCuCeTe_4$ is fully occupied. However, the formal oxidation state of the Te atoms in this net is –0.5, indicating the possibility of a distortion within the Te net. Notice that the [CuTe]⁻ layer also has a square Te net; however, the 2-formal charge on each Te atom in this layer is not expected to lead to a distortion and therefore a superstructure. Consequently, any observed superstructure must be localized on the [CeTe₃] part of the compound.

To probe for this distortion, electron diffraction studies were performed on both $KCuCeTe_4$ and $Na_{0.8}Ag_{1.2}CeTe_4$. Indeed, a superstructure was revealed for both compounds along the ab plane. The supercell reflections are very weak, and occur along both the a* and b* directions. Figure 4.4A shows an electron diffraction pattern of $KCuCeTe_4$ along the ab plane. A densitometric intensity scan obtained from the (hk0) reciprocal plane along the (1k0) row of reflections is shown in Figure 4.4B. The reflections between the (1 -1 0), (1 0 0), and (1 1 0) reflections are due to the $0.348b^*$ superlattice, which corresponds to a 2.87 x b_{sub} (i.e.~ 13Å) lattice dimension. These supercell reflections also occur along the a* direction, at the same exact position, giving an incommensurate supercell of "$2.87a_{sub}$ x $2.87b_{sub}$". However, long axial photographs taken on the x-ray diffractometer for $Na_{0.8}Ag_{1.2}CeTe_4$ suggest that the incommensurate supercell exists only along the b-axis, giving a "$1a_{sub}$ x $2.87b_{sub}$" supercell. It is possible that the "$2.87a_{sub}$ x $2.87b_{sub}$" supercell revealed by electron diffraction is simply a

twinning effect whereby two crystals with a "$1a_{sub} \times 2.87b_{sub}$" supercell are rotated 90° with respect to one another and superimposed under the electron beam, see Figure 4.5. Without further evidence, however, a decision cannot be made with certainty as to the real identity of the supercell. In either case (see Figure 4.6), there exists a distortion within the Te net of the [CeTe$_3$] layer, resulting in an oligomerization of the Te atoms such that the larger unit cell redescribes the Te net's periodicity. Since the supercell is both weak and incommensurate, the single crystal X-ray data needed to actually solve the superstructure could not be obtained at Michigan State University. A collaboration has been established with Professor Michel Evain at the Institute des Matériaux in Nante, France who specializes in solving these types of incommensurate superstructures. Unfortunately, attempts thus far to collect x-ray data have been unsuccessful due to inadequate crystal quality.

Figure 4.4 (A) Selected area electron diffraction pattern of $KCuCeTe_4$ with the beam perpendicular to the layers ([001] direction) showing the $2.87a_{sub} \times 2.87b_{sub}$ superlattice. (B) Densitometric intensity scan along the b^* axis of the electron diffraction pattern (boxed area in photograph) showing the (1k0) family of reflections. The three reflections from the sublattice of $KCuCeTe_4$ are indexed. The two weak peaks are from the superlattice with $b_{super} = 2.87b_{sub}$.

Electron Diffraction of KCuCeTe$_4$

(A)
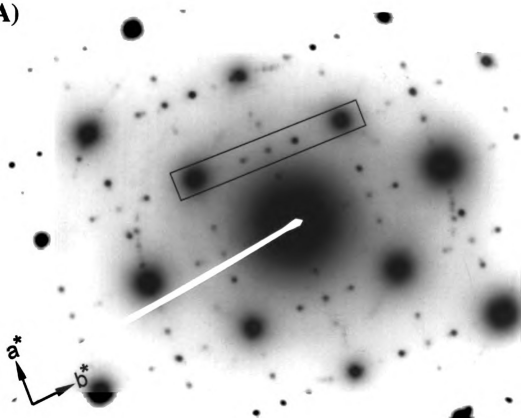
(B)
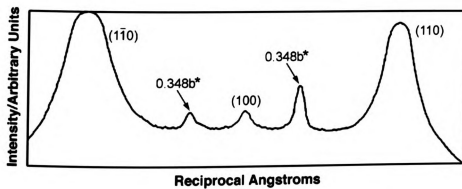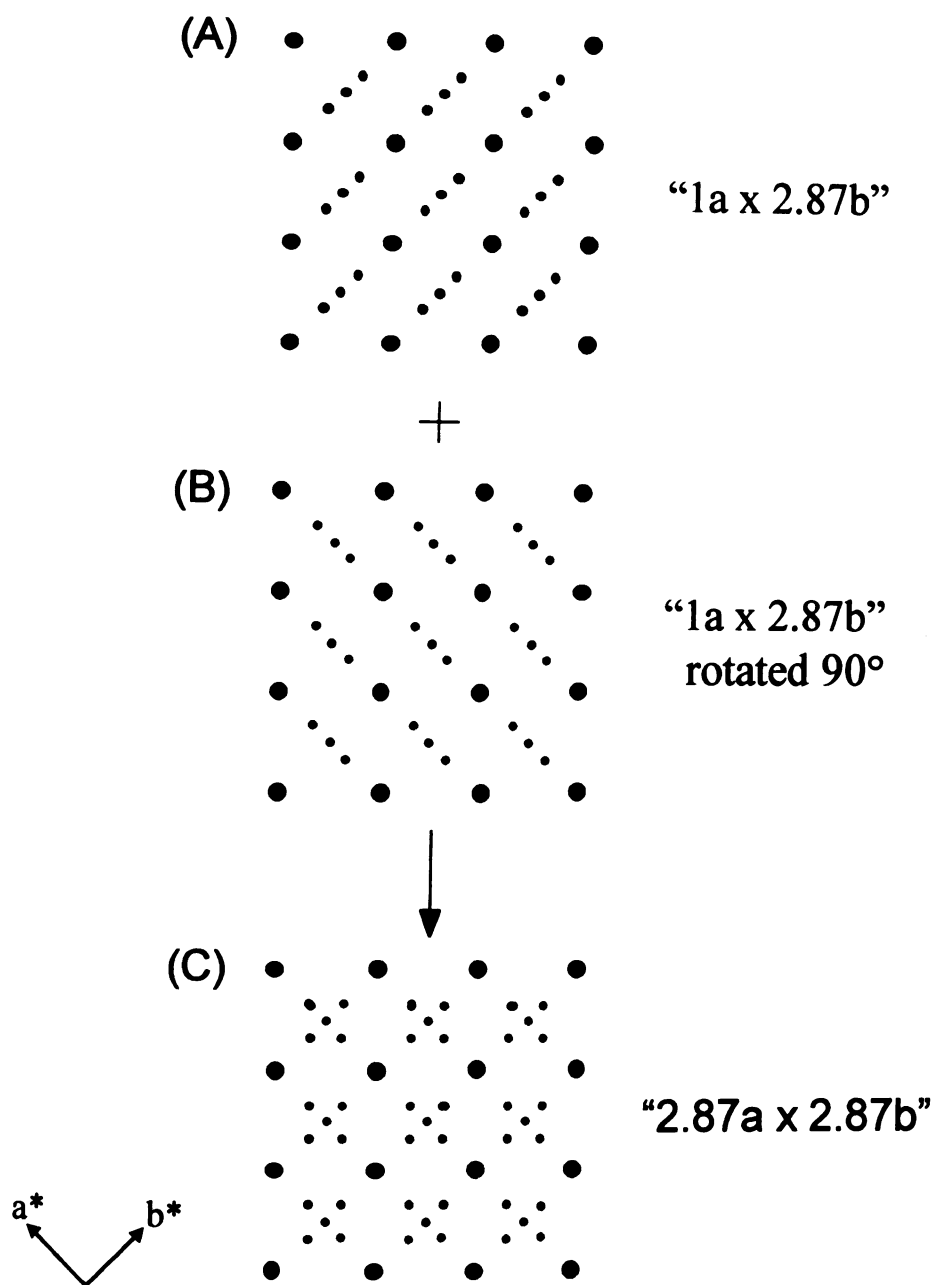
Figure 4.5 Cartoon Schematic of an electron diffraction pattern for (A) a "$1a_{sub}$ x $2.87b_{sub}$" supercell, (B) two "$1a_{sub}$ x $2.87b_{sub}$" supercells rotated 90° with respect to one another and superimposed under the electron beam, and (C) an apparent "$2.87a_{sub}$ x $2.87b_{sub}$" supercell.

(A) $1a_{sub} \times 2.87b_{sub}$
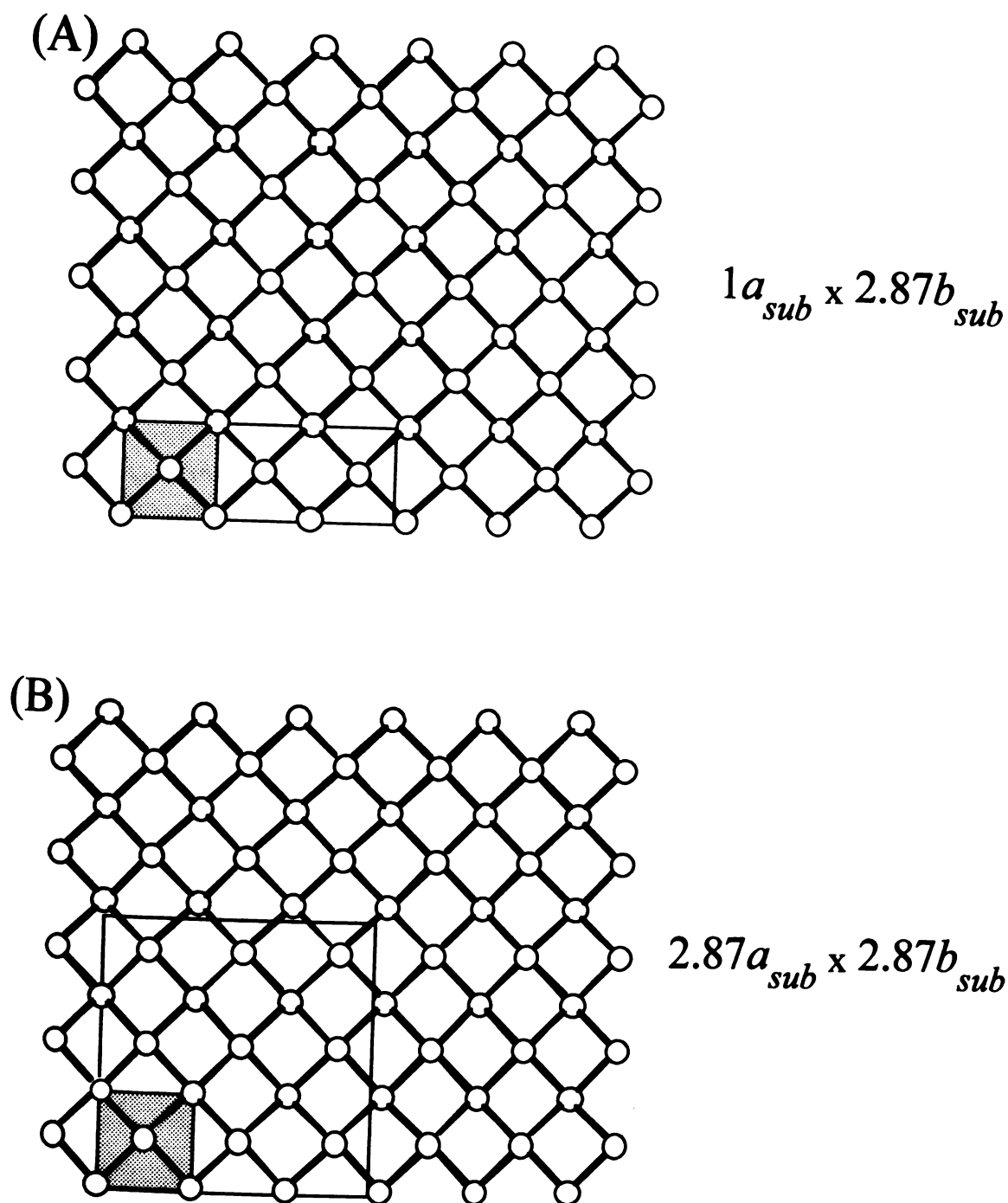
(B) $2.87a_{sub} \times 2.87b_{sub}$

Figure 4.6 View of the Te "net" in KCuCeTe$_4$ showing (A) a "$1a_{sub} \times 2.87b_{sub}$" supercell and (B) a "$2.87a_{sub} \times 2.87b_{sub}$" supercell. The crystallographically determined sublattice is shown in the shaded box for both.

151

Magnetic Susceptibility Measurements of $A_xM_{(2-x)}CeTe_4$ (I –III) – The magnetic susceptibilities of $KCuCeTe_4$ $RbCuCeTe_4$, and $Na_{0.8}Ag_{1.2}CeTe_4$ were measured over the range 5-300K at 6000G, see Figure 4.7. A plot of $1/X_M$ vs T for each show that the materials exhibit nearly Curie-Weiss behavior with only slight deviations from linearity beginning below 50K. Such deviation has been reported for several Ce^{3+} compounds and has been attributed to crystal field splitting of the cation's $^2F_{5/2}$ ground state.[32] At temperatures above 100K, μ_{eff} values of 2.62 μ_B for $KCuCeTe_4$, 2.78 μ_B for $RbCuCeTe_4$, and 2.75 μ_B for $Na_{0.8}Ag_{1.2}CeTe_4$ have been calculated. These values are in accordance with the usual range for Ce^{3+} compounds (2.3-2.5 μ_B). These magnetic moments suggest that the cerium in these compounds are trivalent with a $5f^1$ electronic configuration. The Weiss constants, θ, were calculated to be –31K for $KCuCeTe_4$, -69K for $RbCuCeTe_4$, and –98K for $Na_{0.8}Ag_{1.2}CeTe_4$. These large negative values indicate that there is a certain amount of antiferromagnetic ordering.
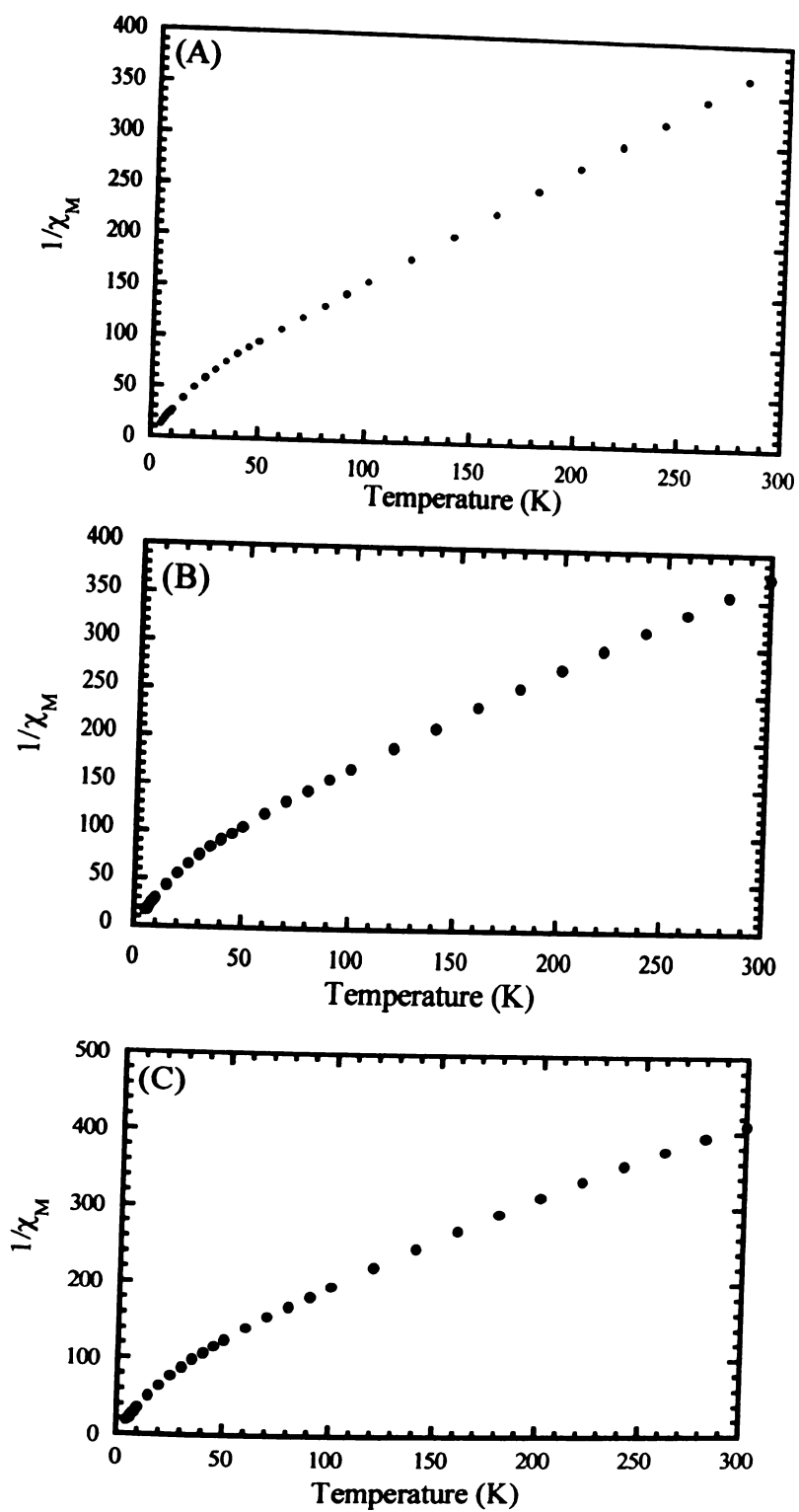
Figure 4.7. Inverse molar magnetic susceptibility $(1/\chi_M)$ plotted against temperature (2-300K) for (A) $KCuCeTe_4$, (B) $RbCuCeTe_4$, and (C) $Na_{0.8}Ag_{1.2}CeTe_4$.

KCu

diffu

Figu

indi

how

be a

diff

con

Na

has

Infrared Spectroscopy of $A_xM_{(2-x)}CeTe_4$ (I –III) – The optical properties of

$KCuCeTe_4$ (I), and $Na_{0.8}Ag_{1.2}CeTe_4$ (III) were determined by measuring the

diffuse-reflectance spectra of each in the Mid-IR region (6000-400 cm^{-1}), see

Figure 4.8. The spectrum of $KCuCeTe_4$ (I) shows no transitions in this region,

indicating that this material is metallic. The spectrum of $Na_{0.8}Ag_{1.2}CeTe_4$ (III),

however, reveals an abrupt optical transition at 0.32 eV, suggesting the material to

be a semiconductor. This difference in properties is most likely due to the

difference in the elemental makeup of the materials. However, another factor that

comes into play is the statistical disorder between the silver and sodium in

$Na_{0.8}Ag_{1.2}CeTe_4$ (III). It would be interesting to know how much this disorder

has an effect on the properties.
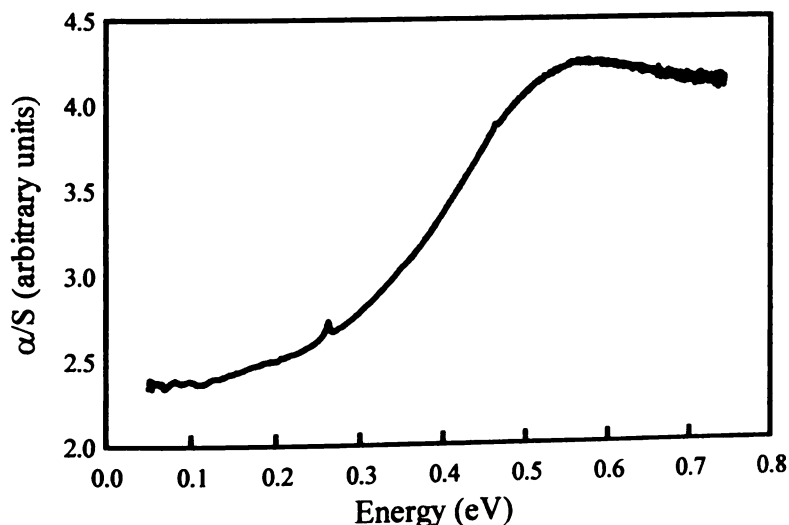
Figure 4.8   Diffuse reflectance optical spectra of $Na_{0.8}Ag_{1.2}CeTe_4$ (in the Mid-IR region).

Charge Transport Measurements of $A_xM_{(2-x)}CeTe_4$ (I –III) – Electrical conductivity data as a function of temperature for a hot-pressed (at 200^oC) pellet of $KCuCeTe_4$ confirms the metallic behavior with a room temperature value of 180 S/cm (See Figure 4.9A). The thermopower data shows a Seebeck coefficient at room temperature of ~3 $\mu V/K$, which suggests that the carriers are holes (see Figure 4.9B). The magnitude and slope of the Seebeck coefficient are consistent with the metallic character of the sample. Therefore, the distortion in the Te layer, which gives rise to the incommensurate superstructure, does not fully open up a gap at the Fermi level of this material. This is probably due to the fact that the distortion itself is very subtle.

The electrical conductivity data of $Na_{0.8}Ag_{1.2}CeTe_4$ as a function of temperature for a room temperature pressed pellet also agree with the optical spectrum, showing semiconducting behavior. The data decrease with decreasing temperature and gives a room temperature value of ~100 S/cm. The thermopower data shows a Seebeck coefficient at room temperature of ~21 $\mu V/K$, higher than that of $KCuCeTe_4$.
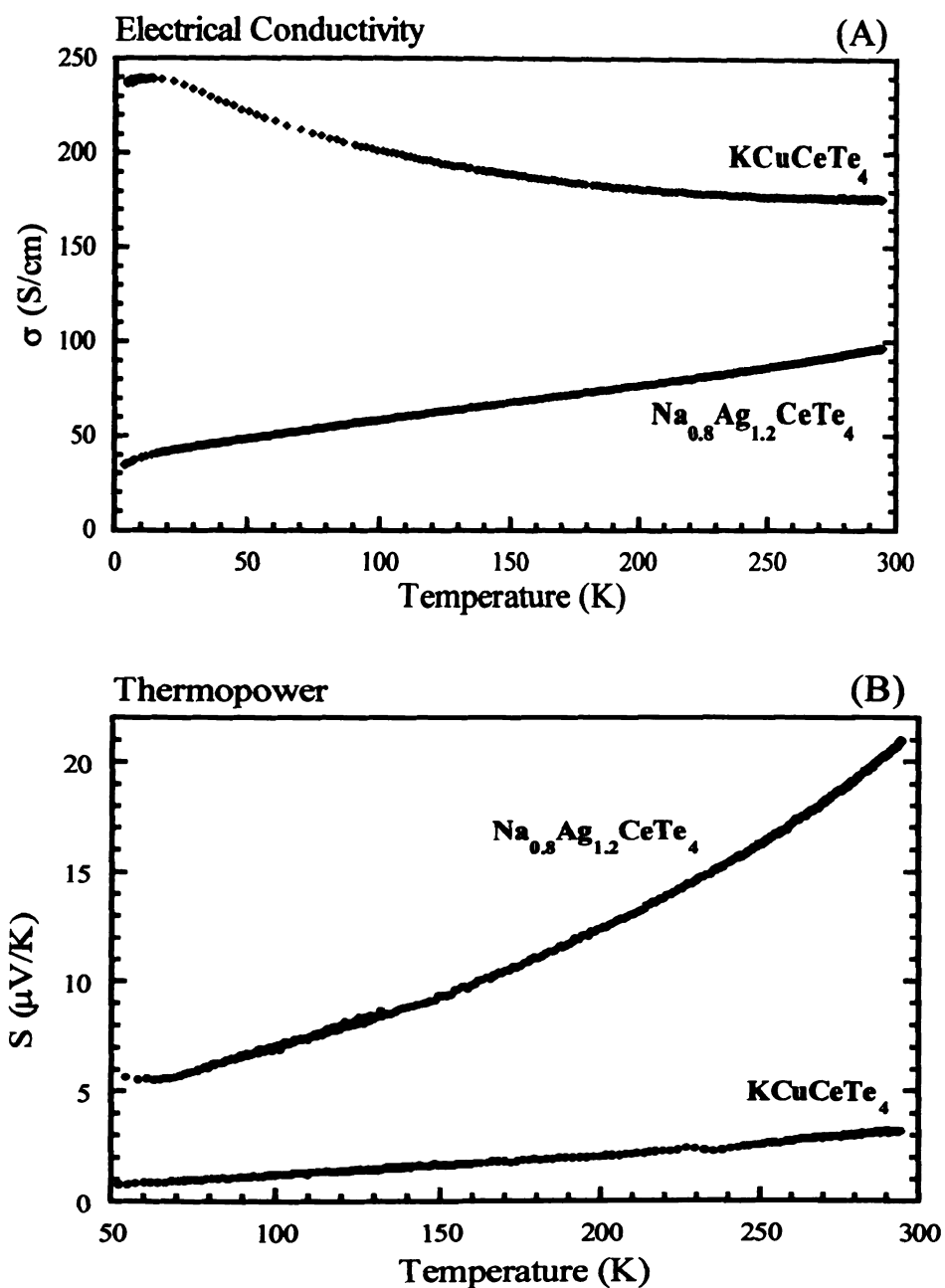
Figure 4.9 (A) Four probe, electrical conductivity data of a hot-pressed pellet of $KCuCeTe_4$ and a room temperature pressed pellet of $Na_{0.8}Ag_{1.2}CeTe_4$ as a function of temperature. (B) Thermopower data of a hot-pressed pellet of $KCuCeTe_4$ and a room temperature pressed pellet of $Na_{0.8}Ag_{1.2}CeTe_4$ as a function of temperature

2. I

com

in t

dow

mac

reg

foll

[Ce

neg

ato

arr

squ

sec

up

in t

tetr

Con

ato

oog

oog

sosy

2. $K_{2.5}Ag_{4.5}Ln_2Te_9$ (Ln = Ce, La) (IV, V)

Structure Description of $K_{2.5}Ag_{4.5}Ln_2Te_9$ (Ln = Ce, La) (IV, V) – The two compounds, $K_{2.5}Ag_{4.5}Ce_2Te_9$ and $K_{2.5}Ag_{4.5}La_2Te_9$, are isostructural and crystallize in the orthorhombic space group, Immm. The two-dimensional structure, as seen down the b-axis, is shown in Figure 4.10. Much like $KCuCeTe_4$, the structure is made up of two "distinct" layers that alternate in an A-B-A-B fashion and can be regarded as an intergrowth compound. For the purpose of this discussion, the following description will be for that of $K_{2.5}Ag_{4.5}Ce_2Te_9$. The first layer, $[CeTe_3]^{0.5-}$, also exists in $KCuCeTe_4$ except now the layer possesses an overall negative charge. This layer once again adopts the $NdTe_3$ structure type with all Ce atoms coordinated to nine Te atoms in a monocapped square anti-prismatic arrangement, see Figure 4.11A. This layer contains a Te net that is perfectly square with all Te-Te distances being equal at 3.1806(5)Å, see Figure 4.11B. The second layer, however, is different from that of $KCuCeTe_4$. Instead of being made up of a "single layer" of tetrahedrally coordinated copper atoms, as was observed in the [CuTe⁻] layer of $KCuCeTe_4$, this layer is now made up of "double layers" of tetrahedrally coordinated silver atoms that share edges in two dimensions. Conceptually, it is as if two "single layers" of tetrahedrally coordinated silver atoms have been sewn together. Interestingly, the Te atom that acts as the point of connection between these "single layers" is eight coordinate, a rather high coordination number for chalcogens. This layer alone is very similar the one that exists in KCu_4S_3[33] and can be written as $[K_{1.5}Ag_{4.5}Te_3]$. The difference, however,

157

is th

This

be v

insic

each

more

[(K⁷

anis

corr

is that, in $K_{2.5}Ag_{4.5}Ce_2Te_9$, another cation exists in-between these "double layers". This cation is disordered between potassium and silver (50:50). This layer can also be viewed as being made up of individual cages where now the cation is sitting inside the cavities of each cage. Finally, the potassium ions are stabilized between each "distinct" layer in a square antiprismatic geometry, see Figure 4.11C. A more descriptive way to write the formula of this compound is therefore $[(K^+)(K_{1.5}Ag_{4.5}Te_3)(CeTe_3^{0.5-})_2]$. The fractional atomic coordinates, isotropic and anisotropic temperature factors, bond distances, and bond angles for both compounds is given in Tables 4.17-4.20.
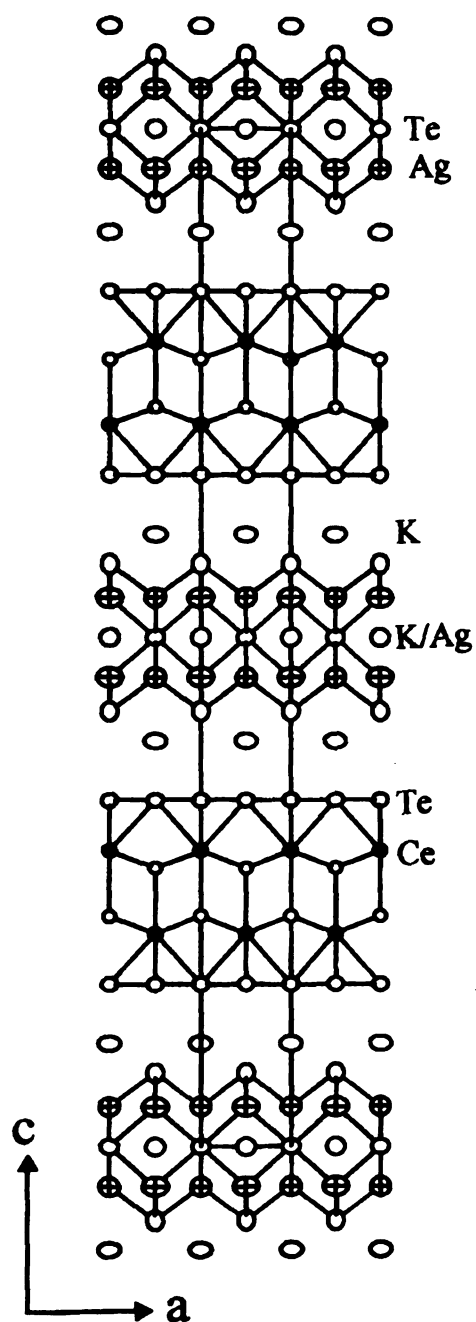
Figure 4.10 ORTEP representation of the extended structure of $K_{2.5}Ag_{4.5}Ce_2Te_9$ as seen down the b-axis (90% probability ellipsoids). The ellipses with octant shading represent Ce, the crossed ellipses represent Ag, the large open ellipses represent K and Te.
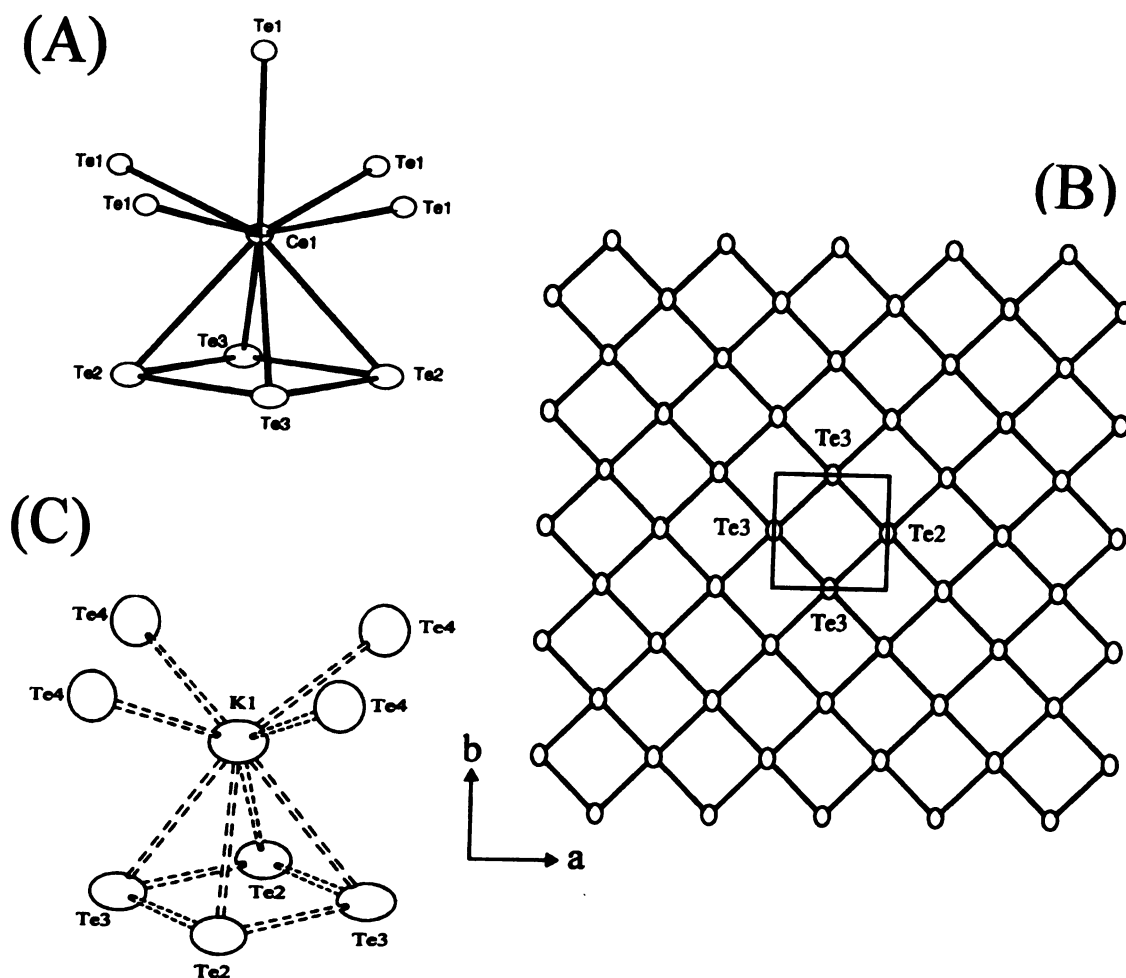
Figure 4.11 ORTEP representations of (A) the coordination environment around Ce in $K_{2.5}Ag_{4.5}Ce_2Te_9$ (50% probability ellipsoids), (B) the "Te net" of $K_{2.5}Ag_{4.5}Ce_2Te_9$ (70% probability ellipsoids), and (C) the coordination environment around K in $K_{2.5}Ag_{4.5}Ce_2Te_9$ (90% probability ellipsoids) The ellipses with octant shading represent Ce and the large open ellipses represent Te.

160

Disp

with

$K_{2,s}$
ator

Ce
Tet 1
Tet 2
Tet 3
Tet 4
Tet 5
Ag1
Ag1
K1 1
K1 2
Ag1

$K_{2,2}$
ator

La
Te
Te
Te
Te
Te
Ag
Ag
K1
K1 2
Ag

t e

Table 4.17   Fractional Atomic Coordinates and Equivalent Isotropic Displacement Parameters (U_{eq}) for $K_{2.5}Ag_{4.5}Ce_2Te_9$ (IV) and $K_{2.5}Ag_{4.5}La_2Te_9$ (V) with Estimated Standard Deviations in Parentheses.

$K_{2.5}Ag_{4.5}Ce_2Te_9$

atom	x	y	z	occupancy	U_{eq}^a, $Å^2$
Ce	0.0	0.0	0.2907(1)	1.0	1.7(1)
Te(1)	0.0	0.0	0.2264(1)	1.0	1.5(1)
Te(2)	0.5	0.0	0.3403(1)	1.0	2.6(1)
Te(3)	0.0	0.5	0.3404(1)	1.0	2.8(1)
Te(4)	0.0	0.0	0.4274(1)	1.0	3.0(1)
Te(5)	0.5	0.5	0.5	1.0	2.9(1)
Ag(1)	0.5	0.0	0.4608(1)	1.0	4.6(1)
Ag(2)	0.0	0.5	0.4607(1)	1.0	4.5(1)
K(1)	0.5	0.5	0.3985(2)	1.0	3.7(2)
K(2)	0.0	0.0	0.5	0.55(4)	3.4(3)
Ag(3)	0.0	0.0	0.5	0.45(4)	3.4(3)

$K_{2.5}Ag_{4.5}La_2Te_9$

atom	x	y	z	occupancy	U_{eq}^a, $Å^2$
La	0.0	0.0	0.2912(1)	1.0	0.9(1)
Te(1)	0.0	0.0	0.2261(1)	1.0	0.9(1)
Te(2)	0.5	0.0	0.3417(1)	1.0	2.2(1)
Te(3)	0.0	0.5	0.3416(1)	1.0	2.0(1)
Te(4)	0.0	0.0	0.4273(1)	1.0	2.2(1)
Te(5)	0.5	0.5	0.5	1.0	2.4(1)
Ag(1)	0.5	0.0	0.4607(1)	1.0	3.4(1)
Ag(2)	0.0	0.5	0.4608(1)	1.0	3.5(1)
K(1)	0.5	0.5	0.3992(2)	1.0	2.5(2)
K(2)	0.0	0.0	0.5	0.54(3)	2.2(2)
Ag(3)	0.0	0.0	0.5	0.46(3)	2.2(2)

[a]U_{eq} is defined as one third of the trace of the orthogonalized U_{ij} tensor

Table 4.18   Anisotropic Displacement Parameters (Å) for $K_{2.5}Ag_{4.5}Ce_2Te_9$ (IV) and $K_{2.5}Ag_{4.5}La_2Te_9$ (V) with Standard Deviations in Parentheses.

$K_{2.5}Ag_{4.5}Ce_2Te_9$

atom	U11	U22	U33	U12	U13	U23
Ce	0.021(1)	0.017(1)	0.013(1)	0	0	0
Te(1)	0.019(1)	0.015(1)	0.013(1)	0	0	0
Te(2)	0.038(2)	0.023(1)	0.018(1)	0	0	0
Te(3)	0.043(2)	0.023(1)	0.017(1)	0	0	0
Te(4)	0.030(1)	0.026(1)	0.034(1)	0	0	0
Te(5)	0.036(2)	0.031(2)	0.021(2)	0	0	0
Ag(1)	0.041(2)	0.063(3)	0.034(2)	0	0	0
Ag(2)	0.065(3)	0.038(2)	0.034(2)	0	0	0
K(1)	0.043(5)	0.048(6)	0.021(4)	0	0	0
K(2)	0.040(4)	0.034(4)	0.029(4)	0	0	0
Ag(3)	0.040(4)	0.034(4)	0.029(4)	0	0	0

$K_{2.5}Ag_{4.5}La_2Te_9$

atom	U11	U22	U33	U12	U13	U23
La	0.005(1)	0.016(1)	0.007(1)	0	0	0
Te(1)	0.004(1)	0.014(1)	0.010(1)	0	0	0
Te(2)	0.018(1)	0.038(1)	0.008(1)	0	0	0
Te(3)	0.019(1)	0.032(1)	0.008(1)	0	0	0
Te(4)	0.011(1)	0.021(1)	0.035(2)	0	0	0
Te(5)	0.028(2)	0.034(2)	0.011(2)	0	0	0
Ag(1)	0.026(2)	0.044(2)	0.033(2)	0	0	0
Ag(2)	0.036(2)	0.036(2)	0.033(2)	0	0	0
K(1)	0.022(4)	0.025(4)	0.027(6)	0	0	0
K(2)	0.017(3)	0.027(3)	0.022(4)	0	0	0
Ag(3)	0.017(3)	0.027(3)	0.022(4)	0	0	0

Table 4.19   Selected Distances (Å) and Bond Angles (deg) for $K_{2.5}Ag_{4.5}Ce_2Te_9$ (IV) with Standard Deviations in Parentheses.

Bond Distances

Ce – Te1	3.270(3), 3.2963(9)	Ag2 – Te5	3.005(3)
Ce – Te2	3.376(2)	Ag1-Ag2	3.1806(4)
Ce – Te3	3.389(2)	K1 – Te2	3.722(7)
Te2 – Te3	3.1806(5)	K1 – Te3	3.709(7)
Ag1 – Te4	2.812(3)	K1 – Te4	3.505(4)
Ag1 – Te5	3.011(3)	K2 – Ag2	3.015(3)
Ag2 – Te4	2.818(3)	K2 – Te5	3.1806(5)

Bond Angles

Te1 – Ce –Te1	74.77(5) x 4	85.72(3) x 2	149.54(9) x 2
Te1 – Ce – Te2	75.20(4) x 4	130.40(5) x 4	138.38(4) x 2
Te1 – Ce – Te3	74.97(4) x 4	130.65(5) x 4	138.28(4) x 2
Te2 – Ce – Te3	56.09(4) x 4		
Te2 – Te3 – Te2	89.653(17) x 4	90.346(17) x 4	179.78(12) x 4
Te4 – Ag1 – Te4	105.78(16) x 1		
Te4 – Ag1 – Te5	113.55(3) x 4		
Te5 – Ag1 – Te5	97.05(11) x 1		
Te4 – Ag2 – Te4	106.32(16) x 1		
Te4 – Ag2 – Te5	113.52(3) x 4		
Te5 – Ag2 – Te5	96.53(11) x 1		
Te2 – K1 –Te3	50.68(10) x 4		
Te2 – K1 – Te4	86.79(7) x 4	136.40(14) x 4	
Te3 – K1 – Te3	74.39(17) x 1		
Te3 – K1 – Te4	87.01(7) x 4	136.16(14) x 4	
Te4 – K1 – Te4	79.55(11) x 2	80.13(11) x 2	130.3(3) x 2
Te5 – K2 – Te5	89.654(16) x 2	90.346(16) x 2	180.00 x 1

Table 4.20 Selected Distances (Å) and Bond Angles (deg) for $K_{2.5}Ag_{4.5}La_2Te_9$ (V) with Standard Deviations in Parentheses.

Bond Distances

La – Te1	3.295(3), 3.3109(9)	Ag2 – Te5	3.008(2)
La – Te2	3.414(2)	Ag1-Ag2	3.1938(4)
La – Te3	3.408(2)	K1 – Te2	3.638(7)
Te2 – Te3	3.1938(5)	K1 – Te3	3.689(7)
Ag1 – Te4	2.821(3)	K1 – Te4	3.496(4)
Ag1 – Te5	3.008(2)	K2 – Ag2	3.004(3)
Ag2 – Te4	2.821(3)	K2 – Te5	3.1938(4)

Bond Angles

Te1 – La –Te1	74.71(5) x 4	85.88(3) x 2	149.43(10) x 2
Te1 – La – Te2	75.23(4) x 4	130.53(5) x 4	138.52(4) x 2
Te1 – La – Te3	75.33(4) x 4	130.43(5) x 4	138.56(4) x 2
Te2 – La – Te3	55.83(4) x 4		
Te2 – Te3 – Te2	89.855(17) x 4	90.145(16) x 4	179.89(13) x 4
Te4 – Ag1 – Te4	106.47(16) x 1		
Te4 – Ag1 – Te5	113.33(3) x 4		
Te5 – Ag1 – Te5	97.17(11) x 1		
Te4 – Ag2 – Te4	106.13(16) x 1		
Te4 – Ag2 – Te5	113.34(3) x 4		
Te5 – Ag2 – Te5	97.48(11) x 1		
Te2 – K1 –Te3	51.35(11) x 4		
Te2 – K1 – Te4	85.79(8) x 4	135.79(15) x 4	
Te3 – K1 – Te3	75.61(18) x 1		
Te3 – K1 – Te4	85.70(8) x 4	135.88(15) x 4	
Te4 – K1 – Te4	80.35(11) x 2	80.60(11) x 2	132.0(3) x 2
Te5 – K2 – Te5	89.855(16) x 2	90.145(16) x 2	180.00 x 1

Transmission Electron Microscopy of $K_{2.5}Ag_{4.5}Ce_2Te_9$ (IV) – The $[CeTe_3^{0.5-}]$ layer in $K_{2.5}Ag_{4.5}Ce_2Te_9$ contains a square Te net that is fully occupied. The formal oxidation state on the Te atoms in this net, however, is –0.75. This value indicates that the Te net is electron deficient and therefore susceptible to distortion. To probe the existence of such a distortion, electron diffraction studies were performed on this material. Figure 4.12A shows a typical electron diffraction pattern for $K_{2.5}Ag_{4.5}Ce_2Te_9$ along the ab-plane which, indeed, shows evidence for a superstructure. A densitometric intensity scan obtained from the (hk0) reciprocal plane along the (h20) row of reflections is shown in Figure 4.12B. The reflections between the (020), (120), and (220) reflections are due to a 0.333a* superlattice, which corresponds to a 3 x a_{sub} (i.e. ~ 13.5 Å) lattice dimension. These supercell reflections also occur along the b* direction, at the same exact position, giving a commensurate "$3a_{sub}$ x $3b_{sub}$" supercell. However, as seen for $KCuCeTe_4$, it is possible that this supercell is an artifact caused by twinning of the crystals underneath the electron beam (rotated 90° with respect to one another) and the true supercell is that of a "$1a_{sub}$ x $3a_{sub}$". Long axial photographs were taken on the x-ray diffractometer for this compound and the results support this premise, showing supercell reflections along only one axis.

Figure 4.12   (A)   Selected   area   electron   diffraction   pattern   of $K_{2.5}Ag_{4.5}Ce_2Te_9$ with the electron beam perpendicular to the layers ([001] direction) showing a twinned $3a_{sub}$ x $3b_{sub}$ domain (i.e.; two $1a_{sub}$ x $3b_{sub}$ supercells that are rotated $90°$ with respect to one another and superimposed). (B) Densitometric intensity scan along the b^*-axis of the electron diffraction pattern of $K_{2.5}Ag_{4.5}Ce_2Te_9$ (Fig 4.11 A) (boxed area in photograph) showing the (h 2 0) family of reflections. The three reflections from the sublattice of $K_{2.5}Ag_{4.5}Ce_2Te_9$ are indexed. The four weak peaks are from the 1a x 3b superlattice.

166

Electron Diffraction of $K_{2.5}Ag_{4.5}Ce_2Te_9$

(A)

$b*$
$a*$

(B)

(020)

0.333a* (120)

0.333a*

(220)

Intensity (arb. units)

Reciprocal Angstroms
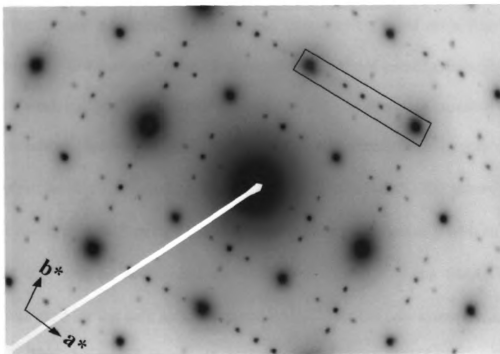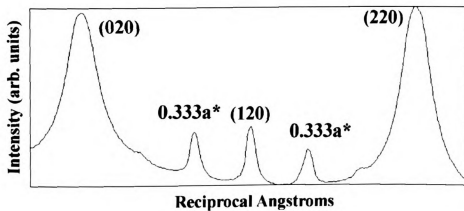
Superstructure Determination of $K_{2.5}Ag_{4.5}Ce_2Te_9$ *(IV)* - Because the "$1a_{sub} \times 3b_{sub}$" supercell of $K_{2.5}Ag_{4.5}Ce_2Te_9$ was commensurate, further attempts were made to collect enough crystallographic data to solve the superstructure and elucidate the Te net distortion. The original data was collected on a Rigaku AFC5 four-circle diffractometer, which unfortunately was not sensitive enough to detect such weak supercell reflections. Another crystal was therefore mounted on the more sensitive Siemens SMART Platform CCD diffractometer using graphite monochromatized Mo $K\alpha$ radiation. The data were collected over a full sphere of reciprocal space, up to 50° in 2θ. The individual frames were measured with an ω rotation of 0.3° and an acquisition times of 60 sec/frame. The SMART[22] software was used for the data acquisition and SAINT[23] for the data extraction and reduction. The absorption correction was performed using SADABS.[24] The structure was solved by direct methods using the SHELXTL[25] package of crystallographic programs.

From the matrix frames, three equivalent monoclinic-C supercells were found, depending on which axis was chosen as the unique axis:

Supercell choice #1	Supercell choice #2	Supercell choice #3
a = 53.31(1) Å	a = 51.05(1) Å	a = 14.129(3) Å
b = 4.5318(9) Å	b = 13.507(3) Å	b = 50.44(1) Å
c = 13.699(3) Å	c = 4.4800(9) Å	c = 4.4492(9) Å
α = 90°	α = 90°	α = 90°
β = 104.84(3)°	β = 94.91(3)	β = 108.37(3)°
γ = 90°	γ = 90°	γ = 90°

After attempting to solve the superstructure in all three cell choices, it was concluded that only one cell choice leads to a logical solution for the superstructure. Supercell choice #1, when applied, led to a crystallographic model which made no chemical sense. Many of the assigned atoms were extremely close to another and the thermal ellipsoids were either very small or very large. Supercell choice #2, when applied, managed to give a solution that made chemical sense. However, this superstructure solution was identical to that of the subcell. The Te net did not exhibit any sort of distortion and the potassium and silver cations were statistically disordered in the same exact fashion as in the subcell. In fact, there was no obvious reason why the unit cell needed to be as large as it was. Finally, when supercell choice #3 was applied, the structural model that was found not only made chemical sense, but possessed a distorted Te net. Below is a comparison of the subcell parameters to those of the correct supercell and the vectorial relationship between the two.

Subcell	Supercell
a = 4.4844(9) Å	a' = 14.130(3) Å
b = 4.5116(9) Å	b' = 50.441(10) Å
c = 50.859(10) Å	c' = 4.4492(9) Å
$\alpha = 90°$	$\alpha = 90°$
$\beta = 90°$	$\beta = 108.37(3)°$
$\gamma = 90°$	$\gamma = 90°$

Vectorial Relationship:

$$a' = -a + 3b \qquad b' = c \qquad c' = a$$

K;:

para

Tab

wer

plat

mer

in t

calc

dens

crys

the

is v

impr

mirr

Analogous data was collected for the isostructural compound, $K_{2.5}Ag_{4.5}La_2Te_9$ and the same results were found. Complete data collection parameters and details of both structure solutions and refinements are given in Tables 4.21.

Another complication, for both compounds, lies in the fact that the crystals were micro-twinned. The morphology of the crystals is that of very thin square plates. This combination allows the crystals to stack and twin very easily, in a merohedral fashion. The crystallographic reflections were therefore overlapping in their positions, leading to an observed electron density much higher than calculated. This results in a poor refinement and significant residual electron density in the Fourier map. Since it seemed impossible to find a truly "single" crystal, attempts were made to correct for this twinning by applying a twin law to the data. Several twin laws were tried, based on modeling how the "twinned" cell is vectorally related to the original cell.[34] The twin law that gave the best improvement on the refinement was one which the two cells are related by a mirror perpendicular to the ac plane:

$$\textbf{Twin Law:} \quad \begin{bmatrix} a' \\ b' \\ c' \end{bmatrix} = \begin{bmatrix} a \\ b \\ c \end{bmatrix} \begin{pmatrix} -1 & 0 & 2 \\ 0 & -1 & 0 \\ 0 & 0 & 1 \end{pmatrix}$$

By applying this twin law, the R factors (R/wR2) in the refinement dropped from

12.09/39.77 to 10.41/32.34. The Flack parameter was also refined, indicating that

42% of the crystal belonged to a fragment defined by this twin law.

Table 4.21   Crystallographic Data for the "1a x 3b" superstructures of $K_{2.5}Ag_{4.5}Ce_2Te_9$ (IV) and $K_{2.5}Ag_{4.5}La_2Te_9$ (V)

	$K_{2.5}Ag_{4.5}Ce_2Te_9$ supercell	$K_{2.5}Ag_{4.5}La_2Te_9$ supercell
crystal habit, color	plate, copper	plate, copper
Diffractometer	Siemens SMART Platform CCD	Siemens SMART Platform CCD
Radiation	Mo-Kα (0.71073Å)	Mo-Kα (0.71073Å)
Crystal Size, mm^3	0.31 x 0.22 x 0.04	0.44 x 0.13 x 0.02
Temperature, K	293	293
Crystal System	Monoclinic	Monoclinic
Space Group	C2/m (#12)	C2/m (#12)
a, Å	14.130(3)	14.431(3)
b, Å	50.441(10)	50.728(10)
c, Å	4.4492(9)	4.5186(9)
β, °	108.37(3)	108.42(3)
V, Å^3	3009.4(10)	3118.7(11)
Z	6	6
μ, mm^{-1}	22.192	21.129
index ranges	$-18 \leq h \leq 18$	$-13 \leq h \leq 18$
	$-65 \leq k \leq 65$	$-65 \leq k \leq 64$
	$-5 \leq l \leq 5$	$-6 \leq l \leq 5$
$2\theta_{max}$, deg	50	50
sec/frame	60	80
total data	11986	9925
unique data	3544	3711
R(int)	0.0842	0.1585
no. parameters	136	136
final R1/wR2[a], %	10.41/32.34	9.84/29.29
GooF	1.076	1.039

[a]$R1 = \Sigma(|F_o| - |F_c|)/\Sigma|F_o|$ $wR2 = \{\Sigma[w(F_o^2 - F_c^2)^2]/\Sigma[w(F_o^2)^2]\}^{1/2}$

Superstructure Description of $K_{2.5}Ag_{4.5}Ce_2Te_9$ (IV) – The superstructure as seen down the c-axis is shown in Figure 4.13. Within the $[K_{1.5}Ag_{4.5}Te_3]$ layer, the disorder between the potassium and silver is now partially resolved, see Figure 4.14A. While one of the crystallographic sites is now fully assigned as silver, the other site retains a 50/50 disorder between K and Ag. The arrangement of the cations across the layer is now periodic in that every third cation is Ag. From this, it is understandable why the supercell is that of a "$1a_{sub}$ x $3b_{sub}$". Within the $[CeTe_3^{0.5-}]$ layer, the Te net is now distorted (as expected). A fragment of this layer is shown in Figure 4.14B and comparison between the Te net in the substructure and superstructure is shown in Figure 4.15. The net is still fully occupied, but now the Te atoms have oligomerized into infinite zig-zag chains. The Te-Te distances range from 2.922(3) – 3.0509(17) Å within the chain and 3.2627-3.3687Å between the chains. The fractional atomic coordinates, isotropic and anisotropic temperature factors, bond distances, and bond angles for both compounds is given in Tables 22-27.
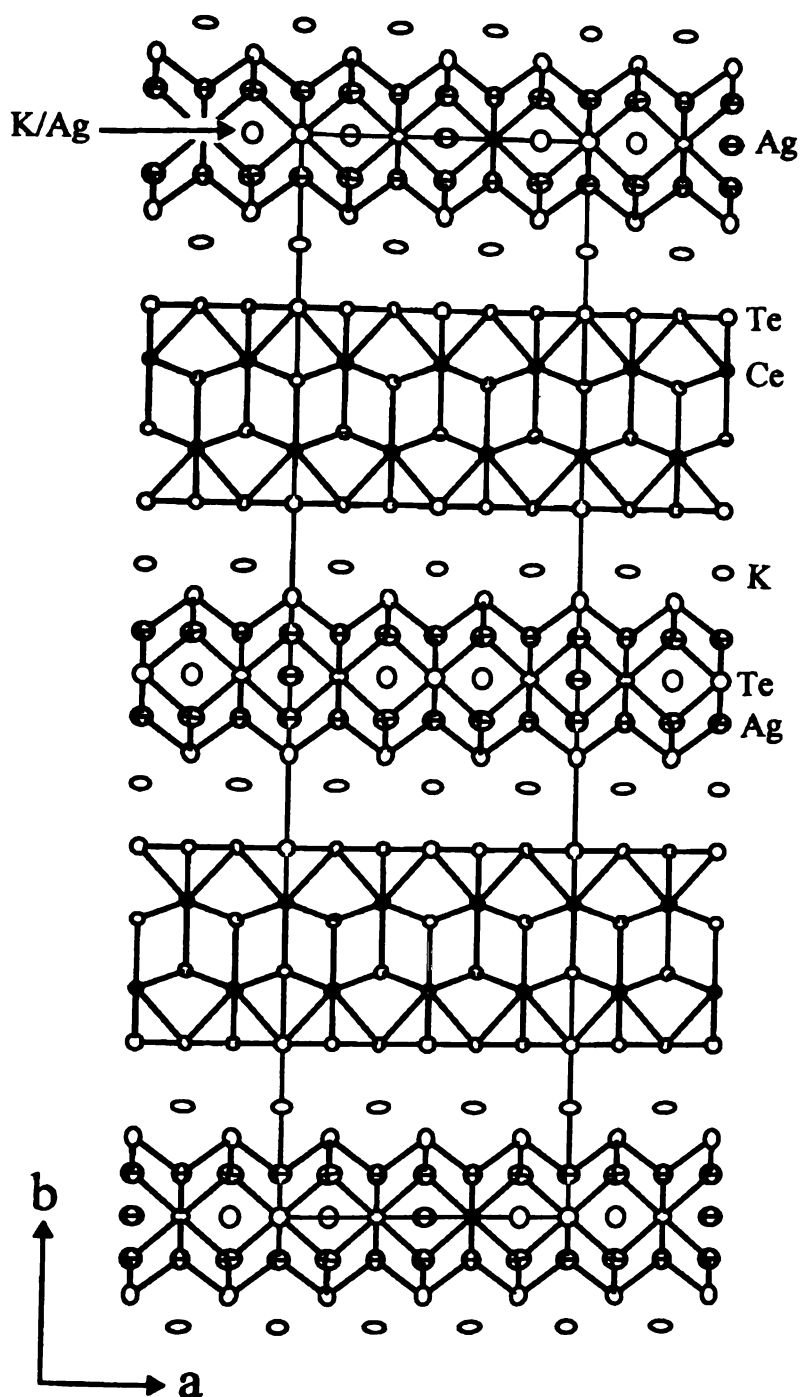
Figure 4.13 ORTEP representation of the "$1a_{sub} \times 3b_{sub}$" superstructure of $K_{2.5}Ag_{4.5}Ce_2Te_9$ as seen down the b-axis (75% probability ellipsoids). The ellipses with octant shading represent Ce, the crossed ellipses represent Ag, the large open ellipses represent K and Te.
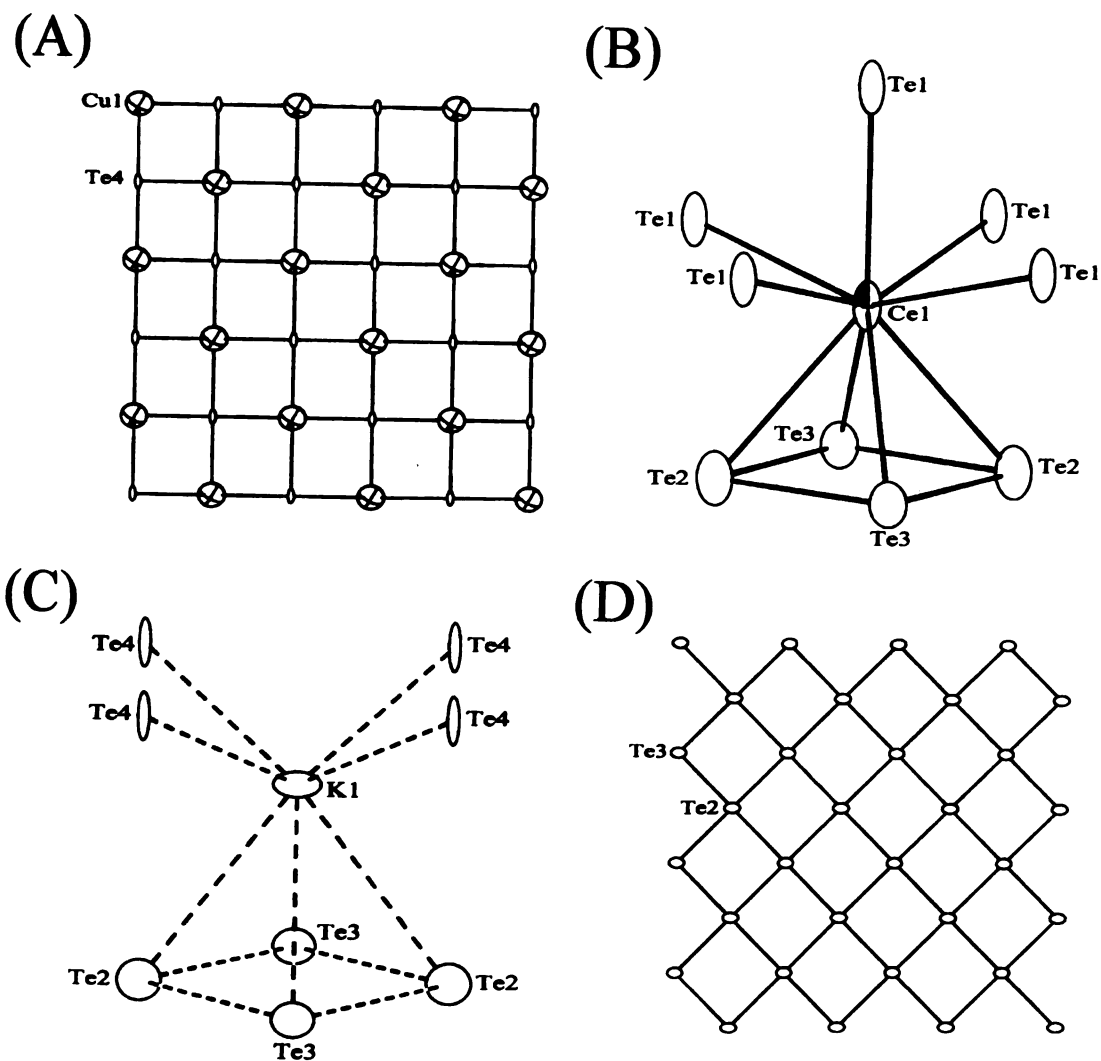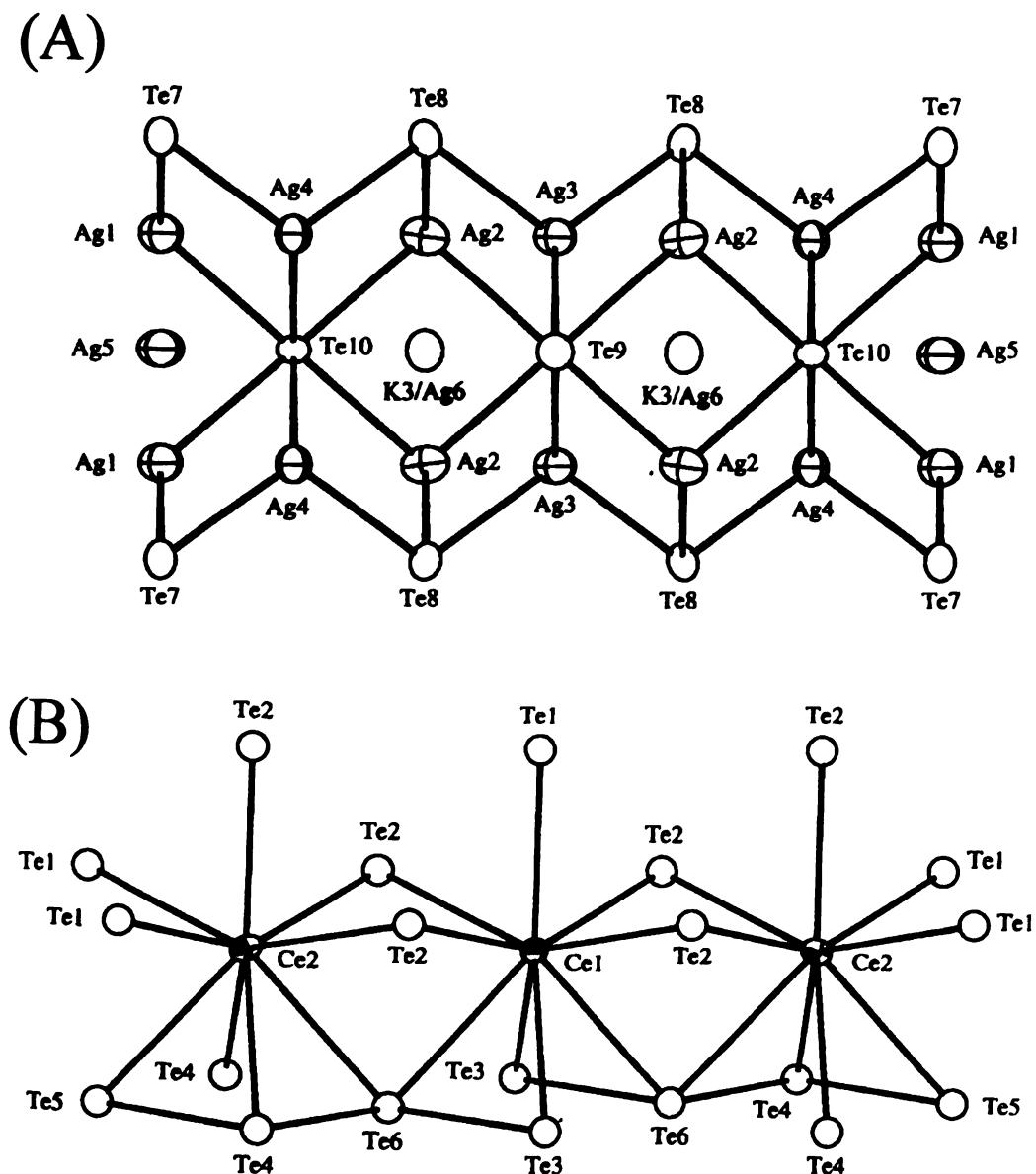
Figure 4.14 ORTEP representation (50% probability ellipsoids) of (A) The $[K_{1.5}Ag_{4.5}Te_3]$ layer of the $1a_{sub} \times 3b_{sub}$ superstructure of $K_{2.5}Ag_{4.5}Ce_2Te_9$, and (B) a fragment of the $[CeTe_3^{0.5-}]$ layer of the $1a_{sub} \times 3b_{sub}$ superstructure of $K_{2.5}Ag_{4.5}Ce_2Te_9$ highlighting the particular coordination environment of Ce. The ellipses with octant shading represent Ce, the crossed ellipses represent Ag, and the large open ellipses represent K and Te.

175

(A)

Te6   Te5   Te4   Te3

(B)

Te6

Te4

b

a

distort

c

a
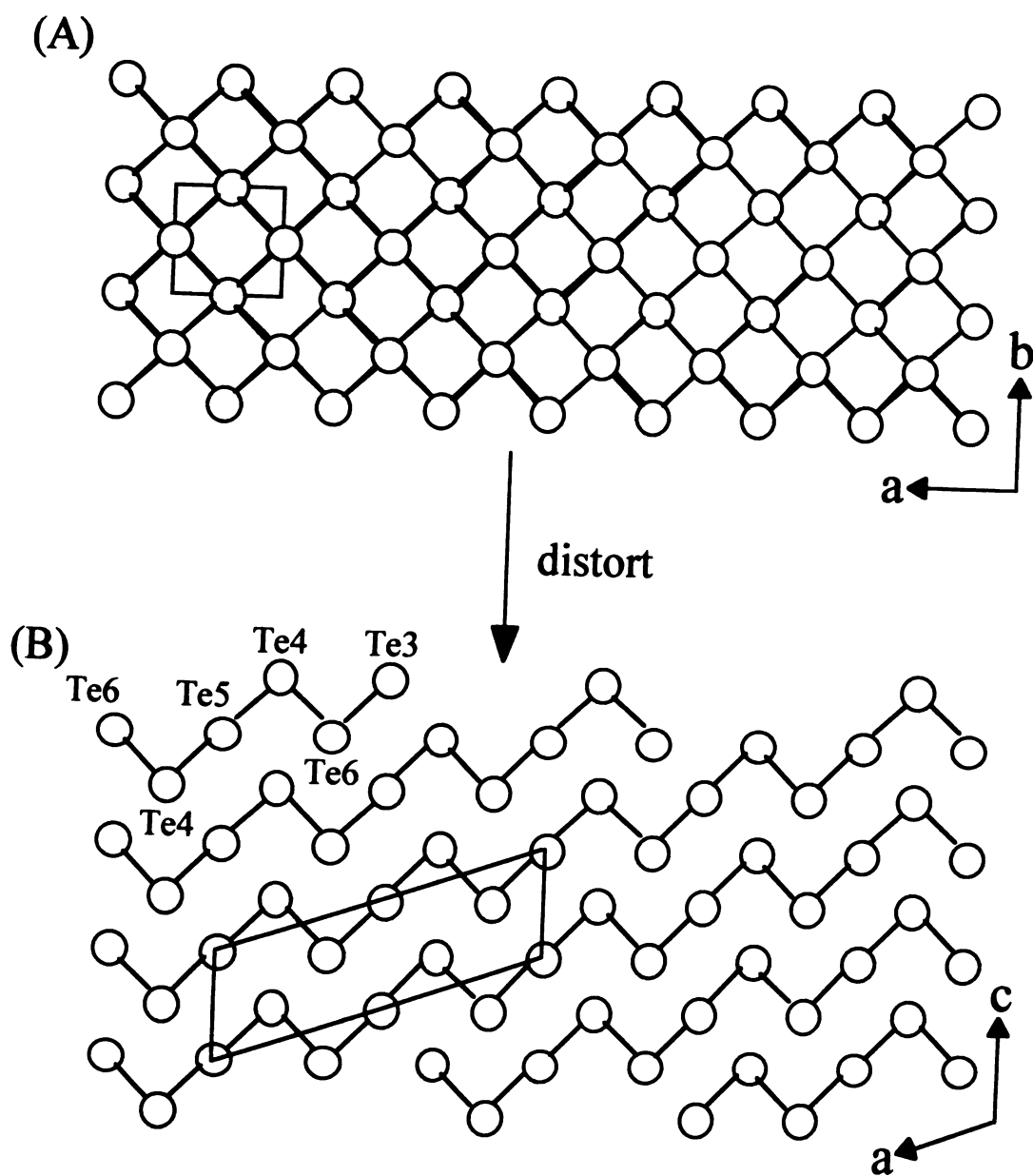
Figure 4.15   View of the Te "nets" in (A) the substructure of $K_{2.5}Ag_{4.5}Ce_2Te_9$ and (B) the $1a_{sub} \times 3b_{sub}$ superstructure of $K_{2.5}Ag_{4.5}Ce_2Te_9$.

176

Table 4.22 Fractional Atomic Coordinates and Equivalent Isotropic Displacement Parameters (U_{eq}) for the "$1a_{sub}$ x $3b_{sub}$" superstructure of $K_{2.5}Ag_{4.5}Ce_2Te_9$ (IV) with Estimated Standard Deviations in Parentheses.

atom	x	y	z	occupancy	U_{eq}^a, Å^2
Ce(1)	0.5	0.2094(1)	0.5	1.0	1.9(1)
Ce(2)	0.3333(1)	0.2906(1)	0.8217(3)	1.0	1.8(1)
Te(1)	0.5	0.2734(1)	0.5	1.0	1.6(1)
Te(2)	0.3334(1)	0.2264(1)	0.8340(3)	1.0	1.8(1)
Te(3)	0.5	0.1597(1)	0.0	1.0	2.5(1)
Te(4)	0.3329(1)	0.3404(1)	0.2981(4)	1.0	2.2(1)
Te(5)	0.5	0.3406(1)	0.0	1.0	3.0(1)
Te(6)	0.3329(1)	0.1595(1)	0.2941(4)	1.0	2.1(1)
Te(7)	0.0	0.5724(1)	-0.5	1.0	3.3(1)
Te(8)	0.3332(1)	0.4275(1)	0.8372(3)	1.0	3.0(1)
Te(9)	0.5	0.5	0.5	1.0	3.2(1)
Te(10)	0.1667(2)	0.5	0.1723(5)	1.0	2.9(1)
Ag(1)	0.0	0.5392(1)	0.0	1.0	5.0(1)
Ag(2)	0.3330(2)	0.4608(1)	0.3382(5)	1.0	4.7(1)
Ag(3)	0.5	0.4606(1)	0.0	1.0	4.8(1)
Ag(4)	-0.1664(2)	0.5393(1)	-0.6742(5)	1.0	4.7(1)
Ag(5)	0.0	0.5	-0.5	1.0	6.1(2)
K(1)	0.5	0.3986(2)	0.50	1.0	3.5(2)
K(2)	-0.1666(5)	0.6014(1)	-0.1800(13)	1.0	4.7(2)
K(3)	0.3324(4)	0.5	0.8389(9)	0.50(2)	4.4(2)
Ag(6)	0.3324(4)	0.5	0.8389(9)	0.50(2)	4.4(2)

^{a}Ueq is defined as one third of the trace of the orthogonalized U_{ij} tensor

Table 4.23 Fractional Atomic Coordinates and Equivalent Isotropic Displacement Parameters (U_{eq}) for the "$1a_{sub}$ x $3b_{sub}$" superstructure of $K_{2.5}Ag_{4.5}La_2Te_9$ (V) with Estimated Standard Deviations in Parentheses.

atom	x	y	z	occupancy	U_{eq}^a, Å^2
La(1)	0.5	0.2093(1)	0.5	1.0	1.1(1)
La(2)	0.3331(1)	0.2914(1)	0.8232(3)	1.0	1.3(1)
Te(1)	0.5	0.2742(1)	0.5	1.0	1.2(1)
Te(2)	0.3332(1)	0.2262(1)	0.8340(3)	1.0	1.2(1)
Te(3)	0.5	0.1586(1)	0.0	1.0	3.1(1)
Te(4)	0.3324(1)	0.3417(1)	0.2997(5)	1.0	1.3(1)
Te(5)	0.5	0.3423(1)	0.0	1.0	3.6(1)
Te(6)	0.3335(1)	0.1585(1)	0.2986(5)	1.0	1.2(1)
Te(7)	0.0	0.5736(1)	-0.5	1.0	2.0(1)
Te(8)	0.3328(1)	0.4273(1)	0.8377(4)	1.0	2.8(1)
Te(9)	0.5	0.5	0.5	1.0	3.2(1)
Te(10)	0.1648(2)	0.5	0.1710(6)	1.0	2.4(1)
Ag(1)	0.0	0.5404(1)	0.0	1.0	2.8(1)
Ag(2)	0.3302(2)	0.4613(1)	0.3381(6)	1.0	3.8(1)
Ag(3)	0.5	0.4611(1)	0.0	1.0	4.2(1)
Ag(4)	-0.1642(2)	0.5395(1)	-0.6727(6)	1.0	3.3(1)
Ag(5)	0.0	0.5	-0.5	1.0	4.4(2)
K(1)	0.5	0.4003(2)	0.5	1.0	2.4(2)
K(2)	-0.1680(5)	0.6008(1)	-0.1788(12)	1.0	2.4(2)
K(3)	0.3298(3)	0.5	0.8345(12)	0.53(2)	2.6(2)
Ag(6)	0.3298(3)	0.5	0.8345(12)	0.47(2)	2.6(2)

^{a}Ueq is defined as one third of the trace of the orthogonalized U_{ij} tensor

Table 4.24 Anisotropic Displacement Parameters (Å) for the "$1a_{sub}$ x $3b_{sub}$" superstructure of $K_{2.5}Ag_{4.5}Ce_2Te_9$ (IV) with Standard Deviations in Parentheses.

atom	U11	U22	U33	U12	U13	U23
Ce(1)	0.020(1)	0.016(1)	0.024(2)	0	13(1)	0
Ce(2)	0.026(1)	0.019(1)	0.014(1)	1(1)	13(1)	4(1)
Te(1)	0.022(1)	0.017(1)	0.012(1)	0	10(1)	0
Te(2)	0.022(1)	0.020(1)	0.015(1)	2(1)	10(1)	3(1)
Te(3)	0.047(2)	0.025(1)	0.003(2)	0	7(1)	0
Te(4)	0.021(1)	0.022(1)	0.026(2)	2(1)	10(1)	0
Te(5)	0.062(2)	0.023(1)	0.002(2)	0	5(1)	0
Te(6)	0.018(1)	0.023(1)	0.026(1)	4(1)	10(1)	4(1)
Te(7)	0.028(1)	0.044(2)	0.022(2)	0	0(2)	0
Te(8)	0.031(1)	0.042(1)	0.013(1)	-1(1)	1(2)	5(1)
Te(9)	0.041(2)	0.040(2)	0.007(2)	0	-2(2)	0
Te(10)	0.031(1)	0.023(1)	0.024(2)	0	-4(2)	0
Ag(1)	0.051(2)	0.046(2)	0.039(3)	0	-3(2)	0
Ag(2)	0.067(2)	0.044(2)	0.019(2)	-1(1)	-1(2)	5(1)
Ag(3)	0.052(2)	0.041(2)	0.037(2)	0	-5(2)	0
Ag(4)	0.036(2)	0.044(2)	0.047(2)	0	-6(2)	0
Ag(5)	0.062(4)	0.041(3)	0.061(5)	0	-8(4)	0
K(1)	0.051(5)	0.014(3)	0.028(5)	0	-6(5)	0
K(2)	0.066(5)	0.015(3)	0.041(5)	-6(2)	-10(6)	4(2)
K(3)	0.044(4)	0.055(4)	0.017(3)	0	-14(3)	0
Ag(6)	0.044(4)	0.055(4)	0.017(3)	0	-14(3)	0

Table 4.25 Anisotropic Displacement Parameters (Å) for the "$1a_{sub}$ x $3b_{sub}$" superstructure of $K_{2.5}Ag_{4.5}La_2Te_9$ (V) with Standard Deviations in Parentheses.

atom	U11	U22	U33	U12	U13	U23
La(1)	0.012(1)	0.003(1)	0.028(2)	0	20(1)	0
La(2)	0.015(1)	0.004(1)	0.030(1)	1(1)	21(1)	2(1)
Te(1)	0.012(1)	0.005(1)	0.026(2)	0	16(1)	0
Te(2)	0.012(1)	0.005(1)	0.026(1)	-1(1)	16(1)	2(1)
Te(3)	0.061(2)	0.003(1)	0.033(3)	0	22(2)	0
Te(4)	0.012(1)	0.006(1)	0.027(1)	1(1)	16(1)	0
Te(5)	0.059(2)	0.004(1)	0.041(2)	0	9(2)	0
Te(6)	0.012(1)	0.006(1)	0.026(1)	4(1)	17(1)	1(1)
Te(7)	0.019(1)	0.014(1)	0.034(2)	0	21(2)	0
Te(8)	0.021(1)	0.033(1)	0.040(2)	-3(1)	25(2)	1(1)
Te(9)	0.044(2)	0.009(2)	0.049(4)	0	23(2)	0
Te(10)	0.028(1)	0.007(1)	0.043(2)	0	22(2)	0
Ag(1)	0.041(2)	0.016(2)	0.024(3)	0	8(2)	0
Ag(2)	0.040(2)	0.037(2)	0.031(2)	-3(1)	2(2)	-2(1)
Ag(3)	0.037(2)	0.041(2)	0.041(4)	0	4(3)	0
Ag(4)	0.029(1)	0.026(1)	0.042(2)	-5(1)	11(2)	-9(1)
Ag(5)	0.055(3)	0.031(3)	0.059(6)	0	39(4)	0
K(1)	0.018(4)	0.025(5)	0.013(5)	0	-20(4)	0
K(2)	0.031(3)	0.012(3)	0.010(2)	2(2)	-20(6)	6(2)
K(3)	0.025(3)	0.016(3)	0.049(5)	0	27(3)	0
Ag(6)	0.025(3)	0.016(3)	0.049(5)	0	27(3)	0

Table 4.26 Selected Distances (Å) and Bond Angles (deg) for the "$1a_{sub}$ x $3b_{sub}$" superstructure of $K_{2.5}Ag_{4.5}Ce_2Te_9$ (IV) with Standard Deviations in Parentheses.

Bond Distances

Ce1 – Te1	3.226(3)			
Ce1 – Te2	3.2370(14), 3.2644(18)	Ag4 – Te7	2.786(3)	
	3.2693(15), 3.3063(18)	Ag4 – Te8	2.794(3)	
Ce1 – Te3	3.353(2)	Ag4 – Te10	2.974(3), 2.989(3)	
Ce1 – Te6	3.377(2)	Ag1 – Ag4	3.126(3). 3.175(2)	
Ce2 – Te1	3.2370(14), 3.3062(18)	Ag2 – Ag3	3.140(2), 3.173(3)	
Ce2 – Te2	3.234(2), 3.240(2)	Ag2 – Ag4	3.145(3), 3.162(4)	
	3.3014(18)	K1 – Te4	3.696(6)	
Ce2 – Te4	3.286(2), 3.422(2)	K1 – Te5	3.675(6)	
Ce2 – Te5	3.368(3)	K1 – Te8	3.464(4), 3.487(4)	
Ce2 – Te6	3.369(2)	K2 – Te3	3.694(7)	
Te3 – Te6	3.0391(18)	K2 – Te4	3.696(6)	
Te4 – Te5	3.0509(17)	K2 – Te6	3.612(6), 3.748(7)	
Te4 – Te6	2.922(3)	K 2 – Te7	3.437(7), 3.512(6)	
Ag1 – Te7	2.784(3)	K2 – Te8	3.446(6), 3.500(8)	
Ag1 – Te10	2.986(3)	Ag5 – Ag1	2.977(3)	
Ag2 – Te8	2.784(3). 2.793(3)	Ag5 – Te10	3.137(2)	
Ag2 – Te9	2.987(3)	K3/Ag6 –Ag2	2.972(4)	
Ag2 – Te10	2.980(3)	K3/Ag6 –Te9	3.141(4)	
Ag3 – Te8	2.793(3)	K3/Ag6 –Te10	3.142(6)	
Ag3 – Te9	2.982(3)			

Table 4.26 continued Selected Distances (Å) and Bond Angles (deg) for the "$1a_{sub} \times 3b_{sub}$" superstructure of $K_{2.5}Ag_{4.5}Ce_2Te_9$ (IV) with Standard Deviations in Parentheses.

Bond Angles

Te1 – Ce1 –Te2	74.84(4)	Te9 – Ag2 – Te10	96.99(10)
Te1 – Ce1 – Te3	138.43(4)	Te8 – Ag3 – Te8	106.45(16)
Te1 – Ce1 – Te6	138.28(4)	Te8 – Ag3 – Te9	113.81(4)
Te2 – Ce1 – Te2	85.85(4), 149.69(8)	Te9 – Ag3 – Te9	96.47(12)
Te2 – Ce1 – Te3	75.20(4), 130.37(5)	Te7 – Ag4 – Te8	106.38(13)
Te2 – Ce1 – Te6	72.94(5), 127.88(5)	Te7 – Ag4 – Te10	114.22(10)
Te3 – Ce1 – Te3	83.13(8)	Te8 – Ag4 – Te10	113.78(9)
Te3 – Ce1 – Te6	53.69(5)	Te10 – Ag4 – Te10	96.53(9)
Te6 – Ce1 – Te6	83.44(7)	Te4 – K1 – Te4	74.84(15)
Te1 – Ce2 – Te2	75.09(5), 149.3(7)	Te4 – K1 – Te5	52.63(10)
Te1 – Ce2 – Te4	75.94(5), 131.42(6)	Te5 – K1 – Te5	74.50(15)
Te1 – Ce2 – Te5	74.75(5)	Te5 – K1 – Te8	86.77(7), 136.24(12)
Te1 – Ce2 – Te6	126.69(6),134.59(6)	Te8 – K1 – Te8	79.59(10), 130.2(2)
Te2 – Ce2 – Te2	74.26(5), 85.80(5)	Te3 – K2 – Te4	74.38(12)
Te2 – Ce2 – Te4	74.70(5), 138.82(5)	Te3 – K2 – Te6	49.14(8)
Te2 – Ce2 – Te5	129.29(5) , 138.34(6)	Te3 – K2 – Te7	87.46(17)
Te2 – Ce2 – Te6	77.66(6), 138.27(6)	Te3 – K2 – Te8	137.61(19)
Te4 – Ce2 – Te4	83.07(6)	Te4 – K2 – Te6	47.13(9)
Te4 – Ce2 – Te5	54.56(4)	Te4 – K2 – Te7	132.59(7)
Te4 – Ce2 – Te6	52.08(6), 59.78(5)	Te4 – K2 – Te8	88.93(15)
Te5 – Ce2 – Te6	83.06(6)	Te6 – K2 – Te6	74.37(12)
Te7 – Ag1 – Te7	106.06(17)	Te6 – K2 – Te7	87.62(13), 135.6(2)
Te7 – Ag1 – Te10	113.90(5)	Te6 – K2 – Te8	87.55(15), 135.4(2)
Te10 – Ag1 – Te10	96.99(14)	Te7 – K2 – Te7	79.61(14)
Te8 – Ag2 – Te8	105.84(13)	Te7 – K2 – Te8	80.96(13), 130.3(2)
Te8 – Ag2 – Te9	113.92(8)	Te8 – K2 – Te8	79.66(15)
Te8 – Ag2 – Te10	113.61(10)	Te6 – Te4 – Te5	95.79(7)

Table 4.27 Selected Distances (Å) and Bond Angles (deg) for the "$1a_{sub}$ x $3b_{sub}$" superstructure of $K_{2.5}Ag_{4.5}La_2Te_9$ (IV) with Standard Deviations in Parentheses.

Bond Distances

La1 – Te1	3.293(3)			
La1 – Te2	3.293(3), 3.312(2)		Ag4 – Te7	2.824(3)
	3.204(15)		Ag4 – Te8	2.845(4)
La1 – Te3	3.422(3)		Ag4 – Te10	3.013(3), 3.029(3)
La1 – Te6	3.436(2)		Ag1 – Ag4	3.151(2). 3.203(3)
La2 – Te1	3.2916(14), 3.349(2)		Ag2 – Ag3	3.205(3), 3.258(3)
La2 – Te2	3.291(2), 3.306(2)		Ag2 – Ag4	3.192(4), 3.199(3)
	3.3487(18)		K1 – Te4	3.696(6), 3.747(8)
La2 – Te4	3.343(2), 3.479(2)		K1 – Te5	3.709(8)
La2 – Te5	3.438(3)		K1 – Te8	3.471(4), 3.503(4)
La2 – Te6	3.414(2)		K2 – Te3	3.718(7)
Te3 – Te6	3.0910(17)		K2 – Te4	3.680(6)
Te4 – Te5	3.1100(17)		K2 – Te6	3.630(6), 3.763(6)
Te4 – Te6	2.984(3)		K 2 – Te7	3.467(6), 3.528(6)
Ag1 – Te7	2.818(3)		K2 – Te8	3.469(6), 3.507(7)
Ag1 – Te10	3.038(3)		Ag5 – Ag1	3.050(2)
Ag2 – Te8	2.831(4). 2.852(3)		Ag5 – Te10	3.165(2)
Ag2 – Te9	3.033(3)		K3/Ag6 –Ag2	2.983(4), 3.005(5)
Ag2 – Te10	2.987(4)		K3/Ag6 –Te9	3.219(5), 3.252(4)
Ag3 – Te8	2.848(4)		K3/Ag6 –Te10	3.179(6), 3.191(4)
Ag3 – Te9	3.001(3)			

Table 4.27 continued   Selected Distances (Å) and Bond Angles (deg) for the "$1a_{sub} \times 3b_{sub}$" superstructure of $K_{2.5}Ag_{4.5}La_2Te_9$ (IV) with Standard Deviations in Parentheses.

Bond Angles

Te1 – La1 –Te2	74.95(4)	Te9 – Ag2 – Te10	98.50(10)
Te1 – La1 – Te3	138.68(4)	Te8 – Ag3 – Te8	106.06(17)
Te1 – La1 – Te6	138.64(4)	Te8 – Ag3 – Te9	113.72(5)
Te2 – La1 – Te2	85.89(4), 149.90(9)	Te9 – Ag3 – Te9	97.69(13)
Te2 – La1 – Te3	75.28(4), 130.10(5)	Te7 – Ag4 – Te8	106.02(12)
Te2 – La1 – Te6	73.28(5), 132.65(6)	Te7 – Ag4 – Te10	114.79(9)
Te3 – La1 – Te3	82.64(7)	Te8 – Ag4 – Te10	113.33(11)
Te3 – La1 – Te6	53.58(4)	Te10 – Ag4 – Te10	96.80(9)
Te6 – La 1 – Te6	82.72(7)	Te4 – K1 – Te4	75.17(18)
Te1 – La 2 – Te2	75.21(5), 149.13(7)	Te4 – K1 – Te5	52.78(12)
Te1 – La 2 – Te4	75.97(6), 129.72(6)	Te5 – K1 – Te5	75.05(18)
Te1 – La 2 – Te5	74.88(5)	Te5 – K1 – Te8	85.49(8), 134.87(15)
Te1 – La2 – Te6	127.10(6), 134.11(6)	Te8 – K1 – Te8	80.75(11), 133.4(3)
Te2 – La2 – Te2	74.29(5), 85.78(5)	Te3 – K2 – Te4	75.41(12)
Te2 – La2 – Te4	76.03(5), 138.99(6)	Te3 – K2 – Te6	49.74(9)
Te2 – La2 – Te5	129.65(5), 138.61(6)	Te3 – K2 – Te7	84.38(13)
Te2 – La2 – Te6	73.10(5), 138.13(6)	Te3 – K2 – Te8	136.85(17)
Te4 – La 2 – Te4	82.94(5)	Te4 – K2 – Te6	48.18(9)
Te4 – La 2 – Te5	57.25(5)	Te4 – K2 – Te7	131.94(17)
Te4 – La2 – Te6	52.40(6), 59.45(5)	Te4 – K2 – Te8	88.13(14)
Te5 – La2 – Te6	83.01(6)	Te6 – K2 – Te6	75.34(12)
Te7 – Ag1 – Te7	106.58(14)	Te6 – K2 – Te7	84.49(14), 135.39(19)
Te7 – Ag1 – Te10	114.20(5)	Te6 – K2 – Te8	86.83(14), 135.70(18)
Te10 – Ag1 – Te10	95.15(12)	Te7 – K2 – Te7	80.47(13)
Te8 – Ag2 – Te8	105.33(14)	Te7 – K2 – Te8	81.50(13), 132.5(2)
Te8 – Ag2 – Te9	113.24(10)	Te8 – K2 – Te8	80.73(14)
Te8 – Ag2 – Te10	113.90(11)	Te6 – Te4 – Te5	96.27(8)

Magnetic Susceptibility and Infrared Spectroscopy of $K_{2.5}Ag_{4.5}Ce_2Te_9$ (IV)

The magnetic susceptibility of $K_{2.5}Ag_{4.5}Ce_2Te_9$ was measured over the range 5-300K at 6000G. A plot of $1/\chi_M$ vs T shows that the material follows Curie-Weiss Law with only slight deviation from linearity beginning below 50K, see Figure 4.16A Such deviation has been reported for several Ce^{3+} compounds and has been attributed to crystal field splitting of the cation's $^2F_{5/2}$ ground state.[32] The data was further corrected for Pauli paramagnetism by applying a χ_{TIP} value of 0.0005 emu/mol. A straight line curve fit to the data above 60K gives a μ_{eff} of 2.63 μ_B, which is in accordance with the usual range for Ce^{3+} compounds (2.3-2.5 μ_B). The Weiss constants, θ, was calculated to be $-31K$, suggesting a certain amount of antiferromagnetic ordering. The diffuse reflectance optical spectra was taken in the Mid-IR region for $K_{2.5}Ag_{4.5}Ce_2Te_9$, see Figure 4.16B. Since the Te net in this compound is clearly distorted, the expected behavior is that of a semiconductor. Indeed, that is what is observed; an abrupt optical gap is observed at 0.26 eV, which can loosely be characterized as its bandgap. An analogous spectrum for $K_{2.5}Ag_{4.5}La_2Te_9$ (not shown here) was obtained which conversely indicates that this material is either a semimetal or a metal. A small optical gap is observed around 0.05-0.07eV. However, the spectroscopic data are unreliable in this region.
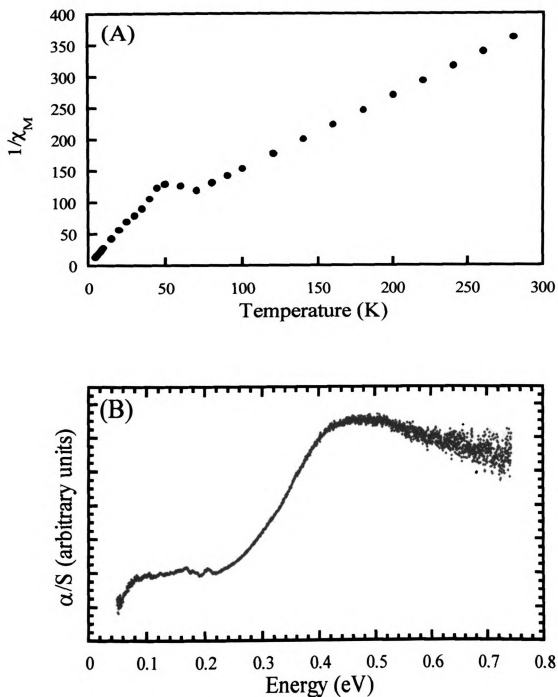
Figure 4.16. (A) Inverse molar magnetic susceptibility ($1/\chi_M$) plotted against temperature (2-300K) for $K_{2.5}Ag_{4.5}Ce_2Te_9$. (B) Diffuse reflectance optical spectra of $K_{2.5}Ag_{4.5}Ce_2Te_9$ (in the Mid-IR region).

Ele

mat

IR

con

both

and

vah

cry:

sup

bou

not

min

and

mar

La

con

wh,

of t

to

citj

Charge Transport Measurements of $K_{2.5}Ag_{4.5}Ln_2Te_9$ (Ln = Ce, La) (IV, V)

Electrical conductivity and thermopower measurements were made on both materials. The data agree with the semiconducting behavior indicated by the Mid-IR diffuse reflectance measurements; the electrical conductivity for both compounds decreases with decreasing temperature. Measurements were made on both a room-temperature pressed pellet and a single crystal of the cerium analog and the results are shown in Figure 4.17A. The room temperature conductivity values are not far apart, ranging from ~13 S/cm for the pellet and ~29 S/cm for the crystal. In a normal polycrystalline pressed pellet, the conductivity values can be suppressed to as little as $1/100^{th}$ of the actual values due to the existence of grain boundaries. However, the pellet used here was a compact of small crystals and not of a polycrystalline powder. Therefore, the number of grain boundaries are minimized. The thermopower data for the cerium analog is shown in Figure 4.17B and gives a room temperature Seebeck coefficient of ~130 µV/K. Therefore, the material is best described as a p-type semiconductor.

Analogous data was collected for a room temperature pressed pellet of the La analog and the results are shown in Figure 4.18. The room temperature conductivity values for the two pellets were 0.3 and 14 S/cm. This is in range with what was observed for the Ce analog. The thermopower data for a pressed pellet of the La analog is shown in Figure 4.18B. While the magnitudes are very similar to that of the cerium analog (~170 mV/K at 300K), the slopes are somewhat different. For the lanthanum analog, there is a reproducible convex dip in the data

arou

yet u

around 170K which does not exist for the cerium analog. The origin of this dip is yet unknown.
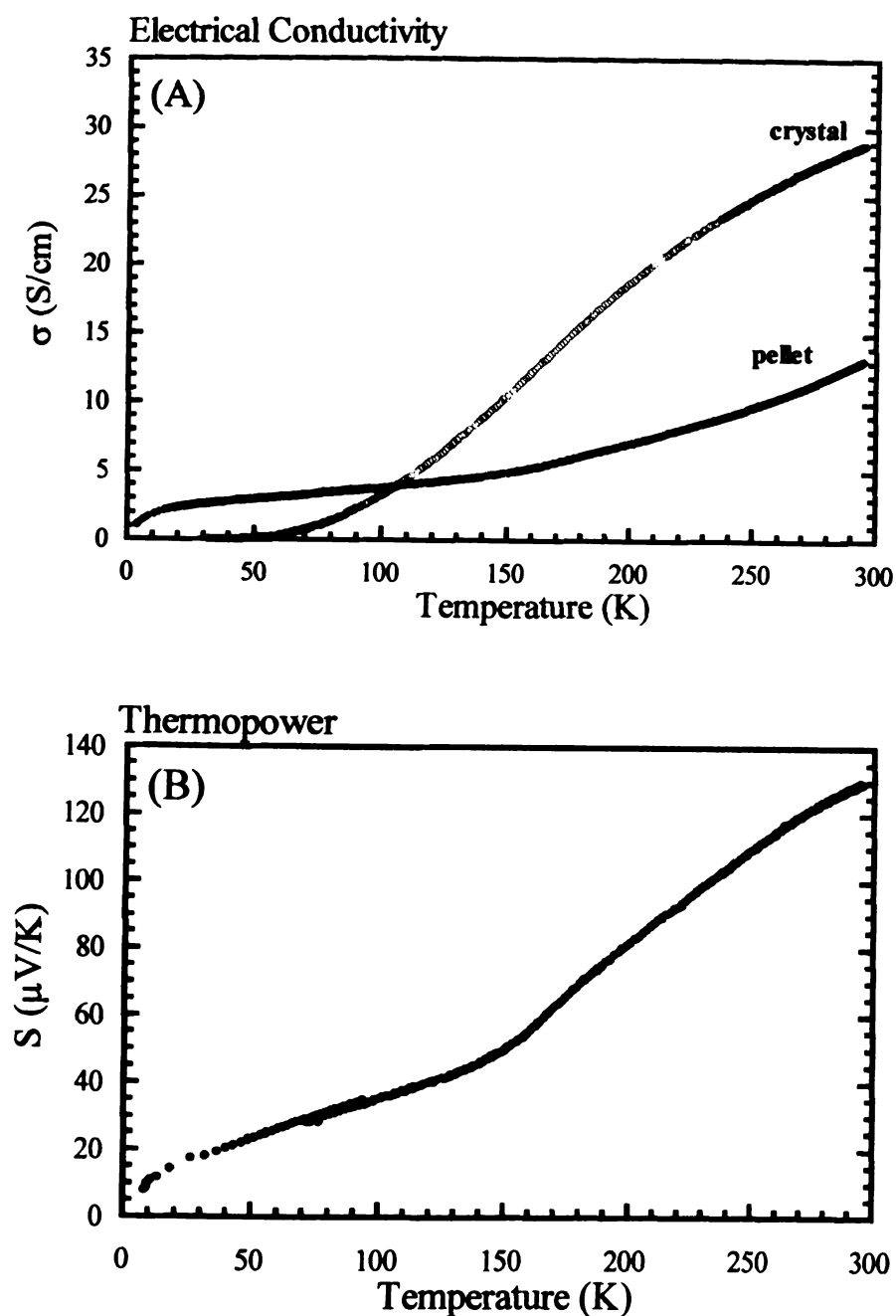
Figure 4.17 (A) Four-probe electrical conductivity data of both a room temperature pressed pellet and crystal of $K_{2.5}Ag_{4.5}Ce_2Te_9$ as a function of temperature. (B) Thermopower data of a crystal of $K_{2.5}Ag_{4.5}Ce_2Te_9$ as a function of temperature.
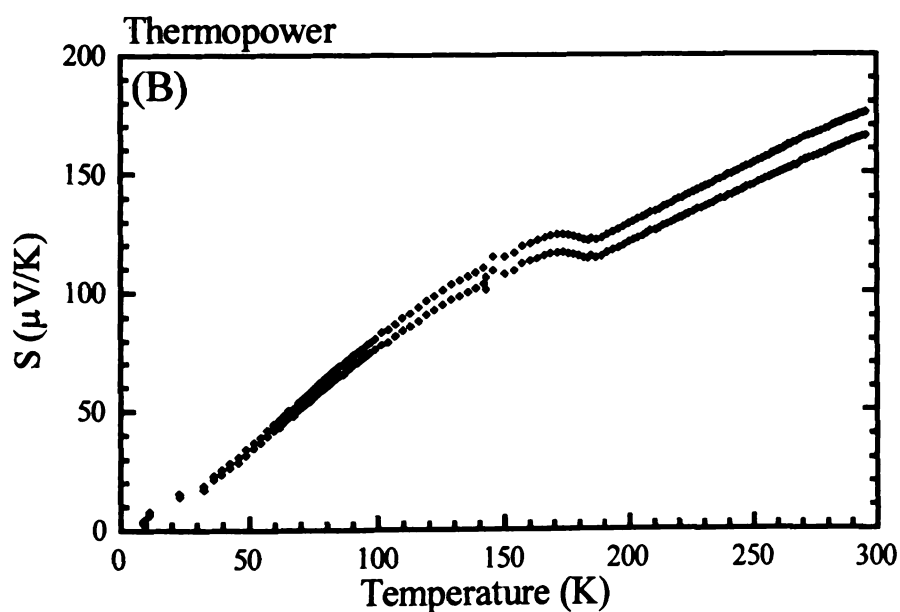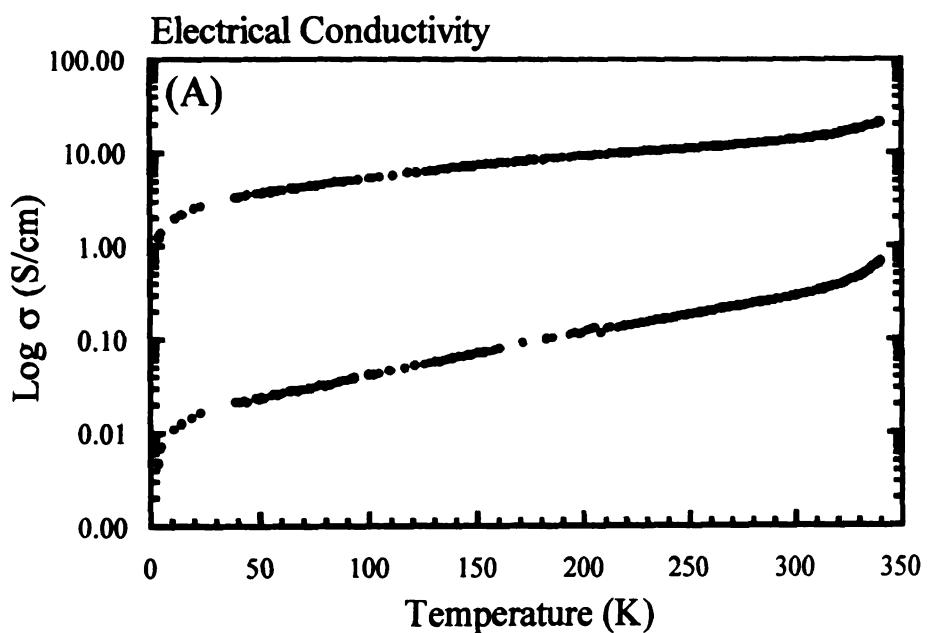
Figure 4.18 (A) Four-probe electrical conductivity data of a room temperature pressed pellet of $K_{2.5}Ag_{4.5}La_2Te_9$ as a function of temperature. (B) Thermopower data of a room temperature pressed pellet of $K_{2.5}Ag_{4.5}La_2Te_9$ as a function of temperature.

190

is sl

coor

tellu

laye

equa

Å y

ator

and

the

each

valu

orig

on t

conf

exac

of ar

phas

has

this

3. $Cu_{0.66}EuTe_2$ (VI)

Structure Description of $Cu_{0.66}EuTe_2$ (VI) – The structure of $Cu_{0.66}EuTe_2$ is shown in Figure 4.19. It adopts the $CaMnBi_2$ structure-type and features 8-coordinate europium atoms in a square-antiprismatic coordination environment of tellurium. The europium atoms are sandwiched between a [CuTe]⁻ anti-PbO type layer and a flat square net of Te atoms. The Te -Te distances in the net are all equal at 3.168(1)Å, a value substantially longer than the normal Te-Te bond of 2.8 Å yet much shorter than the van der Waals contact of 3.8-4.0 Å. The fractional atomic coordinates, isotropic and anisotropic temperature factors, bond distances, and bond angles for both compounds is given in Tables 28-30. The bonds around the europium atoms have been omitted in Figure 4.19 to highlight the stacking of each individual layer. The copper site is only partially occupied and refines to a value of 0.66. Since partial occupancy on copper is unusual and the crystals were originally isolated from a Rb_2Te_x flux, careful elemental analysis was performed on the single crystal after data collection was complete. This analysis not only confirmed the absence of rubidium, but verified the copper composition to be exactly 0.66. Interestingly, this structure type has been encountered in the family of antimonides M_xLaSb_2 (M= Zn, Co, Mn, and Cu; x=0.52-0.87).[35] In all of these phases, the transition metal site is partially occupied (although the reason for this has yet to be addressed). $Cu_{0.66}EuTe_2$ appears to be the first telluride member of this family.

191
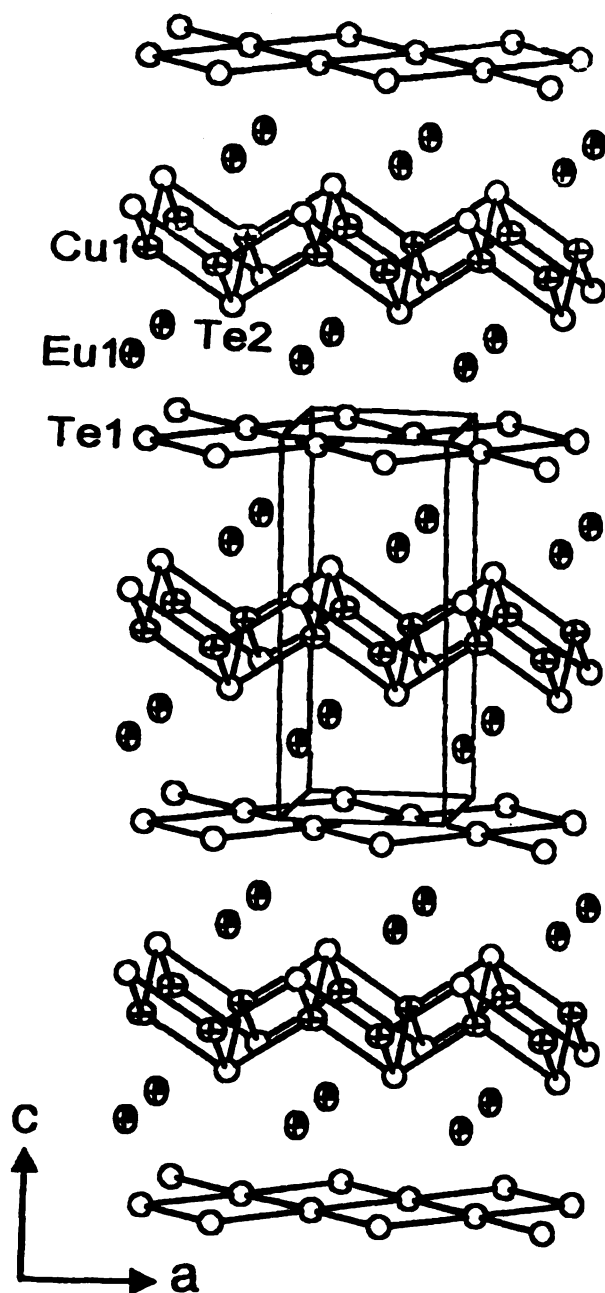
Figure 4.19 ORTEP representation of the structure of $Cu_{0.66}EuTe_2$ as seen down the b-axis (70% ellipsoids). The ellipses with octant shading represent Eu atoms. The crossed ellipses represent Cu atoms and the open ellipses represent Te atoms.

Tab

Disp

Dev

---

atom
Eu
Te(1
Te(2
Cu

 ᵗU,

Tab

Star

ات
Eu
Te1
Te2
Cu

Table 4.28 Fractional Atomic Coordinates and Equivalent Isotropic Displacement Parameters (U_{eq}) for $Cu_{0.66}EuTe_2$ (IV) with Estimated Standard Deviations in Parentheses.

atom	x	y	z	occupancy	U_{eq}^a, $Å^2$
Eu	0.25	-0.25	0.7402(5)	1.0	2.5(2)
Te(1)	0.75	0.25	0	1.0	2.6(2)
Te(2)	0.25	0.25	0.6417(6)	1.0	2.2(2)
Cu	-0.25	0.25	0.5	0.66	3.0(4)

$^a U_{eq}$ is defined as one-third of the trace of the orthogonalized U_{ij} tensor.

Table 4.29 Anisotropic Displacement Parameters (Å) for $Cu_{0.66}EuTe_2$ (IV) with Standard Deviations in Parentheses.

atom	U11	U22	U33	U12	U13	U23
Eu	0.021(2)	0.021(2)	0.033(3)	0	0	0
Te(1)	0.030(2)	0.030(2)	0.018(4)	0	0	0
Te(2)	0.019(2)	0.019(2)	0.027(5)	0	0	0
Cu	0.036(6)	0.036(6)	0.019(9)	0	0	0

Table 4.30   Selected Distances (Å) and Bond Angles (deg) for $Cu_{0.66}EuTe_2$ (IV) with Standard Deviations in Parentheses.

Bond Distances

Eu – Te1	3.482(4) x 8
Eu – Te2	3.326(3) x 7
Te1 – Te1	3.1685(11) x 4
Cu – Te2	2.671(4) x 6

Bond Angles

Te1 – Eu –Te1	54.13(7) x 4	80.10(11) x 2
Te1 – Eu – Te2	78.42(10) x 7	131.78(12) x 8
Te2 – Eu – Te2	84.69(8) x 4	144.6(3) x 2
Te1 – Te1 – Te1	90.00(0) x 4	180.00(0) x 2
Te2 – Cu – Te2	107.23(11) x 4	114.1(2) x 2

KC

bee

stru

the

ator

effe

the

is t

pla

cha

isos

Ag

me

enc

ant

ani

con

sqs

res

4. $A_xM_{(3-x)}EuTe_4$ (VII, VIII)

Structure Description of $A_xM_{(3-x)}EuTe_4$ (VII, VIII) – The structure of

KCu_2EuTe_4 is actually polar, see Figure 4.20. The bonds to europium have now

been included to highlight its square antiprismatic coordination environment. The

structure of KCu_2EuTe_4 can be derived from that of $Cu_{0.66}EuTe_2$ by first restoring

the Cu site to full occupancy and then replacing every other layer of europium

atoms with potassium. This replacement of atoms is reasonable if we compare the

effective ionic radii of Eu^{2+} (1.17Å) to that of K^+ (1.38Å). Thus, we can expect

the europium to be truly divalent since a trivalent europium (ionic radius 0.947Å)

is too small for such a site. As a result, this replacement has caused the n-glide

plane to be lost in moving from $Cu_{0.66}EuTe_2$ to KCu_2EuTe_4 and the symmetry to

change from centrosymmetric to non-centrosymmetric. $Na_{0.2}Ag_{2.8}EuTe_4$ is

isostructural to KCu_2EuTe_4, but now there exists some disorder on the Na site with

Ag, which can be explained again by comparing the effective ionic radii of the two

metals. Na^+ and Ag^+ have an ionic radii of 1.02Å and 1.15Å, respectively, similar

enough to allow the two metals to occupy the same site, which is also square

antiprismatic, see Figure 4.21B. The fractional atomic coordinates, isotropic and

anisotropic temperature factors, bond distances, and bond angles for both

compounds are given in Tables 31-34.

The Te nets in both KCu_2EuTe_4 and $Na_{0.2}Ag_{2.8}EuTe_4$ appear perfectly

square with all shortest Te-Te distances at 3.1371(4)Å and 3.1497(4)Å,

respectively, see Figure 4.21C. This can be an artifact, however, since we know

that

obse

elec

that superstructure modulations (i.e., charge density waves) are frequently observed in compounds with perfectly square net of atoms and are usually electronically driven.[13, 36]
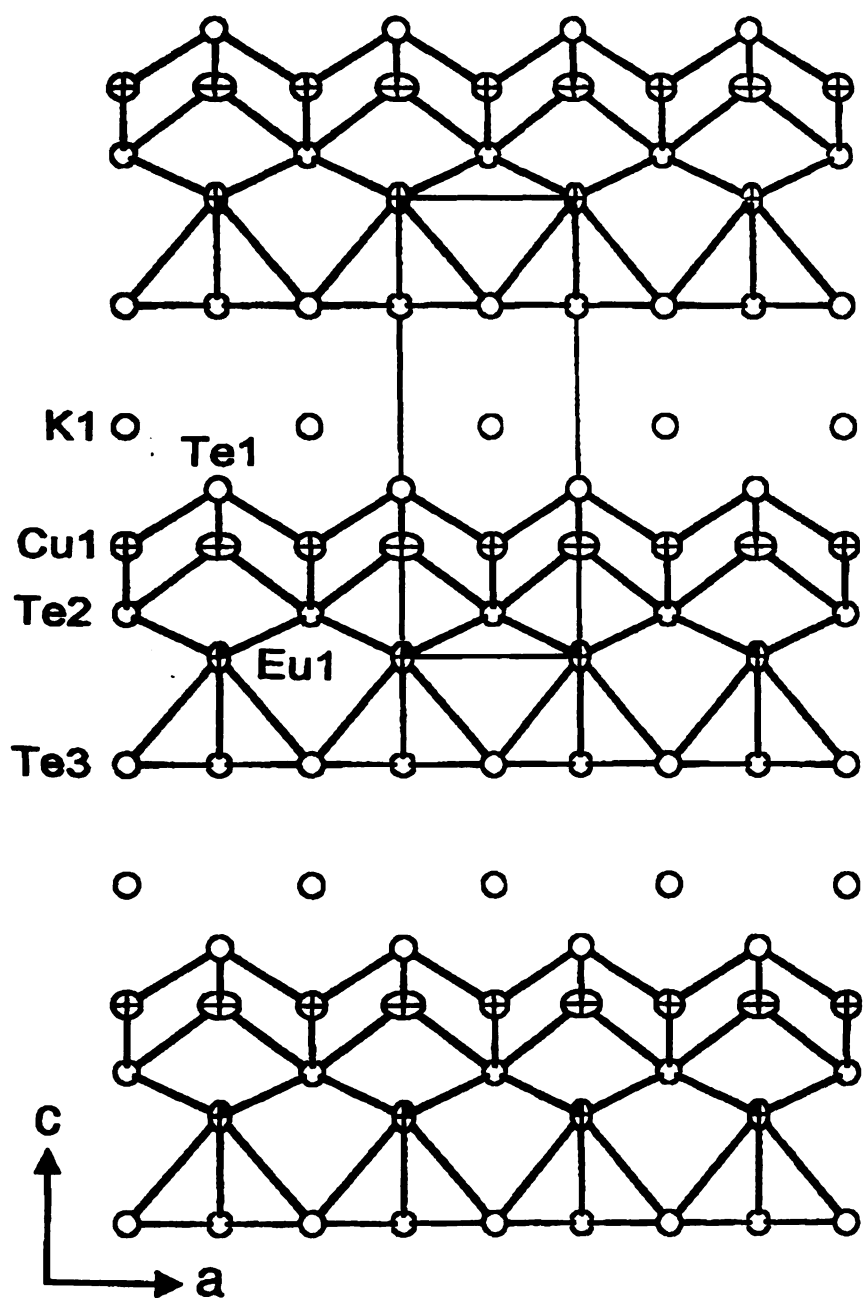
Figure 4.20 ORTEP representation of the structure of KCu_2EuTe_4 (70% ellipsoids) viewed down the b-axis. The ellipses with octant shading represent Eu atoms, the crossed ellipses represent Cu atoms and the open ellipses represent Te and K atoms. The Te3 atoms make the square Te net.

Te2

T

Fig

coo

env

in k
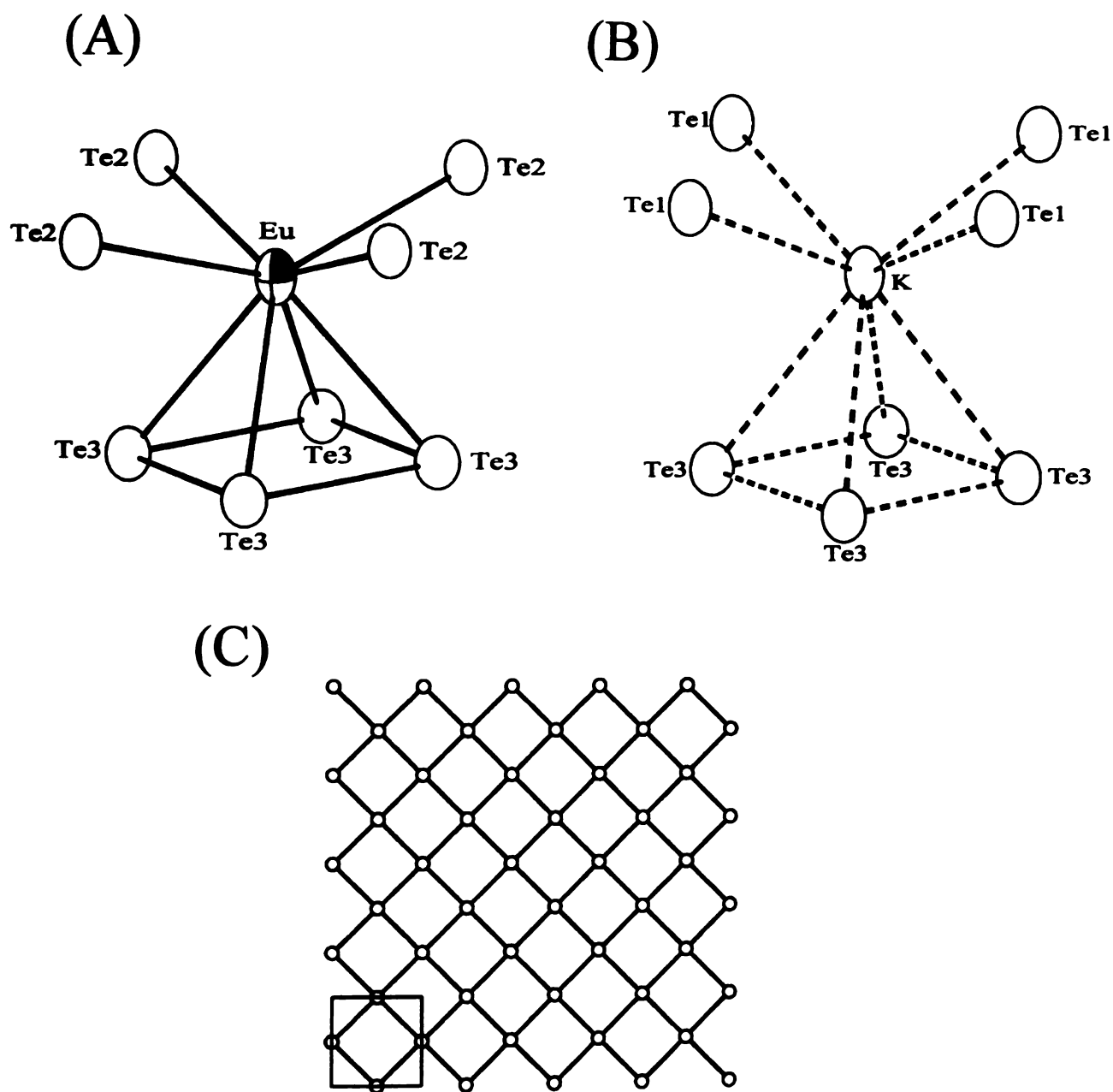
ellip

Figure 4.21 ORTEP representation (80% probability ellipsoid) of (A) the coordination environment around Eu in KCu_2EuTe_4, (B) the coordination environment around K in KCu_2EuTe_4, and (C) a view perpendicular to the Te net in KCu_2EuTe_4. The ellipses with octant shading represent Eu, and the large open ellipses represent K and Te.

Table 4.31 Fractional Atomic Coordinates and Equivalent Isotropic Displacement Parameters (U_{eq}) for KCu_2EuTe_4 (VII) and $Na_{0.2}Ag_{2.8}EuTe_4$ (VIII) with Estimated Standard Deviations in Parentheses.

KCu_2EuTe_4

atom	x	y	z	occupancy	U_{eq}^a, $Å^2$
Eu	0.0	0.0	0.0000(3)	1.0	2.2(1)
Te(1)	0.0	0.0	0.3661(4)	1.0	2.5(1)
Te(2)	0.5	0.5	0.0940(1)	1.0	2.3(1)
Te(3)	0.5	0.0	0.7655(2)	1.0	2.4(1)
Cu	0.5	0.0	0.2416(6)	1.0	4.1(1)
K	0.5	0.5	0.5029(18)	1.0	2.3(2)

$Na_{0.2}Ag_{2.8}EuTe_4$

atom	x	y	z	occupancy	U_{eq}^a, $Å^2$
Eu	0.0	0.0	0.0012(6)	1.0	3.7(2)
Te(1)	0.0	0.0	0.4339(4)	1.0	1.2(1)
Te(2)	0.5	0.5	0.1014(5)	1.0	1.0(1)
Te(3)	0.5	0.0	0.7729(7)	1.0	1.6(1)
Ag(1)	0.5	0.0	0.2768(8)	1.0	1.9(1)
Ag(2)	0.5	0.5	0.5335(5)	0.79	0.6(2)
Na	0.5	0.5	0.5335(5)	0.21	0.6(2)

$^a U_{eq}$ is defined as one-third of the trace of the orthogonalized U_{ij} tensor.

Table 4.32 Anisotropic Displacement Parameters (Å) for KCu_2EuTe_4 (VII) and $Na_{0.2}Ag_{2.8}EuTe_4$ (VIII) with Standard Deviations in Parentheses.

KCu_2EuTe_4

atom	U11	U22	U33	U12	U13	U23
Eu	0.016(1)	0.016(1)	0.034(2)	0	0	0
Te(1)	0.020(1)	0.020(1)	0.035(2)	0	0	0
Te(2)	0.019(1)	0.018(1)	0.032(2)	0	0	0
Te(3)	0.021(1)	0.021(1)	0.031(2)	0	0	0
Cu	0.032(3)	0.065(4)	0.027(3)	0	0	0
K	0.016(3)	0.016(3)	0.036(5)	0	0	0

$Na_{0.2}Ag_{2.8}EuTe_4$

atom	U11	U22	U33	U12	U13	U23
Eu	0.024(2)	0.024(2)	0.064(5)	0	0	0
Te(1)	0.012(2)	0.012(2)	0.013(3)	0	0	0
Te(2)	0.001(1)	0.001(1)	0.028(3)	0	0	0
Te(3)	0.014(2)	0.016(2)	0.019(2)	0	0	0
Ag(1)	0.020(2)	0.020(2)	0.016(2)	0	0	0
Ag(2)	0.009(2)	0.009(2)	0.000(3)	0	0	0
Na	0.009(2)	0.009(2)	0.000(3)	0	0	0

Tal

wit

Table 4.33 Selected Distances (Å) and Bond Angles (deg) for KCu_2EuTe_4 (VII) with Standard Deviations in Parentheses.

Bond Distances

Eu – Te2	3.314(2)
Eu – Te3	3.467(4)
Te3 – Te3	3.1371(4)
Cu – Te1	2.631(5)
Cu – Te2	2.781(5)
K – Te1	3.501(9)
K – Te3	3.72(2)

Bond Angles

Te2 – Eu –Te2	84.03(7) x 4	142.38(17) x 2
Te2 – Eu – Te3	79.61(7) x 8	132.53(8) x 8
Te3 – Eu – Te3	53.79(6) x 4	79.55(10) x 2
Te3 – Te3– Te3	90.00(0) x 4	180.00(0) x 2
Te1 – Cu – Te1	114.9(3) x 1	
Te1 – Cu – Te2	108.93(6) x 4	
Te2 – Cu – Te2	105.8(3) x 1	
Te1 – K – Te1	78.6(3) x 4	127.3(6) x 2
Te1 – K – Te3	88.76(15) x 8	137.3(3) x 8
Te3 – K – Te3	49.9(2) x 4	73.2(4) x 2

Table 4.34 Selected Distances (Å) and Bond Angles (deg) for $Na_{0.2}Ag_{2.8}EuTe_4$ (VIII) with Standard Deviations in Parentheses.

Bond Distances

Eu – Te2	3.341(3)
Eu – Te3	3.375(9)
Te3 – Te3	3.1497(4)
Ag1 – Te1	2.829(8)
Ag1 – Te2	2.959(8)
Ag1 – Ag1	3.1497(4)
Na – Te1	3.338(2)
Na – Te3	3.468(9)

Bond Angles

Te2 – Eu –Te2	83.63(8) x 4	141.1(3) x 2
Te2 – Eu – Te3	79.07(12) x 8	133.65(13) x 8
Te3 – Eu – Te3	55.6(2) x 4	82.6(3) x 2
Te3 – Te3– Te3	90.00(0) x 4	180.0(6) x 2
Te1 – Ag1 – Te1	103.9(4) x 1	
Te1 – Ag1 – Te2	113.95(4) x 4	
Te2 – Ag1 – Te2	97.7(4) x 1	
Te1 – Na – Te1	83.70(6) x 4	141.3(2) x 2
Te1 – Na – Te3	79.96(10) x 8	133.03(10) x 8
Te3 – Na – Te3	54.0(2) x 4	79.9(3) x 2

pro

we

sup

sho

pla

b*

clo

Ho

mi

b*

pro

rot

The

tak

alo

pro

is

b*

sup

the

ad

Transmission Electron Microscopy of $A_xM_{(3-x)}EuTe_4$ (VII, VIII) – In order to

probe for a Te net distortion, we examined both KCu_2EuTe_4 and $Na_{0.2}Ag_{2.8}EuTe_4$

were both examined by electron diffraction and found evidence for a

superstructure arising from a distortion within the square Te net. Figure 4.22A

shows a typical electron diffraction pattern for KCu_2EuTe_4 depicting the (hk0)

plane. The weak spots that appear in this micrograph occur along both the a* and

b* direction and correspond to a 0.286a* x 0.286b* superlattice. This value is

close to (2/7) and therefore the supercell can be modeled as $7a_{sub}$ x $7b_{sub}$.

However, many of the crystals examined under the electron beam were highly

microtwinned and although the modulation seems to appear along both the a* and

b* axes, it is unlikely that the superlattice is that of a $7a_{sub}$ x $7b_{sub}$. This pattern

probably arises from the superimposition of two $1a_{sub}$ x $7b_{sub}$ patterns that are

rotated 90° with respect to one another, as has been found for $K_{0.33}Ba_{0.67}AgTe_2$.[37,38]

The electron diffraction pattern of $Na_{0.2}Ag_{2.8}EuTe_4$, shown in Figure 4.22B, was

taken from a very thin region of a single crystal and contains superlattice spots

along only one direction. Due to the tetragonal symmetry of the subcell, the

propensity of these crystals to twin is seemingly high and a micrograph of this sort

is difficult to obtain, since most showed superlattice spots along both the a* and

b* directions. The spots in this micrograph correspond again to a 1a x 7b

superlattice and it can therefore be concluded that both of these compounds exhibit

the same superlattice. Figure 4.22C is a densitometric intensity scan along the b*-

axis of the electron diffraction pattern of $Na_{0.2}Ag_{2.8}EuTe_4$ (Fig 4.22B). The three

reflections from the tetragonal sublattice are indexed. The four weak peaks are from the 7-fold supercell along this axis.

Figure 4.22 (A) Selected area electron diffraction pattern of KCu_2EuTe_4 with the electron beam perpendicular to the layers ([001] direction) showing a twinned $7a_{sub}$ x $7b_{sub}$ domain (i.e.; two $1a_{sub}$ x $7b_{sub}$ supercells that are rotated 90° with respect to one another and superimposed). (B) Selected area electron diffraction pattern of $Na_{0.2}Ag_{2.8}EuTe_4$ with the electron beam perpendicular to the layers ([001] direction) showing the 1a x 7b superlattice of single crystal region. (C) Densitometric intensity scan along the b*-axis of the electron diffraction pattern of $Na_{0.2}Ag_{2.8}EuTe_4$ (Fig 4.21B) (boxed area in photograph) showing the (-3 k 0) family of reflections. The three reflections from the sublattice of $Na_{0.2}Ag_{2.8}EuTe_4$ are indexed. The four weak peaks are from the 1a x 7b superlattice.

Electron Diffraction of KCu_2EuTe_4 and $Na_{0.2}Ag_{2.8}EuTe_4$
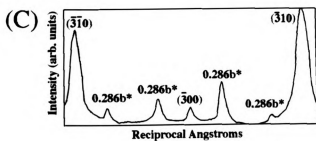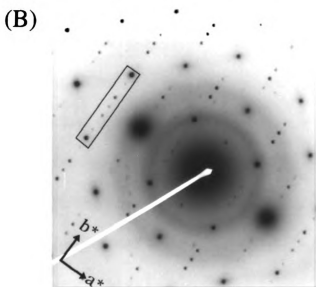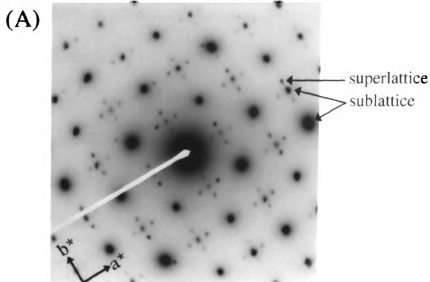
(A)

superlattice
sublattice

$b*$
$a*$

(B)

$b*$
$a*$

(C)

$(\bar{3}10)$ (310)

$0.286b*$ $0.286b*$ $(\bar{3}00)$ $0.286b*$ $0.286b*$

Intensity (arb. units)

Reciprocal Angstroms

206

Va

ov

tha

an

ab

8.5

cor

fro

1or

he

:ha

ıvε

anc

he

for

ın

)K

he

4,(

Magnetic Susceptibility Measurements of $A_xM_{(3-x)}EuTe_4$ (VII, VIII) –

Variable temperature magnetic susceptibility data for KCu_2EuTe_4 was measured over the range of 5-300K at 6000G. A plot of $1/\chi_M$ vs T (see Figure 4.23A) shows that this material exhibits perfect Curie-Weiss behavior. A μ_{eff} value of 7.58 BM and a Weiss constant of $-75K$ was estimated by fitting a straight line to the data above 140K. Analogous data collected for $Na_{0.2}Ag_{2.8}EuTe_4$ at 3000G gave a μ_{eff} of 8.59 BM and a Weiss constant of $-4K$, see Figure 4.23B. These values are consistent with an f^7 configuration or Eu^{2+} (7.9 - 8.0 BM) and are very different from that expected for Eu^{3+} (3.3-3.5 BM).[32]

The issue of charge balancing in all three cases is anything but trivial. The nonstoichiometry in $Cu_{0.66}EuTe_2$ must be taken into consideration, in addition to the superstructures of KCu_2EuTe_4 and $Na_{0.2}Ag_{2.8}EuTe_4$, when assigning formal charges. Since the actual superstructures have not yet been determined, only the average charge per tellurium atom in the net can be calculated, assuming Cu^+, Ag^+, and Eu^{2+}. For $Cu_{0.66}EuTe_2$, it is best to keep the structure in mind when balancing the charges. Since the structure is described as the packing of three layers, the formula can best be described as $[(Cu^+_{0.66}Te^{2-})(Eu^{2+})(Te^{-0.66})]$. The formal charges on KCu_2EuTe_4 and $Na_{0.2}Ag_{2.8}EuTe_4$ can be assigned using the same approach; $[(K^+)(CuTe^-)_2(Eu^{2+})(Te^{-0.5})_2]$ and $[(Na^+_{0.2}Ag^+_{0.8})(AgTe^-)_2(Eu^{2+})(Te^{-0.5})]$. Based on these formulations, the average charge per Te atom in the square net changes from -0.66 in $Cu_{0.66}EuTe_2$ to -0.5 in KCu_2EuTe_4.

$x/1$

$x/1$

Fi

leŋ
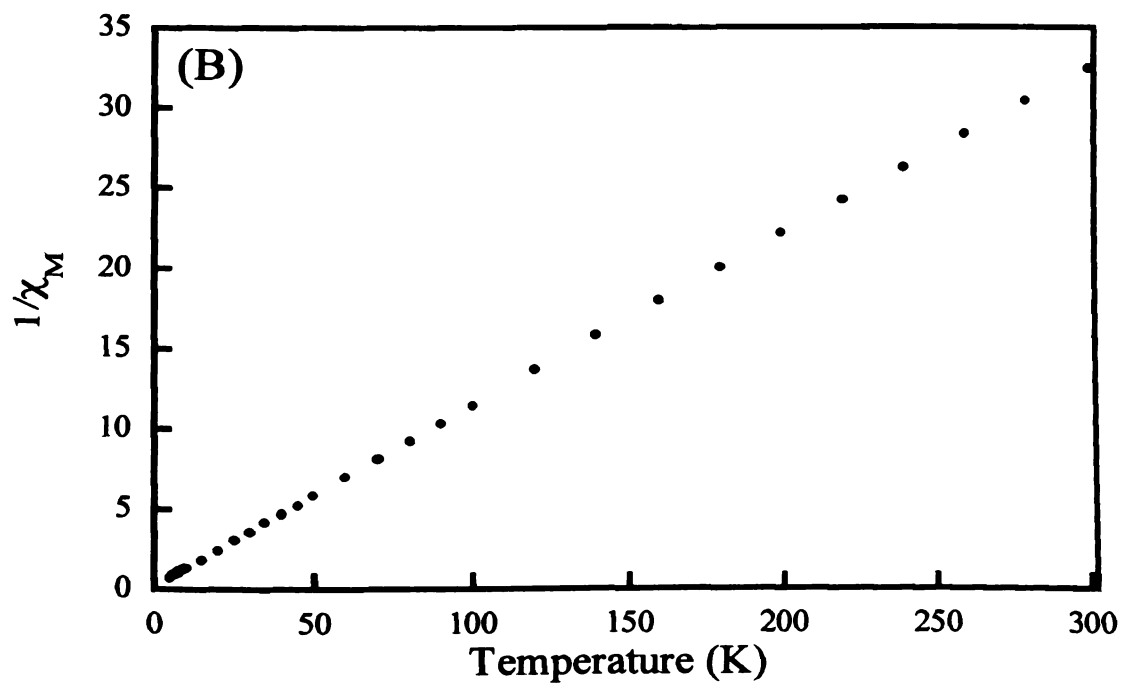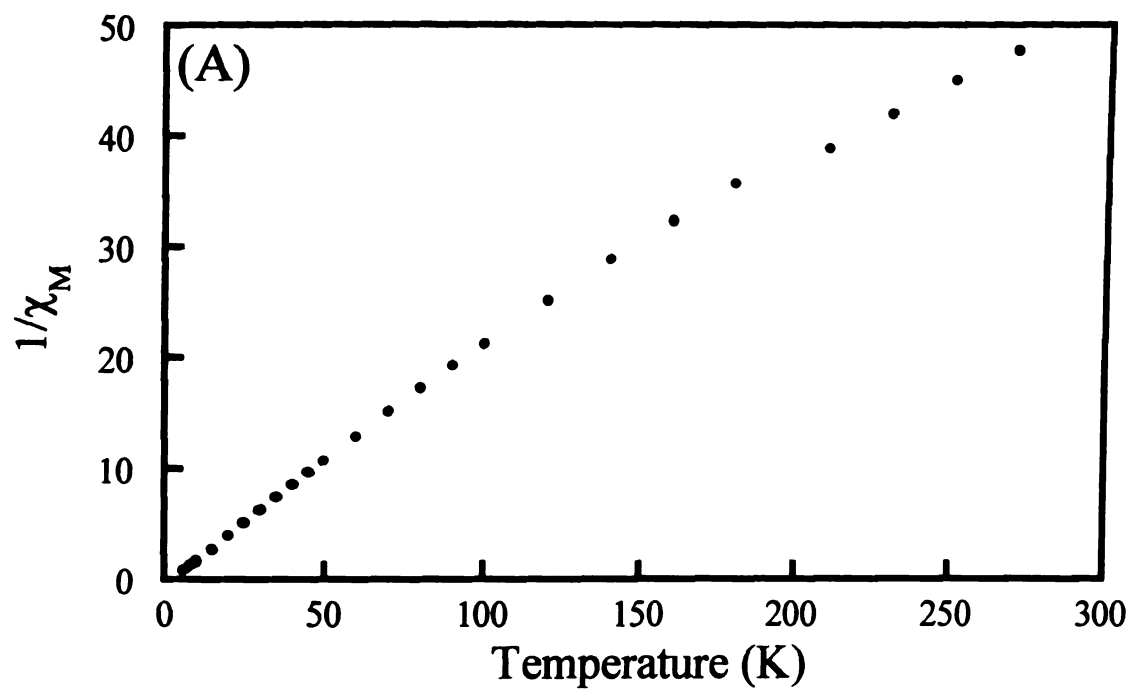
Figure 4.23 Inverse molar magnetic susceptibility $(1/\chi_M)$ plotted against temperature (2-300K) for (A) KCu_2EuTe_4 and (B) $Na_{0.2}Ag_{2.8}EuTe_4$.

KC

dif

Fig

ma

op

Fig

Na

Infrared Spectroscopy of $A_xM_{(3-x)}EuTe_4$ (VII, VIII) – The optical properties of

KCu_2EuTe_4 (V), and $Na_{0.2}Ag_{2.8}EuTe_4$ (VII) were determined by measuring the

diffuse-reflectance spectra of each in the Mid-IR region (6000-400 cm^{-1}), see

Figure 4.24. The spectra of KCu_2EuTe_4 shows no transitions, indicating that this

material is metallic. The spectrum of $Na_{0.2}Ag_{2.8}EuTe_4$, however, reveals an abrupt

optical transition at 0.24 eV, suggesting the material to be semiconducting.
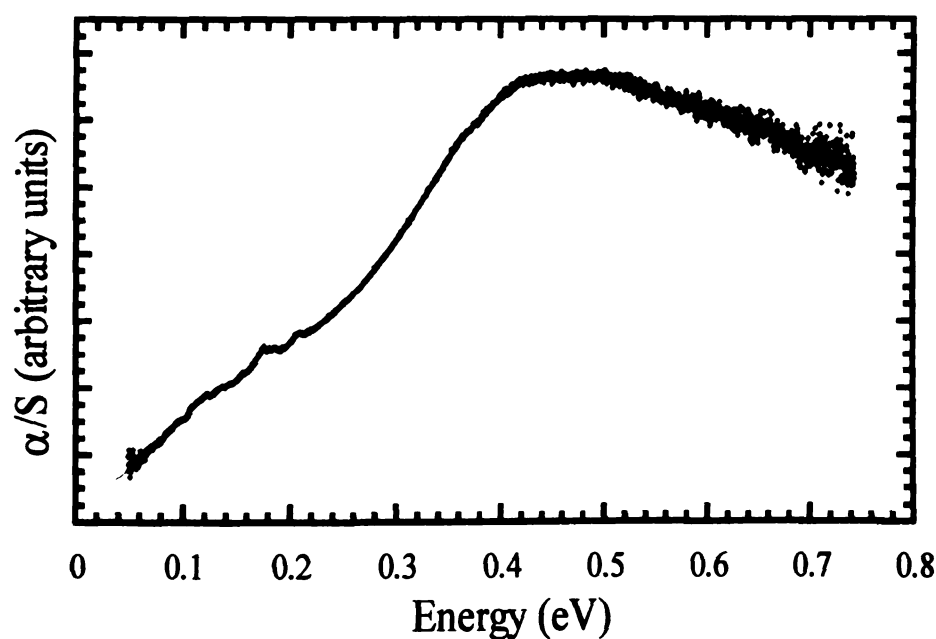
Figure 4.24   Diffuse reflectance optical spectra (in the Mid-IR region) of $Na_{0.2}Ag_{2.8}EuTe_4$.

Charge Transport Properties of $A_xM_{(3-x)}EuTe_4$ (VII, VIII) - Electrical conductivity and thermoelectric power data were measured as a function of temperature for pressed pellets of KCu_2EuTe_4 and $Na_{0.2}Ag_{2.8}EuTe_4$, see Figure 4.25. For KCu_2EuTe_4, the data suggest p-type metallic or semimetallic behavior with a room temperature conductivity of 165 S/cm and a Seebeck coefficient of $^+23$ $\mu V/K$. This agrees with the fact that no optical bandgap was detected for this material in the region 0.1 to 1.0 eV. The data for $Na_{0.2}Ag_{2.8}EuTe_4$ suggest p-type semiconducting behavior with a room temperature conductivity value of 12 S/cm and a Seebeck coefficient of $^+70$ $\mu V/K$.
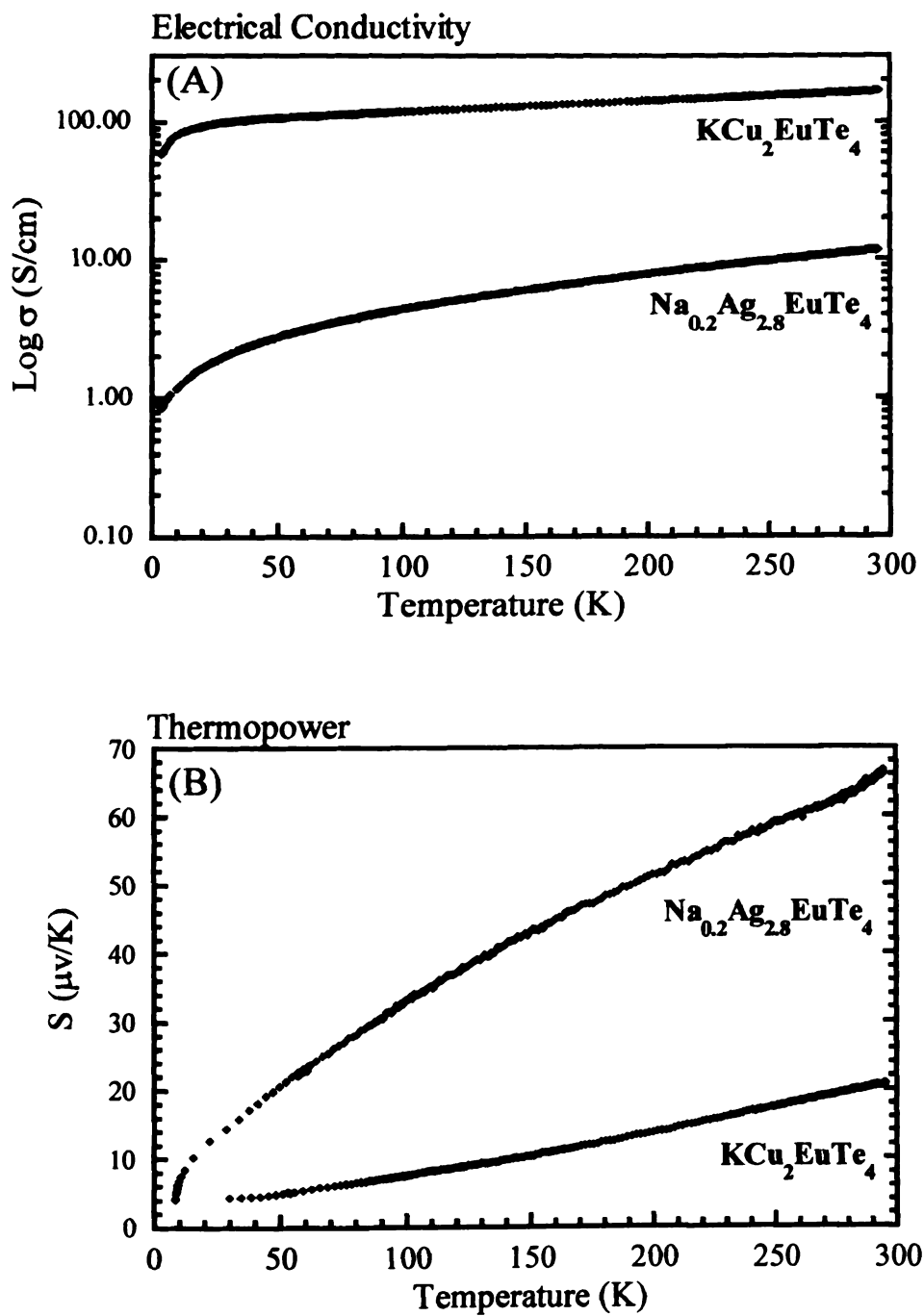
Figure 4.25 (A) Four probe, electrical conductivity data of room temperature pressed pellets of KCu_2EuTe_4 and $Na_{0.2}Ag_{2.8}EuTe_4$ as a function of temperature. (B) Thermopower data of room temperature pressed pellets of KCu_2EuTe_4 and $Na_{0.2}Ag_{2.8}EuTe_4$ as a function of temperature.

5. $K_{0.65}Ag_2Eu_{1.35}Te_4$ (IX)

Structure Description $K_{0.8}Ag_2Eu_{1.2}Te_4$ (IX) – The structure of $K_{0.65}Ag_2Eu_{1.35}Te_4$ viewed down the a-axis is shown in Figure 4.26. At first glance, the structure may appear very similar to that of KCu_2EuTe_4. The layers are polar and are composed of square antiprismatic europium atoms sandwiched between a $[AgTe]^-$ anti-PbO type layer and a flat Te net, see Figure 4.27A. However, unlike KCu_2EuTe_4 which has perfectly square Te net, The Te net in $K_{0.65}Ag_2Eu_{1.35}Te_4$ is modulated, see Figure 4.28. The Te atoms have oligomerized into trimers and heptamers which alternate across the layer in a 1:1 ratio. In addition to alternating with each other, they also alternate back and forth in their direction. This alternating pattern exists not only across the b-axis, but also across the c-axis. Therefore, in order to re-desribe the periodicity of the structure, the b-axis must be multiplied by 10 and the c-axis by 2. Conceptually, the unit cell of $K_{0.65}Ag_2Eu_{1.35}Te_4$ can be considered as a $1a_{sub}$ x $10b_{sub}$ x $2c_{sub}$ supercell over that of KCu_2EuTe_4. However, a direct comparison cannot be made because KCu_2EuTe_4 possesses its own supercell of $1a_{sub}$ x $7b_{sub}$. The reason that the two compounds possess different supercells and therefore different modulated Te nets is because the charge per Te atom on the net is different for each (-0.5 for KCu_2EuTe_4 and –0.675 for $K_{0.65}Ag_2Eu_{1.35}Te_4$). This difference is due to the fact that, in $K_{0.65}Ag_2Eu_{1.35}Te_4$, the potassium sites are disordered with europium (65% K : 35% Eu). Because potassium is monovalent and europium is divalent, the disordering of these elements affects the overall charge on the compound. These

disordered sites, much like the pure Eu sites, are 8-coordinate square antiprismatic with Te, see Figure 4.27B. The fractional atomic coordinates, isotropic and anisotropic temperature factors, bond distances and bond angles are given in Tables 4.35-4.37. The three K/Eu disordered sites were not refined anisotropically due to their very small isotropic tempererature factors. While we do not yet fully understand the origin of these small displacement parameters, we think that they might be due to the fact that there was less than enough observed data. Much of the crystallographic reflections that were expected to be present were either very weak or absent. Overall, only 23% of the data were actually observed which might explain these small displacement parameters. While we believe that this structure model is a very close approximation to the true structure, it is possible that there exists an additional modulation that is either incommensurate or too weak to be observed by X-rays which currently we do not account for. Considering that there still exists some disorder on the potassium sites with europium, this supercell could also succeed in resolving this disorder.
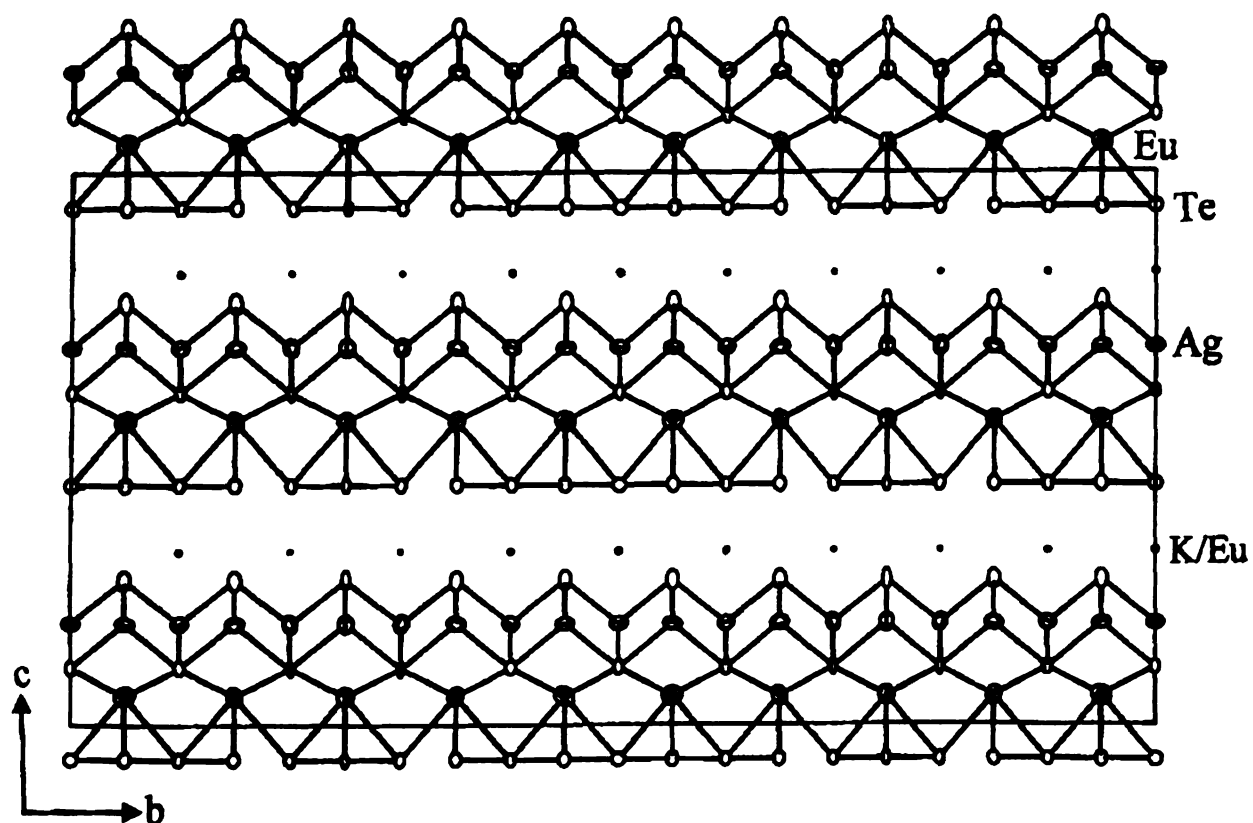
Figure 4.26 ORTEP representation of the structure of $K_{0.65}Ag_2Eu_{1.35}Te_4$ (80% ellipsoids) viewed down the a-axis. The ellipses with octant shading represent Eu atoms, the crossed ellipses represent Ag atoms and the open ellipses represent Te and K atoms.

(A

(B

F
E
K
ra
ra
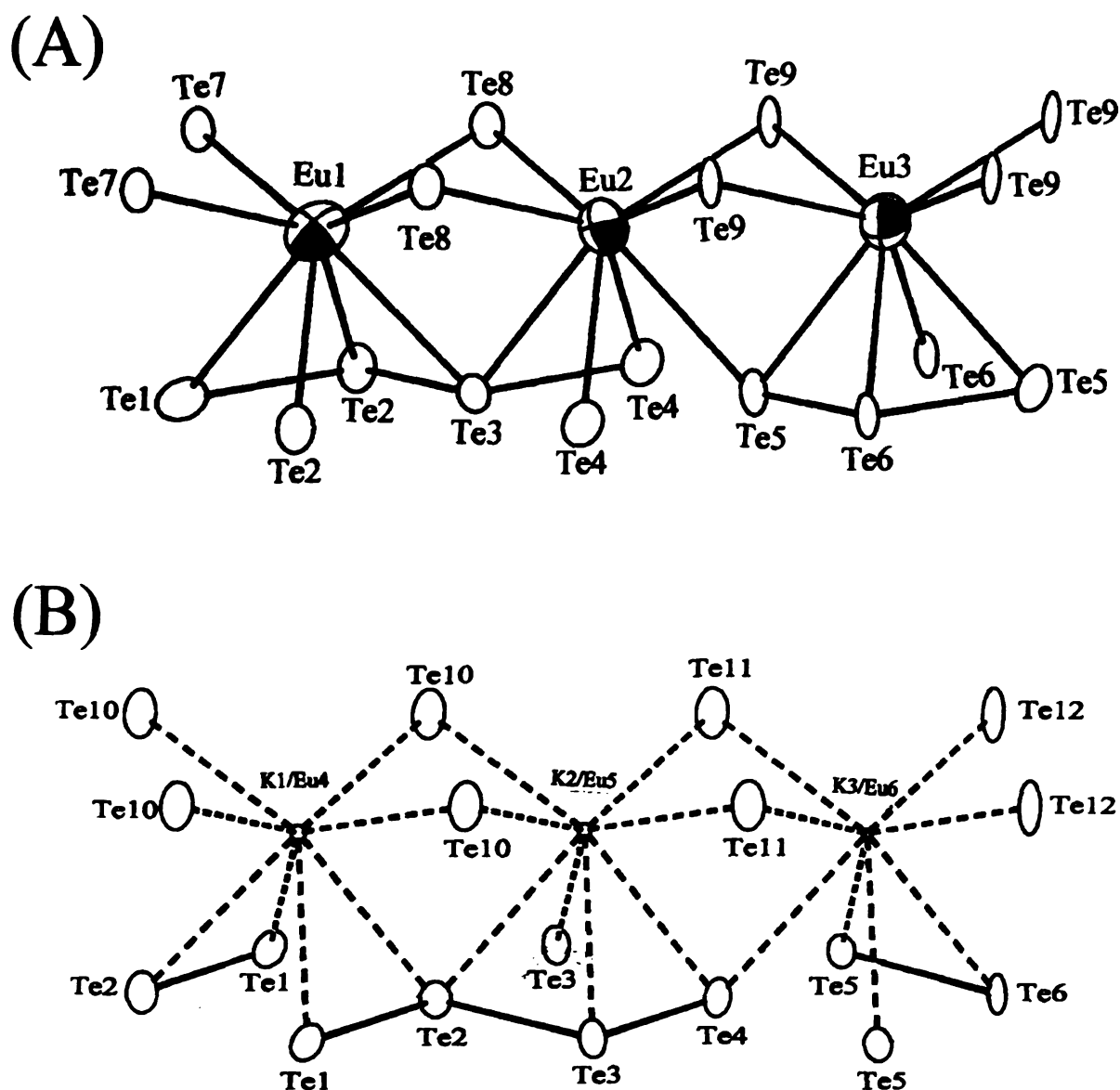
Figure 4.27 ORTEP representation of (A) the coordination environment around Eu in $K_{0.65}Ag_2Eu_{1.35}Te_4$ and (B) the coordination environment around K/Eu in $K_{0.65}Ag_2Eu_{1.35}Te_4$ (90% ellipsoids for both). The ellipses with octant shading represent Eu atoms and the small and large open ellipses represent K/Eu and Te, respectively.

Te4 σ

σ

σ

a
σ

σ

1

1

1
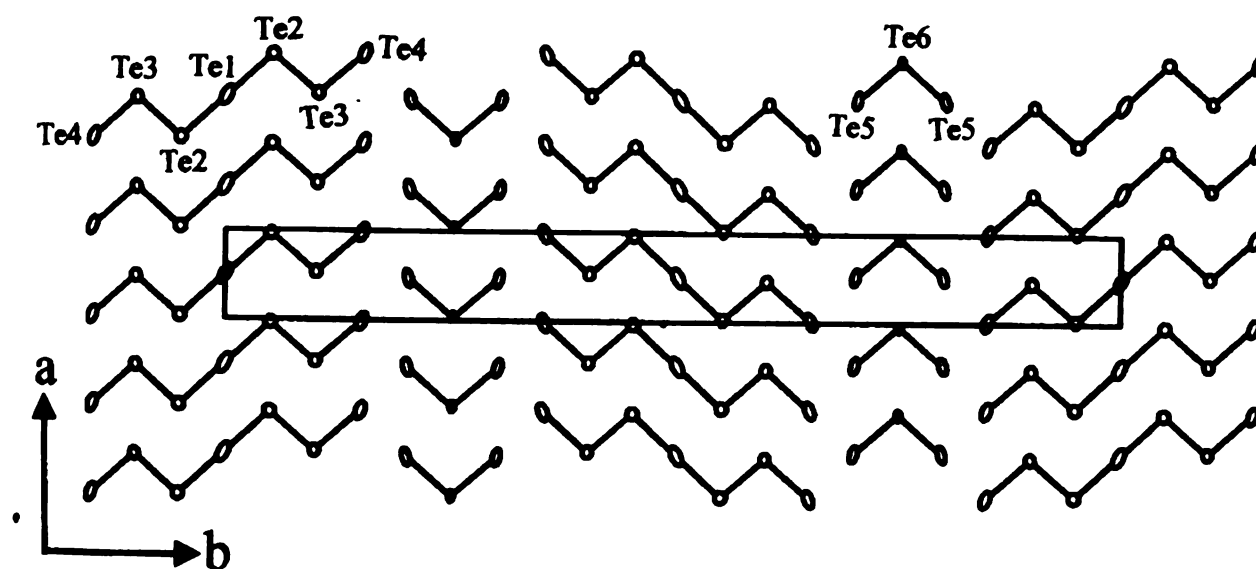
Figure 4.28 ORTEP representation of the Te "net" of $K_{0.65}Ag_2Eu_{1.35}Te_4$ as seen along the ab plane (80% probability ellipsoids) highlighting the arrangement of trimers and heptamers.

Table 4.35 Fractional Atomic Coordinates and Equivalent Isotropic Displacement Parameters (B_{eq}) for $K_{0.65}Ag_2Eu_{1.35}Te_4$ (IX) with Estimated Standard Deviations in Parentheses.

atom	x	y	z	occupancy	$U_{eq}{}^a$, Å^2
Eu(1)	0.5070(13)	0.9500(1)	1.0527(2)	1.0	3.1(1)
Eu(2)	0.5054(13)	0.8500(1)	1.0526(1)	1.0	2.8(1)
Eu(3)	0.4887(14)	0.75	1.0526(1)	1.0	2.9(1)
Te(1)	0.50	1.00	0.9358(3)	1.0	2.4(1)
Te(2)	0.0297(7)	0.9497(1)	09365(2)	1.0	1.6(1)
Te(3)	0.4629(7)	0.9001(1)	0.9358(1)	1.0	1.3(1)
Te(4)	0.0149(9)	0.8501(1)	0.9367(2)	1.0	2.1(1)
Te(5)	0.5253(8)	0.7997(1)	0.9360(2)	1.0	1.9(1)
Te(6)	0.9614(9)	0.75	0.9367(2)	1.0	1.2(1)
Te(7)	1.00	1.00	1.1036(2)	1.0	1.2(1)
Te(8)	1.0057(6)	0.9000(1)	1.1036(1)	1.0	1.4(1)
Te(9)	-0.0037(6)	0.7000(1)	1.1032(1)	1.0	1.3(1)
Te(10)	0.5041(6)	0.9500(1)	1.2635(2)	1.0	2.0(1)
Te(11)	0.5010(6)	0.8500(1)	1.2630(2)	1.0	2.1(1)
Te(12)	0.4948(9)	0.75	1.2632(2)	1.0	2.0(1)
Ag(1)	0.5	1.00	1.1841(3)	1.0	2.3(1)
Ag(2)	1.0020(20)	0.9500(1)	1.1839(2)	1.0	2.3(1)
Ag(3)	-0.5130(20)	0.8999(1)	1.1845(2)	1.0	2.2(1)
Ag(4)	0.9974(14)	0.8500(1)	1.1839(2)	1.0	2.6(2)
Ag(5)	0.4910(16)	0.7000(1)	1.1847(2)	1.0	2.3(1)
Ag(6)	0.0020(30)	0.75	1.1843(3)	1.0	2.6(1)
K(1)	0.0	1.00	0.8168(2)	0.638(16)	0.3(2)
Eu(4)	0.0	1.00	0.8168(2)	0.362(16)	0.3(2)
K(2)	-0.138(8)	0.9000(1)	0.8162(2)	0.650(10)	0.2(1)
Eu(5)	-0.138(8)	0.9000(1)	0.8162(2)	0.350(10)	0.2(1)
K(3)	1.0093(8)	0.7998(1)	0.8170(2)	0.656(11)	0.1(1)
Eu(6)	1.0093(8)	0.7998(1)	0.8170(2)	0.344(11)	0.1(1)

^{a}Ueq is defined as one third of the trace of the orthogonalized U_{ij} tensor

Table 4.36 Anisotropic Displacement Parameters (Å) for $K_{0.65}Ag_2Eu_{1.35}Te_4$ (IX) with Standard Deviations in Parentheses.

Atom	U11	U22	U33	U23	U13	U12
Eu(1)	0.027(1)	0.0035(1)	0.030(1)	-0.0004(1)	-0.0007(1)	0.0005(1)
Eu(2)	0.033(2)	0.0021(1)	0.030(1)	0.0003(2)	0.0000(2)	0.0002(1)
Eu(3)	0.036(2)	0.0023(1)	0.028(2)	0	-0.0003(2)	0
Te(1)	0.039(3)	0.0017(2)	0.015(3)	0	0	0.0015(2)
Te(2)	0.014(1)	0.0012(1)	0.021(2)	-0.0001(1)	-0.0004(2)	0.0000(1)
Te(3)	0.015(1)	0.0009(1)	0.016(1)	-0.0001(1)	0.0006(1)	-0.0001(1)
Te(4)	0.032(2)	0.0011(1)	0.018(2)	-0.0001(1)	-0.0001(2)	0.0008(1)
Te(5)	0.032(2)	0.0008(1)	0.017(2)	0.0001(1)	-0.0006(1)	-0.0006(1)
Te(6)	0.013(2)	0.0004(1)	0.020(2)	0	0.0002(2)	0
Te(7)	0.011(2)	0.0008(1)	0.018(2)	0	0	0.0002(1)
Te(8)	0.013(1)	0.0009(1)	0.019(1)	0.0000(1)	-0.0001(1)	0.0001(1)
Te(9)	0.015(1)	0.0003(1)	0.022(2)	-0.0001(1)	-0.0005(1)	-0.0001(1)
Te(10)	0.012(1)	0.0013(1)	0.034(2)	0.0000(1)	-0.0001(1)	-0.0001(1)
Te(11)	0.014(1)	0.0013(1)	0.034(2)	0.0000(1)	-0.0002(1)	0.0002(1)
Te(12)	0.016(2)	0.0006(1)	0.039(3)	0	-0.0004(1)	0
Ag(1)	0.026(2)	0.0028(2)	0.015(3)	0	0	0.0003(3)
Ag(2)	0.027(2)	0.0030(2)	0.013(2)	0.0002(2)	0.0001(2)	0.0004(2)
Ag(3)	0.025(2)	0.0023(1)	0.018(2)	-0.0002(2)	0.0001(2)	0.0004(2)
Ag(4)	0.032(2)	0.0030(1)	0.017(2)	-0.0003(2)	-0.0005(2)	0.0004(3)
Ag(5)	0.026(2)	0.0017(1)	0.028(2)	-0.0003(2)	-0.0005(2)	-0.0003(3)
Ag(6)	0.031(3)	0.0019(2)	0.029(3)	0	-0.0002(3)	0
K1/Eu4	0.003(2)*					
K2/Eu5	0.002(1)*					
K3/Eu6	0.001(1)*					

*The disordered K/Eu sites were isotropically refined only.

218

Table 4.37   Selected Distances (Å) and Bond Angles (deg) for $K_{0.65}Ag_2Eu_{1.35}Te_4$ (IX) with Standard Deviations in Parentheses.

Bond Distances

Eu1 – Te1	3.496(6)		Ag5 – Te12	2.886(5)
Eu1 – Te2	3.411(6), 3.542(7)		Ag6 – Te9	2.923(5)
Eu1 – Te3	3.501(5)		Ag6 – Te12	2.855(12), 2.905(12)
Eu1 – Te7	3.375(4), 3.416(4)		Ag1 – Ag2	3.197(8), 3186(8)
Eu1 – Te8	3.393(5), 3.401(5)		Ag2 – Ag3	3.159(14), 3.229(14)
Eu2 – Te3	3.505(4)		Ag3 – Ag4	3.142(10), 3.239(11)
Eu2 – Te4	3.444(6), 3.499(7)		Ag4 – Ag5	3.170(6), 3.210(6)
Eu2 – Te5	3.501(4)		Ag5 – Ag6	3.158(13), 3.227(14)
Eu2 – Te8	3.396(5)		Te1 – Te2	3.108(3)
Eu2 – Te9	3.366(5), 3.420(5)		Te2 – Te3	2.974(4)
Eu3 – Te5	3.487(5)		Te3 – Te4	3.033(5)
Eu3 – Te6	3.3552(8), 3.393(8)		Te4 – Te5	3.170(5)
Eu3 – Te9	3.371(5), 3.416(5)		Te5 – Te6	2.986(4)
Ag1 – Te7	2.902(5)		K1/Eu4 – Te1	3.525(6)
Ag1 – Te10	2.899(5)		K1/Eu4 – Te2	3.556(5)
Ag2 – Te7	2.911(5)		K1/Eu4 – Te10	3.404(3), 3.428(3)
Ag2 – Te8	2.912(5)		K2/Eu5 – Te2	3.555(5)
Ag2 – Te10	2.882(10), 2.898(9)		K2/Eu5 – Te3	3.468(5), 3.602(5)
Ag3 – Te8	2.885(9), 2.934(9)		K2/Eu5 – Te4	3.558(5)
Ag3 – Te10	2.895(5)		K2/Eu5 – Te10	3.383(4), 3.441(4)
Ag3 – Te11	2.885(5)		K2/Eu5 – Te11	3.377(4), 3.453(4)
Ag4 – Te8	2.913(5)		K3/Eu6 – Te4	3.554(5)
Ag4 – Te9	2.916(5)		K3/Eu6 – Te5	3.480(5), 3.571(5)
Ag4 – Te11	2.870(7), 2.895(7)		K3/Eu6 – Te6	3.545(5)
Ag5 – Te9	2.899(7), 2.936(8)		K3/Eu6 – Te11	3.397(4), 3.457(4)
Ag5 – Te11	2.880(5)		K3/Eu6 – Te12	3.400(5), 3.424(5)

219

Table 4.37 continued Selected Distances (Å) and Bond Angles (deg) for $K_{0.65}Ag_2Eu_{1.35}Te_4$ (IX) with Standard Deviations in Parentheses.

Bond Angles

Te1 – Eu1 – Te2	53.47(8), 55.83(9)	Te6 – Eu3 – Te9	81.03(16), 132.72(10)
Te1 – Eu1 – Te3	80.61(11)	Te9 – Eu3 – Te9	83.03(7), 140.25(17)
Te1 – Eu1 – Te7	79.89(10), 80.46(11)	Te2 – Te1 – Te2	179.4(2)
Te1 – Eu1 – Te8	133.25(17), 134.33(17)	Te1 – Te2 – Te3	96.14(10)
Te2 – Eu1 – Te2	80.62(11)	Te2 – Te3 – Te4	97.40(12)
Te2 – Eu1 – Te3	50.96(8), 57.69(9)	Te3 – Te4 – Te5	177.55(16)
Te2 – Eu1 – Te7	79.85(15), 134.43(11)	Te4 – Te5 – Te6	94.90(15)
Te2 – Eu1 – Te8	79.30(14), 133.85(10)	Te5 – Te6 – Te5	97.83(18)
Te3 – Eu1 – Te7	130.44(17), 137.08(17)	Te7 – Ag1 – Te7	101.6(2)
Te3 – Eu 1 – Te8	78.00(10), 82.34(10)	Te7 – Ag1 – Te10	112.93(6), 113.54(6)
Te7 – Eu1 – Te7	82.98(7)	Te7 – Ag2 – Te8	102.10(17)
Te7 – Eu1 – Te8	83.25(13), 140.13(13)	Te7 – Ag2 – Te10	113.2(3)
Te8 – Eu1 – Te8	82.49(9)	Te8 – Ag2 – Te10	112.9(3), 113.6(3)
Te3 – Eu2 – Te4	51.75(9), 57.37(9)	Te10 – Ag2 – Te10	102.21(18)
Te3 – Eu2 – Te5	81.11(9)	Te8 – Ag3 – Te8	101.28(17)
Te3 – Eu2 – Te8	78.00(10), 82.21(10)	Te8 – Ag3 – Te10	112.3(2), 114.0(2)
Te3 – Eu2 – Te9	130.41(17), 137.02(17)	Te8 – Ag3 – Te11	112.1(3), 114.3(2)
Te4 – Eu2 – Te4	80.78(11)	Te10 – Ag3 – Te11	103.19(16)
Te4 – Eu2 – Te5	53.86(10), 55.53(9)	Te8 – Ag4 – Te9	101.94(16)
Te4 – Eu2 – Te8	80.66(15), 133.35(10)	Te8 – Ag4 – Te11	112.43(19), 113.89(18)
Te4 – Eu2 – Te9	80.20(15), 133.17(9)	Te9 – Ag4 – Te11	113.20(19)
Te5 – Eu2 – Te8	132.55(18), 135.26(18)	Te11 – Ag4 – Te11	102.57(18)
Te5 – Eu2 – Te9	78.82(10), 80.96(10)	Te9 – Ag5 – Te9	100.88(17)
Te8 – Eu2 – Te8	82.94(8)	Te9 – Ag5 – Te11	112.4(2), 114.2(2)
Te8 – Eu2 – Te9	84.05(13), 140.29(11)	Te9 – Ag5 – Te12	112.8(2), 113.7(2)
Te9 – Eu2 – Te9	83.05(7)	Te11 – Ag5 – Te12	103.40(18)
Te5 – Eu3 – Te5	80.39(15)	Te9 – Ag6 – Te9	101.5(2)
Te5 – Eu3 – Te6	51.41(10), 57.59(11)	Te9 – Ag6 – Te12	112.6(3),113.9(3)
Te5 – Eu3 – Te9	81.86(9), 136.5(2)	Te12 – Ag6 – Te12	102.7(3)
Te6 – Eu3 – Te6	80.71(15)		

Table 4.37 continued   Selected Distances (Å) and Bond Angles (deg) for $K_{0.65}Ag_2Eu_{1.35}Te_4$ (IX) with Standard Deviations in Parentheses.

Bond Angles

Te1 – K1/Eu4 – Te1	79.32(17), 55.83(9)
Te1 – K1/Eu4 – Te2	52.07(9), 55.47(9)
Te2 – K1/Eu4 – Te2	79.76(14)
Te1 – K1/Eu4 – Te10	81.42(7), 81.75(7), 133.89(10), 134.05(10)
Te2 – K1/Eu4– Te10	79.84(8), 82.77(8), 132.08(11), 136.43(11)
Te10 – K1/Eu4 – Te10	82.38(8), 83.06(9), 38.46(19)
Te2 – K2/Eu5 – Te3	50.09(9), 56.69(9)
Te2 – K2/Eu5 – Te4	78.77(10)
Te2 – K2/Eu5 – Te10	79.37(9), 83.43(10)
Te2 – K2/Eu5 – Te11	130.56(12), 137.57(13)
Te3 – K2/Eu5 – Te3	79.02(11)
Te3 – K2/Eu5 – Te4	51.13(9), 56.01(10)
Te3 – K2/Eu5 – Te10	80.88(10), 82.02(10), 132.94(12), 134.34(11)
Te3 – K2/Eu5 – Te11	81.32(10), 82.21(10), 133.25(12), 134.76(11)
Te4 – K2/Eu5 – Te10	131.58(13), 136.32(14)
Te4 – K2/Eu5 – Te11	80.25(10), 82.83(11)
Te10 – K2/Eu5 – Te10	82.50(8)
Te10 – K2/Eu5 – Te11	82.515(10), 138.45(13)
Te11 – K2/Eu5 – Te11	82.39(9)
Te4 – K3/Eu6 – Te5	53.57(10), 54.02(10)
Te4 – K3/Eu6 – Te6	79.45(10)
Te4 – K3/Eu6 – Te11	81.09(15), 81.78(10)
Te4 – K3/Eu6 – Te12	134.19(15), 134.54(15)
Te5 – K3/Eu6 – Te5	79.5(11)
Te5 – K3/Eu6 – Te6	50.29(9), 56.92(10)
Te5 – K3/Eu6 – Te11	81.63(10), 82.12(10), 133.58(1), 134.66(11)
Te5 – K3/Eu6 – Te12	81.21(12), 82.21(12), 133.75(12), 134.61(11)
Te6 – K3/Eu6 – Te11	130.67(13), 138.05(14)
Te6 – K3/Eu6 – Te12	79.47(11), 84.05(11)
Te11 – K3/Eu6 – Te11	82.06(9)
Te11 – K3/Eu6 – Te12	82.25(11), 83.50(11), 137.73(14), 137.97(14)

V

m

4.

of

to

Eu

B)

re

at

se

fi

Magnetic Susceptibility and Infrared Spectroscopy of $K_{0.65}Ag_2Eu_{1.35}Te_4$ (IX)

Variable temperature magnetic susceptibility data for $K_{0.65}Ag_2Eu_{1.35}Te_4$ were measured over the range of 5-300K at 3000G. A plot of $1/\chi_M$ vs T (see Figure 4.29) shows that this material exhibits perfect Curie-Weiss behavior. A μ_{eff} value of 8.53 BM and a Weiss constant of -231K was estimated by fitting a straight line to the data above 50K. These values are consistent with an f^7 configuration for Eu^{2+} (7.9 - 8.0 BM) and are very different from that expected for Eu^{3+} (3.3-3.5 BM).[32]

The diffuse reflectance optical spectra was taken in the Mid-IR region for $K_{0.65}Ag_2Eu_{1.35}Te_4$, see Figure 4.29B. An abrupt optical gap is observed at 0.28eV, which can be assigned as the bandgap and therefore the material is a semiconductor. Below 0.2eV, there is another optical transition, possibly due to f-f interactions on the europium center.
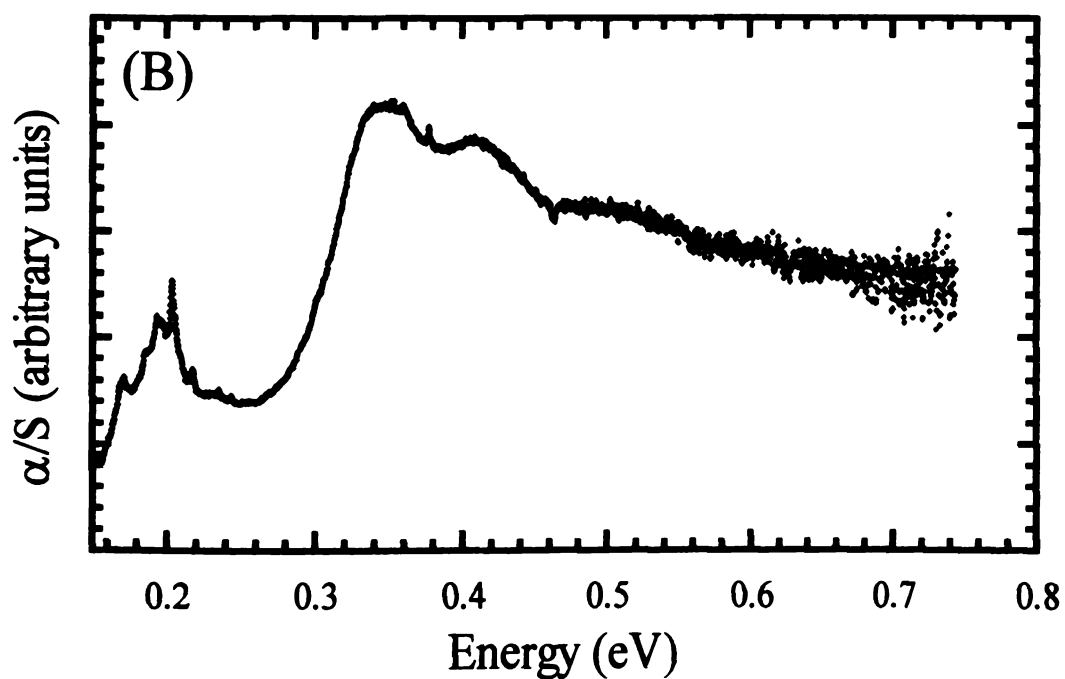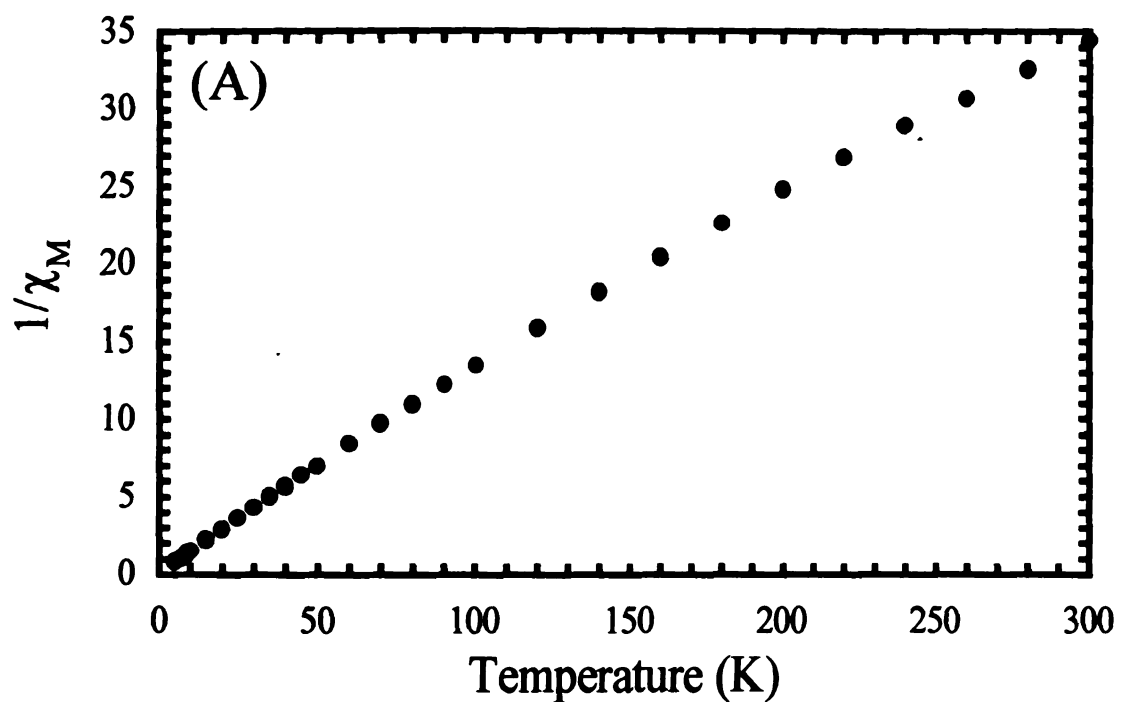
Figure 4.29 (A) Inverse molar magnetic susceptibility ($1/\chi_M$) plotted against temperature (2-300K) for $K_{0.65}Ag_2Eu_{1.35}Te_4$. (B) Diffuse reflectance optical spectra (in the Mid-IR region) for $K_{0.65}Ag_2Eu_{1.35}Te_4$.

Charge Transport Measurements of $K_{0.65}Ag_2Eu_{1.35}Te_4$ - Electrical conductivity and thermoelectric power data were measured as a function of temperature for four single crystals of $K_{0.65}Ag_2Eu_{1.35}Te_4$, see Figure 4.30. The conductivity data for all crystals suggest semiconducting behavior with a sharp decline below 150K. However, the magnitudes differ significantly from crystal to crystal. The room temperature values for these four crystals were 29 S/cm, 132 S/cm, 692 S/cm, and 2892 S/cm. This wide range is very unusual and suggests a problem with either the measurement or the sample. Therefore, measurements were made on several more crystals and the results showed room temperature conductivity values ranging from 10-100 S/cm. While this range is still somewhat large, it gives a better idea as to the conductivity on average. Although the origin of this varying conductivity is still not understood, the fact that it was reproduced suggests that it is particular to the compound and not a problem with the measurement.

The thermopower data for two of the four initial crystals are shown in Figure 4.30B. Although the conductivity values exhibited a wide range, the thermopower values were consistent with a very narrow range of 170-190 $\mu V/K$ at room temperature. The positive sign and decreasing Seebeck coefficient with falling temperature is consistent with a semiconductor and suggest p-type behavior.

224
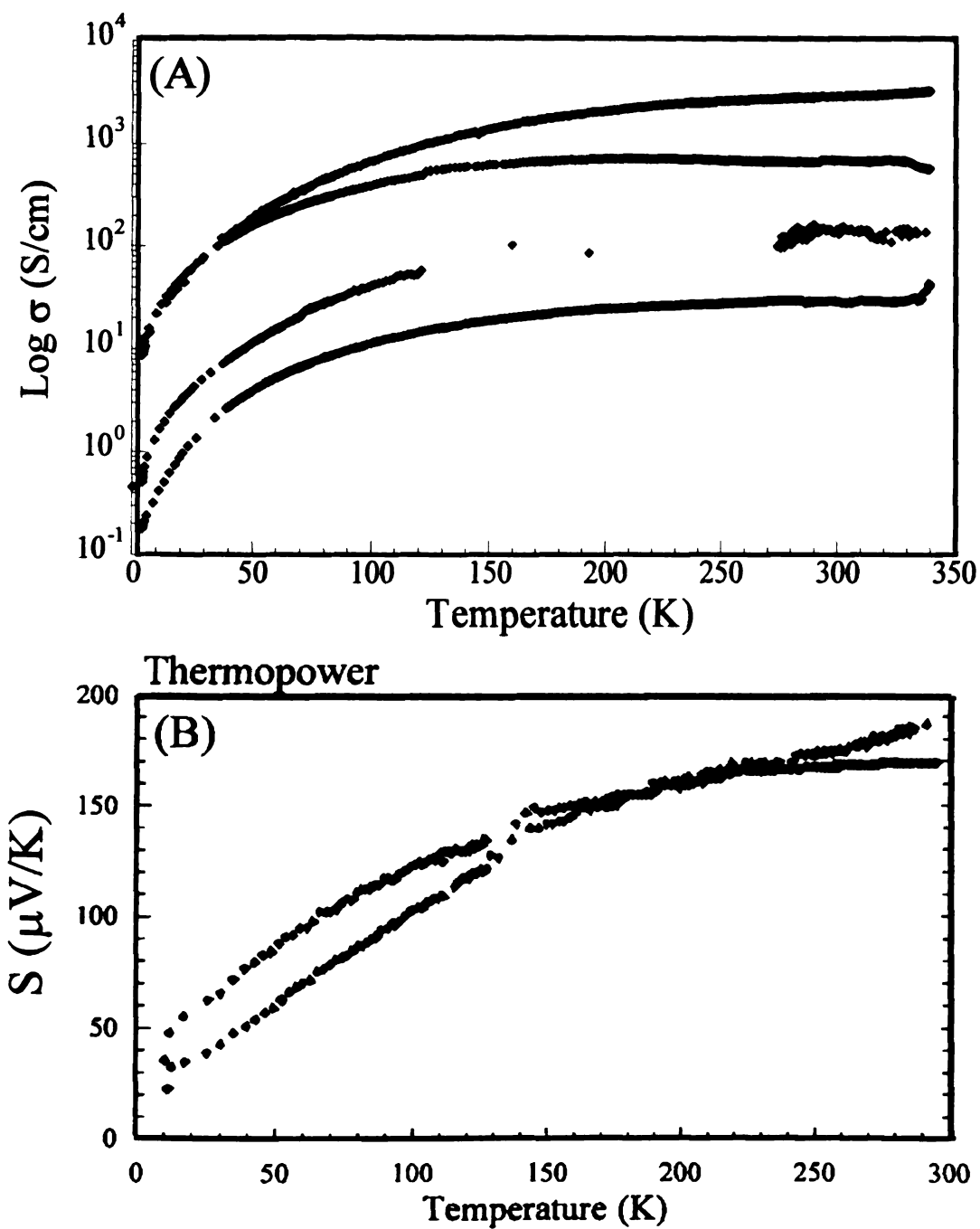
Figure 4.30 (A) Four probe electrical conductivity data for single crystals of $K_{0.65}Ag_2Eu_{1.35}Te_4$ as a function of temperature. (B) Thermopower data for single crystals of $K_{0.65}Ag_2Eu_{1.35}Te_4$ as a function of temperature.

D. Conclusions

Several new compounds of the type $A_wM_xLn_yTe_z$ have been discovered through the use of alkali metal/polytelluride fluxes. The common theme that runs through these compounds is the existence of a Te net. Futhermore, these Te nets have been found to be, in most cases, distorted with the actual distortion being highly dependent on the average charge per Te atom in the net. Below is a summary table which illustrates how very small changes in the average charge can have a drastic effect on the resulting modulation.

Compound Name	Average charge per Te atom in the net	Supercell observed
$KCuCeTe_4$	-0.50	$1a_{sub}$ x $2.87b_{sub}$ (or $2.87a_{sub}$ x $2.87b_{sub}$)
$K_{2.5}Ag_{4.5}Ln_2Te_9$ (Ln = Ce, La)	-0.75	$1a_{sub}$ x $3b_{sub}$
KCu_2EuTe_4	-0.5	$1a_{sub}$ x $7b_{sub}$
$K_{0.65}Ag_2Eu_{1.35}Te_4$	-0.675	$1a_{sub}$ x $10b_{sub}$ x $2c_{sub}$

Interestingly, $KCuCeTe_4$ and KCu_2EuTe_4 possess the same average charge but exhibit different supercells. This is an indication that the modulation in the net not only is affected by the electron count, but also by the remaining part of the structure and its makeup. While some of these Te net distortions were able to be elucidated, others were beyond our capabilities. However, extensive collaboration has been initiated to try and solve the extraordinarily weak or incommensurate

supercells. Most of these materials were determined to be p-type semiconductors with narrow bandgaps ranging around 0.2-0.3 eV. The semiconducting behavior is understood to be caused by the modulations that exist in the Te nets since they act to lower the energy levels at the Fermi level and open up a gap. However, to fully understand the nature of these Te net distortions, further experimental and theoretical work is needed. More of these types of compounds need to be studied in order to systematically build a relationship between the electron count and the type of distortion.

References

[1] Sutorik, A.C.; Albritton-Thomas, J.; Kannewurf, C.R.; Kanatzidis, M.G. *J. Am. Chem. Soc.* **1994**, 116, 7706.

[2] Sutorik, A.C.; Albritton-Thomas, J.; Hogan, T.; Kannewurf, C.R.; Kanatzidis, M.G. *Chem. Mater.* **1996**, 8, 751.

[3] Wu. P.; Ibers, J.A. *J. Solid State Chem.* **1994**, 110, 156.

[4] Cody, J.A.; Ibers, J.A. *Inorg. Chem.* **1995**, 34, 3165.

[5] Cody, J.A.; Mansuetto, M.F.; Pell, M.A.; Chien, S.; Ibers, J.A. *J. Alloys Comp.* **1995**, 219, 59.

[6] Pell, M.A.; Ibers, J.A. *Chem. Ber./Recueil* **1997**, 130, 1.

[7] (a) Christuk, A.E.; Wu, P.; Ibers, J.A. *J. Solid State Chem.* **1994**,110, 330.
(b) Wu. P.; Ibers, J.A. *J. Solid State Chem.* **1994**, 110, 337.

[8] Huang, F.-Q.; Choe, W.; Lee, S.; Chu, J. *Chem. Mater.* **1998**, 10, 1320.

[9] Patschke, R.; Heising, J.; Schindler, J.; Kannewurf, C.R.; Kanatzidis, M.G. *J. Solid State Chem.* **1998**, 135, 111.

[10] Zhang, X.; Schindler, J.L.; Hogan, T.; Albritton-Thomas, J.; Kannewurf, C.R.; Kanatzidis, M.G. *Angew. Chem. Int. Ed. Engl.* **1995**, 32, No. 1, 68.

[11] Zhang, X.; Li, J.; Foran, B.; Lee, S.; Guo, H.-Y.;Hogan, T.; Kannewurf, C.R.; Kanatzidis, M.G. *J. Am. Chem. Soc.* **1995**, 117, 10513.

[12] Gweon, G.H.; Denlinger, J.D.; Clack, J.A.; Allen, J.W.; Olson, C.G.; DiMasi, E.; Aronson, M.C.; Foran, B.; Lee, S. *Phys. Rev. Lett.* **1998**, 81, 886.

[13] Patschke, R.; Heising, J.; Brazis, P.; Kannewurf, C.R.; Kanatzidis, M.G. *Chem. Mater.* **1998**, 10. 695.

[14] Norling, B.K.; Steinfink, H. *Inorg. Chem.* **1966**, 5, 1488.

[15] Krönert, V.W.; Plieth, K.Z. *Z. Anorg. Allg. Chem.* **1965**, 336, 207.

16   (a) Greenwood, N.N.; Earnshaw, E *Chemistry of the Elements*; Pergamon Press: New York, 1984; 1434. (b) Guittard, M.; Flahaut, J. *Synthesis of Lanthanide and Actinide Compounds*, Kluwer Academic Publishers, Netherlands, 1991, 321.

17   Bensch, W.; Dürichen, P. *Chem. Ber.* **1996**, 129, 1489.

18   Patschke, R.; Brazis, P.; Kannewurf, C.R.; Kanatzidis, M.G *J. Mater. Chem.* **1999**, 9, 2293.

19   Feher, F. *Handbuch der Praparativen Anorganischen Chemie:* Brauer, G., Ed.; Ferdinand Enke: Stuttgart, Germany **1954**, 280.

20   Sheldrick, G.M., in *Crystallographic Computing 3*; Sheldrick, G.M.; Kruger, C.; Doddard, R., Eds.; Oxford University Press: Oxford, England **1985**, 175.

21   Gilmore, G.J., *Appl. Cryst.* **1984**, 17, 42.

22   SMART: Siemens Analytical Xray Systems, Inc., Madison, WI, 1994.

23   SAINT: Version 4.0, Siemens Analytical Xray Systems, Inc., Madison WI, 1994-1996.

24   SADABS: Sheldrick, G.M. University of Göttengen, Germany, to be published.

25   Sheldrick, G.M. SHELXTL, Version 5; Siemens Analytical Xray Systems, Inc.; Madison, WI, 1994.

26   (a) Lin, W.; Steinfink, H.; Weiss, F. *J. Inorg. Chem.* **1965**, 4, 877. (b) Wang, R.; Steinfink, H.; Bradley, W.F. *Inorg. Chem.* **1966**, 5, 142. (c) Pardo, M.-P.; Flahaut, J.; Domange, L.C.R. *Bull. Soc. Chim. Fr.* **1964**, 3267. (d) Ramsey, T.H.; Steinfink, H.; Weiss, E. *J. Inorg. Chem.* **1965**, 4, 1154. (e) Norling, B.K.; Steinfink, H. *Inorg. Chem.* **1966**, 5, 1488.

27   Cody, J.; Ibers, J.A. *Inorg. Chem,* **1996**, 35, 3836.

28   Wachhold, M.; Sheldrick, W.J. *Angew. Chem.* **1995**, 107, 490.; *Angew. Chem. Int. Ed Engl.* **1995**, 34, 2109.

29   Lee, S.; Foran, B. *J. Am. Chem. Soc.* **1994**, 116, 154-161.

[30] Park, Y.; Kanatzidis, M.G., unpublished results.

[31] (a) Savelsberg, G.; Schäfer, H. *Z. Naturforsch* **1978**, 33b, 370-373. (b) Berger, R.; Eriksson, L. *J. Less Common Met.* **1990**, 161, 101.

[32] Greenwood, N. N.; Earnshaw, A. *Chemistry of the Elements;* Pergamon Press: New York, 1984; p 1443.

[33] Brown, D.B.; Zubieta, J.A.; Vella, P.A.; Wrobleski, J.T.; Watt, T.; Hatfield, W.E.; Day, P. *Inorg. Chem.* **1980**, 19, 1945.

[34] (a) Anton, H. *Elementary Linear Algebra,* 7th edition, Chapter 3, John Wiley & Sons, New York. (b) Megaw, H.D. *Crystal Structures: A Working Approach,* Chapter 10, **1973**, W.B. Saunders Company, Philadelphia, London, Toronto.

[35] Cordier, G.; Schäfer, H.; Woll, P. *Z. Naturforsch.* **1985**, 40b, 1097.

[36] (a) Gweon, G.-H.; Denlinger, J.D.; Clack, J.A.; Allen, J.W.; Olson, C.G.; DiMasi, E.; Aronson, M.C.; Foran, B.; Lee, S. *Phys. Rev. Lett.* **1998**, 81, 886. (b) DiMasi, E.; Foran, B.; Aronson, M.C.; Lee, S. *Phys Rev. B.* **1996**, 54, 13587. (c) DiMasi, E.; Aronson, M.C.; Mansfield, J.F.; Foran, B.; Lee, S. *Phys. Rev. B.* **1995**, 52, 14516. (d) Foran, B.; Lee, S. *J. Am. Chem. Soc.* **1994**, 116, 154. (e) DiMasi, E.; Foran, B.; Aronson, M.C.; Lee, S. *Chem. Mater.* **1994**, 6, 1867. (e) Foran, B.; Aronson, M.C.; Lee, S. Anderson, M.C. *Chem. Mater.* **1993**, 5, 974.

[37] Zhang, X.; Li, J.; Foran, B.; Lee, S.; Guo, H.-Y.; Hogan, T.; Kannewurf, C.R.; Kanatzidis, M.G. *J. Am. Chem. Soc.* **1995**, 117, 10513.

[38] Hanko, J.A.; Kanatzidis, M.G.; Evain, M.; Gourdon, O.; Boucher, F.; *Submitted for publication.*

Chapter 5

Novel Quaternary Polytelluride Compounds Without Te Nets

A.   Introduction

Over the past decade, the polychalcogenide flux method has become an established technique for discovering new solid state chalcogenides.[1] Although many of the compounds discovered by this method form completely new structure types, others are reminiscent of and can be considered derivatives of known chalcogenides. This is particularly true when lanthanide and actinide metals are involved. The binary LnQ_3 phases ($NdTe_3$[2] and $ZrSe_3$[3]-type), for example, are quite stable. In fact, several new ternary phases have recently been reported in which the structural motifs are related to these LnQ_3 binaries. While $NaLnS_3$ ($Ln=La,Ce$)[4] and ATh_2Q_6 (A = Cs, Rb, K; Q = Se, Te)[5] represent two different variations of the $ZrSe_3$ structure type, ALn_3Te_8 (A = Cs, Rb, K; Ln = Ce, Nd)[6] is closely related to the structure of $NdTe_3$. In an effort to access quaternary phases which are less structurally related to the LnQ_3 binaries, another element was introduced into the synthesis. Copper and silver have proven to be particularly well behaved in this respect and we were able to isolate several new compounds, whereas other elements gave phase-separated ternary compounds. Prior investigations into the A/Cu/Ln/Q (Q=S,Se) system produced several quaternary compounds, including $K_2Cu_2CeS_4$,[7] $KCuCe_2S_6$,[7,8] $KCuLa_2S_6$,[8] $CsCuCe_2S_6$,[8] $KCuCe_2Se_6$,[8] $CsCuCeS_3$,[8] and $KCuUSe_3$[8]. Of these, $K_2Cu_2CeS_4$[7] and $CsCuCeS_3$[8] exhibit mixed chalcogenide valency and appreciable electrical conductivity. At the same time, there has been a rapid expansion in this area by independent

investigators producing such compounds as $CsCuUTe_3$,[9] $BaLnMQ_3$ (Ln=La, Ce, Nd, Er; M=Cu,Ag; Q=S,Se),[10] $BaDyCuTe_3$,[11] $K_{1.5}Dy_2Cu_{2.5}Te_5$,[11] $K_{0.5}Ba_{0.5}DyCu_{1.5}Te_3$,[11] and $KCuEu_2S_6$.[12] These results support the premise that by combining the ionic lanthanide and actinide bonding with the more covalent transition metal bonding, one can access phases with novel structures and properties.[1a] Furthermore, it has become increasingly apparent that the greater the amount of copper or silver in the framework, the more profound the effect of breaking up the known structure types. Of course, a better understanding of this newly emerging family of compounds could be achieved if a wider variety of members were available for study, including the corresponding tellurides. Because of this, we decided to examine the A/M/Ln/Te (M=Cu,Ag) system using polytelluride fluxes and as a result discovered two new quaternary phases, $K_2Ag_3CeTe_4$[13] and $Rb_2Cu_3CeTe_5$.[14] $K_2Ag_3CeTe_4$ has a three-dimensional tunnel framework built from the linking together of $[Ag_2CeTe_4]^{3-}$ layers with Ag and displays the rare combination of being a narrow-gap semiconductor and at the same time being accessible through ion-exchange, while $Rb_2Cu_3CeTe_5$ is two-dimensional and is a perfect example of how the basic LnQ_3 framework can be substantially broken up to form a higher order phase.

B. Experimental Section

1. **Reagents** – The following reagents were used as obtained: Potassium metal, analytical reagent, Spectrum Chemical Mfg. Corp., Gardena, CA;

Rubidium metal, 99.5%, Alfa Aesar, Ward Hill, MA.; Copper metal, electrolytic dust, Fisher Scientific, Fairlawn, NJ; Silver metal coin, 99.9% purity, Liberty Coin, Lansing, MI; Cerium metal, < 250 mesh, Alfa Aesar, Ward Hill, MA; Tellurium powder, 100 mesh, 99.95% purity, Aldrich Chemical Co., Milwaikee, WI; N, N, - Dimethylformamide (DMF) was used as obtained in analytical reagent grade from Aldrich Chemical Co., 998% purity, Milwaukee, WI.

Silver Powder – A silver coin weighing 31.54g was dissolved in 250 mL of 8.4M HNO_3. The solution was heated to 60°C in an acid-resistant fume hood until the silver coin was completely dissolved. The solution was neutralized with ammonium hydroxide and the silver was reduced with formic acid until a pH of 7-8 was reached. The resulting pale grey solid was filtered, washed with copious amounts of distilled water and acetone, and dried in vacuum overnight. The final yield was 31.095g.

Potassium Telluride, K_2Te – Synthesis of this material was performed as described in Chapter 2, Section B.1

Rubidium Telluride, Rb_2Te – Synthesis of this material was performed as described in Chapter 2, Section B.1

2. Synthesis

– All manipulations were carried out under a dry nitrogen atmosphere in a Vacuum Atmospheres Dri-Lab glovebox.

$K_2Ag_3CeTe_4$ (1) – Amount of 0.309g K_2Te (1.5 mmol), 0.162g Ag (1.5 mmol), 0.070g Ce (0.5 mmol), and 0.447g Te (3.5 mmol) were weighed into a vial

in an N_2 filled glovebox. The reagents were thoroughly mixed and loaded into a 9mm carbon coated silica ampoule. The ampoule was removed from the glovebox, evacuated on a Schlenck line to less than 2.0 x 10^{-4} mbar, and flame sealed. The reactants were heated to 400°C in 12hrs, isothermed at that temperature for 12 hrs, raised to 850°C in 22hrs, and isothermed at that temperature for 6 days. The tube was then cooled to 400°C at -4°C hr^{-1}, and then quenched to room temperature in 4 hrs. The excess K_xTe_y flux was removed, under N_2 atmosphere, with DMF to reveal black needle-shaped crystals which appeared to be both air and water stable. Typical yields were 57% yield, based on Ag. Phase homogeneity was confirmed by comparing the powder X-ray diffraction pattern of the product against one calculated using the crystallographically determined atomic coordinates, see Table 5.1 Semiquantitative microprobe analysis on single crystals gave an average composition of $K_{1.8}Ag_{2.2}CeTe_{3.6}$.

$Rb_2Cu_3CeTe_5$ (II) – Amounts of 0.448g Rb_2Te (3.0 mmol), 0.095g Cu (3.0 mmol), 0.070g Ce (1.0 mmol), and 0.447g Te (7.0 mmol) were weighed into a vial in an N_2 filled glovebox. The reagents were thoroughly mixed and loaded into a 9mm carbon coated silica tube. The ampoule was removed from the glovebox, evacuated on a Schlenck line to less than 2.0 x 10^{-4} mbar, and flame sealed. The reactants were heated to 850°C for 24hrs, isothermed at that temperature for 10 days, cooled to 400°C at -3°C/hr, and further cooled to room

temperature at -10°C/hr. The excess Rb_xTe_y flux was removed, under nitrogen atmosphere, with dimethylformamide to reveal black needle-shaped crystals which appeared to be both air and water stable. Typical yields were 45% yield (based on Cu). Phase homogeneity was confirmed by comparing the power X-ray diffraction pattern of the product against the one calculated using the crystallographically determined atomic coordinates, see Table 5.2. Semiquantitative microprobe analysis carried out on randomly selected crystals gave an average composition of $Rb_{2.5}Cu_{3.3}Ce_{1.0}Te_{5.6}$.

Table 5.1   Calculated and Observed X-ray Powder Diffraction Pattern of $K_2Ag_3CeTe_4$ (I)

h k l	d_{calc} (Å)	d_{obs} (Å)	I/I_{max} (obs) (%)
1 0 1	11.4751	12.1064	23.4
2 0 0	8.5992	8.5191	100.0
0 0 2	7.7027	7.6691	49.2
2 0 2	5.7375	5.7863	1.8
3 0 1	5.3729	5.3997	6.4
1 0 3	4.9205	4.9232	2.7
2 0 3	4.4089	4.4030	20.7
2 1 0	4.0830	4.0728	6.5
0 0 4	3.8514	3.8395	13.6
4 0 2	3.7543	3.7376	18.5
2 1 2	3.6075	3.6448	5.0
4 0 3	3.2966	3.2794	12.9
2 0 1	3.1959	3.1800	11.7
5 0 2	3.1408	3.1276	12.9
4 1 1	3.0895	3.0743	58.1
2 0 5	2.9005	2.8974	51.4
2 1 4	2.8016	2.7878	8.6
3 0 5	2.7140	2.6879	7.4
1 0 6	2.5394	2.5488	13.9
6 0 3	2.5029	2.5249	14.4
2 0 6	2.4603	2.4876	4.2

Table 5.1 continued   Calculated and Observed X-ray Powder Diffraction

Pattern of $K_2Ag_3CeTe_4$ (I)

h k l	d_{calc} (Å)	d_{obs}(Å)	I/I_{max} (obs) (%)
7 0 1	2.4263	2.4234	25.7
3 1 5	2.3426	2.3579	12.0
0 2 0	2.3196	2.3131	91.7
4 1 5	2.2038	2.1912	72.3
8 0 0	2.1498	2.1413	20.6
8 0 1	2.1293	2.1186	17.1
4 2 0	2.0415	2.0432	26.0
4 2 2	1.9734	1.9722	17.2
5 2 2	1.8659	1.8688	5.7
7 1 5	1.7748	1.7743	20.4
6 2 2	1.7557	1.7567	15.5
10 0 1	1.7092	1.7086	4.4
2 2 6	1.6878	1.6885	8.4
9 0 5	1.6240	1.6219	14.4
4 0 9	1.5903	1.5910	17.5
8 2 1	1.5686	1.5653	17.0
2 3 0	1.5220	1.5231	46.8

Table 5.2 Calculated and Observed X-ray Powder Diffraction Pattern for $Rb_2Cu_3CeTe_5$ (II)

h k l	d_{calc} (Å)	d_{obs} (Å)	I/I_{max} (obs) (%)
0 0 1	11.4616	11.5477	100.00
2 0 -1	8.8586	8.7086	49.46
2 0 0	8.3862	8.6142	15.43
2 0 -2	5.9379	5.9876	5.98
0 0 2	5.7621	5.7738	22.66
4 0 -1	4.6595	4.6714	10.16
4 0 0	4.3223	4.3071	7.33
2 0 -3	4.1504	4.1667	6.88
0 0 -3	3.8482	3.8492	19.31
3 1 -3	3.3925	3.3622	23.51
0 2 0	3.1139	3.1990	23.35
6 0 -1	30810	3.0800	25.54
4 0 2	2.9578	2.9481	20.94
0 0 4	2.8893	2.8869	32.42
0 2 2	2.7405	2.7442	14.51
5 1 1	2.6983	2.7027	10.92
4 2 0	2.5272	2.5262	8.67
4 0 -5	2.4796	2.4732	14.77
0 2 3	2.4219	2.4233	8.13
4 2 1	2.3559	2.3585	9.76

Table 5.2 continued   Calculated and Observed X-ray Powder Diffraction
Pattern for $Rb_2Cu_3CeTe_5$ (II)

h k l	d_{calc} (Å)	d_{obs}(Å)	I/I_{max} (obs) (%)
8 0 -2	2.3359	2.3357	9.17
0 0 5	2.3133	2.3095	11.13
1 1 -5	2.2541	2.2526	12.76
6 2 -2	2.1944	2.1961	10.37
8 0 0	2.1480	2.1536	18.37
6 2 0	2.1151	2.1125	9.97
4 0 -6	2.0777	2.0833	9.43
1 3 -1	2.0502	2.0487	9.38
6 2 -4	2.0032	1.9976	15.22
0 0 6	1.9285	1.9246	17.23
10 0 0	1.7234	1.7228	10.00
8 0 -7	1.6536	1.6553	31.55
0 0 7	1.6497	1.6497	19.92
12 0 -4	1.5461	1.5464	6.47

3. Physical Measurements – The instrumentation and experimental setup for the following measurements are the same as described in Chapter 2, Section 3: Semiquantitative Energy Dispersive Spectroscopy (EDS), Powder X-ray Diffraction, Magnetic Susceptibility Measurements, and Charge Transport Measurements. The instrumentation and experimental setup for the Infrared Spectroscopy measurements is the same as described in Chapter 3, Section 3.

X-ray Crystallography - The single crystal data sets of both $K_2Ag_3CeTe_4$ and $Rb_2Cu_3CeTe_5$ were collected at the University of Minnesota by Dr. Victor G. Young, Jr. A single crystal of each was mounted on the tip of a glass fiber. Intensity data were collected at 293K (for $K_2Ag_3CeTe_4$) and 173K (for $Rb_2Cu_3CeTe_5$) on a Siemens SMART Platform CCD diffractometer using graphite monochromatized Mo $K\alpha$ radiation. The data were collected over a hemisphere of reciprocal space, up to 50° in 2θ. The individual frames were measured with an ω rotation of 0.3° and an acquisition time of 60 sec/frame for $K_2Ag_3CeTe_4$ and 30 sec/frame for $Rb_2Cu_3CeTe_5$. The SMART[15] software was used for the data acquisitions and SAINT[16] for the data extractions and reductions. The absorption corrections were performed using SADABS.[17] The structures were solved by direct methods using the SHELXTL[18] package of crystallographic programs. The complete data collection parameters and details of the structure solutions and refinements are given in Table 3.3.

Inductively Coupled Plasma Spectroscopy (ICP) - Samples were submitted to the Animal Health Diagnostics Laboratory at Michigan State University for analysis.[19] Experiments were carried out on a Thermo Jarrell Ash Polyscan 61E Simultaneous/Sequential inductively coupled plasma-atomic emission spectrometer (ICP-AES) with vacuum spectrometers and Ar-purged optical paths. The solid powders were weighed onto an analytical balance and then digested in a teflon container in concentrated nitric acid overnight at 95°C. The digest was transferred to a 25mL volumetric flask and diluted with water. Yttrium was used as an internal standard in 2% HNO_3. Multielemental analyses were done by nebulizing the liquid sample into an argon flame (plasma) that was sustained by a surrounding high frequency magnetic field. The photons emitted by the diffracting grating are collimated and directed by a diffraction grating onto a semicircular array of photomultiplier tubes, one for each element to be measured. A computer then converts the photomultiplier signals to concentration units.

Table 5.3   Crystallographic Data for $K_2Ag_3CeTe_4$ (I) and $Rb_2Cu_3CeTe_5$ (II)

Formula	$K_2Ag_3CeTe_4$	$Rb_2Cu_3CeTe_5$
a, (Å)	17.1985(1)	18.6884(1)
b, (Å)	4.6393(2)	6.2384(2)
c, (Å)	15.4055(3)	12.5264(3)
β, (deg)	90.000(0)	112.795(1)
V, (Å^3)	1229.19(3)	1346.34(5)
Space Group	Pnma (#62)	C2/m (#12)
Z value	4	4
F.W (g/mol)	526.16	1526.63
$d_{cal.}$, (g/cm^3)	5.686	5.623
μ, (cm^{-1})	18.262	25.741
crystal (mm^3)	0.31x0.02x0.01	0.16x0.04x0.01
Radiation	Mo Kα	Mo Kα
$2\theta_{max.}$, (deg)	50.0	50.0
Temp., (°C)	293	173
No. data collected	5536	3427
No. unique data	1221	1307
R(int)	0.030	0.044
No. $F_o^2 > 2\sigma (F_o^2)$	1066	1087
No. variables	62	60
R1/wR2, % [a]	3.2/6.6	4.6/11.8
Goof	1.06	1.04

[a] $R1 = \Sigma(|F_o| - |F_c|)/\Sigma|F_o|$ $wR2 = \{\Sigma[w (|F_o^2| - |F_c^2|]^2/\Sigma w|F_o^2|^2\}$

C. Results and Discussion

Structure Description of K₂Ag₃CeTe₄ (1) - The structure of $K_2Ag_3CeTe_4$ is

somewhat related to that of $K_2Cu_2CeS_4$,[7] see Figure 5.1. The basic units that make

up the anionic framework in both compounds are $[CeQ_6]$ octahedra and $[MQ_4]$

(M=Cu,Ag) tetrahedra. In $K_2Cu_2CeS_4$, layers are formed when double rows of

edge sharing $[CuS_4]$ tetrahedra alternate with chains of $[CeS_6]$ octahedra (Figure

5.2A). The layer in $K_2Ag_3CeTe_4$, however, is now corrugated due to the different

way in which the chains of $[CeTe_6]$ octahedra connect to the double rows of

$[AgTe_4]$ tetrahedra (Figure 5.2B). In $K_2Cu_2CeS_4$ the rows of CuS_4 tetrahedra are

arranged centrosymmetrically around chains of CeS_6 octahedra, while in

$K_2Ag_3CeTe_4$ the edge-sharing with $[AgTe_4]$ tetrahedra involves adjacent edges of

$[CeTe_6]$ octahedra. This difference creates a quadruply bridging Te atom (binding

to two Ag and two Ce atoms) and leaves a trans Te atom, bonded to Ce, available

to bind a third Ag atom. The latter acts to link the layers into a three-dimensional

structure (Figure 5.2C). It is interesting that if one removes the Ce atoms, the

remaining $[Ag_3Te_4]$ substructure is still contiguous and three-dimensional. In this

sense, the Ce atoms occupy positions in an open silver telluride framework. The

tunnels in the structure have an oval-shaped cross section with dimensions of

10.63Å (Te1-Te1) x 5.63Å (Te2-Te2) x 8.08Å (Te4-Te4), see Figures 5.2D and

5.3. If the Van der Waals diameters are considered, the tunnels have an accessible

opening of 7.9Å x 2.9Å x 5.3Å. These dimensions are large enough to suggest

that the K^+ cations may be accessible via topotactic ion-exchange. The fractional atomic coordinates, isotropic and anisotropic temperature factors, bond distances, and bond angles for $K_2Ag_3CeTe_4$ are given in Tables 5.4-5.6.

Structure Description of $Rb_2Cu_3CeTe_5$ (II) - $Rb_2Cu_3CeTe_5$ consists of $\frac{1}{\infty}[Cu_3CeTe_5]^{2-}$ layers separated by Rb^+ cations, see Figure 5.4. The Ce atom is seven coordinate, exhibiting a distorted pentagonal bipyramidal geometry in which one η^2-(Te_2^{2-}) unit[20] and three Te^{2-} anions comprise the pentagon and two Te^{2-} anions occupy the axial positions, see Figure 5.5. The pentagonal bipyramids share monotelluride ions, forming $\frac{1}{\infty}[CeTe_5]^{5-}$ chains parallel to the b-axis. Conceptually, these one-dimensional chains derive from the $ZrSe_3$ structure type. By replacing one (Q_2^{2-}) unit in the $ZrSe_3$ framework with a Q^{2-} unit, the coordination environment of the metal changes from bicapped trigonal prismatic to pentagonal bipyramidal. This change in coordination is accompanied by a conversion from two-dimensional layers to one-dimensional chains. Within the $\frac{1}{\infty}[CeTe_5]^{5-}$ chains exist empty distorted tetrahedral pockets of Te atoms which are large enough to accommodate Cu atoms. Each Cu atom is bonded at two points to the axial positions of two neighboring pentagonal bipyramids, and at the remaining sites to the closest edge between these axial positions. The chains, once extended to include the Cu atom, can be written as $\frac{1}{\infty}[Cu_2CeTe_5]^{3-}$. Finally, the layers are formed when the second type of Cu atom "stitches" these chains

together in the a-direction by coordinating to neighboring chains in a distorted tetrahedral arrangement. A view perpendicular to the layers is given in Figure 5.6A. It is interesting to note that if one removes the Ce atoms from the structure, the remaining [Cu_3Te_3] substructure remains contiguous. In this sense, the Ce atoms are situated on both sides of a two-dimensional [CuTe]⁻ substrate. In fact, this copper telluride framework, albeit distorted, bears a close resemblance to the layers of NaCuTe[21], see Figure 5.6B. The fractional atomic coordinates, isotropic and anisotropic temperature factors, bond distances, and bond angles for $Rb_2Cu_3CeTe_5$ are given in Tables 5.7-5.9.
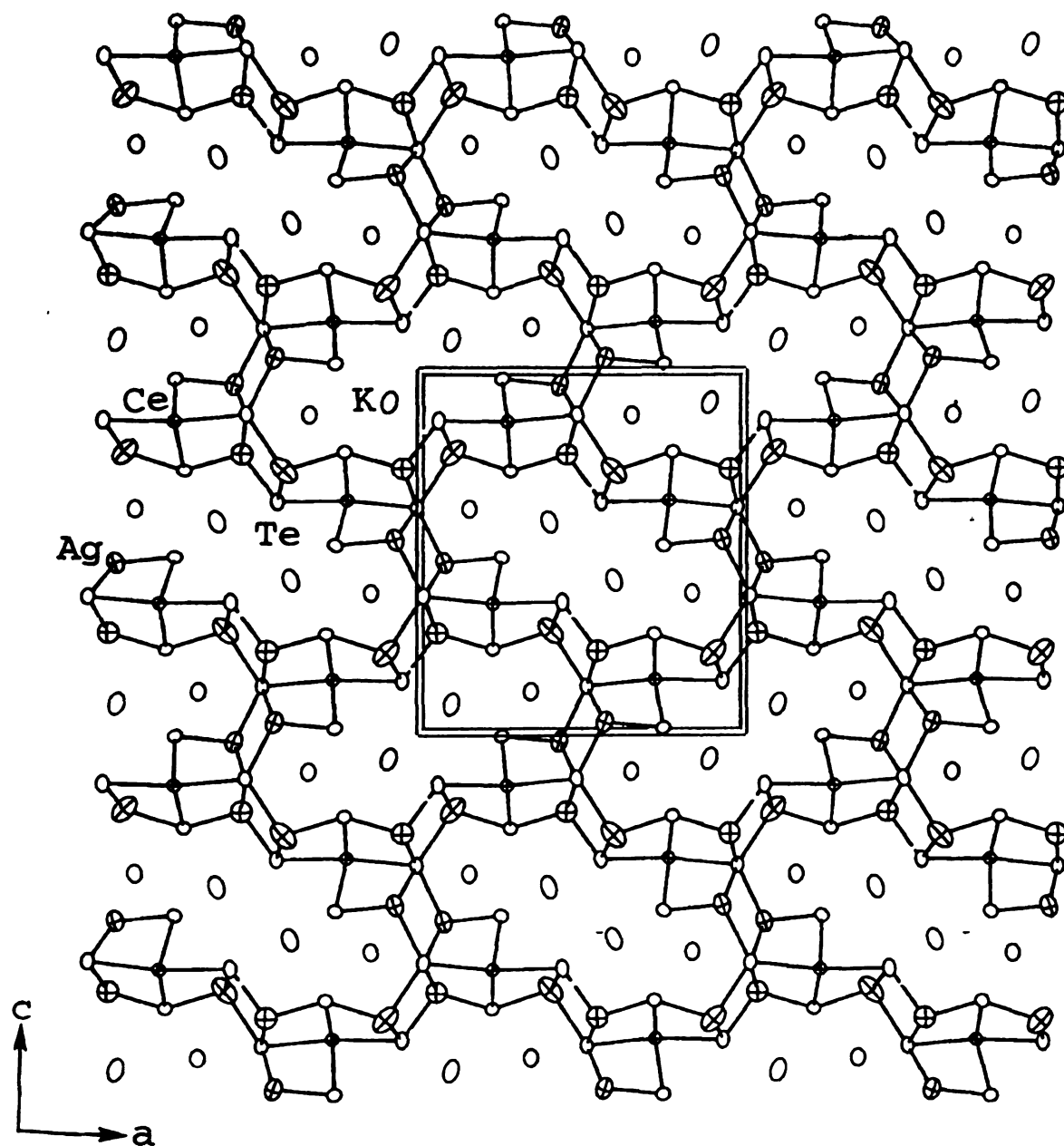
Figure 5.1 ORTEP representation of the structure of $K_2Ag_3CeTe_4$ viewed down the b-axis (90% probability ellipsoids). Ellipses with octant shading represent Ce, crossed ellipses represent Ag, and open ellipses represent K and Te.
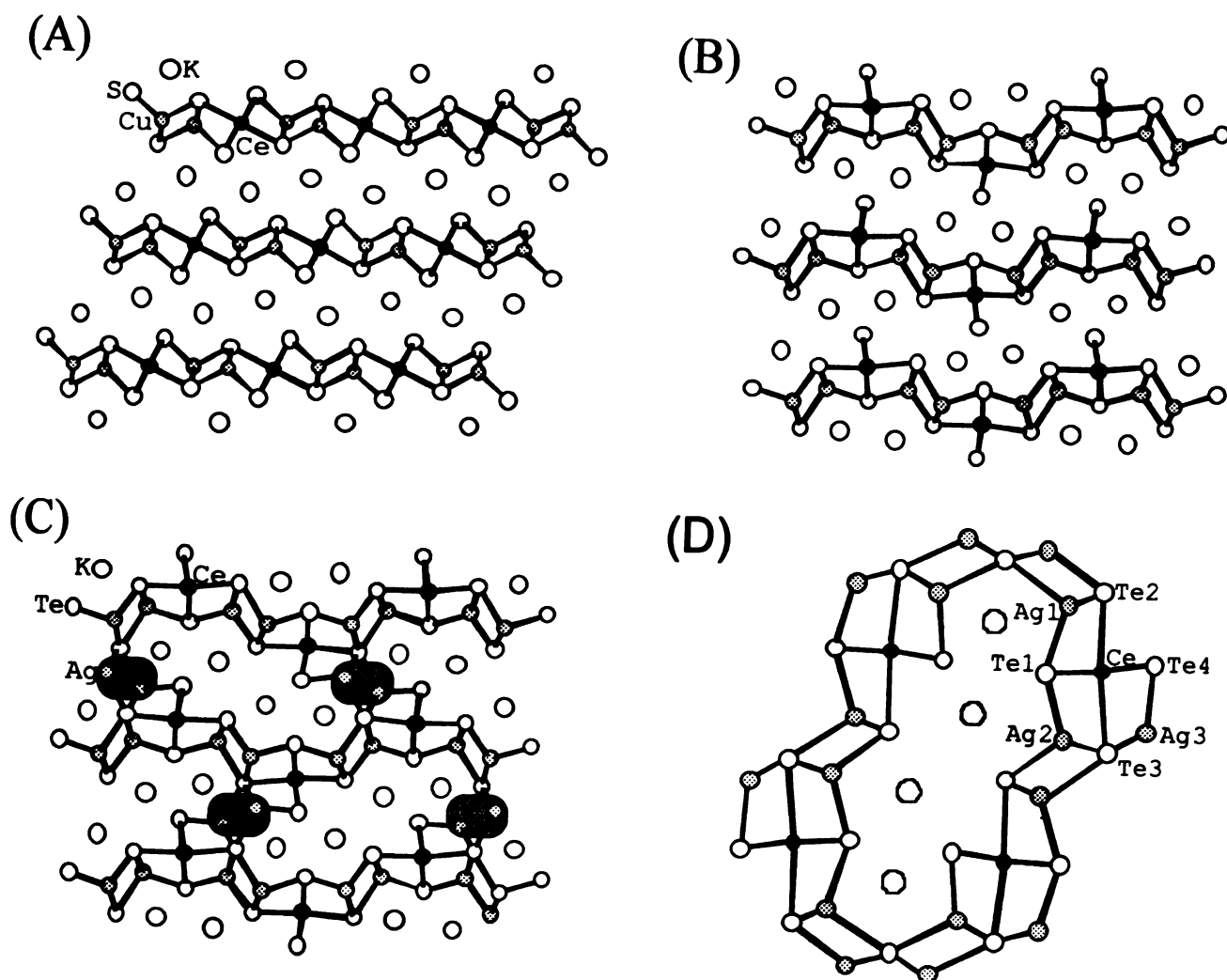
Figure 5.2 (A) Layers of $K_2Cu_2CeS_4$. (B) Corrugated $[Ag_2CeTe_4]^{3-}$ layers in $K_2Ag_3CeTe_4$. (C) Inclusion of the third Ag atoms, between the $[Ag_2CeTe_4]^{3-}$ layers, links them together into a three-dimensional structure. The linking Ag atoms are highlighted by the shaded circle. (D) Tunnel window projection.
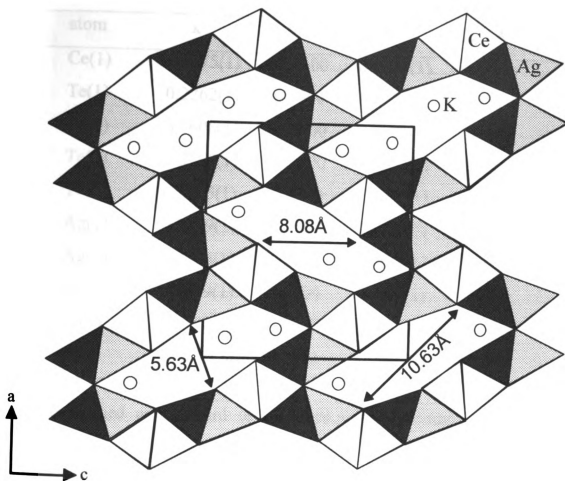
Figure 5.3   Polyhedra representation of the open channels in $K_2Ag_3CeTe_4$ with corresponding dimensions.

Table 5.4 Fractional Atomic Coordinates and Equivalent Isotropic Displacement Parameters (U_{eq}) for $K_2Ag_3CeTe_4$ with Estimated Standard Deviations in Parentheses.

atom	x	y	z	$U_{eq}{}^a$, Å^2
Ce(1)	0.3575(1)	0.2500	0.7714(1)	0.016(1)
Te(1)	0.2262(1)	-0.2500	0.7774(1)	0.017(1)
Te(2)	0.3608(1)	0.2500	0.5598(1)	0.022(1)
Te(3)	0.3769(1)	0.2500	0.9847(1)	0.020(1)
Te(4)	0.4835(1)	-0.2500	0.7506(1)	0.017(1)
Ag(1)	0.2779(1)	-0.2500	0.5978(1)	0.050(1)
Ag(2)	0.2726(1)	-0.2500	0.9525(1)	0.045(1)
Ag(3)	0.4679(1)	-0.2500	0.9301(1)	0.038(1)
K(1)	0.1162(2)	0.2500	0.6558(2)	0.024(1)
K(2)	0.4288(2)	-0.2500	0.3991(2)	0.037(1)

$^aU_{eq}$ is defined as one-third of the trace of the orthogonalized U_{ij} tensor.

Table 5.5 Anisotropic Displacement Parameters (Å) for $K_2Ag_3CeTe_4$ with Standard Deviations in Parentheses

atom	U11	U22	U33	U12	U13	U23
Ce(1)	0.0018(1)	0.0013(1)	0.018(1)	0.0000(0)	0.0000(1)	0.0000(0)
Te(1)	0.0017(1)	0.0015(1)	0.019(1)	0.0000(0)	-0.0001(1)	0.0000(0)
Te(2)	0.0031(1)	0.0019(1)	0.016(1)	0.0000(0)	0.0001(1)	0.0000(0)
Te(3)	0.0027(1)	0.0017(1)	0.017(1)	0.0000(0)	-0.0002(1)	0.0000(0)
Te(4)	0.0017(1)	0.0014(1)	0.021(1)	0.0000(0)	0.0002(1)	0.0000(0)
Ag(1)	0.0064(1)	0.0025(1)	0.060(1)	0.0000(0)	0.0027(1)	0.0000(0)
Ag(2)	0.0040(1)	0.0066(1)	0.028(1)	0.0000(0)	-0.0001(1)	0.0000(0)
Ag(3)	0.0044(1)	0.0043(1)	0.028(1)	0.0000(0)	0.0007(1)	0.0000(0)
K(1)	0.0031(2)	0.0020(2)	0.022(1)	0.0000(0)	-0.0001(1)	0.0000(0)
K(2)	0.0052(2)	0.0031(2)	0.026(1)	0.0000(0)	0.0010(2)	0.0000(0)

The anisotropic displacement factor exponent takes the form: $-2\pi^2 [(ha^*)^2U_{11} + ... + 2hka^*b^* U_{12}]$

Table 5.6   Selected Distances (Å) and Bond Angles (deg) for $K_2Ag_3CeTe_4$ with Standard Deviations in Parentheses.

Bond Distances

Ce – Te1	3.2383(8)	Ag2 – Te1	2.813(2)	K1 – Te4	3.560(2)
Ce – Te2	3.261(1)	Ag2 – Te2	2.828(2)	K2 – Te1	3.888(3)
Ce – Te3	3.303(1)	Ag3 – Te4	2.788(1)	K2 – Te2	3.536(3)
Ce – Te4	3.1898(9)	Ag3 – Te3	2.922(1)	K2 – Te4	3.677(3)
Ag1 – Te1	2.906(2)	K1 – Te1	3.531(2)		
Ag1 – Te2	2.785(1)	K1 – Te3	3.513(2)		

Bond Angles

Te1 – Ce – Te2	92.32(3)	Te2 – Ag1 – Te2	112.81(6)
Te1 – Ce – Te3	92.42(2)	Te2 – Ag1 – Te3	108.26(4)
Te2 – Ce – Te3	173.21(4)	Te1 – Ag2 – Te3	109.34(4)
Te4 – Ce – Te1	175.68(2)	Te1 – Ag2 – Te2	109.30(5)
Te4 – Ce – Te2	83.54(3)	Te2 – Ag2 – Te3	113.06(3)
Te4 – Ce – Te3	91.81(3)	Te3 – Ag2 – Te3	102.51(5)
Te1 – Ag1 – Te3	105.37(5)	Te3 – Ag3 – Te3	110.70(3)
Te2 – Ag1 – Te1	110.90(4)	Te4 – Ag3 – Te3	109.77(4)
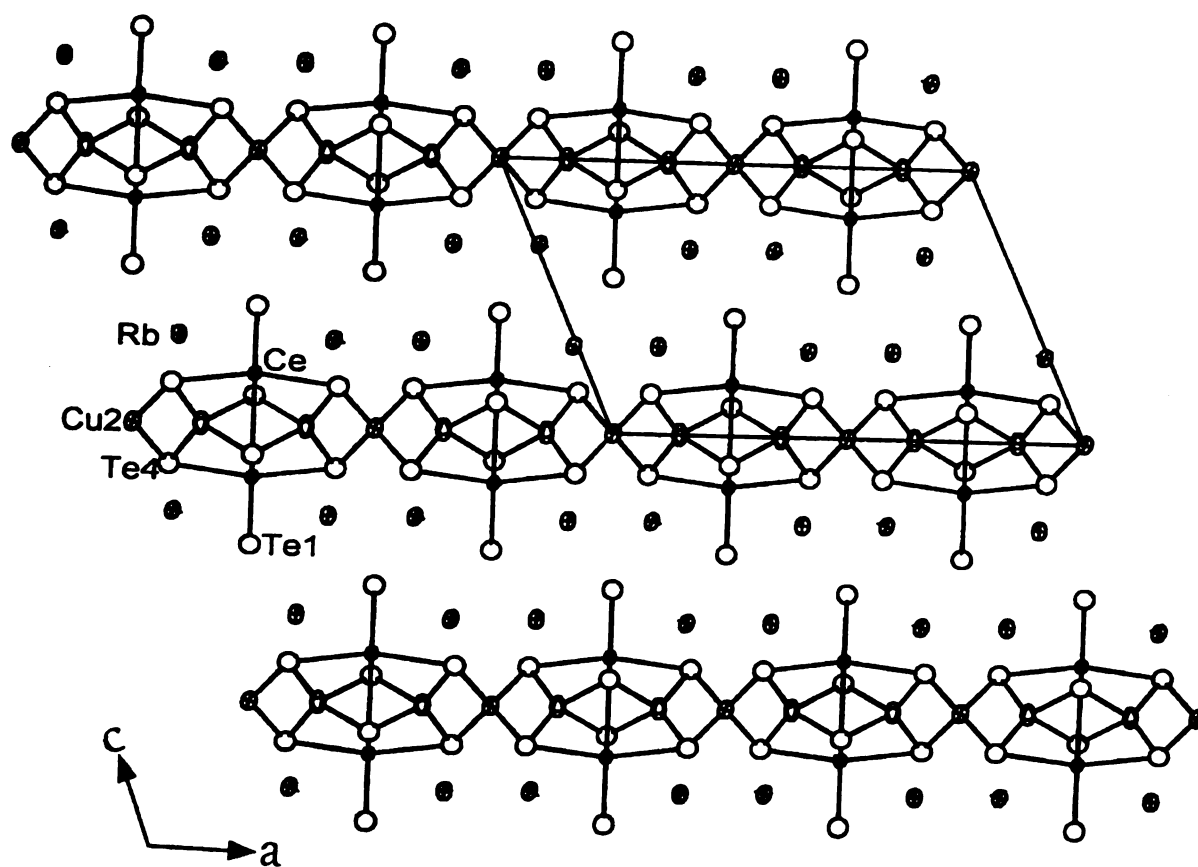
Figure 5.4 ORTEP representation of the structure of $Rb_2Cu_3CeTe_5$ as seen down the b-axis (90% ellipsoids). The ellipses with octant shading represent Ce and Rb, the crossed ellipses represent Cu and the open ellipses represent Te.
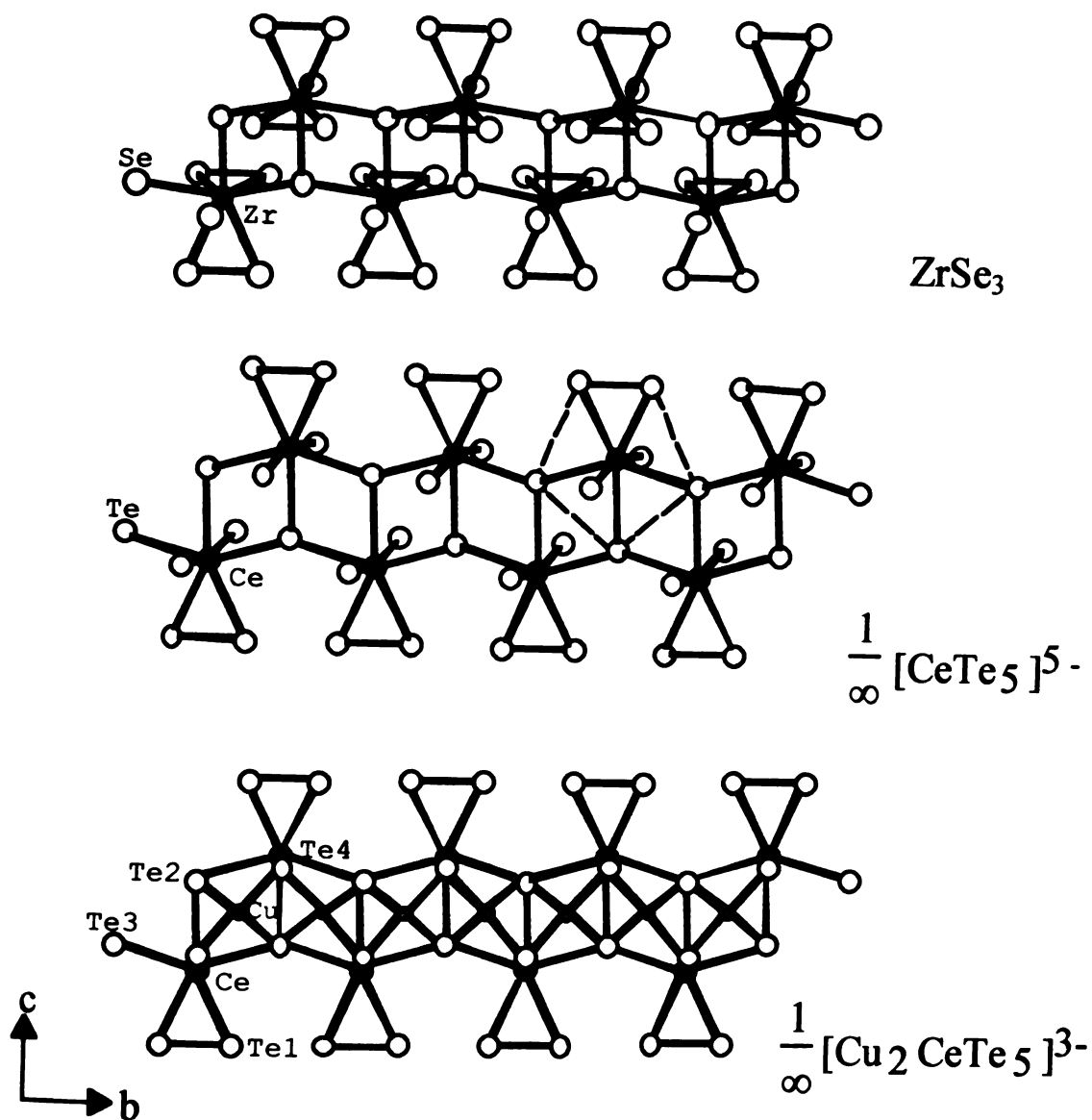
Figure 5.5   Schematic comparison of the two-dimensional layers of $ZrSe_3$, the one-dimensional $\frac{1}{\infty}[CeTe_5]^{5-}$ chains and the $\frac{1}{\infty}[Cu_2CeTe_5]^{3-}$ chains in $Rb_2Cu_3CeTe_5$. The dotted line highlights the pentagonal bipyramidal coordination around Ce.

Cu "stitch"

(A)

[Cu2CeTe5]³⁻ chain

Cu 1

Cu2

Te4   Te2   Te3

b

a

(B)

CuTe-network
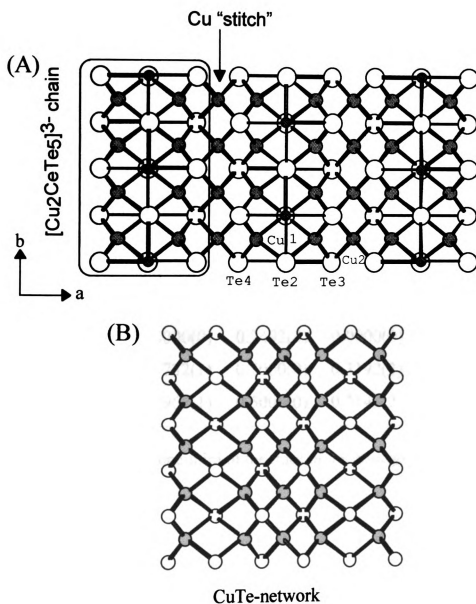
Figure 5.6 (A) View perpendicular to the layers of $Rb_2Cu_3CeTe_5$, illustrating how the second Cu atom stitches together the $\frac{1}{\infty}[Cu_2CeTe_5]^{3-}$ chains to form two-dimensional layers. The ditelluride groups above and below the anionic layers are omitted for clarity. (B) The distorted $[CuTe]^-$, PbO-like layer in $Rb_2Cu_3CeTe_5$.

Table 5.7 Fractional Atomic Coordinates and Equivalent Isotropic Displacement Parameters (U_{eq}) for $Rb_2Cu_3CeTe_5$ with Estimated Standard Deviations in Parentheses.

atom	x	y	z	$U_{eq}{}^a$, $Å^2$
Ce(1)	0.2982(1)	0.0000(0)	0.1854(1)	0.009(1)
Te(1)	0.3626(1)	0.2221(2)	0.4314(1)	0.016(1)
Te(2)	0.2777(1)	0.5000(0)	0.1052(1)	0.010(1)
Te(3)	0.1161(1)	0.0000(0)	0.1464(1)	0.011(1)
Te(4)	0.4604(1)	0.0000(0)	0.1453(1)	0.011(1)
Cu(1)	0.1421(1)	0.2521(4)	0.0009(2)	0.028(1)
Cu(2)	0.0000(0)	0.2492(4)	0.0000(0)	0.020(1)
Rb(1)	0.1732(1)	0.5000(0)	0.3192(2)	0.016(1)
Rb(2)	0.4962(1)	0.5000(0)	0.3148(2)	0.016(1)

$^a U_{eq}$ is defined as one-third of the trace of the orthogonalized U_{ij} tensor.

Table 5.8   Anisotropic Displacement Parameters (Å) for $Rb_2Cu_3CeTe_5$ with Standard Deviations in Parentheses.

atom	U11	U22	U33	U12	U13	U23
Ce(1)	0.0009(1)	0.0008(1)	0.012(1)	0.0000(0)	0.0006(1)	0.0000(0)
Te(1)	0.0022(1)	0.0011(1)	0.014(1)	-0.0003(1)	0.0006(1)	-0.0001(1)
Te(2)	0.0011(1)	0.0008(1)	0.014(1)	0.0000(0)	0.0007(1)	0.0000(0)
Te(3)	0.0009(1)	0.0011(1)	0.015(1)	0.0000(0)	0.0008(1)	0.0000(0)
Te(4)	0.0008(1)	0.0011(1)	0.016(1)	0.0000(0)	0.0008(1)	0.0000(0)
Cu(1)	0.0016(1)	0.0041(1)	0.031(1)	0.0008(0)	0.0012(1)	0.0022(0)
Cu(2)	0.0014(1)	0.0025(2)	0.021(2)	0.0000(0)	0.0011(1)	0.0000(0)
Rb(1)	0.0013(1)	0.0018(1)	0.020(1)	0.0000(0)	0.0009(1)	0.0000(0)
Rb(2)	0.0015(1)	0.0016(1)	0.019(1)	0.0000(0)	0.0010(1)	0.0000(0)

The anisotropic displacement factor exponent takes the form: $-2\pi^2\ [(ha^*)^2U_{11} + ... + 2hka^*b^*\ U_{12}]$

Table 5.9 Selected Distances (Å) and Bond Angles (deg) for $Rb_2Cu_3CeTe_5$ with Standard Deviations in Parentheses.

Bond Distances

Ce – Te1	3.161(1)	Cu2 – Te3	2.721(2)	Rb1 – Te3	3.710(1)
Ce – Te2	3.2538(5)	Cu2 – Te4	2.593(2)	Rb1 – Te4	3.720(2)
Ce – Te3	3.246(2)	Cu1 – Ce1	3.332(2)	Rb2 – Te1	3.694(2)
Ce – Te4	3.253(2)	Cu1 – Cu2	2.650(2)	Rb2 – Te2	3.854(2)
Cu1 – Te2	2.820(2)	Te1 – Te1	2.771(2)	Rb2 – Te3	3.681(2)
Cu1 – Te3	2.591(2)	Rb1 – Te1	3.707(2)	Rb2 – Te4	3.683(1)
Cu1 – Te4	2.593(2)	Rb1 – Te2	3.880(2)		

Bond Angles

Te1 – Ce – Te1	51.99(4)	Te2 – Cu1 – Te2	88.70(6)
Te1 – Ce – Te2	80.54(3)	Te3 – Cu1 – Te2	105.68(8)
Te1 – Ce – Te3	97.33(4)	Te3 – Cu1 – Te4	125.03(9)
Te1 – Ce – Te4	97.00(4)	Te3 – Cu2 – Te3	110.3(1)
Te2 – Ce – Te2	146.92(6)	Te3 – Cu2 – Te4	103.21(4)
Te3 – Ce – Te2	87.85(3)	Te4 – Cu1 – Te2	106.62(8)
Te3 – Ce – Te4	164.05(5)	Te4 – Cu2 – Te4	109.8(1)
Te4 – Ce – Te2	87.63(3)		

Ion Exchange Properties of K₂Ag₃CeTe₄ (1) - Solid-state ion-exchange reactions[22] were indeed performed in which the material was pressed with a fifty fold excess of AI (A = Li, Na, NH₄) and heated at 100°C for 5 days, see Scheme 1.

Scheme 1

$$K_2Ag_3CeTe_4 + 50x\ AI\ \xrightarrow{grind}\ \xrightarrow{press\ pellet}\ \xrightarrow{100°C/5d}\ A_xK_{2-x}Ag_3CeTe_4$$

The products were isolated by washing away the iodide matrix with methanol. The resulting materials appeared to be isostructural as judged by powder x-ray diffraction (Figure 5.7). Elemental analysis by EDS on the polycrystalline material also appeared to support the premise that the potassium had exchanged out of the channels in the framework, giving average compositions of $Li_{1.48}K_{0.52}Ag_3CeTe_4$, $Na_{1.55}K_{0.45}Ag_3CeTe_4$, and $(NH_4)_{1.35}K_{0.65}Ag_3CeTe_4$. Since EDS is a semiquantitative method, the polycrystalline materials were further characterized by ICP to obtain accurate values for the formula. The ICP results for the NaI reacted material were in agreement with those obtained by EDS giving a formula of $Na_{1.26}K_{0.74}Ag_3CeTe_4$. Considering that in typical ion-exchange reactions, multiple cycles are required for complete exchange, where the material has to be isolated and re-reacted with fresh reagents several times, the observed degree of ion-exchange in the first cycle for is remarkably high. Complete exchange is expected in subsequent cycles. The results obtained by ICP for the LiI and NH₄I reacted materials, however, did not agree with those results obtained by

EDS and seemed to indicate that the material exchanged to a much lesser degree. The difference between the two methods is that EDS is surface technique while ICP is a bulk technique. One postulation might be that the exchange for these materials occurred on the surface only and that this exchange was followed by decomposition. By EDS, only the surface of the material is probed which would give rise to the above formulas. If the decomposition product were amorphous, it would not show up in the powder x-ray diffraction pattern. The isomorphous x-ray powder diffraction pattern, however, would come from the amount of unexchanged material within the core of each particle.
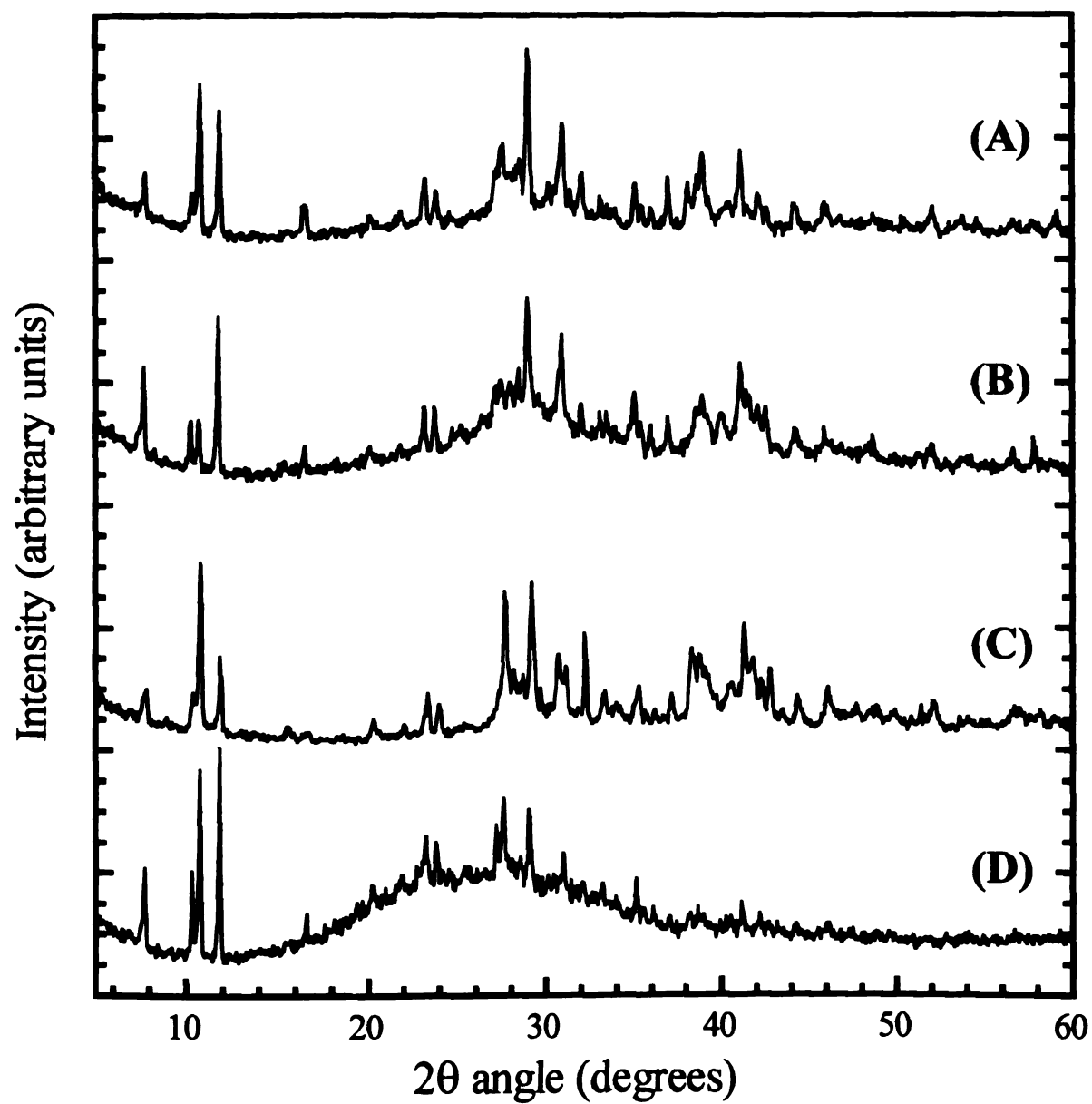
Figure 5.7 Powder XRD patterns of (A) pristine $K_2Ag_3CeTe_4$ before ion-exchange, (B) LiI + $K_2Ag_3CeTe_4$, (C) NaI + $K_2Ag_3CeTe_4$, and (D) NH_4I + $K_2Ag_3CeTe_4$

Magnetic Susceptibility and Infrared Spectroscopy - The magnetic susceptibility of $K_2Ag_3CeTe_4$ was measured over the range 5-300K at 6000G. A plot of $1/\chi_M$ vs T shows that the material follows Curie-Weiss Law with only slight deviation from linearity beginning below 50K, see Figure 5.8A Such deviation has been reported for several Ce^{3+} compounds and has been attributed to crystal field splitting of the cation's $^2F_{5/2}$ ground state.[23] At temperatures above 100K, a μ_{eff} of 2.19 μ_B has been calculated, which is in accordance with the usual range for Ce^{3+} compounds (2.3-2.5 μ_B). The presence of Ce^{3+} is confirmed by infra-red spectroscopy which shows five peaks at 3252 cm^{-1} (0.40 eV), 1648 cm^{-1} (0.20 eV), 1465 cm^{-1} (0.18 eV), 1374 cm^{-1} (0.17 eV), and 872 cm^{-1} (0.11 eV), see Figure 5.8B. These absorptions are electronic in origin and can be attributed to a f-f and/or f-d transition within the f^1 configuration of Ce^{3+}. From this data, it is evident that the material is valence precise and the formal oxidation states can be formalized as $(K^{1+})_2(Ag^{1+})_3(Ce^{3+})(Te^{2-})_4$.

The magnetic susceptibility of $Rb_2Cu_3CeTe_5$ was measured over the range 5-300K at 6000G, and a plot of $1/\chi_M$ vs T shows that the material exhibits nearly Curie-Weiss behavior with only slight deviation from linearity beginning below 50K, see Figure 5.9A. At temperatures above 150K, a μ_{eff} of 2.64μ_B has been calculated, which is in accordance with the usual range for Ce^{3+} compounds (2.3-2.5μ_B). The diffuse reflectance spectra was measured in the Mid-IR region for $Rb_2Cu_3CeTe_5$ and is shown in Figure 5.9B. One broad, well-defined, peak is

present at 3355cm^{-1} (0.42 eV), which could be attributed to a f-f and/or f-d transition within the f^1 configuration of Ce^{3+}. Another explanation may be that that water is being absorbed onto the crystals and this peak is coming from the O-H bending mode of water.

From this we can conclude that Rb$_2$Cu$_3$CeTe$_5$ is a valence precise compound, and thus should expect semiconducting behavior. The formal oxidation states can be formalized as (Rb^{1+})$_2$(Cu^{1+})$_3$(Ce^{3+})(Te^{2-})$_3$(Te$_2^{2-}$).
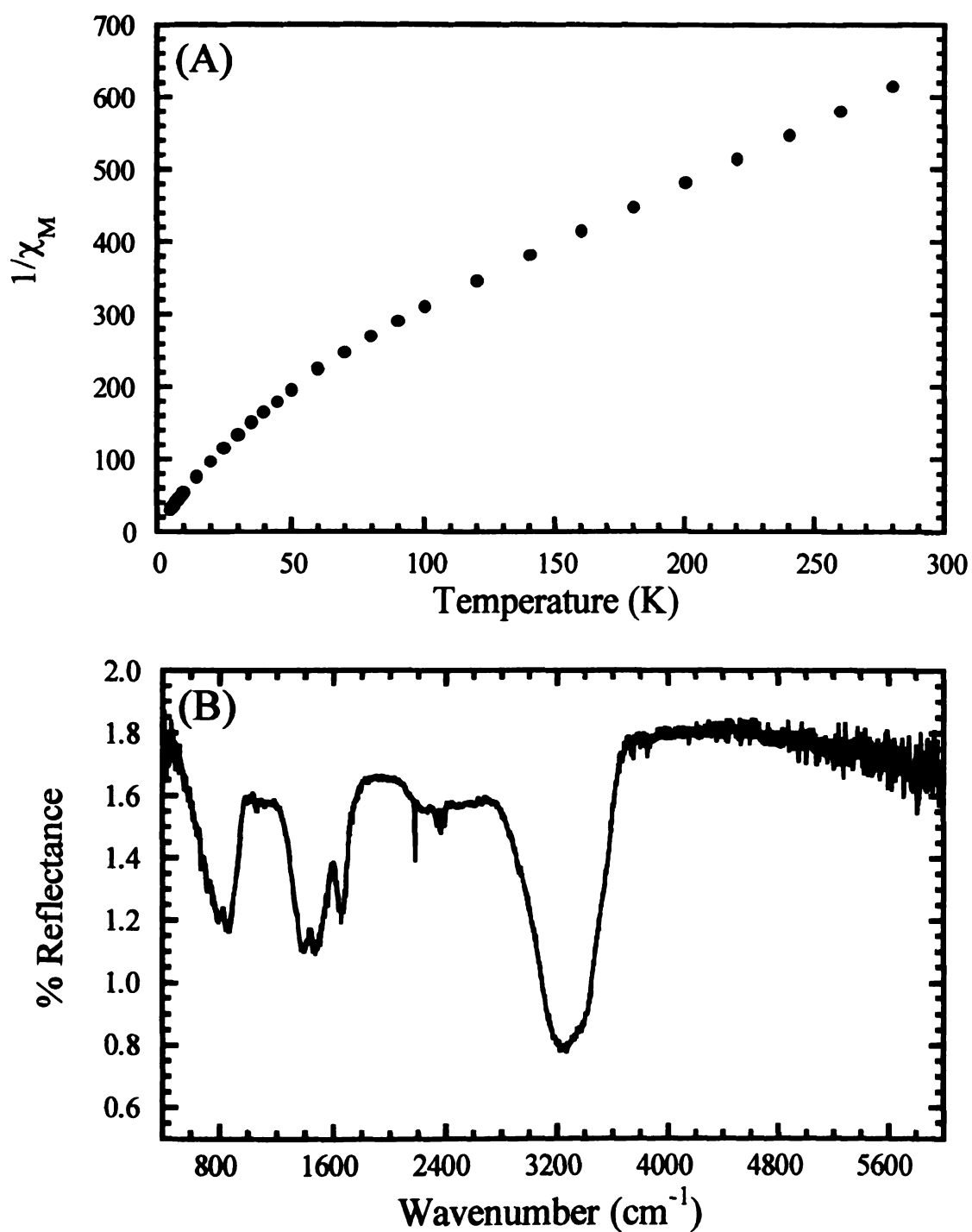
Figure 5.8 (A) Inverse molar magnetic susceptibility ($1/\chi_M$) plotted against temperature (2-300K) for $K_2Ag_3CeTe_4$. (B) Diffuse reflectance optical spectra of $K_2Ag_3CeTe_4$ (in the Mid-IR region).
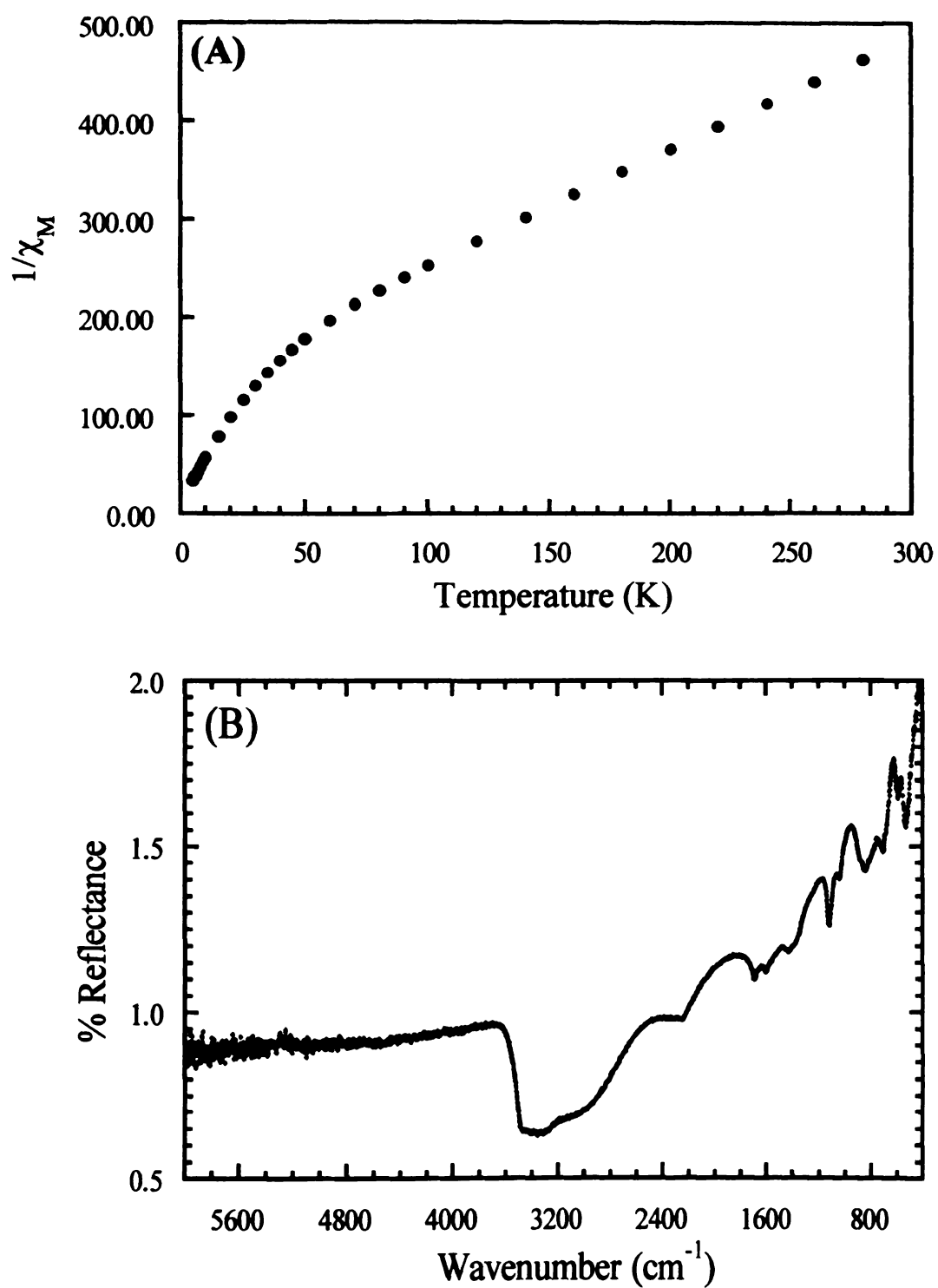
Figure 5.9 (A) Inverse molar magnetic susceptibility ($1/\chi_M$) plotted against temperature (2-300K) for $Rb_2Cu_3CeTe_5$. (B) Diffuse reflectance optical spectra of $Rb_2Cu_3CeTe_5$ (in the Mid-IR region).

Charge Transport Properties - Electrical conductivity data as a function of temperature for both a single crystal and a room temperature pressed pellet of $K_2Ag_3CeTe_4$ show that this material is a narrow gap semiconductor with room temperature values ranging from 0.1 S/cm for the single crystal to 0.01 S/cm for the pressed pellet, see Figure 5.10A. A bandgap of 0.36 eV was obtained by fitting the single crystal conductivity data to the semiconductor equation.[24] The thermopower data for two single crystals of $K_2Ag_3CeTe_4$ show very large Seebeck coefficients ranging from 500 to 700 $\mu V/K$, see Figure 5.10B The positive sign and decreasing Seebeck coefficient with falling temperature are also consistent with a p-type narrow gap semiconductor.

The electrical conductivity of $Rb_2Cu_3CeTe_5$ as a function of temperature measured on single crystals suggests that the material is also a narrow gap semiconductor with a room temperature value of 0.05 S/cm, see Figure 5.11A. A plot of $\log\sigma$ vs 1/T is nonlinear over the entire temperature range of 8-300 K, suggesting the conduction mechanism varies in different temperature regions, possibly due to different type of mid gap states. Thermoelectric power data as a function of temperature show a large Seebeck coefficient at room temperature of +275 $\mu V/K$, see Figure 5.11B. The increasing Seebeck coefficient with decreasing temperature and the positive sign are consistent with a p-type semiconductor.
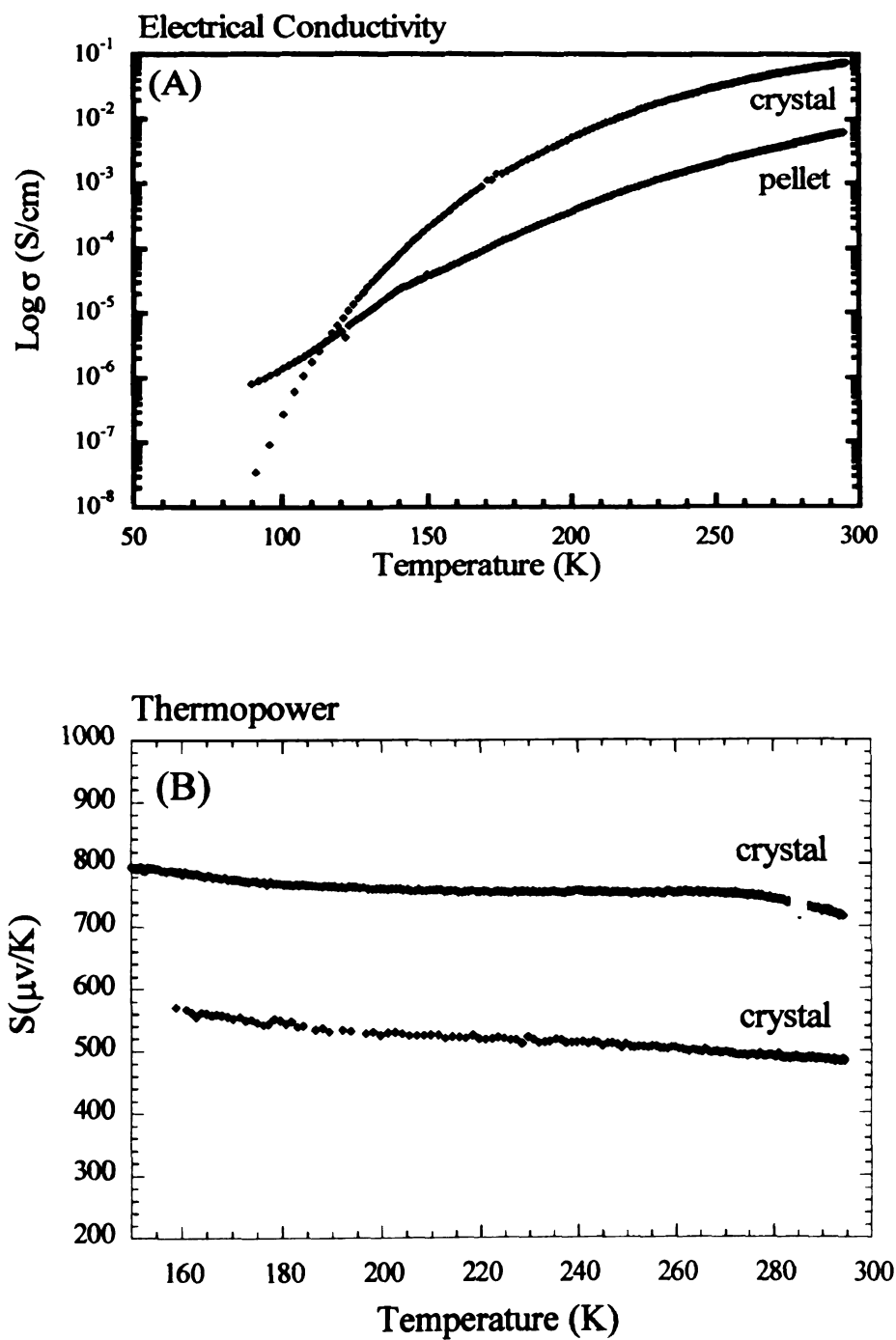
Figure 5.10 (A) Variable temperature, four probe electrical conductivity data for a single crystal and a pressed pellet of $K_2Ag_3CeTe_4$. (B) Variable temperature thermopower data for single crystals of $K_2Ag_3CeTe_4$.
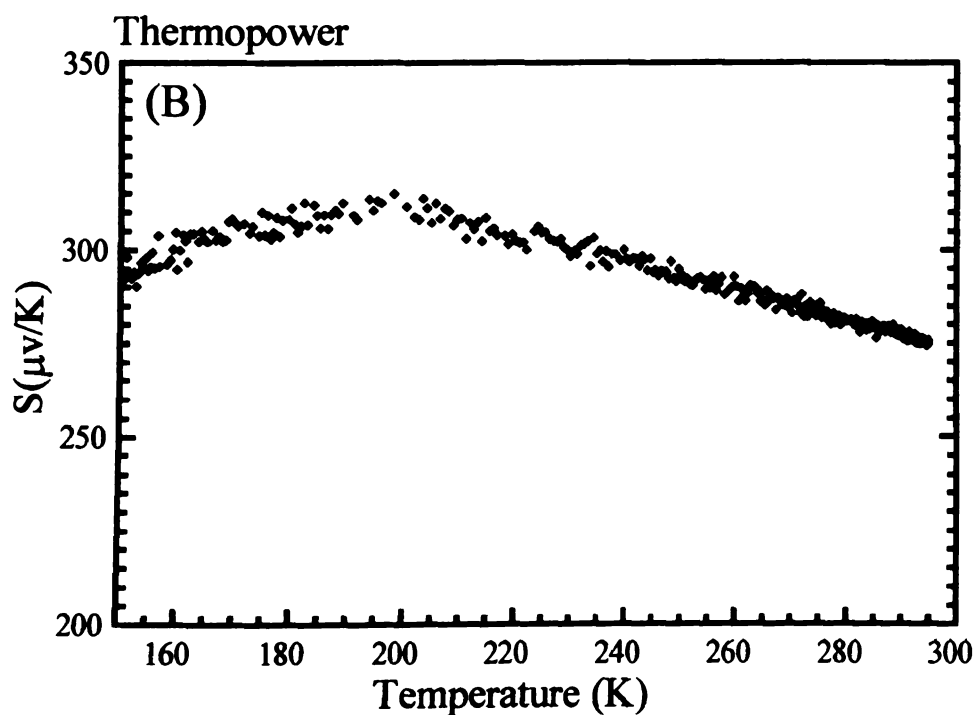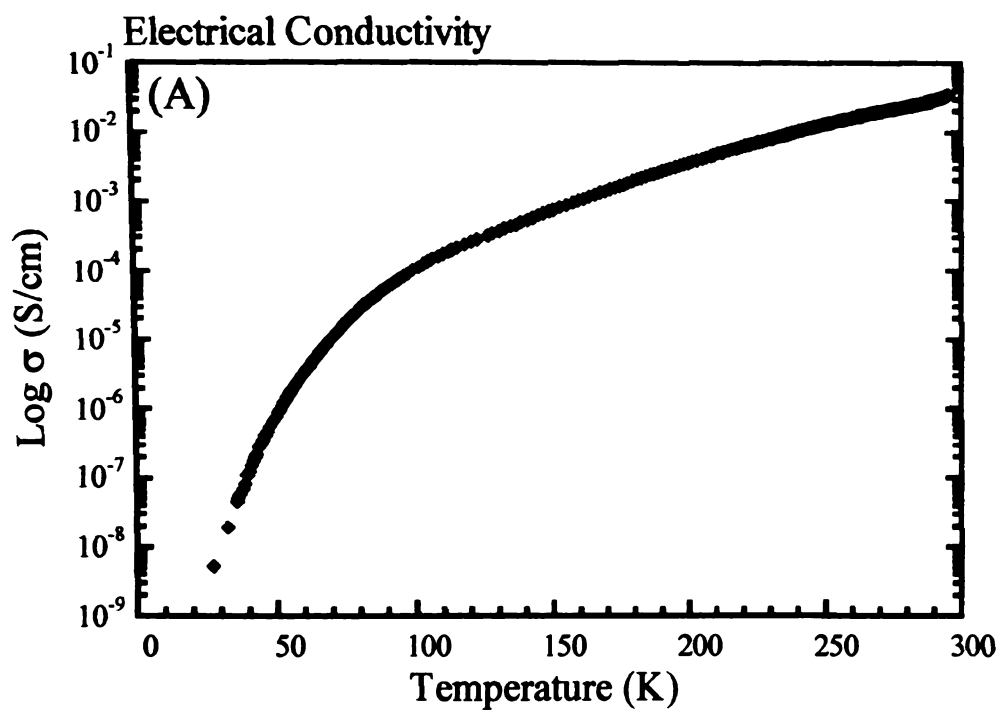
Figure 5.11 (A) Variable temperature, four probe electrical conductivity data for a single crystal of $Rb_2Cu_3CeTe_5$. (B) Variable temperature thermopower data for a single crystal of $Rb_2Cu_3CeTe_5$.

D. Conclusions

In summary, two new quaternary tellurides, $K_2Ag_3CeTe_4$ and $Rb_2Cu_3CeTe_5$, have been discovered by combining either copper or silver with cerium in alkali metal/polytelluride fluxes. Both compounds are "coinage metal rich" in their formulas and possess new structure types. While $K_2Ag_3CeTe_4$ is very unique in that it can undergo topotactic ion-exchange with sodium due to the large open cavities in its structure, $Rb_2Cu_3CeTe_5$ is interesting in that it is structurally related to both CuTe and $CeTe_3$. Both compounds are valence precise, and therefore behave as semiconductors. However, optical bandgaps were not able to be determined for either of these compounds due to the presence of f-f and/or f-d transitions that mask these regions in the diffuse reflectance IR spectra.

It is interesting to note that the formulas of these compounds are very similar, differing only by one Te. From this, one might question whether or not the reverse compounds, $K_2Ag_3CeTe_5$ and/or $Rb_2Cu_3CeTe_4$, exist. There was no evidence for the formation of either of these compounds, even though both formed under relatively similar synthetic conditions. This suggests that the structure types observed here are particularly unique and quite possibly only stabilized under these specific combination of elements.

269

References

[1] (a) Kanatzidis, M.G.; Sutorik, A.C. *Prog. Inorg. Chem.* **1995**, 43, 151 and references therein. (b) Pell, M.A.; Ibers, J.A. *Chem. Ber./ Recueil* **1997**, 130, 1.

[2] Norling, B.K.; Steinfink, H. *Inorg. Chem.* **1966**, 5, 1488.

[3] Krönert, V.W.; Plieth, K. *Z. Anorg. Allg. Chem.* **1965**, 336, 207.

[4] Sutorik, A.C., Kanatzidis, M.G. *Chem. Mater.* **1997**, 9, 387.

[5] (a) Cody, J.A.; Ibers, J.A. *Inorg. Chem.* **1996**, 16, 3273. (b) Wu, P.; Pell, M.A.; Ibers, J.A. *J. Alloys and Compd.* **1997**, 255, 106. (c) Choi, K.-S.; Patschke, R.; Billinge, S.J.L.; Waner, M.J.; Dantus, M.; Kanatzidis, M.G. *J. Am. Chem. Soc.* **1998**, 120, 10706.

[6] Patschke, R.; Heising, J.; Schindler, J.; Kannewurf, C.R., Kanatzidis, M.G. *J. Solid State Chem.* **1998**, 135, 111.

[7] Sutorik, A.C.; Albritton-Thomas, J.; Kannewurf, C.R.; Kanatzidis, M.G. *J. Am. Chem. Soc.* **1994**, 116, 7706.

[8] Sutorik, A.C.; Albritton-Thomas, J.; Hogan, T.; Kannewurf, C.R., Kanatzidis, M.G. *Chem. Mater.* **1996**, 8, 751.

[9] Cody, J.A.; Ibers, J.A. *Inorg. Chem.* **1995**, 34, 3165.

[10] (a) Wu. P.; Ibers, J.A. *J. Solid State Chem.* **1993**, 110, 156. (b) Christuk, A.E.; Wu, P.; Ibers, J.A. *J. Solid State Chem.* **1994**, 110, 330. (c) Wu. P.; Ibers, J.A. *J. Solid State Chem.* **1994**, 110, 337.

[11] Huang, F. Q.; Choe, W.; Lee, S; Chu, J.S. *Chem. Mater.* **1998**, 10, 1320.

[12] Bensch, W.; Dürichen, P. *Chem. Ber.* **1996**, 129, 1489.

[13] Patschke, R.; Brazis, P.; Kannewurf, C.R.; Kanatzidis, M.G. *Inorg. Chem.* **1998**, 37, 6562.

[14] Patschke, R.; Brazis, R.; Kannewurf, C.R.; Kanatzidis, M.G. *J. Mater. Chem.* **1998**, 8, 2587.

[15] SMART: Siemens Analytical Xray Systems, Inc., Madison, WI, 1994.

[16] SAINT: Version 4.0, Siemens Analytical Xray Systems, Inc., Madison WI, 1994-1996.

[17] SADABS: Sheldrick, G.M. University of Göttingen, Germany, to be published.

[18] Sheldrick, G.M. SHELXTL, Version 5; Siemens Analytical Xray Systems, Inc.; Madison, WI, 1994.

[19] Stowe, H.D.; Braselton, W.E.; Kaneene, J.B.; Slanker, *Am. J. Vet. Res* **1985**, 46, 561.

[20] The Te-Te stretch exhibits a Raman shift at ~160 cm^{-1}.

[21] Savelsberg, G; Schäfer, H. *Z. Naturforsch, B.* 1978, **33b**, 370-373.

[22] Chondroudis, K.; Kanatzidis, M.G. *J. Am. Chem. Soc.* **1997**, 119, 2574. (c) Chondroudis, K.; Kanatzidis, M.G. *J. Solid State Chem.* **1998**, 136, 328. (d) Hanko, J.A.; Kanatzidis, M.G. *Angew. Chem. Intl. Ed. Engl.* **1998**, 37, 342.

[23] Greenwood, N.N; Earnshaw, A. *Chemistry of the Elements*; Pergamon Press: New York, 1984; p1443.

[24] (a) Smith, R.A.; *Semiconductors*, 2nd ed.; Cambridge University Press: Cambridge, New York, 1978; p19. (b) Wold, A.; Dwight, K. *Solid State Chemistry: Synthesis, Structure, and Properties of Selected Oxides and Sulfides*; Chapman & Hall: New York, 1993, p 35.

Chapter 6

Cu$_x$UTe$_3$ (x = 0.25 and 0.33): Stabilization of UTe$_3$ in the

ZrSe$_3$ Structure Type via Copper Insertion

A. Introduction

Recently, a survey of the structural chemistry of both ternary and quaternary uranium (and thorium) chalcogenides was presented.[1] Among the most notable in this class include $CsUTe_6$,[2] $Cs_8Hf_5UTe_{30.6}$,[2] $AMUQ_3$ (A = alkali or alkaline earth metal, M=3d metal, Q = S, Se, Te),[2b,3] $CsTiUTe_5$,[2b] $Tl_{0.56}UTe_3$,[4] $K_2UP_3Se_9$,[5] and $Rb_4U_4P_4Se_{26}$.[6] Even more recently, we have described the three novel quaternary uranium chalcogenides, $K_6Cu_{12}U_2S_{15}$,[7] KU_2SbSe_8,[8] and RbU_2SbS_8.[8] Here, we report on our investigations into the copper uranium telluride system which afforded the interesting new compound, Cu_xUTe_3 (x = 0.25 and 0.33). Only two other ternary copper uranium chalcogenide phases have been reported (i.e.: $Cu_2U_3Q_7$[9] and $Cu_2U_6Q_{13}$ (Q=S, Se)[10]) which were found in the sulfide and selenide systems. Although formulated differently, Cu_xUTe_3 (x = 0.25 and 0.33) is isostructural to the previously reported phase, $CuTh_2Te_6$[11] and adopts the layered $ZrSe_3$-structure type. Structurally, these ternary compounds derive from the parent binary layered phases by inserting copper atoms between the layers. The occupancy of the copper site ranges from 0.25 to 0.50. In this sense, these compounds can be compared to the intercalation compounds, Li_xZrQ_3 (0 < x ≤ 3).[12,13] The insertion of a metal atom between these $ZrSe_3$-type layers is, in fact, not unusual. In addition to the Li_xZrSe_3 (0 < x ≤ 3) phases, a series of compounds with the formula ATh_2Q_6 (A = K, Rb, and Cs; Q = Se and Te)[14] has been reported where an alkali metal cation has been inserted between the $ZrSe_3$-type layers, now ThQ_3 (Q = Se and Te). Here, we report on the structure and physicochemical

properties of Cu_xUTe_3 (x = 0.25 and 0.33) and discuss it with respect to the parent binary phase, α–UTe_3.

B. Experimental Section

1. Reagents. The following reagents were used as obtained: (i) copper powder, 99.9% pure, Fisher Scientific Co., Fairlawn, N.J. (ii) uranium powder, 99.7% pure, 60 mesh, Cerac, Milwaukee, WI; (iii) tellurium shots, 99.9% pure, Noranda Advanced Materials, Saint-Laurent, Quebec, Canada.

2. Synthesis – All manipulations were carried out under a dry nitrogen atmosphere in a Vacuum Atmospheres Dri-Lab glovebox.

Cu_xUTe_3 (x = 0.25 and 0.33). Amounts of 0.076 g (3.0 mmol) of Cu, 0.095 g (1.0 mmol) of U, and 0.204 g (4.0 mmol) of Te were weighed into a vial in an N_2-filled glovebox. The starting materials were mixed thoroughly and loaded into a carbon-coated silica ampoule. The ampoule was then evacuated to < 1 x 10^{-4} mbar and flame-sealed. In a computer-controlled furnace, the reaction was heated to 800°C over 36 hours, held at that temperature for 6 days, cooled to 400°C at 4°C/h, further cooled to 100°C at 6°C/h and quenched to 50°C. The ampoule was opened in air to reveal the product, which consisted of purple cubes (25%), black powder (25%) and silver needles and plates (50%). All entities of the product are air- and water-stable. The purple cubes and black powder were identified by semiquantitative energy dispersive spectroscopy (EDS) to be Cu_2Te and UTe_3, respectively. The silver needles and plates gave the same average composition of $Cu_{0.26}U_{1.0}Te_{2.7}$.

3. Physical Measurements - The instrumentation and experimental setup for the following measurements are the same as described in Chapter 2, Section 3: Semiquantitative Energy Dispersive Spectroscopy (EDS), Powder X-ray Diffraction, Transmission Electron Microscopy, and Charge Transport Measurements.

X-ray Crystallography – For reasons outlined in the results and discussion section, several crystals were examined crystallographically. *Crystal #1:* A single crystal with dimensions of 0.02 x 0.05 x 0.10 mm was mounted on the tip of a glass fiber. Intensity data were collected at room temperature on a Rigaku AFC6S four-circle automated diffractometer equipped with a graphite-crystal monochromator. The unit cell parameters were determined from a least-squares refinement using a setting angles of 20 carefully centered reflections in the $8° \leq 2\theta \leq 30°$ range. The data were collected with an ω-2θ scan technique over one-quarter of the sphere of reciprocal space, up to $60°$ in 2θ. Crystal stability was monitored with three standard reflections whose intensities were checked every 150 reflections. No significant decay was detected during the data collection period. An empirical absorption correction based on ψ-scans was applied to all data during initial stages of refinement. The structure was solved by direct methods using SHELXTL[15] package of crystallographic programs. *Crystals #2 and #3:* Single crystals with dimensions of 0.03 x 0.05 x 0.08 mm for crystal #2 and 0.03 x 0.04 x 0.10 mm for crystal #3 were mounted on the tip of a glass fiber.

Intensity data were collected at 173.1K for Crystal #2 and room temperature for Crystal #3 on a Siemens SMART Platform CCD diffractometer using graphite monochromatized Mo Kα radiation. The data were collected over a full sphere of reciprocal space for both crystals, up to 56° in 2θ. The individual frames were measured with an ω rotation of 0.3° and an acquisition time of 60sec for crystal #2 and 30sec for crystal #3. The SMART[16] software was used for the data acquisitions and SAINT[17] for the data extractions and reductions. The absorption corrections were performed using SADABS.[18] The structures were solved by direct methods using the SHELXTL[15] package of crystallographic programs. The complete data collection parameters and details of the structure solutions and refinements for all three crystals are given in Table 6.1.

Table 6.1. Crystallographic Data for Cu_xUTe_3 (x = 0.25 and 0.33)

	Crystal #1	Crystal #2	Crystal #3
Chemical Formula	$Cu_{0.25}UTe_3$	$Cu_{0.33}UTe_3$	$Cu_{0.25}UTe_3$
crystal habit, color	needle, black	needle, black	needle, black
Diffractometer	Rigaku AFC6S	Siemens SMART Platform CCD	Siemens SMART Platform CCD
Radiation	Mo-Kα (0.71073Å)	Mo-Kα (0.71073Å)	Mo-Kα (0.71073Å)
Crystal Size, mm^3	0.02 x 0.05 x 0.10	0.03 x 0.05 x 0.08	0.03 x 0.04 x 0.10
Temperature, K	293	173	293
Crystal System	Monoclinic	Monoclinic	Monoclinic
Space Group	$P2_1/m$ (#11)	$P2_1/m$ (#11)	$P2_1/m$ (#11)
a, Å	6.0944(11)	6.0901(12)	6.0838(12)
b, Å	4.2158(11)	4.2083(8)	4.2140(8)
c, Å	10.3668(9)	10.335(2)	10.361(2)
β, deg	98.874(10)	98.95(3)	98.83(3)
V, $Å^3$	263.16(9)	261.66(9)	262.47(9)
Z	2	2	2
μ, mm^{-1}	47.936	48.529	48.063
index ranges	$0 \leq h \leq 9$	$0 \leq h \leq 7$	$-8 \leq h \leq 7$
	$0 \leq k \leq 6$	$-5 \leq k \leq 5$	$-5 \leq k \leq 5$
	$-15 \leq l \leq 15$	$-13 \leq l \leq 13$	$-13 \leq l \leq 13$
$2\theta_{max}$, deg	60	56	56
total data	1065	692	2521
unique data	1064	691	692
R(int)	N/A	N/A	0.0439
no. parameters	32	32	32
final R1/wR2[a], %	6.26/20.08	5.04/11.80	4.13/10.42
Goof	1.139	1.047	1.190

[a]$R1 = \Sigma (|F_o| - |F_c|) / \Sigma |F_o|$ $wR2 = \{\Sigma[w(F_o^2 - F_c^2)^2] / \Sigma [w (F_o^2)^2]\}^{1/2}$

All structures were solved and refined using the SHELXTL-5 package of crystallographic programs.[15] SHELXTL refines on F^2. An empirical absorption correction was performed during the initial stages of each refinement (based on Ψ-scans for Crystal #1 and SADABS[18] for Crystal #2 and #3).

C. Results and Discussion

Structure Description - The observed crystal structure of Cu_xUTe_3 (x = 0.25 and 0.33) viewed down the b-axis is shown in Figure 6.1. The three-dimensional framework is built from layers very similar to those found in $ZrSe_3$, which are linked together by copper atoms. In α-UTe_3, which adopts the $ZrSe_3$-structure type, each U atom is coordinated to eight Te atoms in a bicapped trigonal prismatic environment. These trigonal prisms stack in one-dimension to form wedge-shaped columns by sharing triangular faces. Layers are then formed when neighboring columns share both their capping and apex monotellurides, see Figure 6.2A. Within these layers, there are ditelluride units that orient with their Te-Te bonds parallel to the a-axis. The Te-Te bond distances are 2.751(1)Å within the ditelluride units and 3.350(1) Å between them. In Cu_xUTe_3 (x = 0.25 and 0.33), however, the Te-Te distances (Te2-Te3 = 3.098(2)Å, Te3-Te2 = 2.987(2) Å) are almost equal, giving rise to infinite chains running along the [100] direction. The copper atom is stabilized in a distorted tetrahedral geometry and sits on a mirror plane, which generates a pair of crystallographically related sites. The distance between these two sites is 2.556Å. Although this Cu-Cu distance is reasonable, the copper atoms probably do not sit on both sites at the same time due to the partial occupancy on this site. The fractional atomic coordinates, isotropic and anisotropic temperature factors, bond distances, and bond angles for Crystal #3 are given in Tables 6.2-6.4.

The cell parameters of Cu_xUTe_3 (x = 0.25 and 0.33), compared to those of α-UTe_3, show only a slight expansion along the c-axis of 0.0548Å and a slight increase in the volume of 0.27Å^3. Consequently, there is essentially no shift in the positions of the peaks in the x-ray powder diffraction pattern. As a result, Cu_xUTe_3 (x = 0.25 and 0.33) cannot be readily distinguished from the α-UTe_3 by casual comparison of the two patterns.

The structure of Cu_xUTe_3 (x = 0.25 and 0.33) is similar to that of $Tl_{0.56}UTe_3$[4] (Figure 6.3). It is therefore instructive to compare these two structures and understand the differences they pose. Both compounds are built from layers of α-UTe_3 with metal atoms inserted between them on partially occupied sites. The difference, however, lies in both the way that the UTe_3 layers stack with respect to one other and how the metal cations insert between these layers. In Cu_xUTe_3 (x = 0.25 and 0.33), the layers of UTe_3 stack in such a way that tetrahedral pockets are formed between the layers for the copper atoms to reside. In $Tl_{0.56}UTe_3$, the layers shift with respect to one another so that a larger, square prismatic pocket is formed for the much larger thallium atom to reside. This shift in the layers completely changes the symmetry of the compound. While Cu_xUTe_3 (x = 0.25 and 0.33) remains isostructural to the α-UTe_3 (monoclinic), $Tl_{0.56}UTe_3$ is orthorhombic.
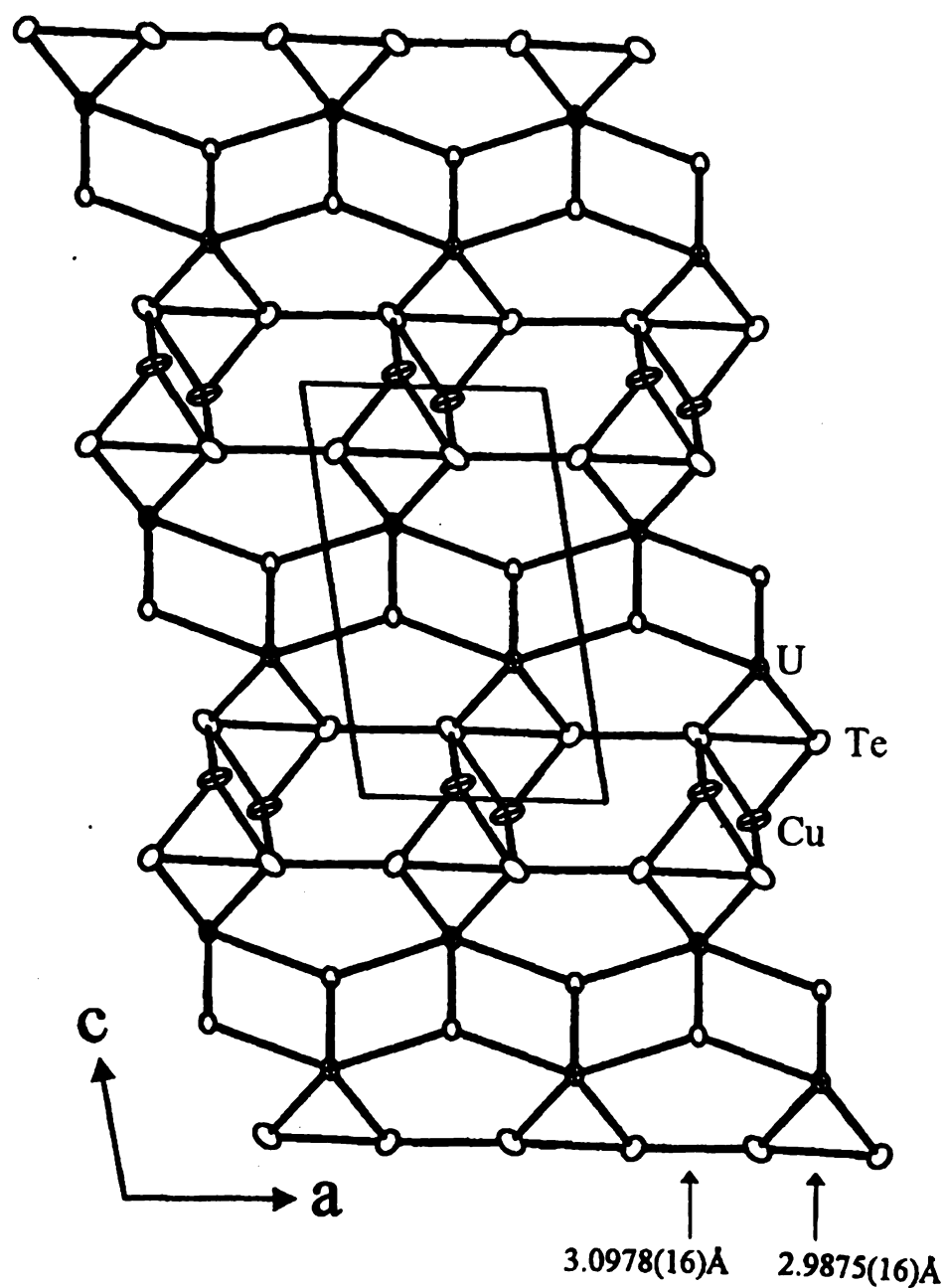
Figure 6.1 ORTEP representation of the structure of Cu_xUTe_3 (x = 0.25, 0.33) as seen down the b-axis (80% ellipsoids). The ellipses with octant shading represent U atoms. The crossed ellipses represent Cu atoms and the open ellipses represent Te atoms.

Table 6.2. Fractional Atomic Coordinates (x 10^4) , Equivalent Isotropic Displacement Parameters (Å^2 x 10^3), and occupancies for $Cu_{0.25}UTe_3$ (Crystal #3) with Estimated Standard Deviations in Parentheses.

atom	x	y	z	U_{eq}^{a}, Å^2	Occ.
U	0.7914(1)	1/4	0.1629(1)	0.0009(1)	1
Te(1)	0.2659(2)	1/4	0.0599(1)	0.0009(1)	1
Te(2)	0.4007(2)	1/4	0.6620(1)	0.0014(1)	1
Te(3)	0.9114(2)	1/4	0.6685(1)	0.0016(1)	1
Cu	0.0930(15)	1/4	0.4656(7)	0.0019(2)	0.25

$^{a}U_{eq}$ is defined as one-third of the trace of the orthogonalized U_{ij} tensor.

Table 6.3 Anisotropic Displacement Parameters (Å^2) for $Cu_{0.25}UTe_3$ (Crystal #3) with Estimated Standard Deviations in Parentheses

	U11	U22	U33	U12	U13	U23
U	0.0008(1)	0.0005(1)	0.0013(1)	0	0.0001(1)	0
Te(1)	0.0007(1)	0.0009(1)	0.0011(1)	0	0.0001(1)	0
Te(2)	0.0016(1)	0.0011(1)	0.0017(1)	0	0.0007(1)	0
Te(3)	0.0019(1)	0.0011(1)	0.0018(1)	0	-0.0004(1)	0
Cu	0.0034(5)	0.0013(4)	0.0012(3)	0	0.0010(4)	0

The anisotropic displacement factor exponent takes the form: $-2\pi^2$ [h^2a^2 U11 + ... + 2hka*b*U12]

Table 6.4 Selected Distances (Å) and Bond Angles (deg) for $Cu_{0.25}UTe_3$ (Crystal #3) with Standard Deviations in Parentheses

Bond Distances

U – Te1	3.1026(10) x 4		Cu – Te2	2.509(4) x 4
U – Te2	3.1272(13) x 4		Cu – Te3	2.540(9) x 2
U – Te3	3.1193(11) x 4		Te2 – Te3	3.1019(19) x 2

Bond Angles

Te1 – U – Te1	85.47(3)	76.01(3)	76.14(3)	141.75(4)
Te1 – U – Te2	151.72(3)	87.98(3)	75.58(3)	128.73(2)
Te1 – U – Te3	149.46(4)	86.98(3)	130.24(3)	73.45(3)
Te2 – U – Te3	57.10(3)	84.66(4)	111.45(3)	
Te2 – Cu – Te3	72.3(2)	112.6(2)		
Te3 – Cu – Te3	119.4(2)	113.3(3)		

ZrSe₃ type (α-UTe₃)   NdTe₃ type (β-UTe₃)
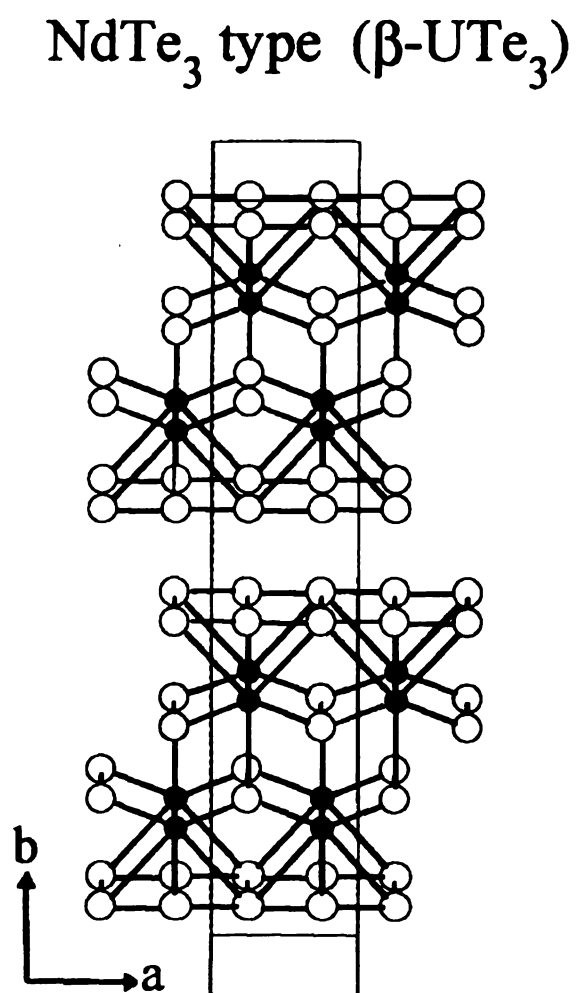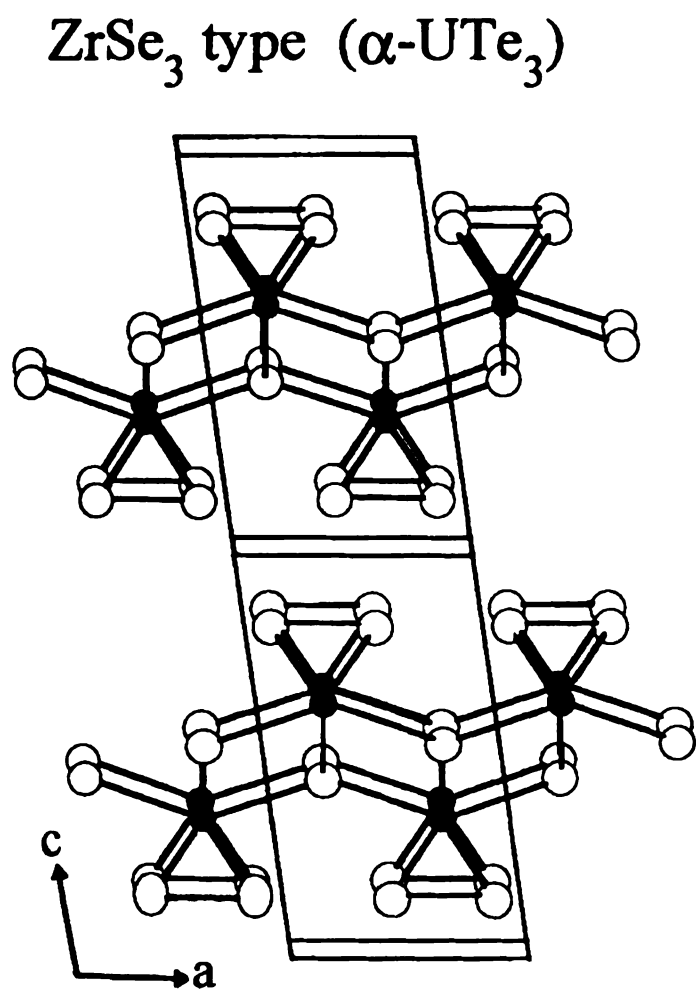
Figure 6.2 Extended stuctures of (A) α-UTe₃ and (B) β-UTe₃.

283
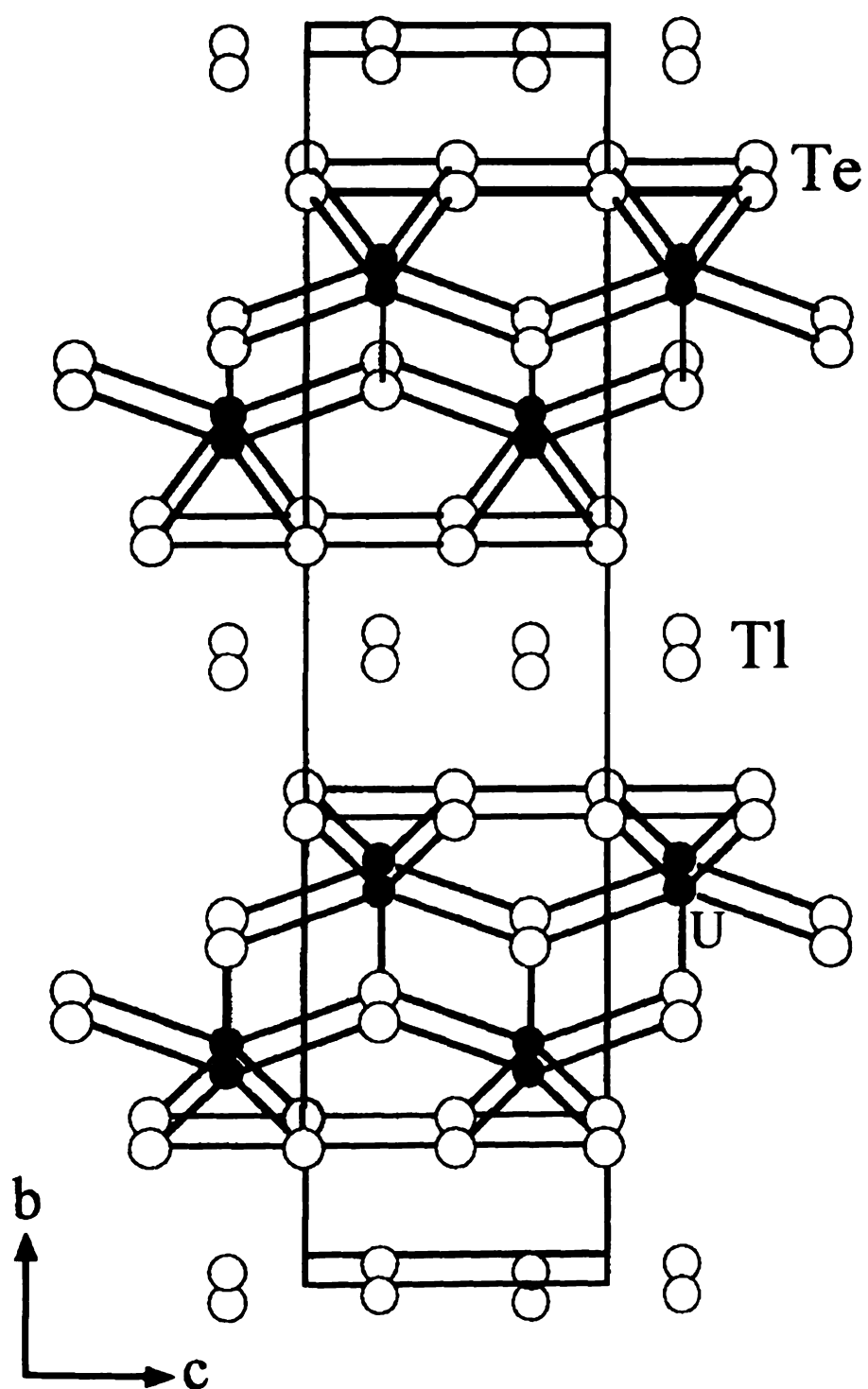
Figure 6.3 Extended structure of $Tl_{0.56}UTe_3$ as seen down the b-axis.

α- vs β-type UTe₃. After the crystals of Cu_xUTe_3 (x = 0.25 and 0.33) were discovered in the reaction mixture, efforts were made to synthesize the compound as a single phase through a rational synthesis. Since reactions of direct combination led to a mixture of Cu_xUTe_3 (x = 0.25 and 0.33) as well as both the α- and β-type[19] UTe_3, we decided to prepare α-UTe_3 as a starting material for further reaction with copper in a second step. The problem that we encountered was that the α–UTe_3 is less thermodynamically stable than the β-UTe_3, making it difficult to prepare pure. The structural difference between the α- and β-UTe_3 lies in the coordination environment of the uranium atoms. As previously described, α-UTe_3 (Figure 6.2A) consists of uranium atoms that are eight coordinate bicapped trigonal prismatic with rows of ditelluride atoms above and below the layers of uranium atoms. In β-UTe_3, which adopts the $NdTe_3$ structure type (see Figure 6.2B), the uranium atoms expand their coordination sphere to include nine Te atoms in a tricapped trigonal prismatic arrangement. β-UTe_3 is structurally more dense and, as a result, the tellurium atoms above and below the plane of uranium atoms are best described as a square Te net. The literature reports the following synthesis to make α-UTe_3.[20]

$$U + 3Te \xrightarrow[\text{1 week}]{650°C} grind \xrightarrow[\text{1 week}]{650°C} \alpha\text{-}UTe_3 \qquad (eq.1)$$
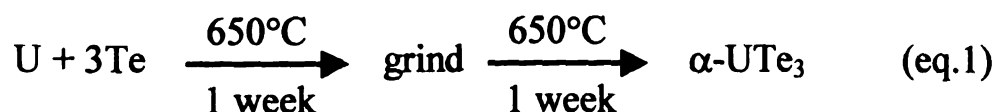
Our attempts to reproduce this synthesis, however, resulted only in β-UTe$_3$. An added complication derived from the fact that there exist several other U$_x$Te$_y$ binary compounds with similar compositions (i.e.: UTe$_{1.87}$,[21] UTe$_2$,[20,22] UTe$_{3.38}$,[20,21,23] UTe$_{3.4}$,[20,24] U$_2$Te$_3$,[25] UTe$_5$,[20,26] U$_2$Te$_5$,[20,27] U$_3$Te$_5$,[28] and U$_7$Te$_{12}$[29]). In order to avoid these binary phases, a series of reactions were run with a U:Te ratio of 1:2.5 and the products were monitored as a function of time over the course of 5 days while heating at 525°C. After one day, the product was determined by powder X-ray diffraction to be pure α-UTe$_3$. The powder patterns surprisingly did not change up to 5 days. These results indicate that at a 1:2.5 ratio, α-UTe$_3$ will consistently form as a pure product. In fact, it does not matter which temperature is chosen for this reaction to occur. As long as the ratio is 1:2.5, the mixture can be heated as high as 900°C for 7 days and α-UTe$_3$ will form as a pure product. When the ratio is changed to 1:3, however, the results were quite different. A second series of reactions were performed where U and Te were mixed in a ratio of 1:3 and heated to 650°C from 1 day to 11 days, see Figure 6.4. After two days, the product was a mixture of the α- and β-UTe$_3$. After 5-7 days, the product was still a mixture but the peaks corresponding to the β-UTe$_3$ grew in intensity while those corresponding to the α-UTe$_3$ decreased in intensity. After 11 days, the product consisted of β-UTe$_3$ only. Finally, a set of experiments was conducted where the U to Te ratio was chosen to be 1:2.5, 1:3.0, 1:3.5, 1:4.0, and 1:4.5. The results are summarized in Table 6.5. From these experiments, it can

be concluded that α-UTe$_3$ is less thermodynamically stable than β-UTe$_3$ at a U:Te ratio of 1:3 and that the product formed depends more strongly on the amount of tellurium added rather than the temperature or time chosen for the reaction to occur.
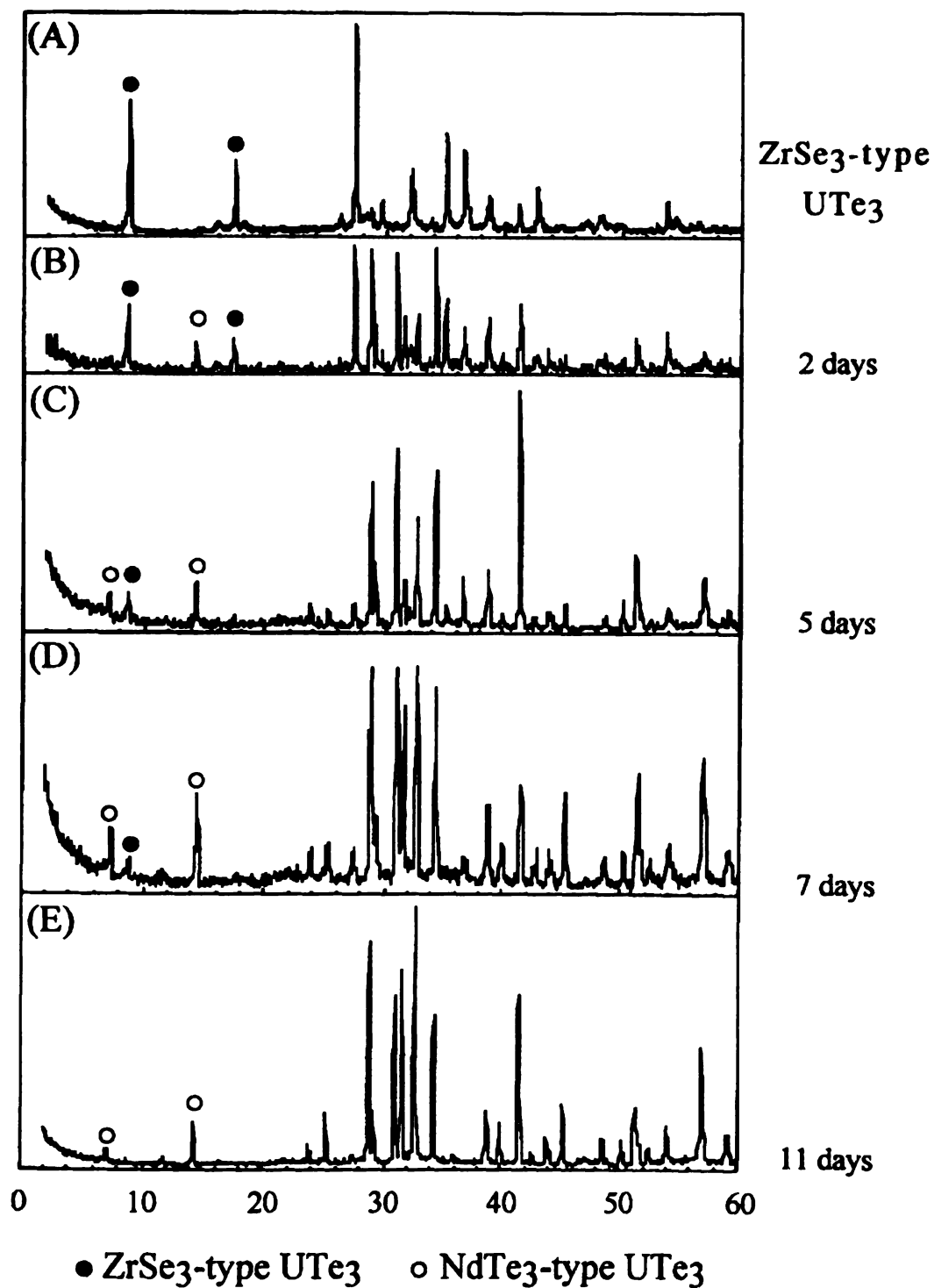
Figure 6.4 X-ray powder diffraction patterns of (A) α-UTe$_3$ and (B)-(E) the products of 1U + 3Te heated to 650°C for 2days, 5days, 7days, and 11 days.

Table 6.5 Relative Stability of the UTe_3 structure types as a function of amount of tellurium added. The reaction was heated to 650° C for one week.

Reaction	Product(s)
1U + 2.5Te	α - UTe_3
1U + 3.0Te	α - and β - UTe_3
1U + 3.5Te	α - and β - UTe_3
1U + 4.0Te	β - UTe_3
1U + 4.5Te	β - UTe_3

The products were determined by powder x-ray diffraction

Once the α-UTe$_3$ was prepared pure, it was used as a starting material for further reaction with copper.

$$xCu + \alpha\text{-UTe}_3 \longrightarrow Cu_xUTe_3 \qquad \text{(eq. 2)}$$

Mixtures of Cu and α–UTe$_3$ in the ratio of 0.25, 0.33, 0.5, 0.75, 1.0, 1.25, and 1.5 to 1.0 were pressed into pellets and heated at 300° C for 2 days in a 13mm pyrex ampoule that was flame sealed under vacuum. *(Note: the Cu metal was first activated by filtering it with copious amounts of dilute hydrochloric acid. If this step is not taken, the oxide coating on the Cu metal prevents it from reacting with the α–UTe$_3$).* The idea was that under mild heating conditions and close physical packing, the copper would be able to insert between the layers of UTe$_3$ and transform to the ternary Cu_xUTe_3 (x = 0.25 and 0.33) phase. As discussed earlier, there is no recognizable difference in the positions of the peaks in the x-ray powder pattern of Cu_xUTe_3 (x = 0.25 and 0.33) compared to that of α-UTe$_3$. However, if the peaks corresponding the elemental copper, which are clearly distinguishable, decrease in intensity or even disappear, this could be evidence for the fact that the copper has inserted between the layers of α-UTe$_3$ and transformed to Cu_xUTe_3 (x = 0.25 and 0.33). The powder patterns of the elemental Cu, the reaction of 0.5Cu + 1.0 α–UTe$_3$ before heating, and the product of 0.5Cu + 1.0 α–UTe$_3$ after heating are shown in Figure 6.5. The peaks from the elemental copper have noticeably disappeared in the product, suggesting that the Cu has successfully been inserted between the layers. The EDS analysis gives an average

composition of $Cu_{0.18}UTe_3$, confirming that there is indeed copper in the product. In order to really determine whether or not the Cu has inserted between the layers, however, more evidence is needed. We are currently in collaboration with Professor Simon Billinge (Dept of Physics, Michigan State University) to study these samples by PDF (pair distribution function). PDF analysis could potentially be very helpful since this technique is capable of probing for and detecting Cu-Te bond distances.
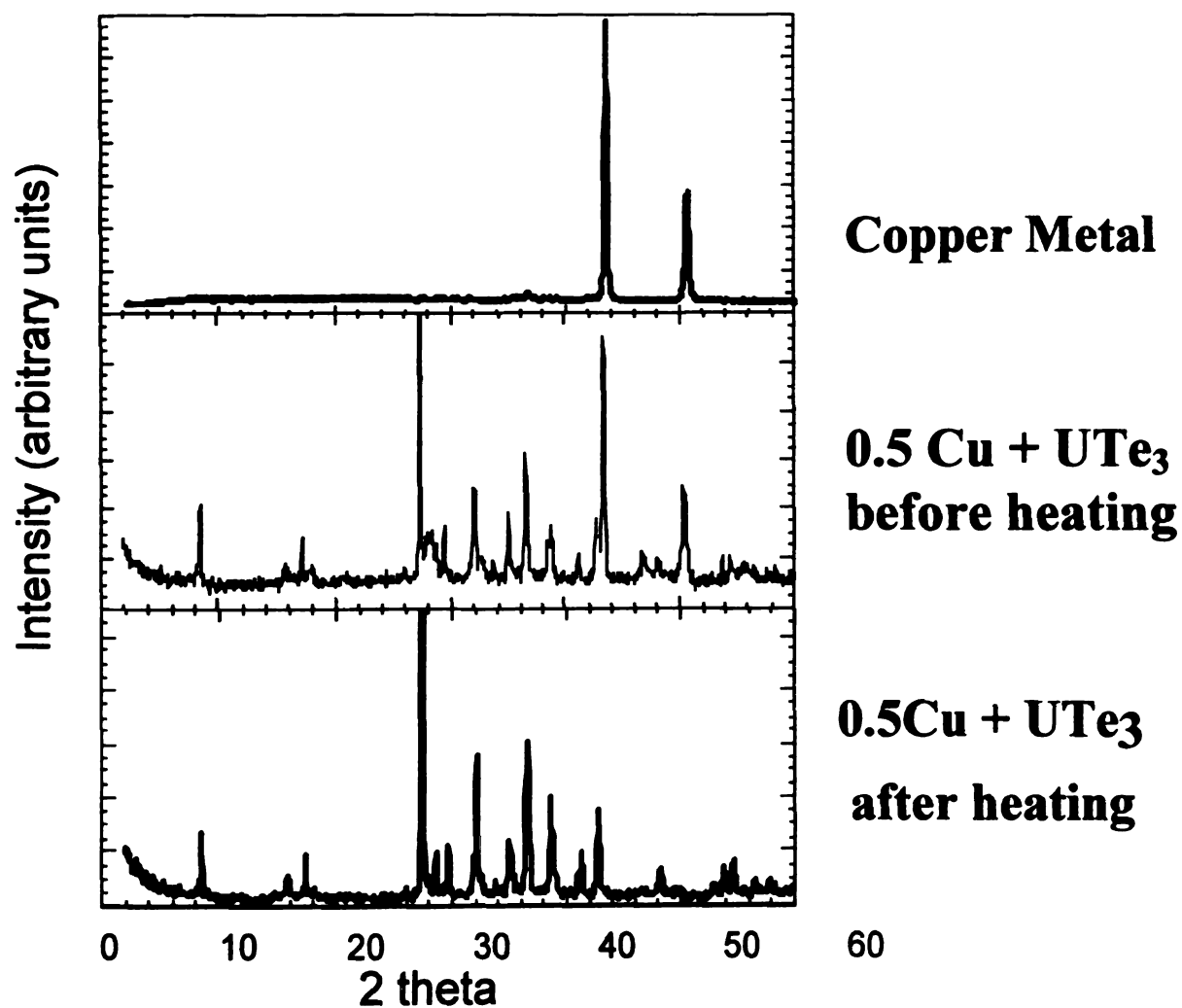
Figure 6.5 Powder x-ray diffraction patterns of (A) elemental copper, (B) 0.5 Cu + 1.0 α–UTe₃ before heating, and (C) 0.5 Cu + 1.0 α–UTe₃ after heating.

Superstructure - In order to balance the charges of Cu_xUTe_3 (x = 0.25 and 0.33), one must understand how the insertion of copper has affected the UTe_3 framework. In order to accommodate the extra +0.25 and +0.33 charge, some atoms in the framework must be reduced. Due to the close proximity of the infinite Te chains in the structure to the copper atoms, it is most likely that these Te atoms are acting as the electron acceptors. This means that some of the Te_2^{2-} units in the parent UTe_3 structure will be reductively cleaved as indeed is observed crystallographically, see Figure 6.1 and Table 6.4. Therefore, a reasonable formula would be $(Cu^+)_x(U^{+4})(Te^{2-})(Te^{1-x})_2$ and it is possible that such a reduction could cause a subtle superstructure to form whereby some of the Te-Te bonds in the chain are broken. Perhaps a clue for the presence of a superstructure comes from the anisotropic temperature factors, U11 and U33, for the Te atoms in the chains (Te2 and Te3), which are larger than those of the uranium and Te1 atoms, see Table 6.3.

Transmission Electron Microscopy - To probe for such a superstructure, we used electron diffraction. Since it was not yet clear as to how the x-value of Cu_xUTe_3 (x = 0.25 and 0.33) would affect any present modulation, the same crystals used for the x-ray structure determination (Crystal #2 and #3) were carefully removed from the glass fiber and prepared for study by transmission electron microscopy (TEM). Both crystals showed evidence for a superstructure, see Figures 6.6 and 6.7. In fact, two different superstructures were found. When the amount of copper in the compound was 0.25, an incommensurate $6.25a_{sub}$ x

$1b_{sub}$ supercell resulted while a commensurate supercell of $6a_{sub}$ x $1b_{sub}$ was found when the amount of copper was 0.33. These results tell us that the amount of copper introduced between the layers directly affects how the Te chains in the structure distort by dictating how many Te_2^{2-} units are being reduced.

Figure 6.6   (A) Selected area electron diffraction pattern of $Cu_{0.25}UTe_3$ with the electron beam perpendicular to the layers ([001] direction) showing the incommensurate superlattice reflections along the a^*-axis.   (B) Densitometric intensity scan along the a^*-axis of the electron diffraction pattern (boxed area on photograph) showing the (h10) family of reflections.   The three reflections from the sublattice of $Cu_{0.25}UTe_3$ are indexed.   The four weak peaks are from the superlattice with $a_{super} = 6.25a_{sub}$.

Electron Diffraction of $Cu_{0.25}UTe_3$
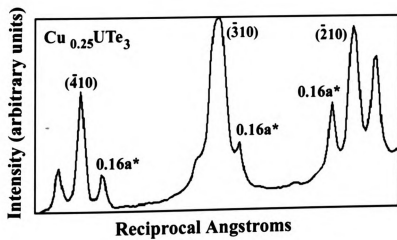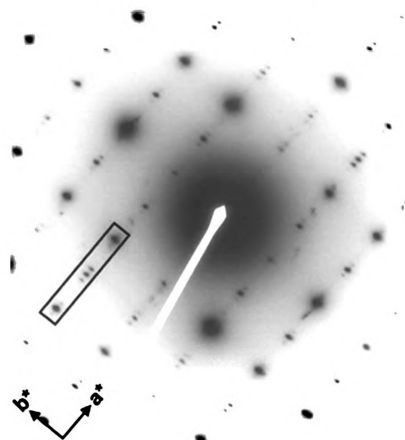
Figure 6.7 (A) Selected area electron diffraction pattern of $Cu_{0.33}UTe_3$ with the electron beam perpendicular to the layers ([001] direction) showing the incommensurate superlattice reflections along the a^*-axis. (B) Densitometric intensity scan along the a^*-axis of the electron diffraction pattern (boxed area on photograph) showing the (h10) family of reflections. The three reflections from the sublattice of $Cu_{0.33}UTe_3$ are indexed. The four weak peaks are from the superlattice with $a_{super} = 6.0a_{sub}$.

Electron Diffraction of $Cu_{0.33}UTe_3$
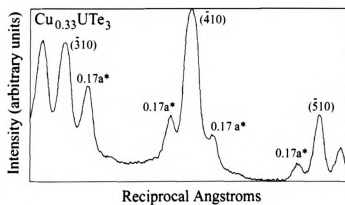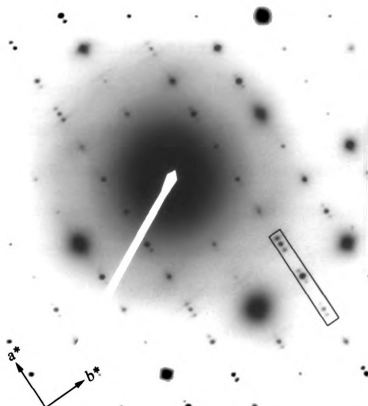
Charge Transport Properties - Charge transport measurements were made on bulk crystals of Cu_xUTe_3 (x = 0.25 and 0.33) as well as on a polycrystalline pressed pellet of the binary α-UTe$_3$. The electrical conductivity and thermopower data on Cu_xUTe_3 (x = 0.25 and 0.33) are shown in Figure 6.8. The room temperature conductivity reaches ~280 S/cm and decreases with decreasing temperature, suggesting a semiconductor. At 250K, there is an anomalous dip in the data. Interestingly, this dip also exists in the thermopower data at the same temperature. While we are unsure of the cause of this anomaly, we are certain that it is not due to a structural transition since single crystal x-ray data was collected for this compound both above and below this temperature and the same crystallographic structure was observed (see Table 6.1). The electrical conductivity of α-UTe$_3$ also indicates semiconducting behavior with a room temperature value of 10 S/cm, almost 30 times less than Cu_xUTe_3 (x = 0.25 and 0.33), see Figure 6.9. However, because these measurements were made on a pressed pellet this drop in conductivity might be largely due to grain boundary affects.

The thermopower data of Cu_xUTe_3 (x = 0.25 and 0.33) suggests that the material is a p-type semiconductor down to 40K. Below this temperature, the material undergoes a p-n transition. At 300K, the thermopower is 20 μV/K. In an attempt to further probe this transition from p-type to n-type, charge transport measurements were made on a pressed pellet of the binary α-UTe$_3$, for

comparison (see Figure 6.9). The thermopower data of α-UTe$_3$, which is independent of grain boundaries, gives a behavior more characteristic of that of a semiconductor and shows at room temperature value of 550 μV/K. The data is lacking the p-n transition found in Cu$_x$UTe$_3$ (x = 0.25 and 0.33). From these measurements, it is evident that these properties are drastically affected by the insertion of copper between the layers of α –UTe$_3$. Due to the low temperature at which the p-n transition occurs for Cu$_x$UTe$_3$ (x = 0.25 and 0.33), it is difficult to ascertain the cause. It is interesting, however, that this type of transition has been reported to occur in MTe$_5$ (M = Zr, Hf)[30] (at 80K for HfTe$_5$ and 145K for ZrTe$_5$) and to this date has defied an explanation.
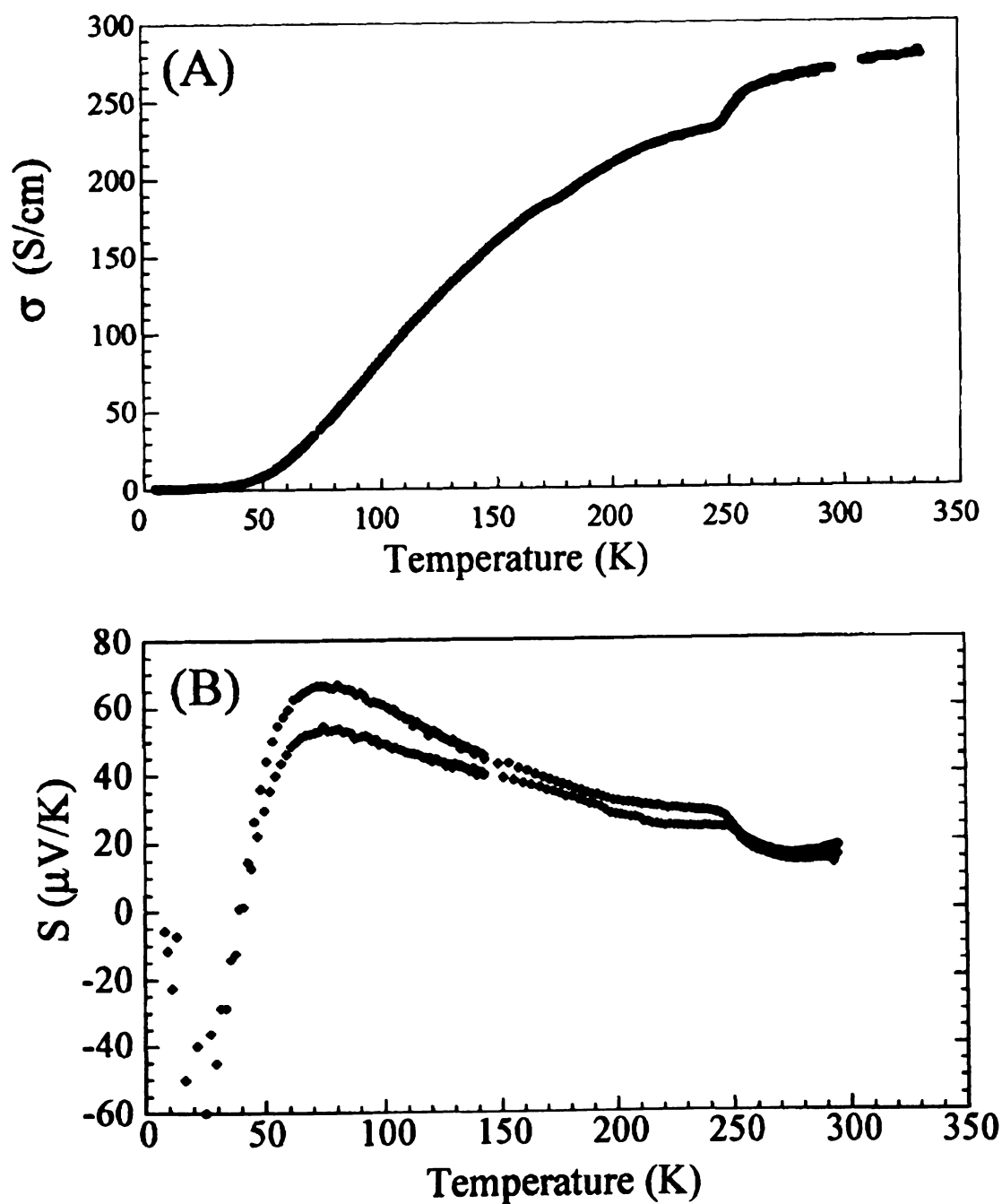
Figure 6.8 (A) Variable temperature, four probe electrical conductivity for bulk crystals of Cu_xUTe_3 (x = 0.25 and 0.33). (B) Variable temperature thermopower data for bulk crystals of Cu_xUTe_3 (x = 0.25 and 0.33).
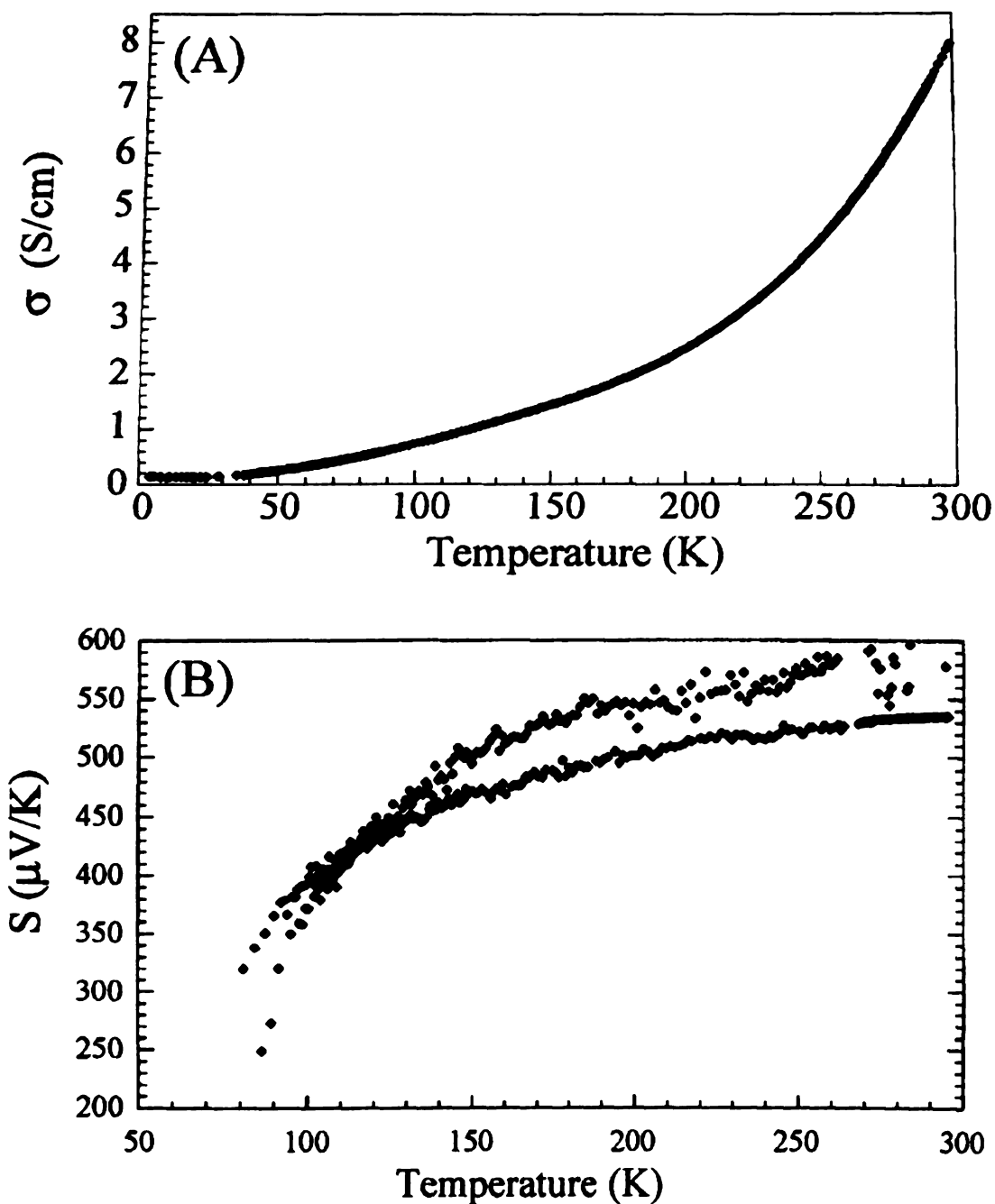
Figure 6.9 (A) Variable temperature, four probe electrical conductivity for a room temperature pressed pellet of α-UTe₃. (B) Variable temperature thermopower data for a room temperature pressed pellet of α-UTe₃.

302

D. Conclusions

The discovery of Cu_xUTe_3 (x = 0.25 and 0.33) has provided us with the opportunity to take a closer look at the relative stabilities of the binary UTe_3 structure types and has given us some insight as to how the structure of Cu_xUTe_3 (x = 0.25 and 0.33) may be stabilized. As a result, we have determined that α-UTe_3 is less thermodynamically stable than β-UTe_3 and that by inserting copper between the layers of α-UTe_3, the physical properties of the material are drastically affected. Although our attempts to insert Cu directly between the layers of α-UTe_3 through solid state diffusion methods were unsuccessful, others have reported on the electrochemical insertion of Cu in $ZrTe_3$.[31] It would be interesting to see if copper could be inserted in α-UTe_3 electrochemically. While electrical conductivity measurements indicate that Cu_xUTe_3 (x = 0.25 and 0.33) is a semiconductor, thermopower measurements revealed an interesting p-n transition at low temperatures. Finally, electron diffraction studies indicate the existence a *6.0-6.25a_{sub} x 1b_{xub}* supercell. The type of supercell depends on the amount of copper in the compound and is assumed to be electronically driven by structural modulations within the Te chains of the structure.

References

[1] Narducci, A.A.; Ibers, J.A. *Chem. Mater.* **1998**, 10, 2811.

[2] (a) Cody, J.A.; Mansuetto, M.F.; Pell, M.A.; Chien, S.; Ibers, J.A. *J. Alloys Compd.* **1995**, 219, 59. (b) Cody, J.A.; Ibers, J.A. *Inorg. Chem.* **1995**, 34, 3165.

[3] (a) Sutorik, A.C.; Albritton-Thomas, J.; Hogan, T.; Kannewurf, C.R.; Kanatzidis, M.G. *Chem. Mater.* **1996**, 8 751.

[4] Tougait, O.; Daoudi, A.; Potel, M.; Noël, H. *Mater. Res. Bull.* **1997**, 32, 1239-1245.

[5] Chondroudis, K.; Kanatzidis, M.G. *C. R. Acad. Sci. Paris* **1996**, 322, 887-894.

[6] Chondroudis, K.; Kanatzidis, M.G. *J. Am. Chem. Soc.* **1997**, 119, 2574-2575.

[7] Sutorik, A.C.; Patschke, R.; Schindler, J.; Kannewurf, C.R.; Kanatzidis, M.G. *Chem. Eur. J.*, In press.

[8] Choi, K.-S.; Kanatzidis, M.G. *Chem. Mater.*, In press

[9] Daoudi, A.; Lamire, M.; Levet, J.C.; Nöel, H. *J. Solid State Chem.* **1996**, 123, 331.

[10] (a) Nöel, H.; Potel, M. *J. Less-Common Met.* **1985**, 113, 11-15. (b) Nöel, H. *J. Less-Common Met.* **1980**, 72, 45-49.

[11] Narducci, A.A.; Ibers, J.A. *Inorg. Chem.*, **1998**, 3798-38001.

[12] Sourisseau, C.; Gwet, S.P.; Gard, P. *J. Solid State Chem.* **1988**, 72, 257-271 and references therein.

[13] Finckh, W.; Felser, C.; Tremel, W.; Ouvrard, G. *J. Alloys Comp.* **1997**, 262, 97-100.

[14] (a) Cody, J.A.; Ibers, J.A. *Inorg. Chem.*, **1996**, 35, 3836-3838. (b) Wu, E.J.; Pell, M.A.; Ibers, J.A. *J. Alloys. Comp.*, **1997**, 255, 106-109. (c) Choi, K.-S.; Patschke, R.; Billinge, S.J.L.; Waner, M.J.; Dantus, M.; Kanatzidis, M.G. *J. Am. Chem. Soc.*, **1998**, 120, 10706-10714.

[15] Sheldrick, G.M. SHELXTL, Version 5; Siemens Analytical Xray Systems, Inc.; Madison, WI, 1994.

[16] SMART: Siemens Analytical Xray Systems, Inc., Madison, WI, 1994.

[17] SAINT: Version 4.0, Siemens Analytical Xray Systems, Inc., Madison WI (1994-1996).

[18] SADABS: Sheldrick, G.M. University of Göttengen, Germany, to be published.

[19] Nöel, H.; Levet, J.C. *J. Solid State Chem.* **1989**, 79, 28-33.

[20] Boehme, D.R.; Nichols, M.; Snyder, R.L.; Matheis, D.P. *J. Alloys Compd.*, **1992**, 179, 37-59.

[21] Haneveld, A.J. Klein; Jellinek, F. *J. Less-Common Met.* **1969**, 18, 123-129.

[22] (a) Stöwe, K. *J. Solid State Chem.*, **1996**, 127, 202-210. (b) Haneveld, A.J. Klein; Jellinek, F. *J. Less-Common Met.*, **1970**, 21, 45-49.

[23] Suski, W.; Wojakowski, A.; Blaise, A.; Salmon, P.; Fournier, J.; Mydlarz, T. *J. Magn. Mater.* **1976**, 3, 195.

[24] (a) Breeze, E.W.; Brett, N.H. *J. Nucl. Mater.* **1971**, 40, 113-115. (b) Breeze, E.W.; Brett, N.H.; White, J. *J. Nucl. Mater.* **1971**, 39, 157-165.

[25] Tougait, O.; Potel, M.; Levet, J.C.; Noel, H. *Eur. J. Sol. State Inor.* **1998**, 35, 67-76.

[26] (a) Nöel, H. *Inorg. Chim. Acta.*, **1985**, 109, 205-207. (b) Nöel, H. *Mater. Res. Bull.* **1984**, 19, 1171-1175.

[27] (a) Tougait, O.; Potel, M.; Padiou, J.; Noel, H *J. Alloys Compd.* **1997**, 262, 320-324. (b) Stöwe, K. *Z.anorg. allg. Chem.* **1996**, 622, 1423-1427.

[28] Tougait, O.; Potel, M.; Nöel, H. *J. Solid State Chem.* **1998**, 139, 356-361.

[29] Tougait, O.; Potel, M.; Nöel, H. *Inorg. Chem.* **1998**, 37 (20), 5088-5091.

[30] Littleton, R.T.; Tritt, T.M.; Feger, C.R.; Kolis, J.; Wilson, M.L.; Marone, M.; Payne, J.; Verebeli, D.; Levy, F. *Appl. Phys. Lett.*, **1998**, 72 (16), 2056-2058.

[31] Finchk, W.; Felser, C.; Tremel, W.; Ouvrard, G. *J. Alloys Comp.* **1997**, 262-263, 97.

Chapter 7

Synthesis and Thermoelectric Studies of the Cage Compounds, $A_2MCu_8Te_{10}$

(A = K, Rb, Cs; M = Ba, Eu)

A. Introduction

Recently, there has been an increased interest in finding better materials for thermoelectric applications.[1] As of today, the leading thermoelectric material remains as Bi_2Te_3 and its alloys. Although this material is excellent for use in small scale thermoelectric devices, it finds its limitation when trying to apply it to larger scale refrigeration units. The problem with this material is that it has a poor efficiency and is therefore very expensive to use. The efficiency of a thermoelectric material is directly related to a property called the figure of merit. The figure of merit, ZT, is a unitless parameter made up of the thermopower (S), the electrical conductivity (σ), and the thermal conductivity (κ), see equation 1.

$$ZT = \frac{S^2\sigma T}{\kappa} \qquad \text{(eq. 1)}$$

In order to increase the efficiency of a material, one must maximize ZT by simultaneously maximizing the thermopower (S) and electrical conductivity (σ) while minimizing the thermal conductivity (κ). This has proven to be very challenging since these parameters are not independently controllable. While many scientists have focused their efforts on optimizing known materials through doping studies, we have decided to take more of an "exploratory" approach. This approach has proven to be very useful and through it, we have found many promising new materials. One of the most interesting is a family of compounds

having the formula $A_2MCu_8Te_{10}$ (A = K, Rb, Cs; M = Ba, Eu).[2] These compounds fit the description for a "phonon-glass-electron crystal" (PGEC) which was introduced by Slack[3] as the limiting characteristic for a superior thermoelectric. A PGEC material features cages (or tunnels) in its crystal structure inside which reside atoms small enough to "rattle". This "rattling" creates a phonon damping effect which causes the thermal conductivity to be dramatically reduced. One system in which this rattling effect has been well illustrated is the skutterudites.[4] Here, we report on the anisotropic two-dimensional stucture of $A_2BaCu_8Te_{10}$ (A = K, Rb, Cs) and discuss it in relation to its electrical conductivity, thermopower, and heat capacity. In addition, substitutional doping experiments were performed associated with the Ba sites.

B. Experimental Section

1. Reagents – The following reagents were used as obtained: Potassium metal, analytical reagent, Spectrum Chemical Mfg. Corp., Gardena, CA; Rubidium metal, 99.5%, Alfa Aesar, Ward Hill, MA.; Cesium metal, 99.98%, Alfa Aesar, Ward Hill, MA; Barium Telluride, 99.5%, 25 mesh, Cerac, Milwaukee, WI; Europium metal powder, 99.9%, <250 mesh, Alfa Aesar, Ward Hill, MA; Europium metal chunk, 99.9%, Chinese Rare Earth Information Center, Inner Mongolia, China; Copper metal, electrolytic dust, Fisher Scientific, Fairlawn, NJ; Tellurium powder, 100 mesh, 99.95% purity, Aldrich Chemical Co., Milwaukee, WI. Tellurium shots, 99.9% pure, Noranda Advanced Materials, Saint-Laurent,

Quebec, Canada. * The europium metal chunk was cut into fine shavings with a hacksaw and flamed under vacuum in a sealed quartz ampoule to remove the oxide coating before being used. The tellurium shots were ground to a fine powder before being used.

Potassium Telluride, K₂Te - Synthesis of this material was performed as described in Chapter, Section B.1.

Rubidium Telluride, Rb₂Te - Synthesis of this material was performed as described in Chapter, Section B.1.

Cesium Telluride, Cs₂Te - Synthesis of this material was performed as described in Chapter, Section B.1.

Europium Telluride, EuTe - The following procedure was modified from that given in the literature.[5] 4.330g (0.028 mol) of Eu powder was weighed in an N_2 filled glovebox and combined with 3.636g (0.028 mmol) Te in a 500 mL single neck round bottom flask. The flask was connected to a glass adapter with a stopcock joint and removed from the glovebox. The flask and adapter was then connected to a condenser apparatus and chilled to -78°C using a dry ice/acetone bath. Approximately 400mL of NH_3 were condensed, under an N_2 atmosphere, onto the reagents, giving a dark blue solution. The solution was stirred via a Teflon coated magnetic stir bar and the reaction mixture was maintained at -78° for up to 24 hours. The dry ice was then removed and the NH_3 was allowed to evaporate off as the flask warmed up to room temperature under a constant flow of N_2 (approximately 10 hours). A second portion of NH_3 was added and the process

310

was repeated to ensure complete reaction of the reagents. The resulting light brown powder was evacuated on a Schlenck line for approximately 5 hours and taken into an N_2 filled glovebox where it was ground to a fine powder. Due to europium's strong ability to coordinate to ammonia, another step was necessary to remove all of the ammonia from the product. The powder was loaded into a 13 mm silica ampoule and placed on a vacuum line outside of the glovebox. The ampoule was gently heated with a flame under dynamic vacuum to remove the coordinated ammonia. The ampoule was then flame sealed and taken back into the N_2 filled glovebox. *Caution: If the last step to remove the coordinated ammonia is not performed, one risks an explosion in subsequent reactions of EuTe in closed ampoules.*

2.   **Synthesis** – All manipulations were carried out under a dry nitrogen atmosphere in a Vacuum Atmospheres Dri-Lab glovebox.

$A_2BaCu_8Te_{10}$ (A = K, Rb, Cs) (I-III) and $Rb_2EuCu_8Te_{10}$ (IV) – Polycrystalline ingots of $A_2BaCu_8Te_{10}$ (A = K, Rb, Cs) and $Rb_2EuCu_8Te_{10}$ were prepared in two steps. A polycrystalline powder was first synthesized by heating a mixture of A_2Te (1 mmol), BaTe or EuTe (1 mmol), Cu (8 mmol), and Te (8 mmol) in a computer controlled furnace to 520°C in 12 hours, isotherming at this temperature for 4-7 hours, and quickly cooling to room temperature in 5 hours. The polycrystalline powder sample is then placed in a long silica tube with a diameter of 5mm and flame sealed. The sealed tube is placed into a gentle flame to melt the compound and immediately quenched to liquid nitrogen temperatures.

This liquid nitrogen quenching process helps avoid the formation of vacuum pockets inside the ingot. An alternative method to prepare these ingots is to combine the two steps into one by directly reacting the starting materials in the flame and quenching the molten product in liquid nitrogen. No isolation was needed since the compounds were prepared from direct combination of the elements. The identity of both the polycrystalline powder samples and the ingots of $A_2BaCu_8Te_{10}$ (A = K, Rb, Cs) were confirmed by comparing the powder X-ray diffraction patterns of the products against the one calculated using single crystal X-ray data (see Tables 7.1-7.3). The identity of $Rb_2EuCu_8Te_{10}$ was confirmed by comparing the powder X-ray diffraction pattern of the product against the calculated for $Rb_2BaCu_8Te_{10}$ (see Table 7.4)

Table 7.1   Calculated and Observed X-ray Powder Diffraction Pattern for $K_2BaCu_8Te_{10}$ (I)

h k l	d_{calc} (Å)	d_{obs}(Å)	I/I_{max} (obs) (%)
2 0 0	11.4000	11.4696	71.22
4 0 0	5.7000	5.7412	50.24
2 0 -2	3.5089	3.5211	60.00
2 2 0	3.3240	3.3438	53.17
4 0 -2	3.2541	3.2297	53.17
4 2 0	2.9671	2.9594	100.00
6 0 -2	2.8508	2.8638	71.71
5 1 -2	2.8003	2.8098	59.02
5 3 0	2.0654	2.0696	53.17
5 3 -1	2.0289	2.0214	65.85
0 2 3	1.9229	1.9241	62.44

Table 7.2   Calculated and Observed X-ray Powder Diffraction Pattern for
$Rb_2BaCu_8Te_{10}$ (II)

h k l	d_{calc} (Å)	d_{obs} (Å)	I/I_{max} (obs) (%)
2 0 0	11.6671	1.6400	57.01
4 0 0	5.8335	5.8643	38.91
5 1 -1	3.7114	3.7172	36.20
2 0 -2	3.5009	3.4718	28.51
4 0 -2	3.3047	3.2873	37.56
1 1 -2	3.1266	3.2223	42.08
6 0 1	3.0745	3.0666	81.45
7 1 -1	3.0063	2.9954	100.00
5 1 2	2.3404	2.3436	25.79
7 1 2	2.0468	2.0450	46.61
7 1 -3	2.0369	2.0395	40.72
8 2 1	2.0245	2.0248	45.25
3 1 3	1.9686	1.9682	34.39
3 3 -2	1.9375	1.9365	56.11
7 3 -1	1.9170	1.9127	47.51
6 2 -3	1.8674	1.8691	38.91
3 3 2	1.8179	1.8207	43.44
5 1 3	1.8092	1.8160	33.94

Table 7.3 Calculated and Observed X-ray Powder Diffraction Pattern for $Cs_2BaCu_8Te_{10}$ (III)

h k l	d_{calc} (Å)	d_{obs} (Å)	I/I_{max} (obs) (%)
0 2 0	11.8805	11.9806	27.74
0 4 0	5.9402	5.9651	17.20
1 4 1	3.8143	3.8137	35.78
2 0 0	3.5545	3.6627	14.01
0 0 2	3.4830	3.4766	23.86
0 2 2	3.3423	3.3331	19.69
2 1 1	3.1384	3.2329	21.08
1 6 1	3.0985	3.0973	66.99
2 4 0	3.0501	3.0507	100.00
2 3 1	2.9399	2.9370	38.97
1 11 0	2.0668	2.0675	26.77
1 9 2	2.0175	2.0187	17.89
0 12 0	1.9801	1.9810	19.00
0 10 2	1.9629	1.9633	19.28
2 1 3	1.9375	1.9367	33.98
3 3 2	1.9019	1.9011	23.44
2 11 1	1.7844	1.7845	29.13
0 0 4	1.7415	1.7405	12.34
0 14 0	1.6972	1.6979	18.72

Table 7.4 Calculated and Observed X-ray Powder Diffraction Pattern for $Rb_2EuCu_8Te_{10}$ (IV)

h k l	d_{calc} (Å)	d_{obs} (Å)	I/I_{max} (obs) (%)
2 0 0	11.6671	11.8960	52.96
4 0 0	5.8335	5.8660	34.96
6 0 -1	3.7905	3.7879	30.59
2 0 -2	3.5009	3.4683	32.13
0 0 2	3.4039	3.4069	32.13
2 2 0	3.3694	3.3371	47.81
4 0 -2	3.3047	3.3024	36.76
6 0 1	3.0745	3.0623	81.23
7 1 -1	3.0063	3.0017	100.00
4 2 -1	2.8912	2.8860	70.44
4 0 2	2.6744	2.6984	37.28
6 2 0	2.6095	2.6071	27.51
7 1 1	2.5577	2.5639	43.70
8 0 1	2.4750	2.4634	23.65
9 1 -2	2.2307	2.2322	26.99
6 0 -3	2.2031	2.2070	30.33
5 3 -1	2.0669	2.0741	62.98
7 1 -3	2.0369	2.0387	60.41
8 0 2	1.9917	1.9927	47.56
11 1 -2	1.9523	1.9578	37.02
7 3 -1	1.9170	1.9155	60.41
5 3 -2	1.8774	1.8789	44.47
1 1 -4	1.6779	1.6795	29.31

3. Physical Measurements – The instrumentation and experimental setup for the following measurements are the same as described in Chapter 2, Section B.3: Powder X-ray Diffraction, Infrared Spectroscopy, and Magnetic Susceptibility Measurements.

Charge Transport Measurements – The thermopower and electrical conductivity were measured at Clemson University in collaboration with Professor Terry Tritt and his student, Nathan Lowhorn, using two different systems. One was a helium flow cryostat with a temperature range from 3 - 310 K. The other was a closed-cycle refrigeration system with a temperature range from 12 - 310 K. Both systems were computer-controlled using LabVIEW software. Samples were mounted by electroplating the ends of the samples with Ni and then soldering them to two copper blocks. The two copper blocks served as current leads and thermoelectric voltage leads. The two junctions of a 3 mil AuFe (0.07 at. % Fe) vs. Chromel thermocouple were embedded in the copper blocks to measure the temperature difference across the sample. (A small amount of epoxy and "cigarette paper" was used to electrically insulate the junction.) A 39 Ω metal-film resistor was attached as a heater to one of the copper blocks. Au voltage leads for measuring resistance were attached to the sample with silver paint. This whole apparatus attached to a "custom designed chip" that plugged into the measurement system. One of the copper blocks was thermally connected to the chip which was thermally sunk to the probe head of the helium flow cryostat or the cold finger of

317

the closed cycle refrigerator system. Typical sample size was 3-4 mm in diameter and 4-7 mm long.

The heat capacity measurements were also performed in collaboration with Professor Terry Tritt and his student, Nathan Lowhorn, at Clemson University. The PPMS system used has a temperature range of 1.8 - 400 K, can accommodate samples of mass from 1 - 200 mg, and is fully automated and computer-controlled. The sample platform has a heater and thermometer underneath and is contained in a removable sample puck. "Apiezon N grease" was placed on the sample platform, and the heat capacity of the puck with grease was measured. Then the sample was placed in the grease for thermal contact to the platform; and the heat capacity of the puck, grease, and sample was measured. The heat capacity of the puck with grease was subtracted from the total to give the heat capacity of the sample. The system uses a relaxation technique to measure the heat capacity.

Raman Spectroscopy – Raman spectra were recorded on a Holoprobe Raman Spectrograph equipped with a 633 nm HeNe laser and a CCD camera detector. The instrument was coupled to an Olympus BX60 microscope. Each sample was simply placed onto a small glass slide and a 50x objective lens was used to choose the area of the specimen to be measured. The spot size of the laser beam when using the 50x objective lens was 10μm.

Differential Thermal Analysis (DTA) – DTA experiments were performed on a computer controlled Shimadzu DTA-50 thermal analyzer. Approximately 30-60mg of sample was ground and placed in a quartz ampoule and flame sealed

318

under vacuum. For a reference, a quartz ampoule of equal mass was filled with Al_2O_3 and flame sealed under vacuum. The sample and reference were heated to the desired temperature at 10°C/min, isothermed for 10 minutes, and cooled to 50°C at -10°C/min. The residues of the DTA experiment was examined by power X-ray diffraction. To determine if the sample has congruently melted, the X-ray powder pattern before and after the DTA experiments were compared.

Single Crystal X-ray Diffraction – The single crystal X-ray data for both $K_2BaCu_8Te_{10}$ (I) and $Cs_2BaCu_8Te_{10}$ (II) were collected previously by Dr. Xiang Zhang, who also performed the structure solutions.[2] Intensity data for $Rb_2BaCu_8Te_{10}$ (II) were collected on a Siemens SMART Platform CCD diffractometer using graphite monochromatized Mo Kα radiation. A single crystal was mounted on the tip of a glass fiber. The data were collected over a full sphere of reciprocal space, up to 50° in 2θ. The individual frames were measured with an ω rotation of 0.3° and acquisition time of 30 sec/frame. The SMART[6] software was used for the data acquisition and SAINT[7] for the data extraction and reduction. The absorption correction was performed using SADABS[8]. The structure was solved by direct methods using the SHELXTL[9] package of crystallographic programs. Complete data collection parameters and details of all structure solutions and refinements are given in Tables 7.5.

Table 7.5 Crystallographic Data for $A_2BaCu_8Te_{10}$ (A = K, Rb, Cs)

	*$K_2BaCu_8Te_{10}$	$Rb_2BaCu_8Te_{10}$	*$Cs_2BaCu_8Te_{10}$
crystal habit, color	chunk, black	chunk, black	chunk, black
Diffractometer	Rigaku AFC6S	Siemens SMART Platform CCD	Rigaku AFC6S
Radiation	Mo-Kα (0.71069Å)	Mo-Kα (0.71073Å)	Mo-Kα (0.71069Å)
Crystal Size, mm^3	0.40 x 0.15 x 0.10	0.23 x 0.x28 x 0.05	0.60 x 0.25 x 0.10
Temperature, K	293	173	293
Crystal System	monoclinic	monoclinic	orthorhombic
Space Group	C2/m (#12)	C2/m (#12)	Immm (#71)
a, Å	23.245(5)	24.034(5)	7.109(2)
b, Å	6.950(5)	7.0388(14)	23.761(16)
c, Å	7.061(5)	7.0120(14)	6.966(3)
β, °	101.23(4)	103.86(3)	N/A
V, Å^3	1119(1)	1151.7(4)	1177(2)
Z	2	2	2
μ, mm^{-1}	22.39	25.509	23.97
index ranges	$0 \leq h \leq h$	$-31 \leq h \leq 30$	$0 \leq h \leq h$
	$0 \leq k \leq k$	$-9 \leq k \leq 9$	$0 \leq k \leq k$
	$-1 \leq l \leq l$	$-8 \leq l \leq 9$	$0 \leq l \leq l$
$2\theta_{max}$, deg	50	50	50
sec/frame	N/A	30	N/A
total data	3577	5276	658
unique data	3504	1425	634
R(int)	N/A	0.0961	N/A
no. parameters	57	57	35
final R/Rw^a, %	8.8/11.30	N/A	3.0/6.0
final R1/wR2^b, %	N/A	11.38/30.22	N/A
GOF	4.80	N/A	2.87
Goof	N/A	11.47	N/A

^{a}R $= \Sigma (|F_o| - |F_c|)/ \Sigma |F_o|$ Rw $= \{ \Sigma [w(F_o - F_c)^2] / \Sigma [w (F_o)^2] \}^{1/2}$

^{b}R1 $= \Sigma (|F_o| - |F_c|)/ \Sigma |F_o|$ wR2 $= \{ \Sigma [w(F_o^2 - F_c^2)^2] / \Sigma [w (F_o^2)^2] \}^{1/2}$

* The single crystal X-ray data for $K_2BaCu_8Te_{10}$ and $Cs_2BaCu_8Te_{10}$ were collected previously by Dr. Xiang Zhang, who also performed the structure solutions.[2]

320

C. Results and Discussion

Structure Description – The structure type of $A_2BaCu_8Te_{10}$ (A = K, Rb, Cs) has been found to strongly depend on the identity of the alkali metal. While $K_2BaCu_8Te_{10}$ and $Rb_2MCu_8Te_{10}$ (M = Ba, Eu) crystallize in the monoclinic space group, C2/m, $Cs_2BaCu_8Te_{10}$ crystallizes in the orthorhombic space group, Immm. Therefore, all four compounds are not isostructural. However, the two structure types are very similar. Figure 7.1 shows the extended structure of $Rb_2BaCu_8Te_{10}$. It is a two-dimensional structure built from anionic $[BaCu_8Te_{10}]^{2-}$ layers that are separated by Rb^+ cations.   The $[BaCu_8Te_{10}]^{2-}$ layers can be further broken down into Cu_8Te_{12} pentagonal dodecahedral cages, see Figure 7.2A. These cages each encapsalate one Ba^{2+} cation, which are coordinated by twelve Te atoms. Interestingly, the cages have a strong affinity for cations with a high charge/radius ratio, and so, given a choice between a Rb^+ and Ba^{2+} cation, it will encapalate the latter. This preference appears to be electrostatic in origin so as to reduce the negative charge of the $[Cu_8Te_{10}]^{4-}$ cage. The coordination environment of the copper atoms is a slightly distorted tetrahedron. Each Cu_8Te_{12} cage contains three mutually perpendicular sets of ditelluride units.   By sharing two pairs of oppositely spaced ditellurides, the cages form layers along the a-axis. The third ditelluride unit remains unshared. In addition to the three ditelluride units, each cage possesses monotellurides which are coordinated to four Cu atoms in a square pyramidal geometry. The Te-Te bond distance of the three ditelluride units range from 2.798(5) Å to 2.862(5) Å, while the Cu-Te bond distances range from

321

2.576(4) Å to 2.686(5) Å. The Rb^+ cations are stabilized between the layers and are each coordinated by ten Te atoms. If the Cu atoms are included, one can see that the cations are actually sitting inside a "cup" that is made up of part of a pentagonal dodecahedral cage, see Figure 7.2B. The fractional atomic coordinates, isotropic and anisotropic temperature factors, bond distances, and bond angles for $Rb_2BaCu_8Te_{10}$ is given in Tables 7.6-7.8.

The extended structure of $Cs_2BaCu_8Te_{10}$ is shown in Figure 7.3. The difference between this structure type and that of $Rb_2BaCu_8Te_{10}$ lies in the way that the anionic layers stack with respect to one another. In $Rb_2BaCu_8Te_{10}$, the Rb^+ ions are each coordinated by ten Te atoms. While this coordination environment is large enough to stabilize potassium and rubidium, it is not large to stabilize a cesium ion. Therefore, the $[BaCu_8Te_{10}]^{2-}$ layers are forced to shift with respect to one another to create a larger space for the cesium ion to reside. As a result, the symmetry of the structure drops from orthorhombic to monoclinic. As shown in Figure 7.4B, the cesium ions are now coordinated to eleven Te atoms in a tri-capped square antiprismatic geometry and again sit inside a "cup" formed from part of a pentagonal dodecahedral cage.
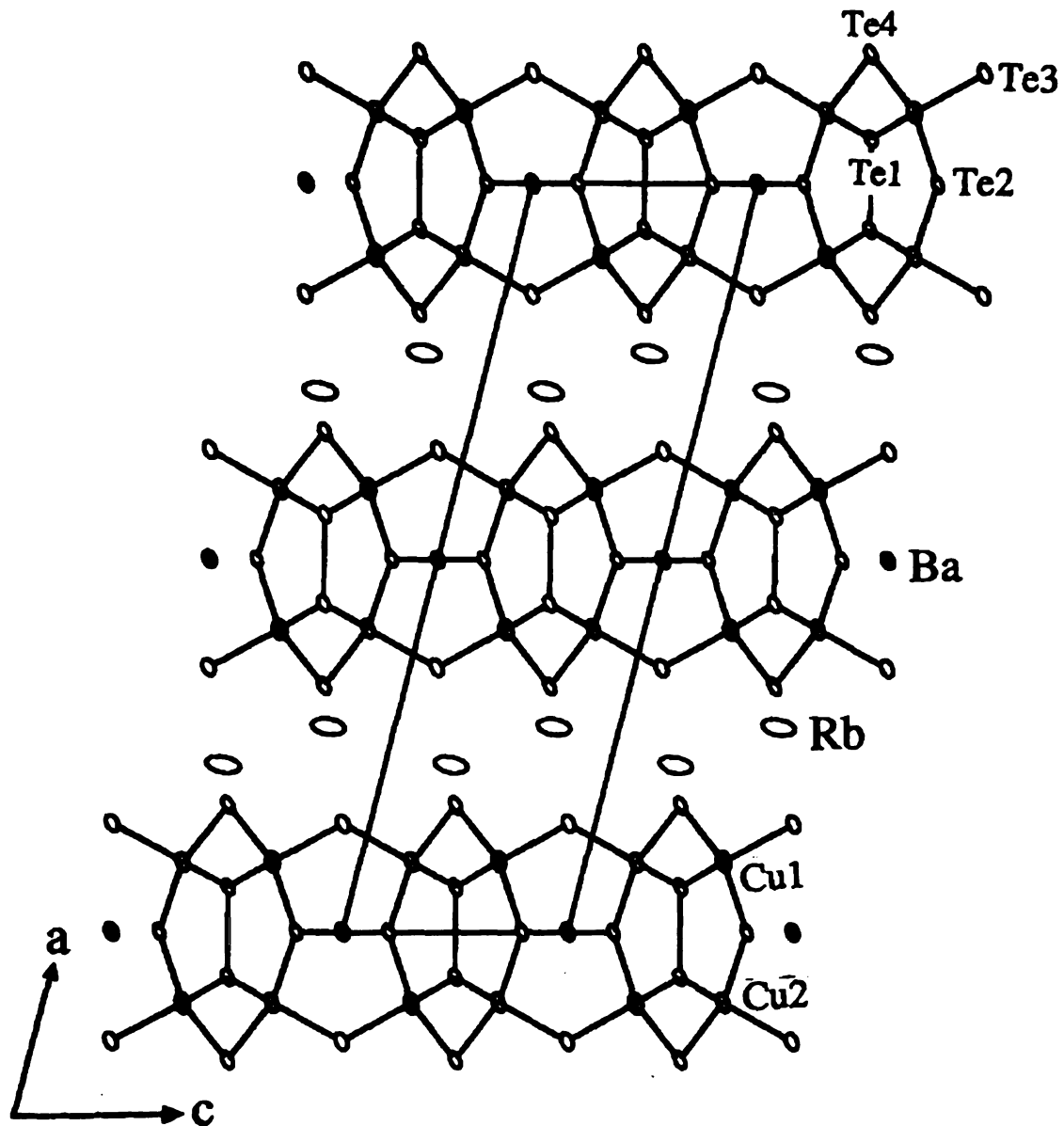
Figure 7.1 ORTEP representation of the extended structure of $Rb_2BaCu_8Te_{10}$ as seen down the b-axis (90% ellipsoid probability). The ellipses with octant shading represent Ba atoms, the crossed ellipses represent Cu atoms, and the large open ellipses represent Rb and Te atoms.
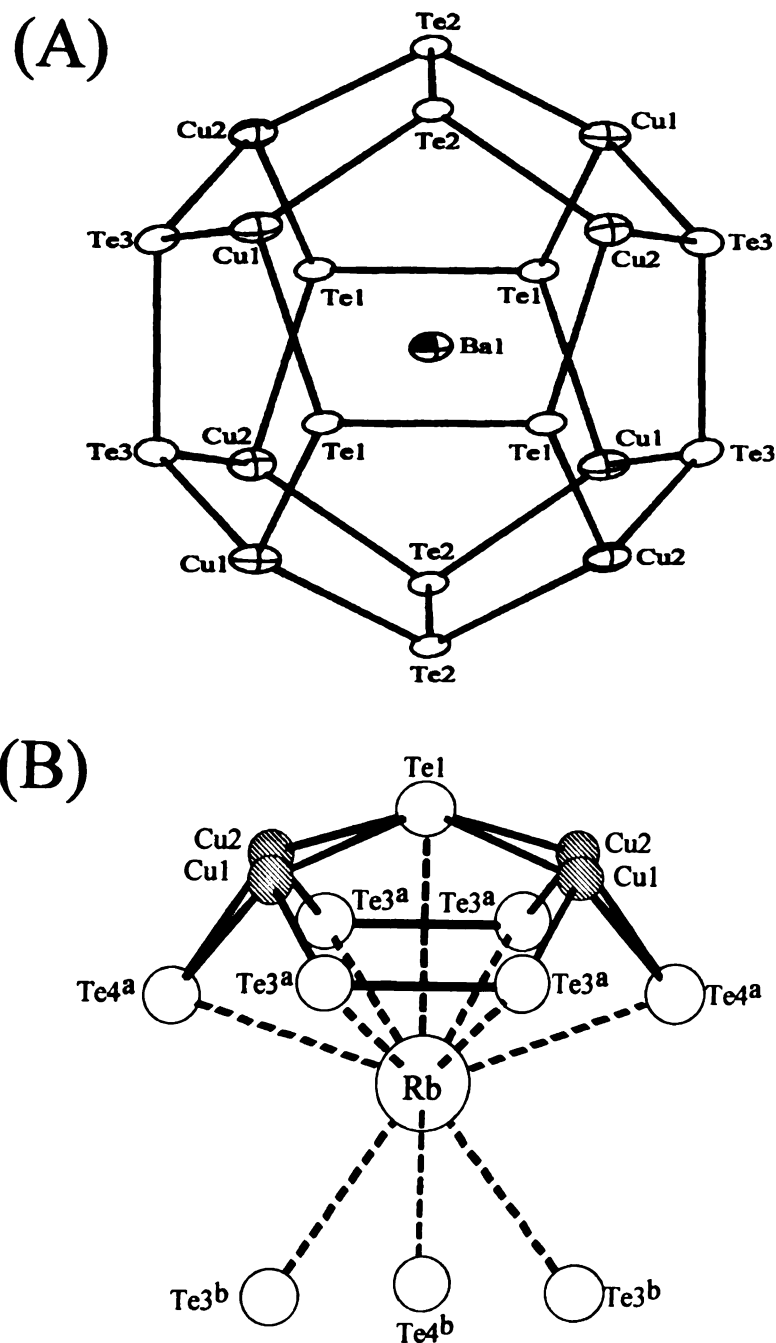
Figure 7.2 (A) ORTEP representation of the barium filled $[Cu_8Te_{12}]$ cages of $Rb_2BaCu_8Te_{10}$ (50% ellipsoid probability ellipsoid) and (B) the coordination environment around Rb in $Rb_2BaCu_8Te_{10}$. Bond distances include: Rb-Te1 = 3.848(6)Å, Rb-Te3[a] = 4.057(7)Å, Rb-Te3[b] = 3.729(5)Å, Rb-Te4[a] = 3.742(2)Å, Rb-Te4[b] = 3.906(8) Å. The ellipse with octant shading represents Ba, the crossed and striped ellipses represent Cu atoms, and the large open ellipses represent Te atoms.
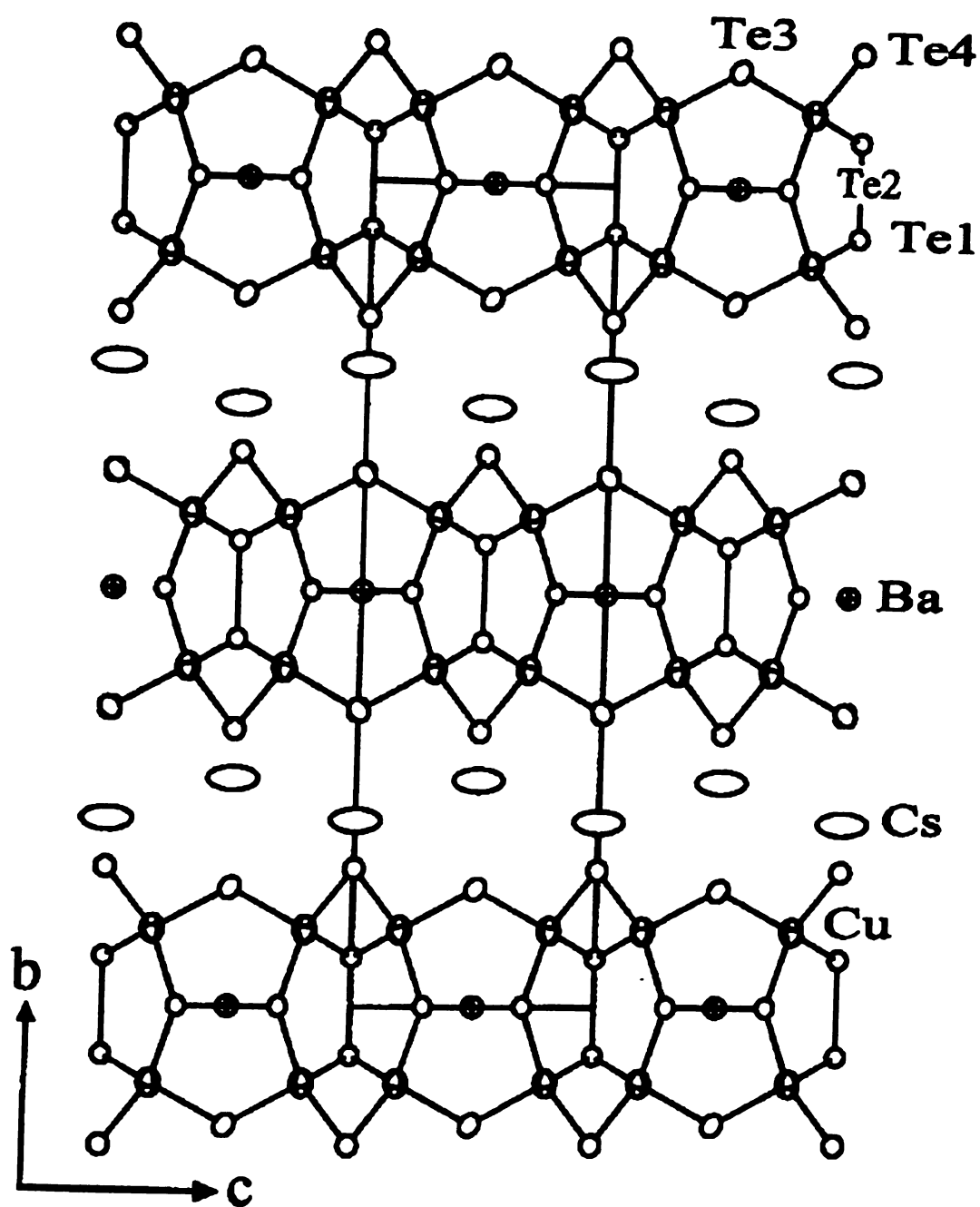
Figure 7.3 ORTEP representation of the extended structure of $Cs_2BaCu_8Te_{10}$ as seen down the a-axis (90% probability ellipsoids). The ellipses with octant shading represent Ba atoms, the crossed ellipses represent Cu atoms, and the large open ellipses represent Cs and Te atoms.

Figure 7.4 Coordination environments around (A) Rb in $Rb_2BaCu_8Te_{10}$ (for comparison) and (B) Cs in $Cs_2BaCu_8Te_{10}$. Bond distances include: Cs-Te1 = 3.959 Å, Cs-Te3^a = 4.238 Å, Cs-Te3^b = 3.825 Å, Cs-Te4^a = 3.820 Å, Cs-Te4^b = 4.328 Å

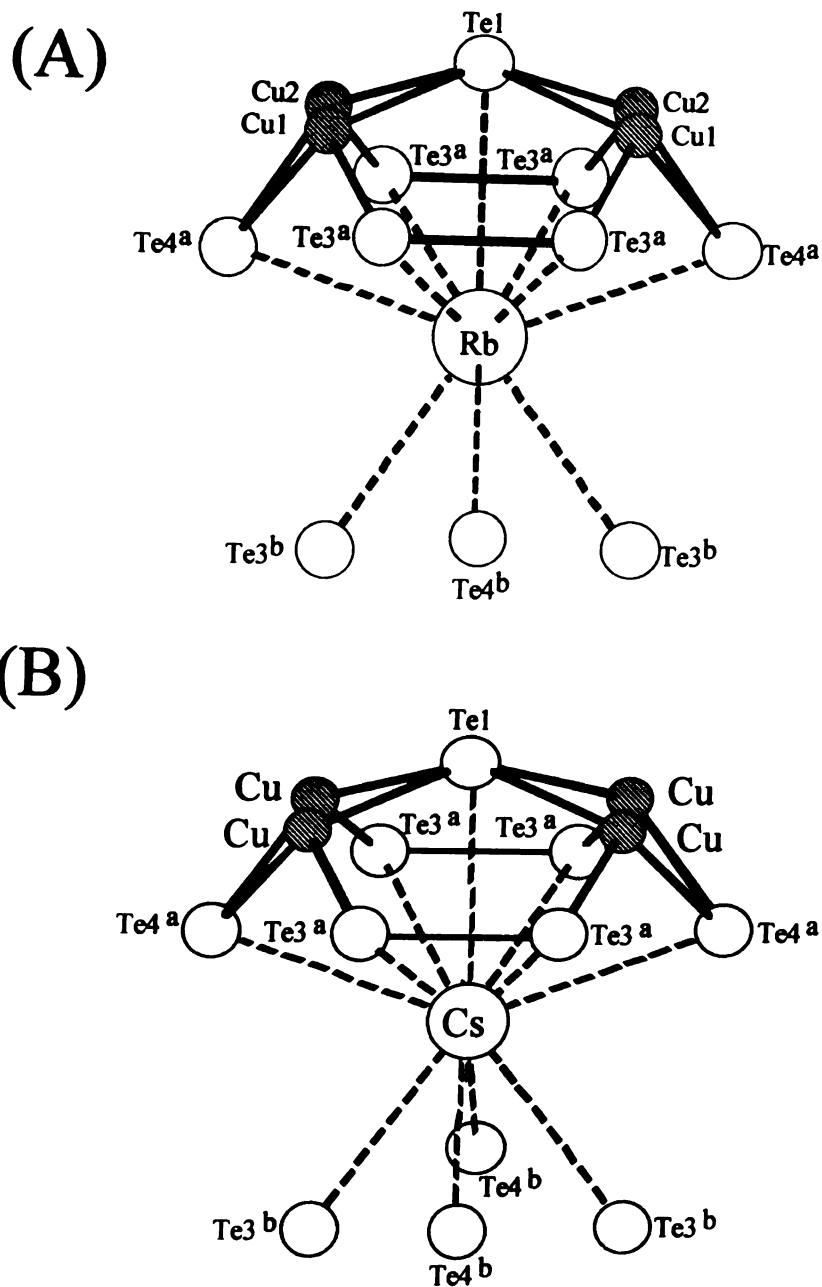**Table 7.6** Fractional Atomic Coordinates and Equivalent Isotropic Displacement Parameters (U_{eq}) for $Rb_2BaCu_8Te_{10}$ with Estimated Standard Deviations in Parentheses.

atom	x	y	z	occupancy	U_{eq}^a, $Å^2$
Ba	0.0	-0.50	0.0	1.0	2.0(1)
Te(1)	-0.0600(1)	-0.50	0.4518(4)	1.0	1.6(1)
Te(2)	0.0030(1)	0.0	0.2043(3)	1.0	1.5(1)
Te(3)	-0.1458(1)	-0.3031	-0.1190(3)	1.0	1.9(1)
Te(4)	0.1707(1)	0.0	0.6413(4)	1.0	1.8(1)
Cu(1)	0.0949(2)	-0.1920(5)	0.3843(6)	1.0	2.4(1)
Cu(2)	-0.0940(2)	-0.1930(5)	0.2286(5)	1.0	2.2(1)
Rb	0.2247(2)	0.50	0.7076(13)	1.0	5.5(3)

$^a U_{eq}$ is defined as one-third of the trace of the orthogonalized U_{ij} tensor.

Table 7.7 Anisotropic Displacement Parameters (Å) for $Rb_2BaCu_8Te_{10}$ with Standard Deviations in Parentheses.

atom	U11	U22	U33	U23	U13	U12
Ba	0.029(2)	0.013(2)	0.021(2)	0	0.014(1)	0
Te(1)	0.026(1)	0.007(1)	0.018(1)	0	0.014(1)	0
Te(2)	0.025(1)	0.008(1)	0.015(1)	0	0.012(1)	0
Te(3)	0.029(1)	0.012(1)	0.020(1)	0.001(1)	0.014(1)	0.003(1)
Te(4)	0.028(1)	0.011(1)	0.019(1)	0	0.016(1)	0
Cu(1)	0.042(2)	0.013(2)	0.022(2)	-0.002(1)	0.015(2)	-0.002(1)
Cu(2)	0.036(2)	0.014(2)	0.021(2)	-0.003(1)	0.017(1)	0.001(1)
Rb	0.029(3)	0.023(2)	0.115(6)	0	0.021(3)	0

Table 7.8 Selected Distances (Å) and Bond Angles (deg) for $Rb_2BaCu_8Te_{10}$ with Standard Deviations in Parentheses.

Bond Distances

Cu1– Te1	2.681(4)		Cu2 – Cu2	2.717(7)
Cu1 – Te2	2.686(5)		Te1 – Te1	2.798(5)
Cu1 – Te3	2.581(4)		Te2 – Te2	2.862(5)
Cu1 – Te4	2.612(5)		Te3 – Te3	2.772(4)
Cu2 – Te1	2.679(4)		Rb – Te1	3.848(6)
Cu2 – Te2	2.681(4)		Rb – Te3	3.729(5), 4.057(7), 4.336(8)
Cu2 – Te3	2.576(4)		Rb – Te4	3.742(2), 3.906(8)
Cu2 – Te4	2.623(4)		Ba – Te1	3.768(3)
Cu1 – Cu1	2.703(7)		Ba – Te2	3.7791(11)
Cu1 – Cu2	2.720(5)		Ba – Te3	3.673(2)

Bond Angles

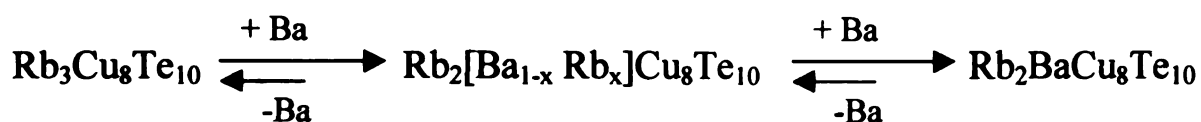|				
Te1 – Cu1 – Te2	106.97(16)		Te2 – Cu2 – Te3	108.45(14)
Te1 – Cu1 – Te3	108.37(14)		Te2 – Cu2 – Te4	115.74(14)
Te1 – Cu1 – Te4	111.15(15)		Te3 – Cu2 – Te4	105.33(16)
Te2 – Cu1 – Te3	107.94(15)		Te1 – Rb – Te3	65.35(10), 144.61(6)
Te2 – Cu1 – Te4	115.84(14)		Te1 – Rb – Te4	70.22(9), 126.2(2)
Te3 – Cu1 – Te4	106.33(16)		Te3 – Rb – Te3	39.95(9), 69.80(12), 93.94(15), 117.4(2)
Te1 – Cu2 – Te2	107.55(16)		Te1 – Ba – Te1	180.0
Te1 – Cu2 – Te3	108.72(14)		Te1 – Ba – Te3	69.96(5), 110.04(5)
Te1 – Cu2 – Te4	110.85(14)		Te3 – Ba – Te3	44.33(6), 135.67(6), 180.0

Charge Transport Properties - Physical measurements were previously made on single crystals of $Rb_2BaCu_8Te_{10}$ and the results are shown in Figure 7.5. The electrical conductivity mostly decreases with decreasing temperature which is characteristic of a semiconductor. Above 200K, however, the conductivity flattens out to a value around 125 $\mu V/k$ and then starts to decrease around 250K. This is an indication that the bandgap of this material is very small and that at higher temperatures, the material acts more like a semimetal. The thermopower data is given in Figure 7.5B and suggests p-type behavior. Although the magnitude of the thermopower suggest semiconducting behavior, the slope is more reminiscent of a metal. Besides the anomalies in the data, the results seemed very promising for thermoelectrics, especially when taking into consideration the very low thermal conductivity. The thermal conductivity (now shown here) is 3.5 mW/cm-K at room temperature and ranges from 2.5-5.0 above 180K. This coupled with the fact that these compounds melt congruently, which is also a very important property for thermoelectrics, led us to perform an extensive study on these materials.

Figures 7.6-7.8 show both the electrical conductivity and thermopower for polycrystalline ingots of $A_2BaCu_8Te_{10}$ (A = K, Rb, Cs), respectively. For all three materials, the electrical conductivity data give metallic behavior with room temperatures ranging from 28 - 580 S/cm. The thermopower values range from approximately 30-55 $\mu V/K$ at room temperature, suggesting p-type behavior. The common feature of all the thermopower data is that it decreases with decreasing

temperature until exhibiting a small peak below 50K. This peak is believed to be a phonon drag peak as magneto-heat capacity measurements reveal no magnetic effects in these samples.

By comparing these measurements to those of the single crystal measurements for $Rb_2BaCu_8Te_{10}$, a few things become apparent. First, the single crystal data suggest the material to be semiconductor while those on the ingots suggest metallic behavior. This difference cannot simply be explained by grain boundary effects in the ingot because this effect acts to inhibit the conductivity, not enhance it. This suggests that perhaps the materials are doped and that the doping impurities act to create a degenerate semiconductor. This is supported by the fact that the magnitudes of the conductivity have such a wide range. Although not discussed here, there exists two ternary compounds that are isostructural to $A_2BaCu_8Te_{10}$ (A = K, Rb, Cs). These are $Rb_3Cu_8Te_{10}$ and $Cs_3Cu_8Te_{10}$.[2] The difference is that for these compounds, the Rb^+ and Cs^+ ions also occupy the space inside the cages of the structure. Charge transport measurements on these ternary compounds indicate p-type metallic behavior. Knowing this, one possible explanation is that the samples are actually a solid solution between $A_2BaCu_8Te_{10}$ and $A_3Cu_8Te_{10}$. To test for this, polycrystalline ingots were made with an excess of Ba (10% - 40%). The excess Ba in the reaction should force the equilibrium more completely towards the formation of $Rb_2BaCu_8Te_{10}$, see Scheme 1.

Scheme 1.

$$Rb_3Cu_8Te_{10} \underset{-Ba}{\overset{+Ba}{\rightleftharpoons}} Rb_2[Ba_{1-x} Rb_x]Cu_8Te_{10} \underset{-Ba}{\overset{+Ba}{\rightleftharpoons}} Rb_2BaCu_8Te_{10}$$

The results from these experiments are shown in Figure 7.9. The added Ba in the syntheses appears to have simultaneously decreased the conductivity while increasing the thermopower in a systematic fashion. The addition of 40% Ba changes the electrical conductivity from that of a metal to that of a semiconductor. This data is much closer to that of the single crystal data and therefore supports the above argument.

Finally, measurements were made on samples where the Ba has been substituted with Eu. By placing a heavier atom inside the cage, it might be possible to further minimize the thermal conductivity. Experiments were also performed to synthesize $Rb_2EuCu_8Te_{10}$ with an added amount of Eu in the reaction and measure their properties. The results are shown in Figure 7.10. The substitution of Eu for Ba in $Rb_2BaCu_8Te_{10}$ increased the conductivity to approximately 1800 S/cm at room temperature and decreased the thermopower to 17 µV/K. Additonal Eu in the synthesis had relatively no affect on the properties. For all measurements, the room temperature values are given in Table 7.9.
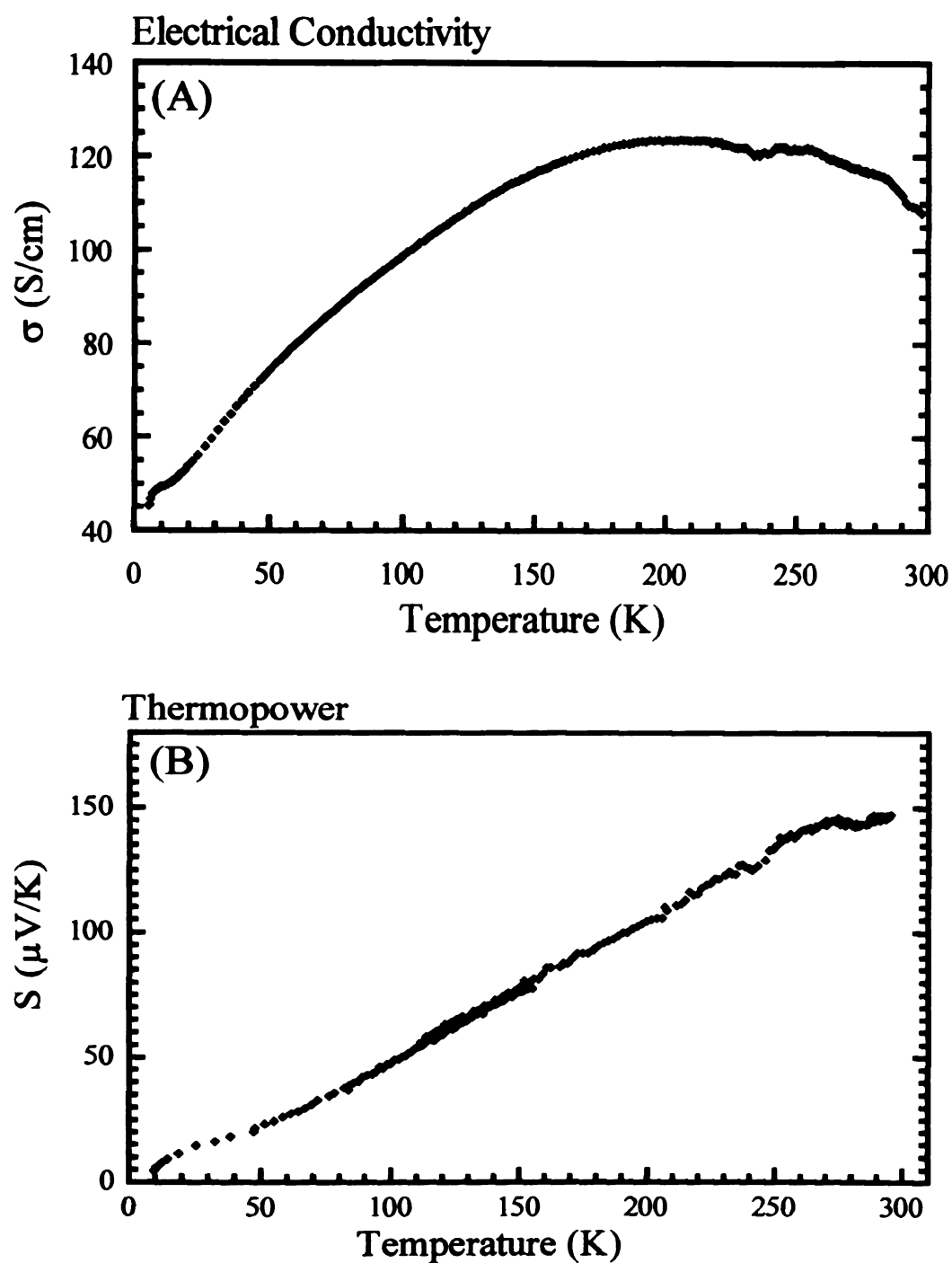
Figure 7.5 (A) Variable temperature electrical conductivity data for a single crystal of $Rb_2BaCu_8Te_{10}$ and (B) Variable temperature thermopower data for a single crystal of $Rb_2BaCu_8Te_{10}$.
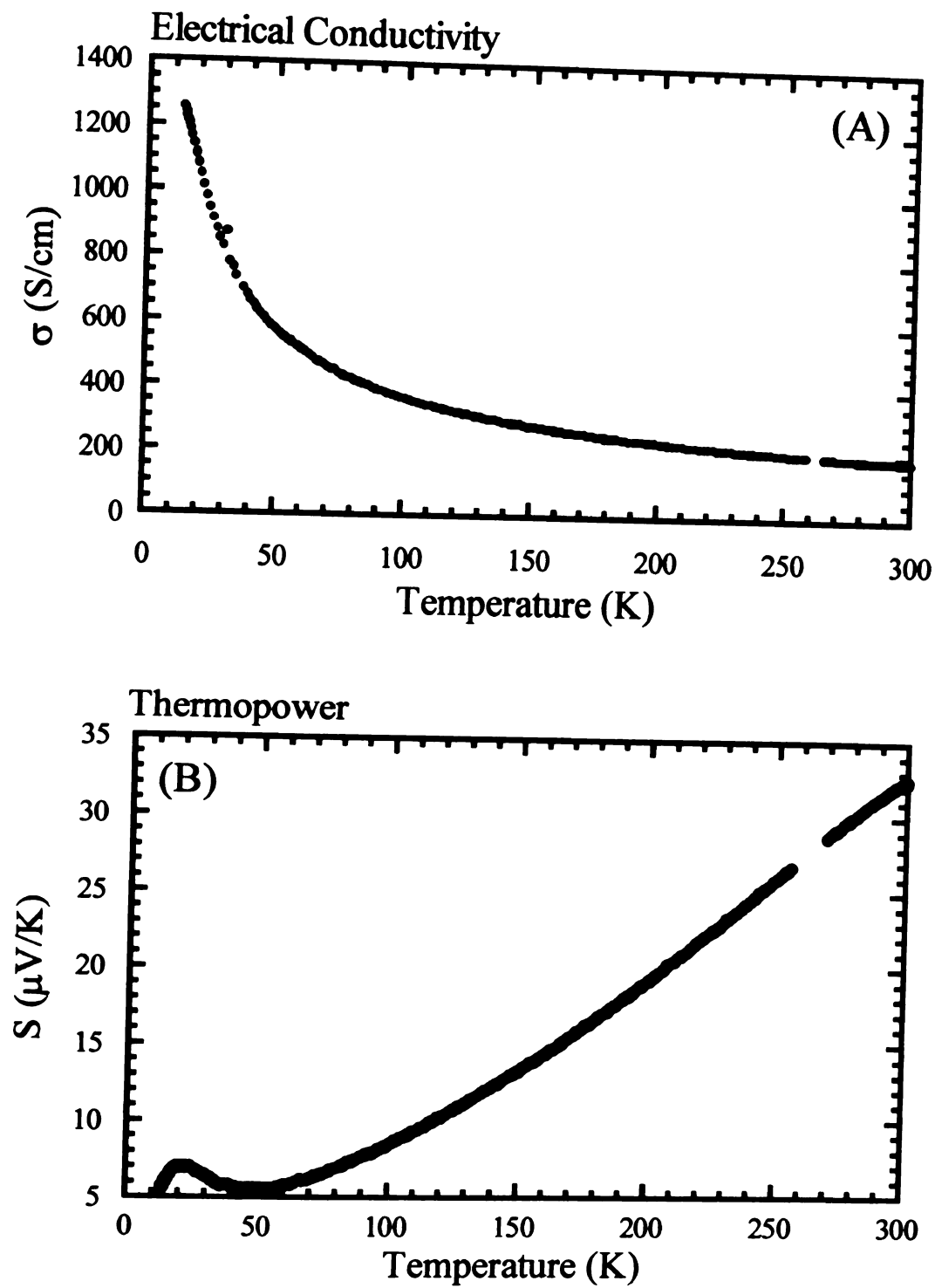
Figure 7.6 (A) Variable temperature electrical conductivity data for an ingot of $K_2BaCu_8Te_{10}$ and (B) Variable temperature thermopower data for an ingot of $K_2BaCu_8Te_{10}$.
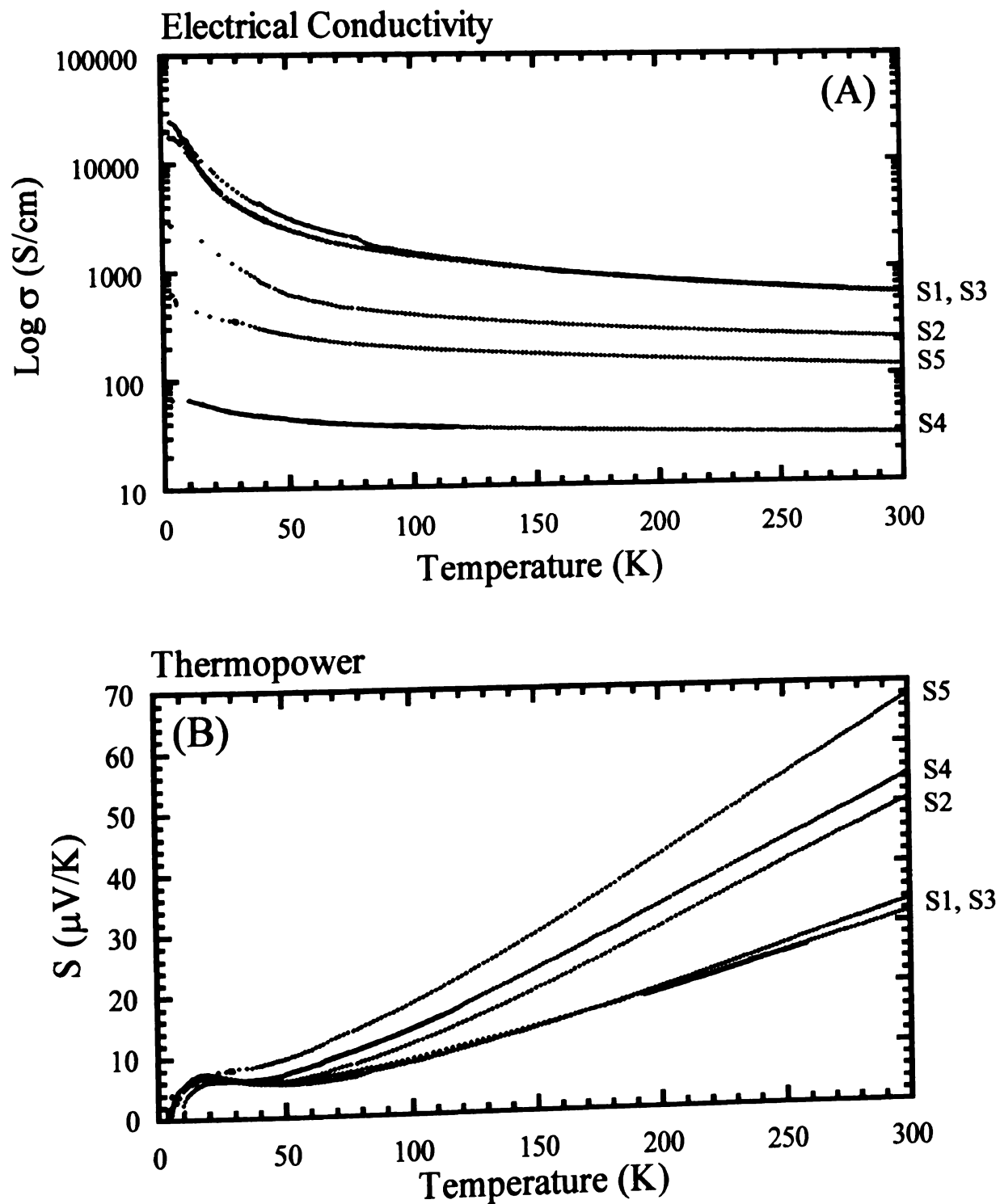
Figure 7.7 (A) Variable temperature electrical conductivity data and (B) Variable temperature thermopower data for five ingots of $Rb_2BaCu_8Te_{10}$ (Samples S1- S5).

Figure 7.8 (A) Variable temperature electrical conductivity data and (B) Variable temperature thermopower data for four ingots of $Cs_2BaCu_8Te_{10}$ (Samples S6 - S9).

Electrical Conductivity
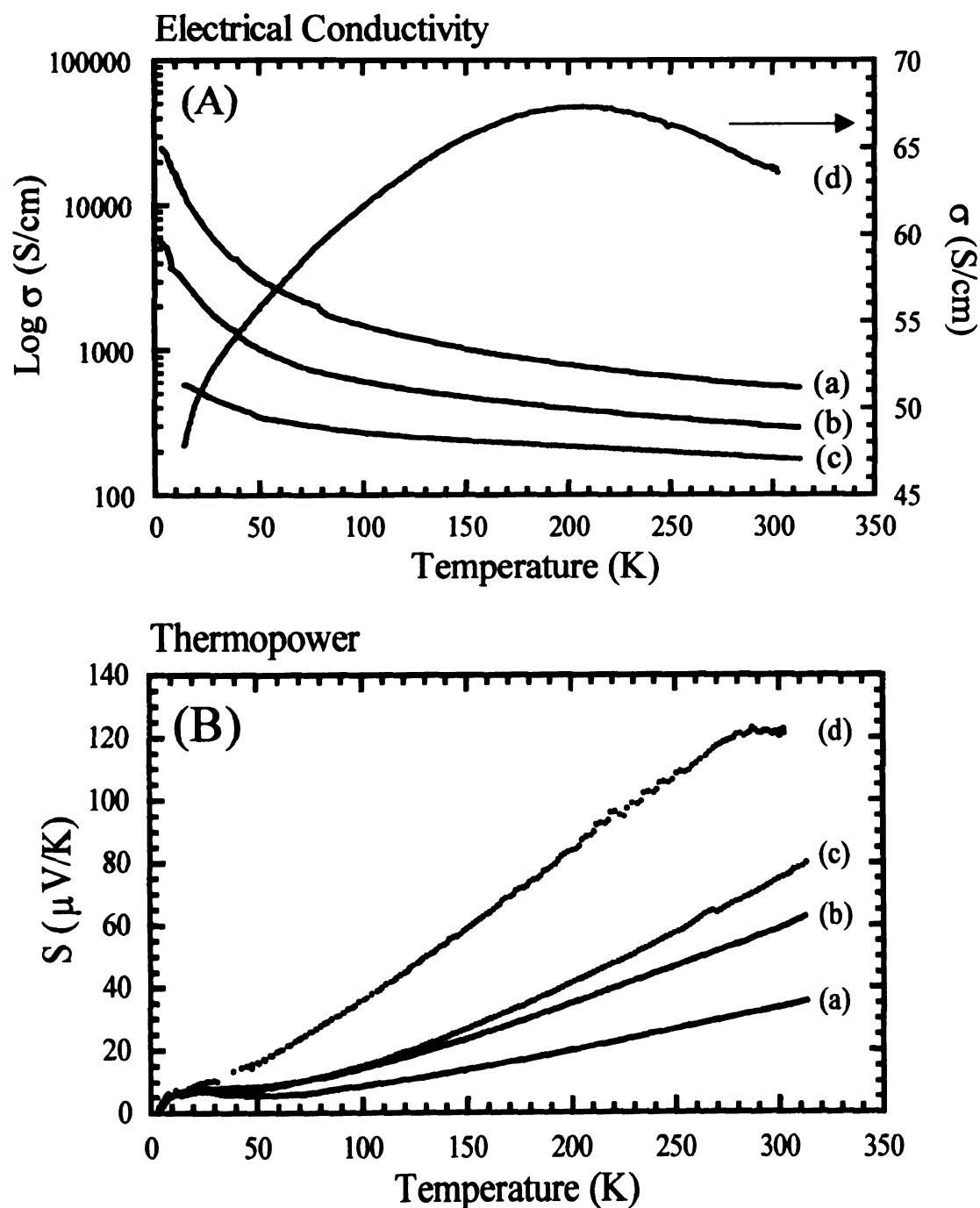
Thermopower

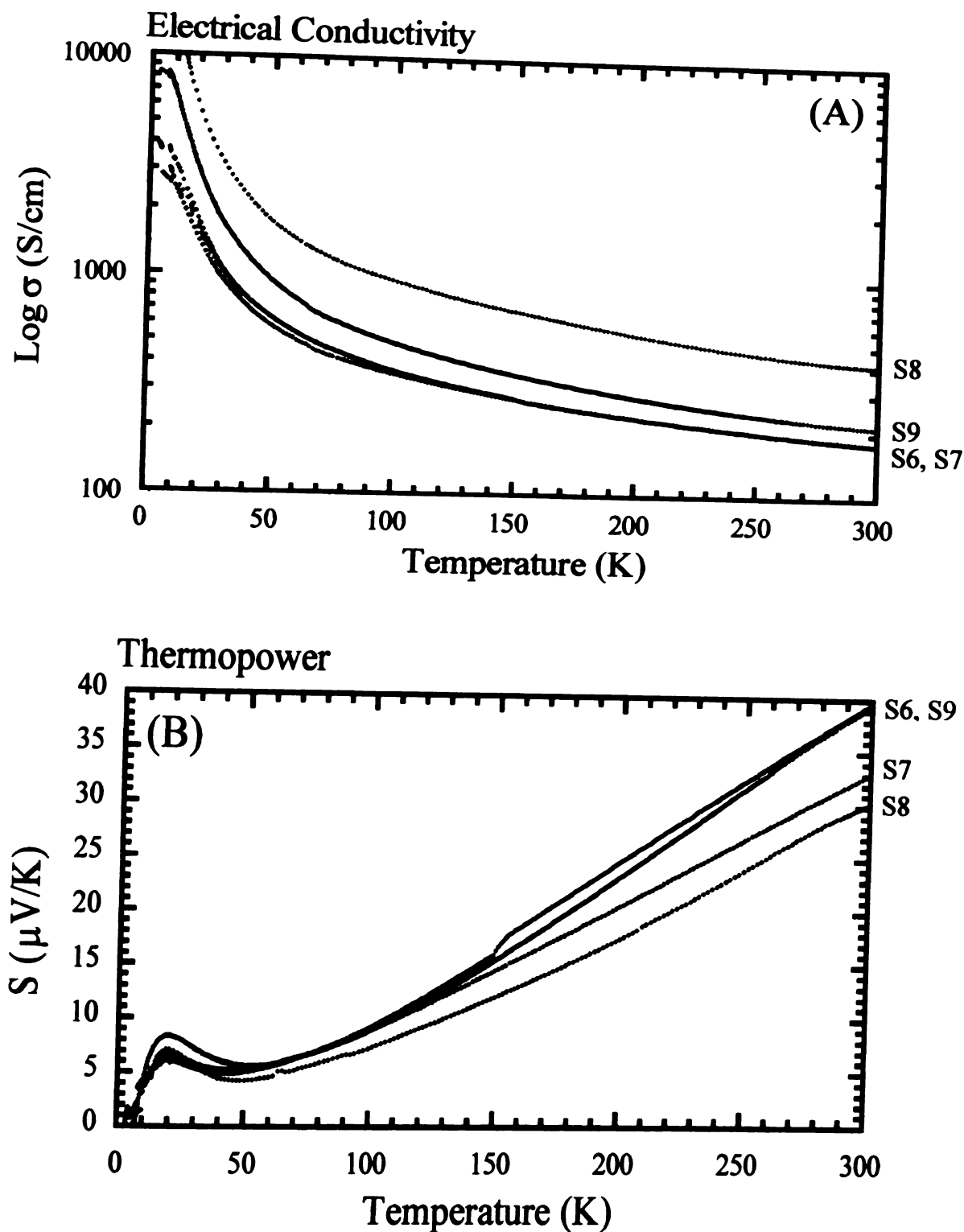**Figure 7.9** (A) Variable temperature electrical conductivity data and (B) variable temperature thermopower data for (a) $Rb_2BaCu_8Te_{10}$, (b) $Rb_2BaCu_8Te_{10}$ + 0.1Ba, (c) $Rb_2BaCu_8Te_{10}$ + 0.3Ba, and (d) $Rb_2BaCu_8Te_{10}$ +0.4Ba. All measurements were made on ingots.

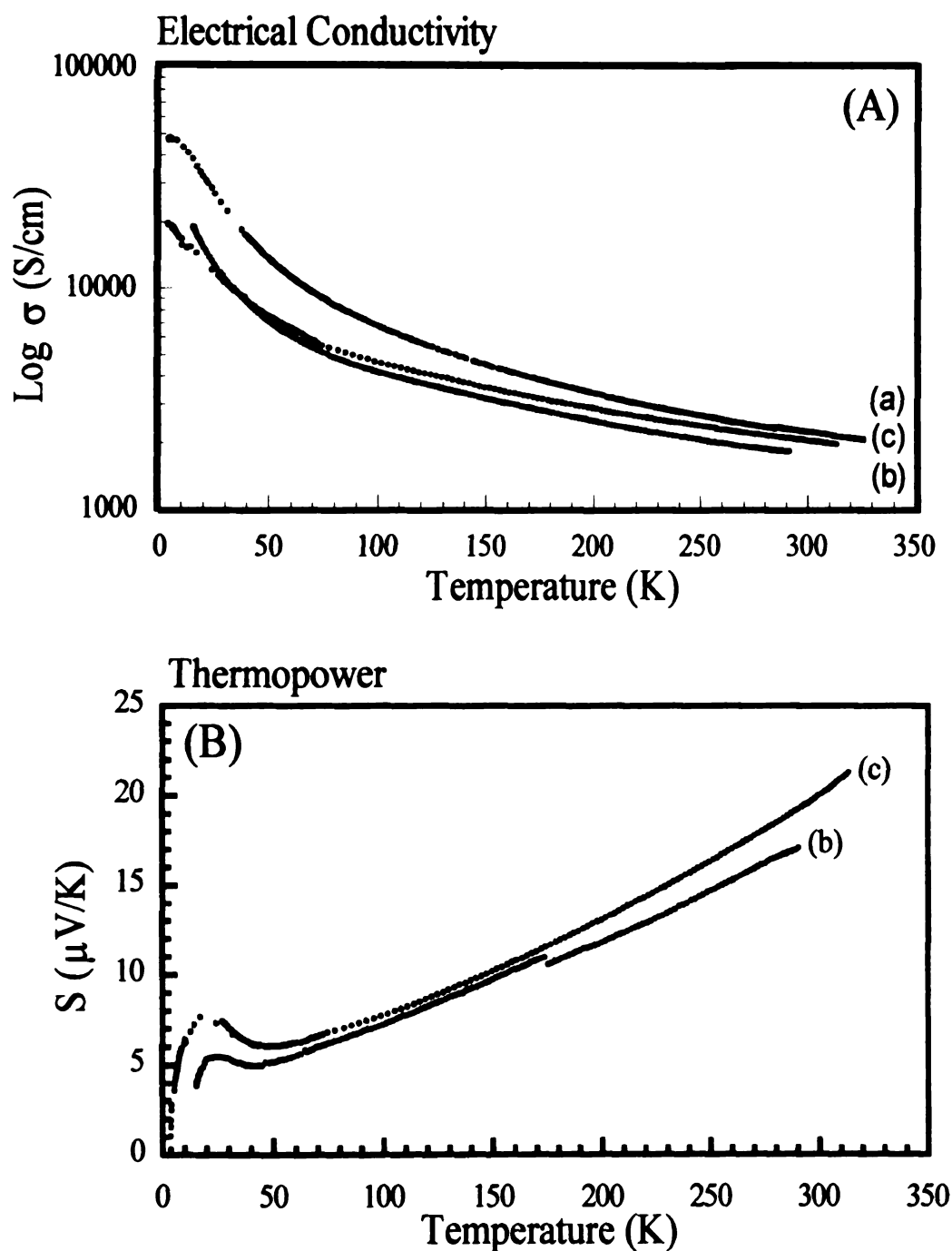**Figure 7.10** (A) Variable temperature electrical conductivity data for (a) a pressed pellet of $Rb_2EuCu_8Te_{10}$, (b) an ingot of $Rb_2EuCu_8Te_{10}$, and (c) an ingot of $Rb_2EuCu_8Te_{10} + 0.2Eu$. (B) Variable temperature thermopower data for (b) an ingot of $Rb_2EuCu_8Te_{10}$, and (c) an ingot of $Rb_2EuCu_8Te_{10} + 0.2Eu$.

Infrared Spectroscopy - The diffuse reflectance optical spectra was taken in the Mid-IR region for $Rb_2BaCu_8Te_{10}$, $Cs_2BaCu_8Te_{10}$ and $Rb_2EuCu_8Te_{10}$, see Figure 7.11. Optical gaps are observed at 0.28 eV, 0.30 eV, and 0.23 eV, respectively, for the three compounds. This data suggest that these materials are probably semiconductors, despite the fact that the charge transport measurements suggest metallic behavior. The absorption edge of $Rb_2EuCu_8Te_{10}$, however, is much broader than that of $A_2BaCu_8Te_{10}$ (A = Rb, Cs). One explanation for this might be that this sample has more of a contribution from the ternary $Rb_3Cu_8Te_{10}$ compound which makes the overall material more of a semimetal.

Contrary to this data, Density Functional Theory (DFT) calculations have been performed on $Cs_2BaCu_8Te_{10}$[10], which gave a calcuated DOS where the Fermi Level falls into a deep pseudo-gap. Because this gap is not completely empty, the material must be characterized as semimetal. The narrow-gap semiconductor versus semimetal characterizaion is hard to address unequivocally at this stage because we are pushing against the accuracy limits of our computational technique. Therefore, additional experiments were necessary to resolve this issue, see heat capacity results below.
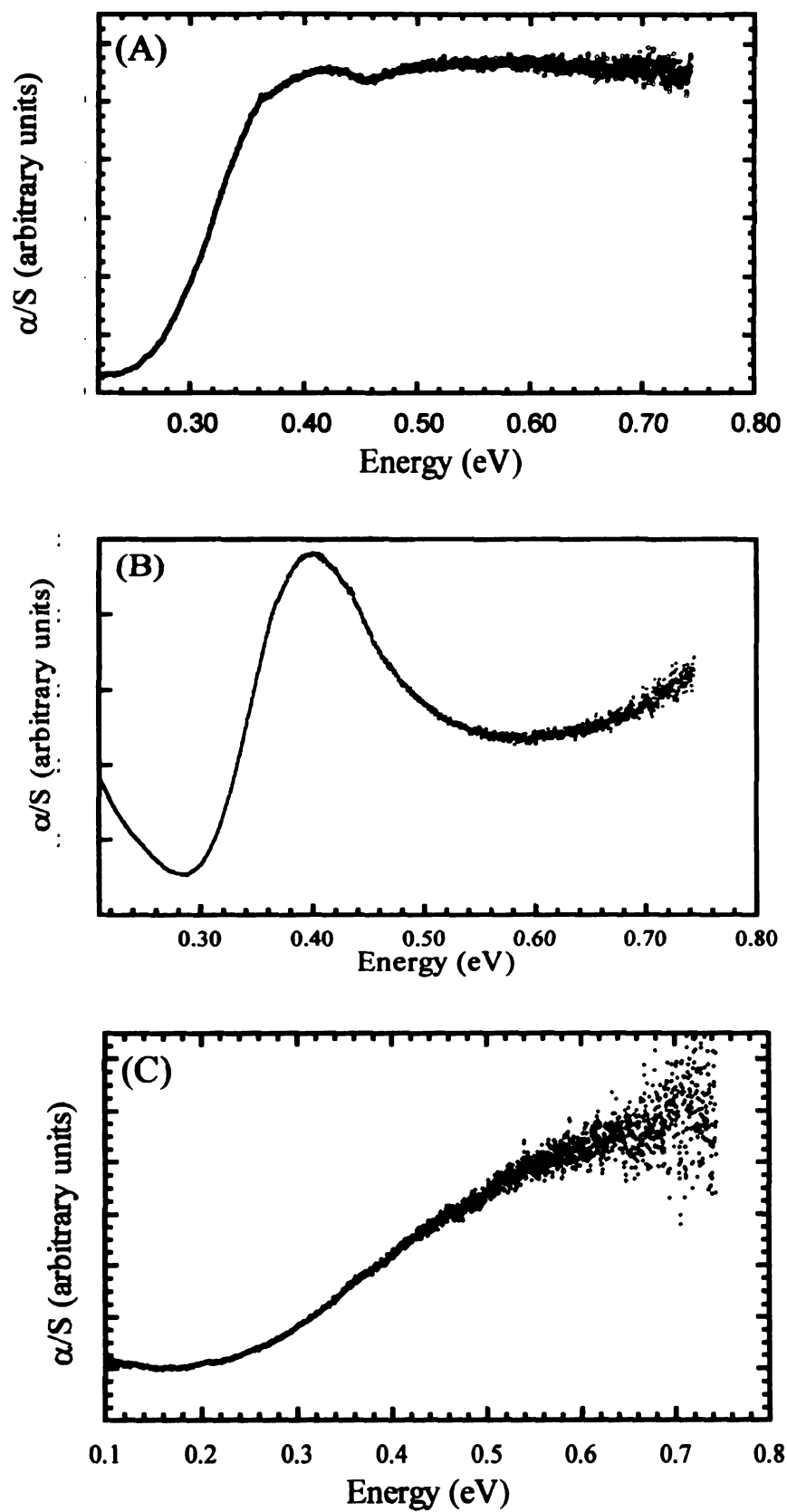
Figure 7.11 Diffuse reflectance optical spectra of (A) $Rb_2BaCu_8Te_{10}$, (B) $Cs_2BaCu_8Te_{10}$ and (C) $Rb_2EuCu_8Te_{10}$ (in the Mid-IR region).

Heat Capacity - The heat capacity was measured for both $Rb_2BaCu_8Te_{10}$ and $Cs_2BaCu_8Te_{10}$ and the results are shown in Figure 7.12. All samples show a typical heat capacity temperature dependence. By plotting the data as Heat capacity/T vs T^2, see Figure 7.13, it is possible to derive the Debye temperatures, Θ_D, through the following relationships,

$$C_P = \gamma T + \beta T^3 \qquad \text{(eq. 2)}$$

$$\Theta_D = \left[\frac{1.944}{\beta} \right]^{1/3} \times 10 \qquad \text{(eq. 3)}$$

where the first term of eq. 2, γT, is the electronic contribution to the heat capacity and the second term, βT^3, is the lattice contribution to the heat capacity. The Debye temperature is proportional to the stiffness of the lattice, i.e., the stiffness of the interatomic force constants and bonding energies. If the Debye temperature is low, the material should possess a low thermal conductivity. The advantage to measuring the heat capacity over thermal conductivity is that much less sample is needed to perform the experiment and the experiment itself is easier to perform. The Debye temperatures for the $Rb_2BaCu_8Te_{10}$ ranged from 345-354K while those for the $Cs_2BaCu_8Te_{10}$ samples were somewhat lower ranging from 312-320K, see Table 7.9. Application of a magnetic field had no effect on the temperature dependence or the magnitude of the heat capacity. The γ values for both compounds were also derived from the low temperature data (Table 7.9) and they average 0.279 mJ/mol-K^2. For semiconductors with a well-defined energy gap, γ

= 0. Typical metals have γ values ranging from $0.008 - 10.7$ mJ/mol-K^2. However, there are examples of semiconductors that have a $\gamma > 0$ within the range observed here.[11] The deviation from zero can be explained again by the argument that these samples are doped with impurities making the material a degenerate semiconductor. Therefore, from these results, we can conclude that the $A_2BaCu_8Te_{10}$ (A = Rb, Cs) materials are narrow gap semiconductors.
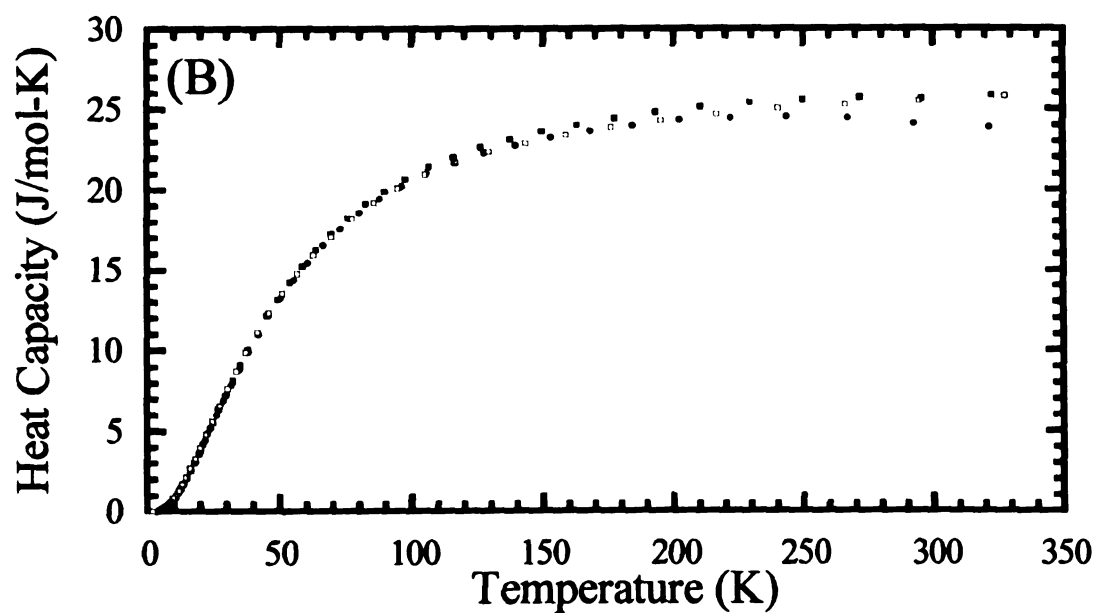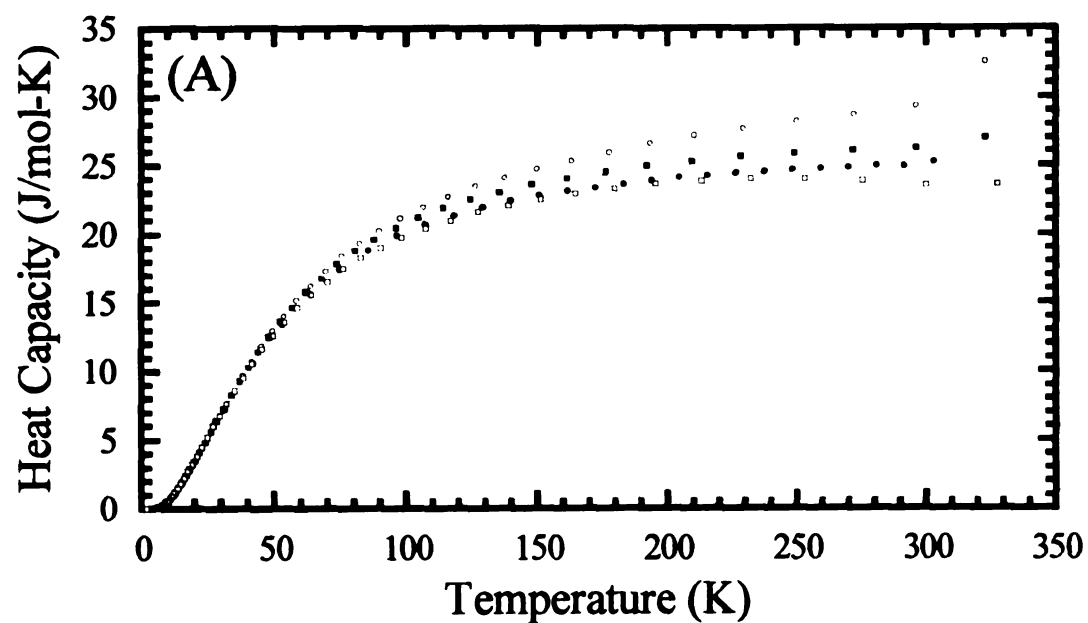
Figure 7.12 Heat capacity (J/mol-K) data for (A) four ingots of $Rb_2BaCu_8Te_{10}$ and (B) three ingots of $Cs_2BaCu_8Te_{10}$ as a function of temperature.
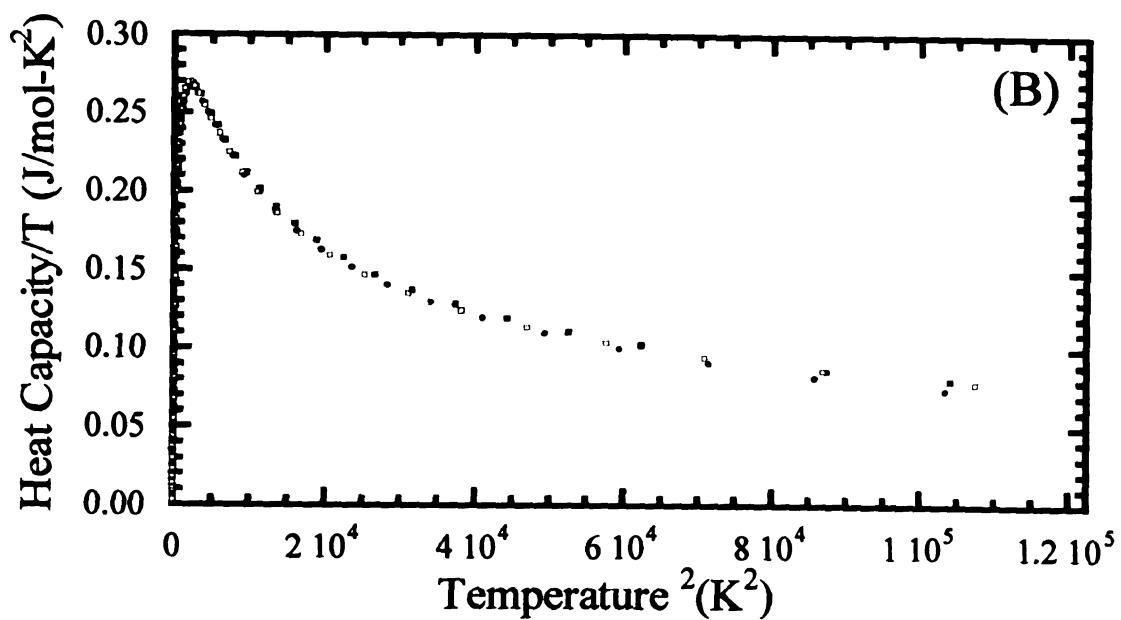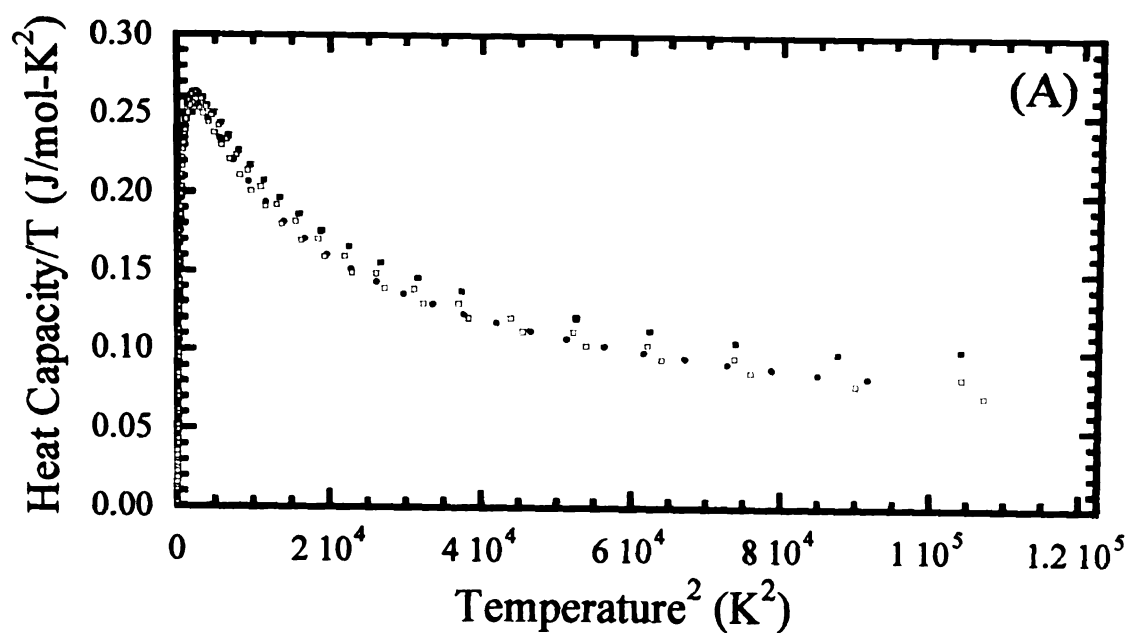
Figure 7.13 Heat capacity/T data (J/mol-K^2) vs T^2 data for (A) four ingots of Rb$_2$BaCu$_8$Te$_{10}$ and (B) three ingots of Cs$_2$BaCu$_8$Te$_{10}$.

Table 7.9 Room temperature values for the electrical conductivity, thermopower, and heat capacity of $A_2MCu_8Te_{10}$ (A = K, Rb, Cs; M = Ba, Eu) and the Debye temperatures and γ values derived from the heat capacity

Compound	Type	Electrical Conductivity σ (S/cm)	Thermopower S (μV/K)	Heat Capacity (J/mol-K)	Debye Temperature Θ_D (K)	γ value (mJ/mol -K^2)
$K_2BaCu_8Te_{10}$	ingot	185 S/cm	33 μV/K	———	———	——
$Rb_2BaCu_8Te_{10}$	crystal	108 S/cm	150 μV/K	———	———	——
$Rb_2BaCu_8Te_{10}$	ingot (S1)	588 S/cm	33 μV/K	22 J/mol-K	345K	0.223
$Rb_2BaCu_8Te_{10}$	ingot (S2)	233 S/cm	54 μV/K	29 J/mol-K	354K	——
$Rb_2BaCu_8Te_{10}$	ingot (S3)	588 S/cm	32 μV/K	27 J/mol-K	350K	0.519
$Rb_2BaCu_8Te_{10}$	ingot (S4)	28 S/cm	55 μV/K	23 J/mol-K	352K	0.200
$Rb_2BaCu_8Te_{10}$	ingot (S5)	120 S/cm	68 μV/K	———	———	——
$Rb_2BaCu_8Te_{10}$ + 0.1 Ba	ingot	303 S/cm	59 μV/K	———	———	——
$Rb_2BaCu_8Te_{10}$ + 0.3 Ba	ingot	182 S/cm	75 μV/K	———	———	——
$Rb_2BaCu_8Te_{10}$ + 0.4 Ba	ingot	64 S/cm	122 μV/K	———	———	——
$Cs_2BaCu_8Te_{10}$	ingot (S6)	172 S/cm	42 μV/K	24 J/mol-K	320K	0.335
$Cs_2BaCu_8Te_{10}$	ingot (S7)	179 S/cm	33 μV/K	26 J/mol-K	312K	0.239
$Cs_2BaCu_8Te_{10}$	ingot (S8)	417 S/cm	30 μV/K	25 J/mol-K	312K	0.156
$Cs_2BaCu_8Te_{10}$	ingot (S9)	250 S/cm	40 μV/K	———	———	——
$Rb_2EuCu_8Te_{10}$	pellet	2273 S/cm	14 μV/K	———	———	——
$Rb_2EuCu_8Te_{10}$	ingot	1852 S/cm	17 μV/K	———	———	——
$Rb_2EuCu_8Te_{10}$ + 0.2Eu	ingot	2273 S/cm	20 μV/K	———	———	——

Raman Spectroscopy - The Raman spectra of $Rb_2BaCu_8Te_{10}$ and $Cs_2BaCu_8Te_{10}$ are shown in Figure 7.14 and shows shifts at $121 cm^{-1}$ and $140 cm^{-1}$. These can be assigned as the stretching vibration of the ditelluride units in the structure. Unfortunately, the experimental apparatus prevented being able to observe any vibrations below $90 cm^{-1}$, which would most likely be the "rattling" modes of the A^+ (A = Rb, Cs) or Ba^{2+} ions.

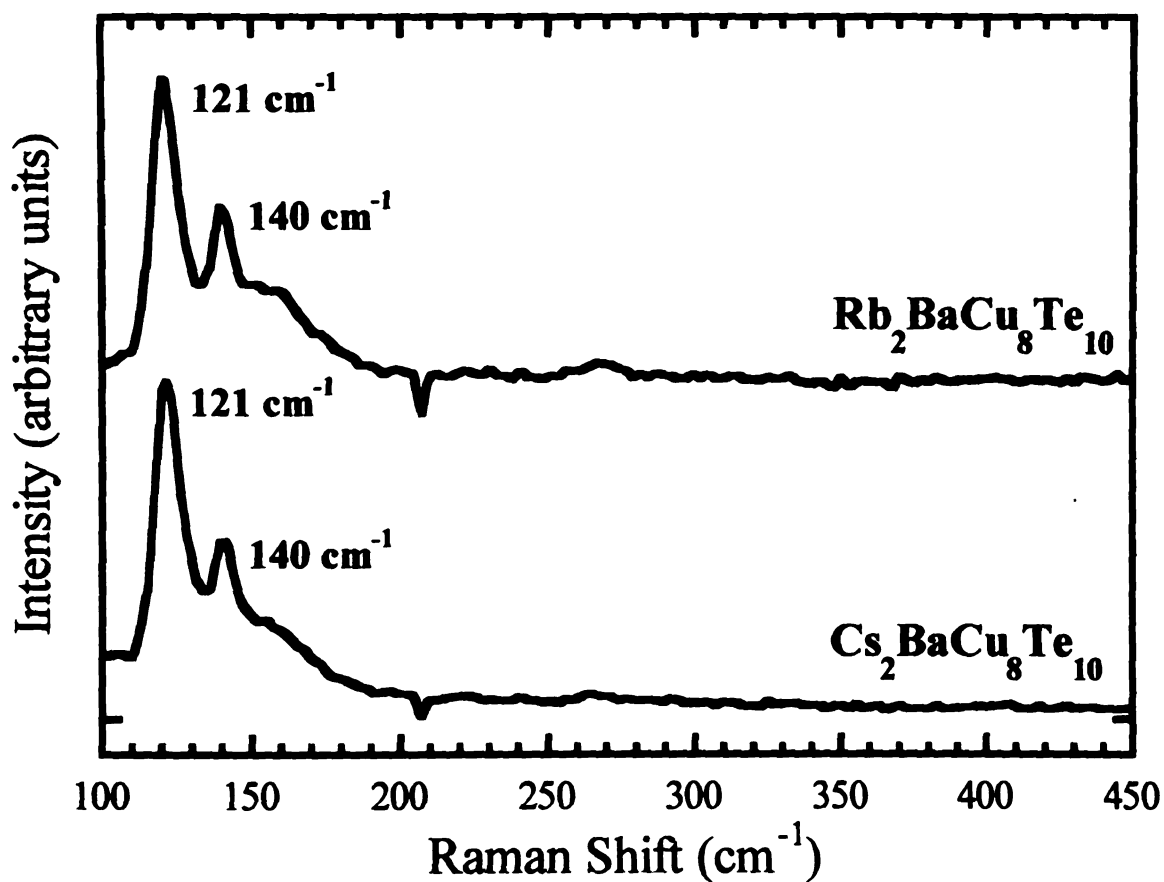**Figure 7.14**   Raman Spectra of $Cs_2BaCu_8Te_{10}$ and $Rb_2BaCu_8Te_{10}$

Magnetic Susceptibility – Variable temperature magnetic susceptibility data

for $Rb_2EuCu_8Te_{10}$ was measured over the range of 5-300K at 6000G. A plot of

$1/\chi_M$ vs T (see Figure 7.15A) shows that this material exhibits perfect Curie-Weiss

behavior. A μ_{eff} value of 6.95 BM and a Weiss constant of -17K was estimated by

fitting a straight line to the data above 100K. This value is less than what is

expected for an f^7 configuration or Eu^{2+} (7.9 - 8.0 BM) but very different from

that expected for Eu^{3+} (3.3-3.5 BM).[12]   Recall, however, that the charge transport

measurements on $Rb_2EuCu_8Te_{10}$ indicate that the material is actually a solid

solution between $Rb_2EuCu_8Te_{10}$ and $Rb_3Cu_8Te_{10}$ and the true composition is

$Rb_2[Eu_{1-x}Rb_x]Cu_8Te_{10}$. Thus, we should expect a lower μ_{eff} value since there is

less than one paramagnetic center per formula. That is indeed what is observed

and the data appears to support this argument. The μ_{eff} value can therefore be used

to calculate the true chemical formula, which is $Rb_{2.24}Eu_{0.76}Cu_8Te_{10}$.

The magnetic susceptibility was also measured for $Rb_2EuCu_8Te_{10}$ at 3000G and

careful diamagnetic corrections were made.

The molar magnetic susceptibility plotted vs temperature for

$Rb_2BaCu_8Te_{10}$ is shown in Figure 7.15B. Since there are no unpaired electrons on

the compound, it is expected to behave diamagnetic. However, if the material is

slightly paramagnetic after all diamagnetic corrections are performed, the material

is said to possess Pauli paramagnetism. Pauli paramagnetism is proportional to

the density of states (DOS) at the Fermi Level and therefore, its contribution is due

to conduction electrons of a metallic material since a semiconducting material has no free electrons at the Fermi Level.[11] Therefore, it is possible to get a qualitative idea as to whether or not $Rb_2BaCu_8Te_{10}$ is a metal or a semiconductor from the magnetic susceptibility data. The data shows negative values down to 10K, suggesting "true" diamagnetic behavior. The positive values below 10K can be attributed to small paramagnetic impurities in the sample. From this, we can conclude that there are essentially no free electrons at the Fermi Level and the material is a narrow gap semiconductor.
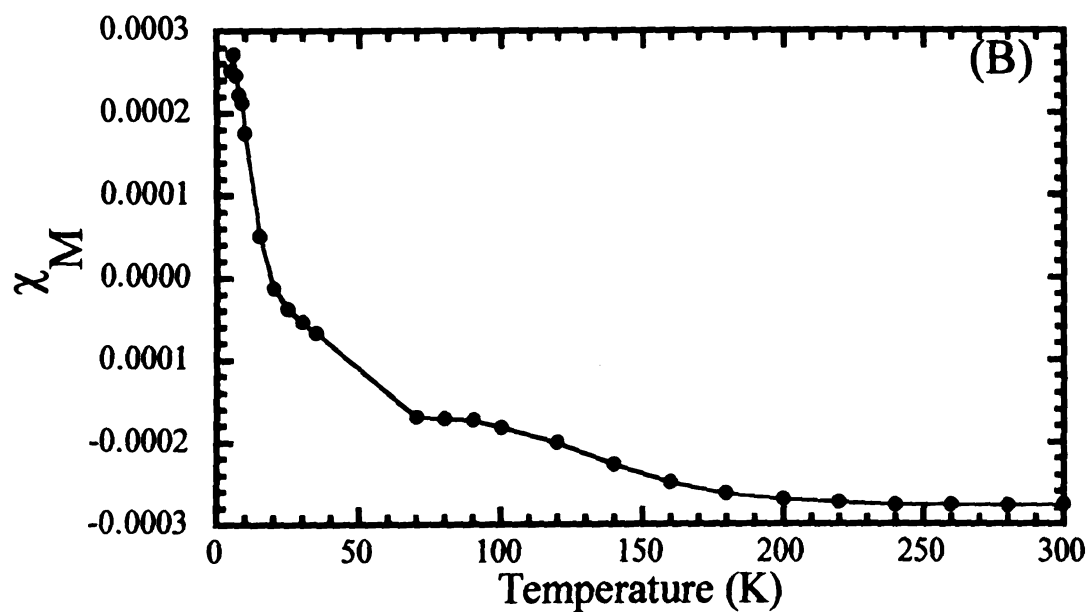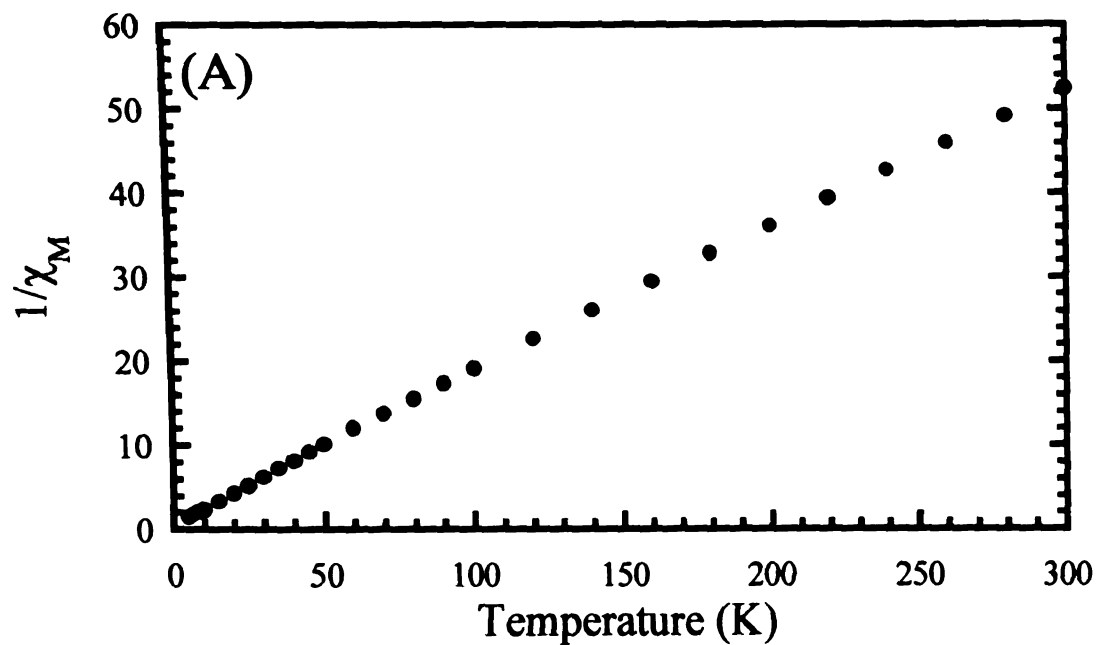
Figure 7.15 (A) Inverse molar magnetic susceptibility ($1/\chi_M$) plotted against temperature (2-300K) for $Rb_2EuCu_8Te_{10}$ and (B) Molar magnetic susceptibility (χ_M) plotted against temperature (2-300K) for $Rb_2BaCu_8Te_{10}$.

Thermal Analysis - The DTA spectra of $A_2MCu_8Te_{10}$ (A = Rb, Cs; M = Ba, Eu) show several endothermic and exothermic peaks below 650°C , see Figure 7.16. The powder X-ray diffraction patterns before and after heating are the same, suggesting that the materials melt congruently. However, the fact there are several peaks in the DTA spectra indicates that either the thermal behavior is very complicated or the materials are not pure. The question of purity can once again be explained by the previous argument that the material is likely a solid solution between $A_3Cu_8Te_{10}$ and $A_2MCu_8Te_{10}$. While $Rb_3Cu_8Te_{10}$ has been reported to decompose around 400°C, $Rb_2BaCu_8Te_{10}$ is believed to melt congruently at approximately 500°C. From Figure 7.17A, it can therefore be crudely estimated that the most intense thermal events at 491°C and 454°C are the melting and recrystallization temperatures, respectively, for $Rb_2BaCu_8Te_{10}$. The other six thermal events can be attributed to either the melting and recrystallization of the solid solution phase(s), $Rb_{2+x}Ba_{1-x}Cu_8Te_{10}$ (0 < x < 1), or the decomposition of $Rb_3Cu_8Te_{10}$. Figures 7.17B and 7.17C show similar phenomena for $Rb_2EuCu_8Te_{10}$ and $Cs_2BaCu_8Te_{10}$, respectively. From the charge transport measurements, it could be predicted that, with added Ba or Eu in the synthesis, the products would be more of a single phase and that the lower temperature thermal events could be eliminated. The DTA spectra of $Rb_2MCu_8Te_{10}$ + 0.4M (M = Ba, Eu), however, suggest otherwise. There does not seem to be any noticeable improvement in the DTA diagram and it appears as if the location and intensity of the thermal events varies from sample to sample. In fact, if the intensity of the higher temperature

thermal events gives any indication as to the percentage of $A_2MCu_8Te_{10}$ (A = K, Rb, Cs; M = Ba, Eu) present in the sample over $A_3Cu_8Te_{10}$ or $Rb_{2+x}Ba_{1-x}Cu_8Te_{10}$ $(0 < x < 1)$, the spectra shown in Figure 7.16 are thus far the most single phase. Given the observed behavior, we cannot at this stage unequivocally conclude that these materials actually melt congruently.
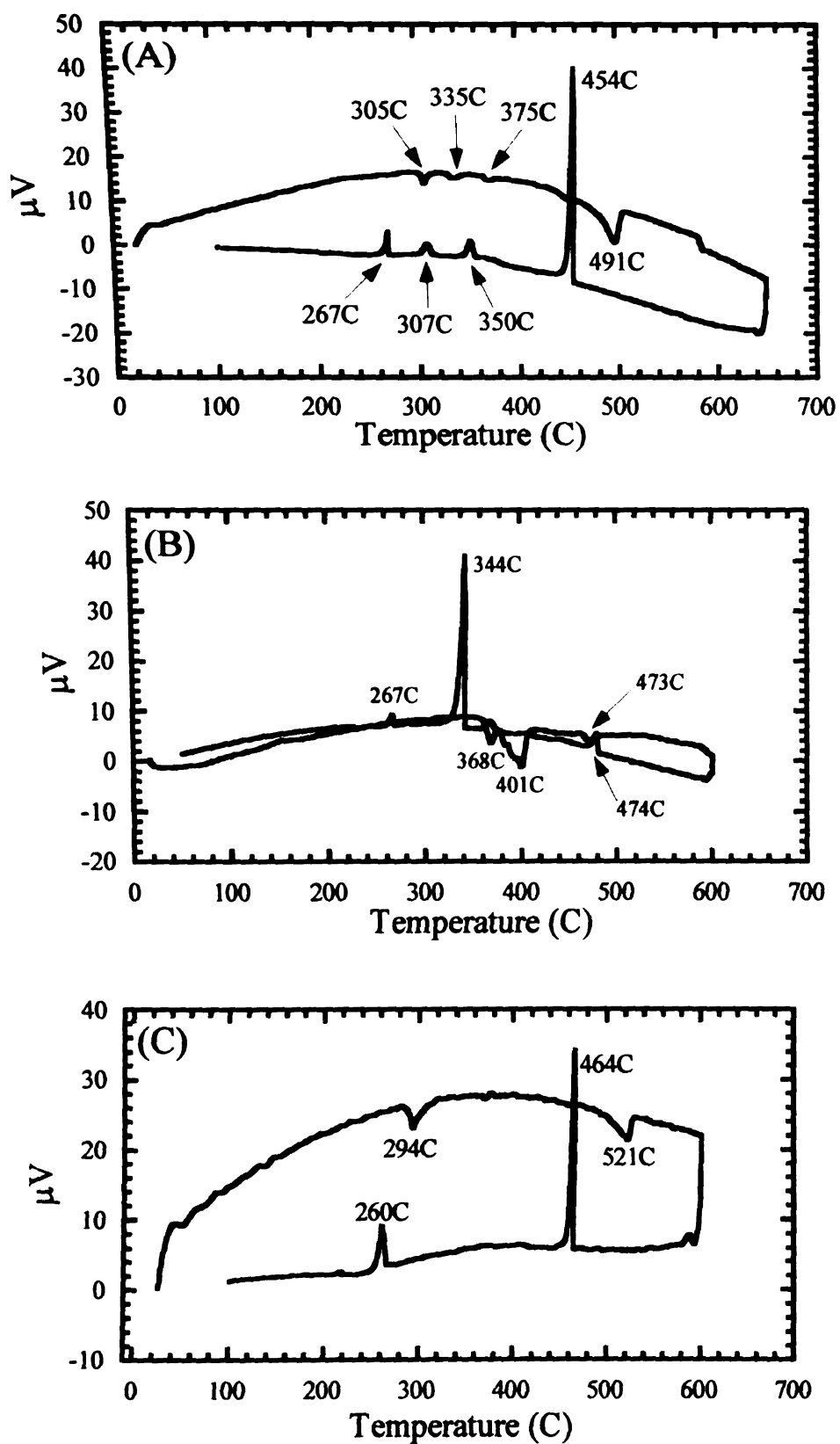
Figure 7.16 – DTA diagrams of (A) $Rb_2BaCu_8Te_{10}$, (B) $Rb_2EuCu_8Te_{10}$, and (C) $Cs_2BaCu_8Te_{10}$

D. Conclusions

Although a lot of work has been done to try and understand the physical properties of the compounds, $A_2MCu_8Te_{10}$ (A = K, Rb, Cs; M = Ba, Eu), a lot more work needs to be done. For example, we are still not completely certain that the compound $Rb_2EuCu_8Te_{10}$ really exists. While the physical data collected thus far seems to suggest that it does, we have not yet been able to obtain single crystals for a structure determination. Also, we have not yet been able to synthesize the compounds $A_2BaCu_8Te_{10}$ (A = K, Rb, Cs) in a completely pure ingot form. The "Ba rich" experiments, however, have led us in the right direction and allowed us to understand that these materials are most likely solid solutions of the type $A_2[Ba_{1-x}A_x]Cu_8Te_{10}$ (A = K, Rb, Cs), giving rise to semimetallic to metallic properties. Although we have experimentally observed a bandgap for these materials, the DFT calculations suggest metallic behavior. By measuring the heat capacity and measuring the magnetic susceptibility, however, we were able to support the fact that that these materials are indeed semiconductors and now believe that the theoretical calculations have underestimated the magnitude of the gap. Differential thermal analysis appears to be a very useful tool in determining the purity of the sample. This, coupled with electrical conductivity data should make it possible to fine-tune the synthesis to yield pure $A_2BaCu_8Te_{10}$ (A = K, Rb, Cs) samples in ingot form. Once the synthesis is optimized, thermal conductivity measurements need to be performed. Further optimization of the electrical

properties will include doping the sample with Se and/or Sb. These experiments

are currently in progress for $K_2BaCu_8Te_{10}$.

References

1 "Thermoelectric Materials – New Directions and Approaches", *Mat. Res. Soc. Symp. Proc.*, **1997**, vol 478. Edited by T.M. Tritt, M.G. Kanatzidis, H.B. Lyon, and G.D. Mahan

2 Zhang, X.; Park, Y.; Hogan, T.; Schindler, J.L.; Kannewurf, C.R.; Seong, S.; Albright, T.; Kanatzidis, M.G. *J. Am. Chem. Soc.* **1995**, 117, 10300.

3 (a) Slack, G.A.; "New Materials and Performance Limits for Thermoelctric Cooling" <u>CRC Handbook of Thermoelectrics</u>, CRC Press (Boca Raton, 1995), p 407. (b) Slack. G.A., in "Solid State Physics", eds. Ehrnereich, H; Seitz, F.; Turnbull, D. (Academic, New York, 1977), Vol 34, P.1.

4 (a) Nolas, G.S.; Slack, G.A.; Morelli, D.T.; Tritt, T.M., Ehrlich, A.C. *J. Appl. Phys.* **1996**, 79, 4002. (b) Nolas, G.S.; Morelli, D.T.; Tritt, T.M. *Annu. Rev. of Mat. Sci.* **1999**, 29, 89.

5 Parkin, I.P.; Fitzmaurice, J.C. *Polyhedron* **1993**, 12, 1569.

6 SMART: Siemens Analytical Xray Systems, Inc., Madison, WI, 1994.

7 SAINT: Version 4.0, Siemens Analytical Xray Systems, Inc., Madison WI, 1994-1996.

8 SADABS: Sheldrick, G.M. University of Göttengen, Germany, to be published.

9 Sheldrick, G.M. SHELXTL, Version 5; Siemens Analytical Xray Systems, Inc.; Madison, WI, 1994.

10 Patschke, R.; Zhang, X.; Singh, D.; Schindler, J.; Kannewurf, C.R.; Lowhorn, N.; Tritt, T.; Nolas, G.; Kanatzidis, M.G. *Manuscript in preparation.*

11 Kittel, C., *Introduction to Solid State Physics*, John Wiley & Sons, Inc. 1986, pp 141 and 413-416.

12 Greenwood, N. N.; Earnshaw, A. *Chemistry of the Elements*; Pergamon Press: New York, **1984**, 1443.

354